

University of Kentucky

UKnowledge

---

Theses and Dissertations--Molecular and Cellular Biochemistry

Molecular and Cellular Biochemistry

---


2021

## PRE-CLINICAL ADVANCEMENTS IN BIOMARKERS, TOOLS, AND THERAPEUTICS FOR A METABOLIC NEURODEGENERATIVE DISEASE

Zoë Simmons

University of Kentucky, zoerainesimmons@gmail.com

Author ORCID Identifier:

 <https://orcid.org/0000-0001-6730-7881>

Digital Object Identifier: <https://doi.org/10.13023/etd.2021.327>

[Right click to open a feedback form in a new tab to let us know how this document benefits you.](#)

### Recommended Citation

Simmons, Zoë, "PRE-CLINICAL ADVANCEMENTS IN BIOMARKERS, TOOLS, AND THERAPEUTICS FOR A METABOLIC NEURODEGENERATIVE DISEASE" (2021). *Theses and Dissertations--Molecular and Cellular Biochemistry*. 56.

[https://uknowledge.uky.edu/biochem\\_etds/56](https://uknowledge.uky.edu/biochem_etds/56)

This Doctoral Dissertation is brought to you for free and open access by the Molecular and Cellular Biochemistry at UKnowledge. It has been accepted for inclusion in Theses and Dissertations--Molecular and Cellular Biochemistry by an authorized administrator of UKnowledge. For more information, please contact [UKnowledge@lsv.uky.edu](mailto:UKnowledge@lsv.uky.edu).

## **STUDENT AGREEMENT:**

I represent that my thesis or dissertation and abstract are my original work. Proper attribution has been given to all outside sources. I understand that I am solely responsible for obtaining any needed copyright permissions. I have obtained needed written permission statement(s) from the owner(s) of each third-party copyrighted matter to be included in my work, allowing electronic distribution (if such use is not permitted by the fair use doctrine) which will be submitted to UKnowledge as Additional File.

I hereby grant to The University of Kentucky and its agents the irrevocable, non-exclusive, and royalty-free license to archive and make accessible my work in whole or in part in all forms of media, now or hereafter known. I agree that the document mentioned above may be made available immediately for worldwide access unless an embargo applies.

I retain all other ownership rights to the copyright of my work. I also retain the right to use in future works (such as articles or books) all or part of my work. I understand that I am free to register the copyright to my work.

## **REVIEW, APPROVAL AND ACCEPTANCE**

The document mentioned above has been reviewed and accepted by the student's advisor, on behalf of the advisory committee, and by the Director of Graduate Studies (DGS), on behalf of the program; we verify that this is the final, approved version of the student's thesis including all changes required by the advisory committee. The undersigned agree to abide by the statements above.

Zoë Simmons, Student

Dr. Matthew Shawn Gentry, Major Professor

Dr. Trevor Creamer, Director of Graduate Studies

**PRE-CLINICAL ADVANCEMENTS IN BIOMARKERS, TOOLS, AND THERAPEUTICS FOR A  
METABOLIC NEURODEGENERATIVE DISEASE**

---

DISSERTATION

---

A dissertation submitted in partial fulfilment of the  
requirements for the degree of Doctor of Philosophy in the  
College of Medicine at the University of Kentucky

By  
Zoë Raine Simmons  
Lexington, Kentucky  
Director: Dr. Matthew S. Gentry, Professor of Molecular and  
Cellular Biochemistry  
Lexington, Kentucky  
2021

Copyright © Zoë Raine Simmons 2021  
<https://orcid.org/0000-0001-6730-7881>

## ABSTRACT OF DISSERTATION

### **PRE-CLINICAL ADVANCEMENTS IN BIOMARKERS, TOOLS, AND THERAPEUTICS FOR A METABOLIC NEURODEGENERATIVE DISEASE**

Glycogen is the storage form of glucose and a highly important substrate for cellular metabolism. Characterization of the enzymes and mechanisms of glycogen metabolism began over 70 years ago and over the last 20 years, a previously unknown protein called laforin has emerged as an important contributor to glycogen metabolism homeostasis. Multiple labs demonstrated that laforin is a glycogen phosphatase and mutations in the gene encoding laforin cause the formation of aberrant glycogen-like aggregates called Lafora bodies (LBs). LBs are cytoplasmic, water-insoluble aggregates that drive neurodegeneration and early death in Lafora disease (LD) patients. The direct relationship between mutated laforin, LB formation, and LB neurotoxicity highlights the importance of glycogen metabolism in the brain. To translate this knowledge into effective LD therapeutics, a comprehensive analysis of pre-clinical biomarkers, a new set of tools, and advancements in therapeutic strategies are needed.

Consistent with the clinical phenotype, the laforin KO mouse model possesses LBs that drive neurodegeneration. A few studies have pointed to inflammatory responses in both astrocytes and microglia. However, these data need to be considered thoroughly to understand their relationship to LD. Two primary measures of pre-clinical LD therapeutic efficacy are to ablate LBs and reverse astrocyte activation. In the present work, we provide a longitudinal analysis of LBs and soluble glycogen and provide physiological evidence of the propensity of LBs to aggregate. In this same study, we provide evidence to suggest that microglia, not astrocytes, are drivers of an inflammatory response in LD.

Another potential therapeutic target is glycogen metabolism, however, the exact relationship between central carbon metabolism and laforin loss-of-function has yet to be defined and is essential for exploring therapeutic options to target it. Herein, we showcase a longitudinal discovery of changes to citric acid cycle intermediates specific to the brain of the aging laforin KO and WT mouse model. We find that metabolite load in adult mice is lower in laforin KOs compared to WT, however the metabolic signatures of aged laforin KOs and WT mice overlap. Using a predictive biomarker analysis tool, we find that a recently proposed driver of metabolic dysregulation in laforin KO mice,



glucosamine sequestration by PGBs, may also be driving aspects of metabolic disarray in aging. These results have generated hypotheses regarding damaged metabolic pathways in LD and aging that may be targeted for treatment.

These data are yet another indicator that laforin is critical for brain glycogen metabolism. While laforin is known to remove phosphate from glycogen, how phosphate impacts normal glycogen homeostasis or how hyperphosphorylation is detrimental to glycogen homeostasis and LB formation remain under investigation. Progress in this discovery could be accelerated with additional tools. The study presented here showcases the generation and characterization of six laforin nanobodies and their epitopes and demonstrates that one inhibits laforin's phosphatase activity. These laforin nanobodies could be useful tools for discovering the importance of glycogen phosphate and its modulation by laforin, WT laforin crystallization, laforin physical interactions, and laforin's dynamic localization. Overall, these nanobodies represent an important set of tools that will open new avenues to illuminate the mechanism of laforin's role in normal glycogen metabolism and LD.

Other applications of the laforin nanobodies are *in vitro* detection assays for pre-clinical/clinical assessment of laforin recovery treatments. Two theoretical therapeutic options for laforin recovery include premature termination codon (PTC) readthrough therapy and adeno-associated viral vector (AAV) therapy. Both these therapeutic strategies aim to deliver corrected genetic information for proper translation of the protein of interest. In the study we present here, we generate one sandwich ELISA with two putative functions for either PTC readthrough or AAV pre-clinical/clinical development using the laforin nanobodies.

This work has advanced pre-clinical biomarkers, tools, and therapeutics for LD, a metabolic neurodegenerative disease. The results of which will be the basic framework of effective therapeutic development for several possible treatment routes and mechanistic insights into glycogen metabolism.

KEYWORDS: Lafora disease, biomarkers, nanobodies, drug screening, metabolomics, neurodegeneration.

---

Zoë Raine Simmons

*(Name of Student)*

---

07/09/2021

Date

**PRE-CLINICAL ADVANCEMENTS IN BIOMARKERS, TOOLS, AND THERAPEUTICS FOR A  
METABOLIC NEURODEGENERATIVE DISEASE**

By  
Zoë Raine Simmons

Dr. Matthew Shawn Gentry  
\_\_\_\_\_  
Director of Dissertation

Dr. Trevor Creamer  
\_\_\_\_\_  
Director of Graduate Studies

07/09/2021  
\_\_\_\_\_  
Date

## **DEDICATION**

To all the teachers.

## ACKNOWLEDGMENTS

### THANK YOU TO—

**My advisor:** Dr. Matthew Gentry, for offering me an enormous breadth of trust and for the opportunity to develop trust in myself (but verify, of course).

**The Vander Kooi Lab:** For being wise. You were a lifeline I called many times.

**My Gentry Lab colleagues and friends:** For always pointing me in the right direction. I hope I have been able to return the favor. If not, then in the future. Please stay connected. LinkedIn: @zoerainesimmons

**Dr. Ramon Sun and the Sun Lab:** For helping me run hundreds upon hundreds of samples on your mass specs.

**My doctoral dissertation committee:** Dr. Sylvie Garneau-Tsodikova, Dr. Harry LeVine, and Dr. Haining Zhu, for being my referees.

**My parents:** Wendy and Bill Simmons, for your genetic material. For patiently waiting for this eternity of education to finish. For insisting since I was a child that “you can do it” despite my efforts to be disagreeable.

**My brother:** Wynn Simmons, for continually and genuinely believing in me, without a shadow of a doubt.

**My partner:** Alex Eberle, for many semesters of dropping me off and picking me up from lab. For doing extra chores when I’m burnt out. For snapping me out of existential crises. For agreeing to move to the Northeast even though it’s colder.

**Antihistamines:** Cetirizine and Loratadine, for remedying the debilitating allergies I developed when I moved here.

**Spell check.**

## TABLE OF CONTENTS

<b>ACKNOWLEDGMENTS .....</b>	<b>v</b>
<b>LIST OF TABLES .....</b>	<b>x</b>
<b>CHAPTER 1. The glycogen dysmetabolism hypothesis of neurodegenerative diseases: convergent clues from neuropathology to biochemistry .....</b>	<b>1</b>
1.1 Introduction .....	1
1.2 Technological advances for quantifying and analyzing glycogen .....	3
1.3 Hypothesis: Aberrant glycogen metabolism is an underlying cause of neurodegenerative disease.....	5
1.3.1 Glycogen and cognitive function .....	5
1.3.2 Glycogen and neural energetics .....	6
1.4 Lafora disease.....	8
1.4.1 LD PGBs drive disease pathogenesis.....	8
1.4.2 Lafora body localization.....	10
1.4.3 Lafora body architecture .....	11
1.4.4 Aberrant glycogen metabolism in Lafora disease .....	11
1.4.5 Clinical evidence of brain metabolic defects in LD.....	12
1.5 Pompe disease - glycogen storage disease type II .....	14
1.5.1 Aberrant glycogen in Pompe disease - glycogen storage disease type II (GSD II) 14	
1.5.2 Aberrant metabolism in Pompe disease .....	15
1.6 Aging .....	16
1.6.1 Aberrant glycogen in aging .....	16
1.6.2 Aberrant metabolism in aging .....	17
1.7 Temporal lobe epilepsy.....	19
1.7.1 Aberrant glycogen in temporal lobe epilepsy .....	19
1.7.2 Aberrant metabolism in temporal lobe epilepsy .....	20
1.8 Amyotrophic lateral sclerosis.....	22
1.8.1 Aberrant glycogen in amyotrophic lateral sclerosis .....	22
1.8.2 Aberrant glycogen metabolism in amyotrophic lateral sclerosis .....	22
1.9 Alzheimer's disease.....	24
1.9.1 Aberrant glycogen in Alzheimer's disease .....	24
1.9.2 Glycogen metabolism in Alzheimer's disease .....	25

1.10	<i>Conclusions and future directions</i> .....	26
<b>CHAPTER 2. Pathological biomarkers of a glycogen metabolism disorder in the aging brain 31</b>		
2.1	<i>Introduction</i> .....	31
2.2	<i>Methods</i> .....	34
2.2.1	Mouse models and tissue preparation .....	34
2.2.2	Histology.....	34
2.2.3	Gas-chromatography mass spectrometry (GCMS) analysis of glycogen .....	34
2.2.4	Quantification and statistical analysis.....	35
2.3	<i>Results</i> .....	36
2.3.1	Longitudinal analysis of glycogen and PGBs in the brain, skeletal muscle, and heart 36	
2.3.2	Longitudinal analysis of glycogen and PGBs in the hippocampus, cerebellum, and brainstem .....	38
2.3.3	Average size and size variation of LD and aging PGBs in the hippocampus .	39
2.3.4	Longitudinal analysis of Gfap and Iba1 inflammatory markers.....	41
2.4	<i>Discussion</i> .....	77
2.4.1	Soluble versus insoluble glycogen in the LKO mouse.....	77
2.4.2	LB aggregation and diverging characteristics of corpora amylacea .....	78
2.4.3	Inflammation markers of LD .....	79
2.5	<i>Final conclusions</i> .....	80
<b>CHAPTER 3. Metabolic changes during aging compared with a neurodegenerative disease 81</b>		
3.1	<i>Introduction</i> .....	81
3.2	<i>Methods</i> .....	84
3.2.1	Mouse models and tissue preparation .....	84
3.2.2	Gas Chromatography-Mass Spectrometry (GC-MS) analysis .....	84
3.3	<i>Results</i> .....	86
3.3.1	TCA metabolite signatures of the aging WT and LKO brain .....	86
3.3.2	TCA metabolite signatures of the aging WT and LKO skeletal muscle and heart 87	
3.3.3	TCA metabolite signatures of laforin heterozygote aging mice .....	87
3.3.4	Statistical analysis of TCA metabolite profile variation in aging WT, LKO, and laforin heterozygotes and biomarker prediction of LD and aging .....	88
3.4	<i>Discussion</i> .....	89

<b>CHAPTER 4. Generation and characterization of a laforin nanobody inhibitor .....</b>	<b>106</b>
4.1 Introduction.....	106
4.2 Methods .....	108
4.2.1 VHH library generation .....	108
4.2.2 Isolation of laforin specific nanobodies .....	109
4.2.3 Sequence verification, alignment, and evolutionary analysis .....	109
4.2.4 Screening for VHH expression .....	109
4.2.5 Small scale pulldowns .....	110
4.2.6 Nanobody purification .....	110
4.2.7 Size exclusion analysis of VHH-laforin complexes.....	111
4.2.8 Hydrogen Deuterium Exchange Mass Spectrometry (HDX) .....	111
4.2.9 Phosphatase assays .....	112
4.3 Results .....	113
4.3.1 Anti-laforin nanobody primary screen.....	113
4.3.2 Size-exclusion analysis of anti-laforin nanobodies complexed to laforin... 113	
4.3.3 Nanobody epitope mapping via Hydrogen-Deuterium Exchange Mass Spectrometry (HDX) .....	114
4.3.4 Nb72 inhibits the general phosphatase activity of laforin .....	114
4.3.5 Nb72 inhibits the glycogen phosphatase activity of laforin .....	115
4.4 Discussion .....	117
<b>CHAPTER 5. A nanobody-based ELISA screen for PTC readthrough of <i>Epm2a</i>.....</b>	<b>131</b>
5.1 Introduction.....	131
5.2 Methods .....	134
5.2.1 cDNA generation and sequencing.....	134
5.2.2 Reporter plasmid cloning.....	134
5.2.3 Cell culture transfections and drug treatments .....	135
5.2.4 SDS-PAGE and Western Blot.....	135
5.2.5 Enzyme assays .....	136
5.2.6 Laforin purification .....	136
5.2.7 Nanobody purification and HRP-conjugation .....	136
5.2.8 Enzyme-Linked Immunosorbent Assay (ELISA) .....	137
5.2.9 para-Nitrophenyl phosphate (pNPP) assay.....	137
5.3 Results .....	138
5.3.1 PTC mutations in <i>Epm2a</i> .....	138
5.3.2 A Western blot assay for screening PTCs.....	138
5.3.3 An enzymatic assay for screening PTCs.....	139
5.3.4 A nanobody based ELISA screening approach .....	141

5.4 Discussion ..... 144

**CHAPTER 6. Concluding remarks..... 159**

    6.1.1 Summary and future directions ..... 159

    6.1.2 Final conclusions..... 160

**BIBLIOGRAPHY ..... 161**

**VITA ..... 187**



## LIST OF TABLES

Table 1.1 Glycogen storage diseases. ....	28
Table 2.1 Descriptive statistics of PGB diameters.....	60
Table 4.1 DNA sequences of the six laforin binding nanobodies. ....	125
Table 5.1 Epm2a PTC mutations and corresponding nucleotide changes at the mRNA and gene level. ....	148

## LIST OF FIGURES

Figure 1.1 Electron microscopy (EM) and Periodic Acid Schiff stain (PAS) of glycogen deposits/PGBs. ....	29
Figure 1.2 Diagram of glycogen deposits/PGBs in neurodegenerative diseases.....	30
Figure 2.1 Whole brain PAS stain and GCMS analysis of glucose polymers on WT and LKO mice aged 1-, 3-, 6-, 9-, 12-, and 24-months.....	43
Figure 2.2 Whole brain Periodic Acid Schiff (PAS) staining. ....	44
Figure 2.3 Whole brain KM279 and IV58B6 IHC analysis of WT and LKO mice aged 1-, 3-, 6-, 9-, 12-, and 24-months. ....	45
Figure 2.4 Whole brain KM279 IHC. ....	46
Figure 2.5 Whole brain IV58B6 IHC. ....	47
Figure 2.6 Skeletal muscle and heart PAS stain and KM279 IHC analysis of WT and LKO mice aged 1-, 3-, 6-, 9-, 12-, 24-months. ....	48
Figure 2.7 Skeletal muscle Periodic Acid Schiff (PAS) staining. ....	49
Figure 2.8 Heart Periodic Acid Schiff (PAS) staining.....	50
Figure 2.9 Skeletal muscle KM279 IHC. ....	51
Figure 2.10 Heart KM279 IHC. ....	52
Figure 2.11 Brain region-of-interest KM279 and IV58B6 IHC analysis of WT and LKO mice aged 1-, 3-, 6-, 9-, 12-, 24-months. ....	53
Figure 2.12 Hippocampus KM279 IHC. ....	54
Figure 2.13 Brainstem KM279 IHC.....	55
Figure 2.14 Cerebellum KM279 IHC.....	56
Figure 2.15 Hippocampus IV58B6 IHC. ....	57
Figure 2.16 Brainstem IV58B6 IHC.....	58
Figure 2.17 Cerebellum IV58B6 IHC.....	59
Figure 2.19 Whole brain GFAP IHC. ....	62
Figure 2.20 Hippocampus GFAP IHC.....	63
Figure 2.21 Brainstem GFAP IHC. ....	64
Figure 2.22 Cerebellum GFAP IHC. ....	65
Figure 2.23 Whole Brain Iba1 IHC.....	66
Figure 2.24 Whole brain Iba1 IHC.....	67
Figure 2.25 Brainstem Iba1 IHC. ....	68
Figure 2.26 Cerebellum Iba1 IHC. ....	69
Figure 2.30 Quantitative and qualitative analysis of KM279 IHC on WT and LKO hippocampus of 6, 9, 12, 24-month-old mice. IHC analysis was performed using the Indica labs tissue analysis software (HALO) "Area Quantification" and ruler tool.....	73
Figure 2.31 Whole brain and region-of-interest cell count analysis of GFAP expressing astrocytes and Iba1 expressing microglia of 1, 3, 6, 9, 12-month-old-mice. ....	74
Figure 2.32 Whole brain GFAP IHC analysis on WT and laforin heterozygote brains aged 1, 3, 6, 9, 12-months. IHC analysis was performed using the Indica labs tissue analysis software (HALO) "Multiplex IHC" and "Area Quantification". ....	75
Figure 2.33 Whole brain Iba1 IHC analysis on WT and laforin heterozygote brains aged 1, 3, 6, 9, 12-months. IHC analysis was performed using the Indica labs tissue analysis software (HALO) "Multiplex IHC" and "Area Quantification". ....	76

Figure 3.1 Metabolomics workflow.....	91
Figure 3.2 WT brain TCA metabolites.....	92
Figure 3.3 WT versus LKO brain TCA metabolites.....	93
Figure 3.4 WT skeletal muscle TCA metabolites.....	94
Figure 3.5 WT versus LKO skeletal muscle TCA metabolites.....	95
Figure 3.6 WT heart TCA metabolites.....	96
Figure 3.7 WT versus LKO heart TCA metabolites.....	97
Figure 3.8 WT versus laforin heterozygote brain TCA metabolites.....	98
Figure 3.9 WT versus laforin heterozygote skeletal muscle TCA metabolites.....	99
Figure 3.10 WT versus laforin heterozygote heart TCA metabolites.....	100
Figure 3.11 PCA plots of brain TCA metabolites.....	101
Figure 3.12 PCA plots of skeletal muscle TCA metabolites.....	102
Figure 3.13 PCA plots of heart TCA metabolites.....	103
Figure 3.14 Biomarkers of LD and aging.....	105
Figure 4.1 Anti-laforin nanobody guide tree.....	119
Figure 4.2 Direct antigen binding nanobodies and comparison of their sequences.....	120
Figure 4.3 Size-exclusion (SEC) analysis of anti-laforin nanobodies complexed to laforin. .....	121
Figure 4.4 HDX analysis of anti-laforin nanobody binding of Nb41, Nb57, and Nb72....	123
Figure 4.5 Laforin activity in the presence of Nb72.....	124
Figure 4.6 Nanobody sequence alignment.....	126
Figure 4.7 HDX analysis of anti-laforin nanobody binding of Nb40, Nb50, and Nb73....	128
Figure 4.8 Anti-laforin nanobody sequence alignments.....	129
Figure 4.9 Laforin-nanobody activity assays.....	130
Figure 5.1 12 PTC mutations in Epm2a cause Lafora disease.....	147
Figure 5.2 Western blot screening of aminoglycoside induced readthrough of R241X.	149
Figure 5.3 Description of the dual gene reporter system.....	150
Figure 5.4. Enzymatic screening for identifying nonsense mutations responsive to aminoglycoside treatment.....	151
Figure 5.5 Enzymatic screening for identifying nonsense mutations responsive to G418 or escin treatment.....	152
Figure 5.6 Enzymatic screening for variability in gentamicin induced readthrough.....	153
Figure 5.7 Enzymatic screening of Epm2a R241X readthrough in NIH3T3 and HEK293 cells.....	154
Figure 5.8 Plate binding saturation curves of putative laforin capture or detection nanobodies.....	155
Figure 5.9 Saturation curves of laforin detection antibodies, Nb57-HRP and polyclonal anti-laforin antibody #113.....	156
Figure 5.10 Working range of recombinant laforin at optimized antibody concentrations. .....	157
Figure 5.11 Laforin nanobody ELISA detection from whole cell lysates.....	158

## CHAPTER 1. The glycogen dysmetabolism hypothesis of neurodegenerative diseases: convergent clues from neuropathology to biochemistry

### 1.1 Introduction

Despite several decades of profound progress in neurology and neuroscience, many neurodegenerative disorders remain largely untreatable<sup>1</sup>. Considering that the primary risk factor for neurodegenerative disorders is age and that by 2030 all baby boomers will be at least 65, the proportion of people most prone to neurodegenerative diseases will rise from the current ~15% (2020) to ~25% by 2060<sup>2-4</sup>. By 2040, deaths by these disorders are predicted to out-pace other prominent age-related fatalities due to lung cancer, colon cancer, liver cirrhosis, multiple sclerosis, female breast cancer, and malignant melanoma<sup>5</sup>. These statistics reflect the current and future US social and economic burdens with respect to age-related diseases. Recent progress has made significant contributions to identifying neurodegenerative hallmarks, including neuronal cell loss, atrophy, astrogliosis, pathological protein inclusions, inflammation, oxidative stress, mitochondrial dysfunction, ER stress, activation of microglia, hypoxia, and neuronal dysfunction<sup>3,6,7</sup>. Unfortunately, these hallmarks have not yielded disease altering therapies and treating neurodegeneration remains a futile battle<sup>8,9</sup>.

One emerging theory that may offer a new set of molecular targets is that metabolic defects underlie many neurodegenerative pathologies<sup>1,7</sup>. Clinical investigations of metabolic changes in neurodegenerative disorders identified <sup>18</sup>Fluorodeoxyglucose Positron Emission Tomography (<sup>18</sup>FDG PET) hypometabolism as a common, if not universal, characteristic of these disorders<sup>10</sup>. While dysregulated glucose metabolism is a clinical hallmark, the molecular underpinnings are still being defined. Additionally, metabolic vulnerabilities of specific neuronal clusters often accompany neurodegenerative disorders<sup>11</sup>.

Systemic glucose has been considered the primary fuel for the brain, but a growing body of literature strongly implies that glycogen, the mammalian glucose storage cache, plays an indispensable role in brain function<sup>12</sup>. The underappreciation of brain glycogen comes from historic skepticism about its very existence that stymied advances in brain glycogen metabolism until very recently when methodologies were developed to detect it<sup>13</sup>. Earlier attempts to quantify brain glycogen were undermined by the fact that it quickly degrades from the hypoxic brain<sup>14</sup>. This obstacle has been surmounted by rapid preservation methods including either immediate flash freezing or microwave fixation that are required to preserve it for robust and repeated quantification<sup>15</sup>. This understanding led to the recent discovery that 25% of brain glycogen contains glucosamine, a key building block for protein glycosylation<sup>16</sup>.

The basic architecture of glycogen and its metabolic enzymes are well-documented. Glucose polymers are linked via  $\alpha$ -1,4-glycosidic bonds via glycogen synthase (GS) that are branched approximately every 13 glucose residues with  $\alpha$ -1,6-glycosidic bonds via

glycogen branching enzyme (GBE). Glycogen is degraded by glycogen debranching enzyme (GDE) that releases single branched glucose moieties and glycogen phosphorylase (GP) that catalyzes the cleavage of two subunits of glucose<sup>13</sup>. Glucosamine is incorporated into brain glycogen by GS and released by the concerted efforts of GP and GDE<sup>16</sup>. Glycogen is also degraded in the lysosome by acid  $\alpha$ -glucosidase (GAA)<sup>17</sup>. As glycogen is the major glucose cache, its metabolism is tightly regulated in a tissue-dependent manner<sup>18</sup>. Aberrant glycogen metabolism results in glycogen storage disorders (GSDs), wherein glycogen is synthesized and accumulates yet it is not broken down<sup>17</sup>. In the case of Pompe disease (GSD II), mutations in GAA result in normal glycogen accumulating at a far greater rate than it can be broken down. However, many GSDs feature an aberrant glycogen that cannot be broken down by GAA, GDE, and/or GP<sup>19</sup>. Thus, aberrant glycogen is a diseased form that prevents cellular use of the glucose that is stored in it<sup>20</sup>.

Aberrant glycogen deposits are called polyglucosan bodies (PGBs) that were first identified in the aging brain by Purkinje<sup>21</sup>. The aging PGB, called corpora amylacea, originates from astrocytes and contains cellular debris. Corpora amylacea have been widely thought of as waste containers and recent work has proposed a route of expulsion from the brain to the cerebral spinal fluid and lymphatic meningeal system<sup>22</sup>. Another subset of PGBs are intracellular PGBs that are a common feature of CNS GSDs that were first identified in 1911 by Gonzalo Rodríguez-Lafora, a disciple of Alzheimer, Cajal, Vogt, Minkowski, and Kraepelin<sup>23</sup>. Lafora's discovery unmasked the pathophysiology of a GSD that produced a rare, insidious, and quickly fatal childhood dementia later named Lafora's disease (LD)<sup>24</sup>. Lafora predicted that a metabolic disorder causes the formation of the LD PGBs that drive LD progression. Greater than 100 years since Lafora's discovery, data from multiple laboratories support Lafora's hypothesis<sup>25-28</sup>. Strikingly, PGBs of varied physical morphologies have been identified in many other neurodegenerative disorders, not currently classified as GSDs (**Table 1.1A-F**)<sup>29-35</sup>.

In this chapter, recent data is highlighted that demonstrates glycogen dysmetabolism and PGBs as an integral factor of several neurodegenerative disorders, including Pompe disease, LD, aging, temporal lobe epilepsy (TLE), amyotrophic lateral sclerosis (ALS), and Alzheimer's disease (AD). The differing histopathology and anatomical locations of PGBs is described in each of these diseases and glycogen dysmetabolism is a potential common metabolic phenotype. We frame the progression of LD as an extreme phenotype of a metabolic imbalance that is driven by aberrant glycogen. As such, recent success regarding LD basic research and clinical therapeutic translation is a potential path for new therapeutics of common neurodegenerative disorders. We aim to inspire investigation of the glycogen dysmetabolism hypothesis of neurodegenerative diseases.

## 1.2 Technological advances for quantifying and analyzing glycogen

Several quantitative biochemical and histological staining methods to quantify glycogen have made large contributions to the investigation of brain glycogen but are limited in specificity, spatial scale, and/or resolution<sup>13,15</sup>. Biochemical assays are quantitative, requiring a large volume of sample that limits their ability to assess spatial distribution<sup>36</sup>. Nuclear magnetic resonance spectroscopy (MRS) is quantitative and can be performed on live subjects but is also limited in spatial resolution<sup>37</sup>. Electron microscopy yields detailed observations within an area limited to several micrometers<sup>15</sup>. Histological examination by light microscopy using PAS has been a historically preferred method to determine regional, cellular, and subcellular glycogen distribution<sup>19</sup>. However, PAS staining is not glycogen specific as it reacts with other carbohydrate polymers like glycoproteins and proteoglycans<sup>38</sup>.

A series of method and tool advancements for accurate and sensitive glycogen detection have recently emerged. The generation and development of two anti-glycogen antibodies, IV58B6 and ESG1A9, have been important for mapping and determining brain wide spatial arrangements and morphological characteristics of glycogen with high specificity using immunohistochemistry (IHC) or immunofluorescence (IF)<sup>15</sup>. IHC studies using either of the anti-glycogen antibodies revealed glycogen stores in the hippocampus, cerebellum, and cortex (especially the molecular layers) of the mouse and rat brain<sup>39</sup>. Studies utilizing these two antibodies has detected a heterogeneous storage pattern of glycogen at multiple spatial scales, which suggests that glycogen distribution and architecture may underlie local energy requirements and metabolism. The addition of secondary and tertiary labeling has allowed for the detection of glycogen at the subcellular level and has shown that glycogen in mice is normally localized to the fine processes of astrocytes while trace amounts are found in neurons<sup>15</sup>.

More recently, two significant advancements using mass spectrometry have been pioneered for accurate glycogen quantification and distribution analysis. An analytical method for quantifying carbohydrate polymers was developed using gas chromatography-coupled mass spectrometry (GCMS) that provides robust analysis of purified glycogen from tissue and quantification of the free glucose monomers<sup>40</sup>. Another novel workflow was developed to quantify and spatially visualize glycogen *in situ* using matrix-assisted laser desorption/ionization traveling-wave ion-mobility high-resolution mass spectrometry (MALDI TW IMS)<sup>16</sup>. This novel MALDI workflow has allowed exploration of the relationship between PGBs, glycogen, and protein N-linked glycosylation in specific brain regions (see section 1.4.3 and 1.4.4).

While these advanced glycogen analysis methods have largely been performed on mouse and rat samples, it is likely that the brain distribution, storage, and usage of glycogen differ among other species as well<sup>15</sup>. Regional glycogen storage may also depend on the metabolic state of the brain including the sleep cycle and circadian rhythm. Limited studies have shown that aging also influences glycogen dynamics<sup>39</sup>.

These and other integral factors on brain glycogen dynamics require more in-depth study especially with longitudinal dimensions to understand the extent of their influence in health and disease and may be facilitated with these technological advances.

### **1.3 Hypothesis: Aberrant glycogen metabolism is an underlying cause of neurodegenerative disease**

Although a range of shared therapeutic targets have been identified for neurodegenerative disorders, current therapeutics are only symptom managing<sup>41</sup>. Glucose hypometabolism, mitochondrial dysfunction, oxidative stress, hypoxia, and glutamate dysregulation are widely correlated with neurodegeneration<sup>3,6,7</sup>. Recent studies hypothesized that the causative pathology is metabolic failure, as several neurodegenerative disorders contain metabolic defects in specific vulnerable neural populations<sup>7,42</sup>. Thus, rescue of 'brain energetics' is an emerging therapeutic concept for neurodegenerative disorders and aging. Tactics for 'brain energy' rescue in neurodegenerative disorders include the rescue of brain glucose metabolism that deteriorates in a progressive, disease and region specific manner<sup>7</sup>. Brain glucose and glycogen metabolism is essential to cognitive function<sup>43</sup>. Glycogenolysis is necessary for memory formation and retention and deficiencies in glycogen catabolism may be tied to memory impairment associated with neurodegenerative dementias<sup>44,45</sup>. Glycogen is also implicated in neural energetics as it regulates K<sup>+</sup> and glutamate levels, which are known to drive action potentials<sup>46</sup>. Hyperexcitability is found in early stages of AD when mild cognitive impairments present and is a main feature of TLE<sup>47,48</sup>.

The pathological condition directly relating glycogen dysmetabolism to neurodegeneration is LD. In LD, monogenetic linked glycogen metabolism failure is the cause of PGB accumulation that drives a very severe childhood dementia accompanied by severe epilepsy<sup>25-28</sup>. By knocking out or decreasing the activity of GS in LD mouse models, LD mice no longer form PGBs and there is a rescue in neurodegeneration and seizure susceptibility<sup>25,28,49</sup>. LD is also associated with the hallmark conditions of neurodegenerative diseases like glucose transport, glutamate uptake, autophagy, oxidative stress, and inflammation<sup>50</sup>. As such, data and conclusions from LD models provide key insights for investigating the hypothesis that glycogen dysmetabolism underlies other multifactored/sporadic neurodegenerative diseases, especially for those in which PGBs are found, like in AD, TLE, and ALS.

#### **1.3.1 Glycogen and cognitive function**

Supporting evidence that glycogen dysmetabolism is an underlying cause of many neurodegenerative diseases are the critical contributions that glycogen makes to brain function. Glycogen is an obligatory substrate of long-term potentiation (LTP), synaptic plasticity, learning, and memory<sup>51-55</sup>. This role is highlighted by the fact that CNS specific GSKO animals have a significant deficit in their ability to learn an instrumental conditioning task, a complete absence of LTP, and additional deficits in activities indicative of synaptic strength like decreased neurotransmission at the pre-synaptic



terminal<sup>55</sup>. Cognitive deficits in learning and memory are key prognostic indicators for many neurodegenerative diseases, including LD<sup>42,56</sup>. In LD, severity of cognitive symptoms at onset is the highest prognostic factor of decreased survival, where the average survival time is eleven years after onset. Thus, cognitive decline may be the most important factor associated with the fatal complications in LD that are related to aspiration pneumonia, status epilepticus, or other common complications of chronic neurodegenerative diseases<sup>50</sup>. These findings demonstrate the fundamental role of brain glycogen in cognition, which is a primary clinical measure of all neurodegenerative dementias<sup>57</sup>. Therefore, a potential avenue for discovering new molecular targets in neurodegenerative diseases is brain glycogen metabolism as it plays an active role in cognitive abilities and changes in synaptic strength underlying learning and memory acquisition. LD mice have severe brain PGB accumulation, increased susceptibility to induced seizures, and changes to synaptic transmission and LTP<sup>27</sup>. Strikingly, LD mice exhibit episodic memory defects with age, providing additional evidence of a causal link between glycogen dysmetabolism and cognitive challenges in neurodegenerative diseases<sup>51</sup>. Thus, the basic science of LD and corresponding mouse models can be used as templates to investigate the relationship of glycogen dysmetabolism and cognition in other neurodegenerative diseases, where the cognitive deterioration is slower, survival time is longer, and the driving pathology is less clearly defined.

### **1.3.2 Glycogen and neural energetics**

The critical contribution of glycogen to neural energetics is rapidly emerging. The majority of brain glycogen is stored in astrocytes, thus the influence of glycogen on neurons is thought to be regulated through astrocytes<sup>58-60</sup>. Indeed, a well-known neurotrophic feature of astrocytes is their influence on ion homeostasis and glutamate clearance<sup>61</sup>. K<sup>+</sup> efflux is a universally understood phenomenon of the action potential, first studied on squids by Hodgkin and Huxley in 1953, and in the absence of K<sup>+</sup> ion clearance neuronal hypersynchronization burst firing and seizures occur<sup>62-64</sup>. Astrocytic Na<sup>+</sup>/K<sup>+</sup> pumps are sensitive to increases in extracellular K<sup>+</sup> and consume energy during increased axonal activity<sup>65-67</sup>. Inhibition of glycogenolysis in astrocytes, even in the presence of glucose, impairs K<sup>+</sup> uptake<sup>62</sup>. Therefore, energy that fuels fundamental mechanisms of neural homeostasis is glycogen derived.

Glutamate is the dominant excitatory neurotransmitter and requires rapid removal after synaptic transmission by cellular uptake<sup>61</sup>. Defects in glutamate transmission have been linked to epileptic and neurodegenerative disorders and astrocytic glycogen functions as a substrate for *de novo* synthesis of glutamate<sup>1,44,54</sup>. Conversely, glutamate recycling triggers glycogenolysis to produce energy for Na<sup>+</sup> restoration and for the conversion of glutamate to glutamine<sup>68</sup>. As astrocytes are glycolytic, the energy required for glutamate-glutamine cycling comes from the conversion of glucose to lactate<sup>12</sup>. Both glutamine and lactate shuttle from astrocytes to neurons where glutamine is converted to glutamate and lactate is thought to be used as an exogenous substrate of neuronal oxidative metabolism<sup>69</sup>. The latter phenomenon is a controversial hypothesis known as

the astrocyte-neuron lactate shuttle (ANLS) hypothesis postulating that lactate is the primary fuel of neurons and it is produced by astrocytes<sup>53</sup>. An enticing hypothesis, considering studies using mouse and rat olfactory neurons show that systemic glucose is not sufficient to sustain neuronal energy consumption<sup>12</sup>.

The ANLS hypothesis suggests a critical utility for the metabolite mainly thought of as a waste product of anaerobic metabolism<sup>70</sup>. In fact, lactate has recently been suggested to be a major carbohydrate fuel across all cells and tissues<sup>71</sup>. The ANLS hypothesis is based on the observation that cells with high rates of glycolysis or glycogenolysis can form and shuttle lactate into diverse groups of cells whose ATP demands are unmet<sup>72,73</sup>. Cells receiving lactate can convert it into glucose or feed it directly into oxidative metabolism<sup>74</sup>. Systemic glucose or glycogen contained by neurons is an insufficient fuel supply to meet their ATP demands<sup>74</sup>. Extracellular lactate can support olfactory neuronal compound action potentials independent of glucose or other monosaccharide availability<sup>12</sup>. A recent *in vivo* study found that arousal/startle response in mice triggers a rapid lactate release from astrocytes that is followed by increased lactate levels in neurons<sup>75</sup>. Further, glucose shuttling is improbable as astrocytes lack glucose-6-phosphatase and they cannot release free glucose<sup>60</sup>. Therefore, oxidative metabolism dependent neurons may receive astrocytic glycogen derived lactate for direct entry into the TCA cycle. These data indicate that glycogen availability is an important contributor to the maintenance of proper equilibrium between excitatory and inhibitory neurotransmission, which is deficient in neurodegenerative diseases.

The extent to which glycogen supports brain neural activities remains to be seen. Several reviews have classified glycogen as a key, even obligatory, fuel for the brain, though more investigation is needed to understand the extent of its role<sup>12,15,43,76-78</sup>. Current hypotheses based on cell culture studies pose that astrocytic glycogen is used to support neuronal excitation during either hypoglycemia or compounded energy demands<sup>76</sup>. A possible nuanced role of glycogen in neural energetics is highlighted by the fact that CNS glycogen synthase knockouts (GSKOs) are more susceptible to pharmacologically induced hippocampal seizures, but neuron specific GSKOs show less susceptibility<sup>55,79</sup>. This suggests cell specific regulation of glycogen metabolism. Interestingly, forebrain and neuron specific GSKOs do not show the same seizure susceptibility but do show significant deficiencies in LTP and acquisition of instrument to learning tasks<sup>79</sup>. These studies and brain glycogen mapping studies highlight how regional, cellular, and subcellular spatial arrangements of glycogen may impose regional and cell specific glycogen metabolism<sup>15</sup>. Moreover, glucose hypo-metabolic footprints seen by <sup>18</sup>FDG PET are regionally and disease specific and metabolic imbalances are hypothesized to arise from specific regional and/or cellular neuronal populations<sup>1</sup>. Neural energetics continue to emerge as a therapeutic target to which glycogen metabolism is clearly linked. Further, regional and cellular locations of glycogen linked metabolic perturbances are likely important. As such, the location of PGBs in neurodegenerative diseases may provide important clues into their disease specific metabolic pathologies.

## 1.4 Lafora disease

### 1.4.1 LD PGBs drive disease pathogenesis

LD is an autosomal recessive childhood dementia and glycogen storage disorder that severely affects the CNS resulting in death before age 30<sup>80</sup>. LD patients carry autosomal recessive mutations in either *Epm2a*, which encodes the glycogen phosphatase laforin, or *Epm2b*, which encodes the E3 ubiquitin ligase malin<sup>81–87</sup>. A hallmark of LD is increasing numbers of cytoplasmic PGBs found throughout most tissues in LD patients and mouse models<sup>80</sup> (**Figure 1.1A**). These PGBs drive worsening bouts of generalized myoclonic epilepsy and neurodegeneration<sup>25–28</sup>. Additionally, the original LB brain biopsy performed by Lafora reported sclerosis of medium-sized pyramidal cells, increased glia, and perivascular bleeding<sup>24</sup>. Laforin and malin KO mouse models have been generated and replicate LB formation, increased susceptibility to induced seizures, spontaneous myoclonus, neurodegeneration, and glial activation<sup>88,89</sup>.

Utilizing genetic models and pre-clinical treatments, multiple labs have demonstrated that LD PGBs are both a diagnostic pathological feature and the drivers of LD<sup>25–28</sup>. Laforin KO and malin KO mice lacking the GS activator Protein Targeting to Glycogen (PTG) exhibit greatly reduced LB accumulation, resolved neurodegeneration, myoclonus, and seizure susceptibility<sup>25,26</sup>. Malin KO mice lacking at least 50% of *GSY1* activity do not exhibit LBs, neurodegeneration, or abnormal electrophysiological properties<sup>27,28</sup>. Conversely, constitutively active GS in genetically modified mouse and fly models results in neurodegeneration, as shown by progressive death of cerebellar Purkinje neurons<sup>90</sup>. These results indicate that genetically decreasing glycogen load results in disease rescue, while overaccumulation of glycogen can drive neuronal death.

The LD mouse models have also been key to defining additional pathways that are perturbed, many being common to other neurodegenerative diseases, apoptotic dysfunction, endoplasmic reticulum stress, reduced clearance of misfolded toxic proteins through the ubiquitin proteasome system, and astrogliosis<sup>91–94</sup>. Multiple genetic manipulations have been performed to establish that these effects are important features of LD pathophysiology, though secondary to LD PGB accumulation. For example, LD mouse models have an impairment of autophagy as measured by an increase in p62. Rescue of p62 levels, as well as LTP, kainate induced seizures, and neuroinflammation is genetically achieved by crossing a malin KO mice with mice lacking one copy of *GYS1*, thereby decreasing GS activity by 50%. Moreover, mice with a constitutively active brain specific GS or overexpressing PTG accumulate PGBs and exhibit increased p62 levels, which are further increased when crossed with an LD mouse. These results indicate that LB accumulation drives the autophagy and neurological impairments in LD. Furthermore, they demonstrate that decreasing GS activity to 50% ablates many of the clinical issues. In further support of these data, administration of an inducer of autophagy partially restores autophagy defects, neuroinflammation, endoplasmic reticulum stress, and seizure susceptibility in the

absence of LB reduction<sup>95</sup>. Collectively, these data demonstrate that autophagy, seizure activity, cognitive defects, endoplasmic reticulum stress, neurodegeneration, and neuroinflammation are secondary to and driven by LB accumulation.

### 1.4.2 *Lafora body localization*

LD PGBs were first described in a 1911 report on LD patient brain biopsies, where Lafora observed them virtually exclusive to neurons in the cortical and spinal tissue<sup>24</sup>. Patient biopsies reported PGBs in the ganglion cells of the second, third, and fourth layers of the cerebral cortex, and in the cells of the quadrigeminal, visual, oblongata, and posterior horns of the spinal cord. In LD mouse models, LBs are prevalent in the hippocampus, cerebellum, cortex, and brainstem (**Figure 1.2A**)<sup>80</sup>. Since Lafora's initial sighting, LD PGBs were historically thought to mainly exist in neurons. Within the last three years however, two independent investigations using a combination of immunofluorescent techniques published the same conclusion that astrocytes harbor the vast majority of PGBs in the brains of LD mouse models<sup>96,97</sup>. Only 4% of neurons contained LD PGBs while they were found in 99% of astrocytes<sup>96</sup>. Further, astrocytic PGBs have been described as more abundant in the astrocytic processes rather than the soma<sup>96,97</sup>. Trace quantities of LD PGBs have been recently sighted in microglia, which is consistent with the original work of Lafora<sup>24,97</sup>. Whether the microglia containing LD PGBs had engulfed them or if the aggregates form inside them is not yet known.

Interestingly, microglia activation, a neuroinflammation marker of LD measured by Iba1, is rescued in a malin KO model crossed with a mouse model unable to accumulate glycogen in astrocytes<sup>98</sup>. In this double KO model, the LD PGBs are greatly diminished in contrast to the malin KO model. These results further support the data indicating that neuronal LBs represent a very small fraction of total LBs<sup>96,97</sup>. However, rescue of astrocytic LBs do not rescue susceptibility to kainate-induced seizures, indicating that LBs may drive secondary pathophysiology in a cell specific manner<sup>98</sup>. Interestingly, astrocytic LD PGBs are less similar to neuronal LBs than they are to corpora amylacea in terms of their distribution in the brain, size, clustering, and presence of neo-epitopes recognized by IgMs<sup>96</sup>. Further, p62, a scaffold protein that can be bound by ubiquitin and guide its binding partners to autophagosomes and autophagic processes, is indicated to be a main feature of astrocytic, but not neuronal LD PGBs, and is also found in corpora amylacea<sup>96,99,100</sup>. Further study is needed to determine if, like corpora amylacea, astrocytic PGBs are being expelled to the CSF. If so, perhaps astrocytic PGBs traversing the perivascular space promotes perivascular bleeding, as documented in Lafora's 1911 report.

### 1.4.3 *Lafora body architecture*

By electron microscopy (EM) native LD PGBs range from 2-10+  $\mu\text{m}$  and are formed of clusters of 'glycogen-like' particles and fibrillar material (**Figure 1.1A**)<sup>80,101</sup>. LD PGBs, like glycogen and starch, can be digested with  $\alpha$ -amylase that hydrolyzes  $\alpha$ -1-4-glycosidic linkages<sup>102-104</sup>. Like brain glycogen, LD PGBs contain ~75% glucose and ~25% glucosamine<sup>16</sup>. Multiple groups identified that LD PGBs stain similarly to plant starch with iodine, Best's carmine, methenamine-silver nitrate, and PAS-dimedone. However, LD PGBs were metachromatically different than starch by Alcan and Toluidine blue methods<sup>102,104</sup>. If native LD PGBs are boiled, mechanically agitated, or lintnerized and viewed by light microscopy the polysaccharide forms into a network assembly in the same way that starch disassembles with the same methods<sup>20</sup>. Since mammalian glucose polymerization is performed exclusively by glycogen synthase, LD PGBs are aberrant glycogen whose structural features are more comparable to starch<sup>105</sup>.

LD PGBs purified from brain and muscle have glucose chains dramatically longer than normal glycogen that allows the chains to form helical structures making them more resistant to degradation<sup>36,106,107</sup>. Long glucose polymers of starch, generally longer than normal glycogen, form a clustered arrangement of branch points giving rise to helical structures that expel water<sup>105,108</sup>. A confounding factor of LD PGBs is their elevated phosphate content in comparison to starch and glycogen<sup>89</sup>. In starch, the role of phosphate is to break up the tight helical associations. Therefore, the phosphorylation and dephosphorylation of starch is a tightly regulated process critical for controlled access of  $\beta$ -amylases and dispersal of glucose<sup>109,110</sup>. By keeping to the starch analogy, the LD PGB hyperphosphorylation should increase the solubility of LD PGBs, not decrease it. Thus, phosphorylation has been suggested to have little to do with glycogen solubility and its role is poorly understood<sup>105,107</sup>. The normal biochemical role of glycogen phosphate and the relationship of LD PGB hyperaccumulated phosphate to LD is still unclear and continued investigation in this area will be highly informative.

### 1.4.4 *Aberrant glycogen metabolism in Lafora disease*

LD PGBs form due to glycogen dysmetabolism caused by loss of function to the E3-ubiquitin ligase malin or the glycogen phosphatase laforin with mutations in either gene resulting in a similar histological phenotype<sup>25-28</sup>. While mutations in either gene result in PGBs, the exact mechanism leading to PGBs has not been defined. Malin is an E3-ubiquitin ligase that ubiquitinates several enzymes involved in glycogen metabolism, glycogen debranching enzyme (*AGL/GDE*), protein targeting to glycogen (*PTG/R5*), a regulatory subunit of protein phosphatase 1 (*PP1*), laforin, and glycogen phosphorylase<sup>49,84,111-114</sup>. Malin-dependent ubiquitination of glycogen phosphorylase results in nuclear localization of glycogen phosphorylase that impacts nuclear glycogen metabolism and histone acetylation<sup>114</sup>. Laforin is the only human glycogen phosphatase and interacts with a number of proteins involved in glycogen metabolism<sup>86,115-117</sup>.

However, the exact mechanism(s) by which the loss of function of either laforin or malin create aberrant hyperphosphorylated glycogen still needs to be resolved. Additionally, many unanswered questions about the role of nuclear glycogen metabolism and how brain glycogen metabolism is regulated remain.

This is of clinical interest considering that LD patients die of neurological complications although PGBs are also abundant in the skeletal muscle and heart<sup>82</sup>. Tissue specific regulation of glycogen metabolism is well studied<sup>105</sup>. Interestingly, the LD PGBs architecture is also tissue specific, showing the longest and most starch-like chain length distribution in the brain, followed by those from heart, and then skeletal muscle<sup>20</sup>. A positive correlation between PGB chain length and degree of tissue deterioration has been suggested as neuronal tissue is the first to degenerate in LD<sup>20</sup>. Therefore, tissue regulated glycogen metabolism may influence the pathogenic features of LD PGBs that promote more mild or severe cellular dysregulation.

Cellular metabolism is rescued by LD PGB breakdown using an amylase fusion protein that can enter mouse brain tissue and break up LD PGBs<sup>118</sup>. Moreover, depletion of astrocytic LBs, which are the predominant form of LBs, in a malin KO mouse results in the partial rescue of central carbon, amino acid, and lipid metabolic pathways<sup>98</sup>. In many nervous system diseases, glycosylation is severely depleted<sup>119</sup>. In laforin KO mice and GSD III mouse models, glycogen derived glucosamine were determined to be higher than age matched controls<sup>16</sup>. Further, N-linked glycosylation defects were linked to brain regions where PGBs are most abundant. Impressively, the aberrant glycosylation footprint of LD mice resemble normal conditions after treatment with the amylase fusion protein<sup>16,118</sup>. These data suggest that PGB formation likely sequesters glucosamine, leading to metabolic disarray in the mouse. Furthermore, they emphasize that glycogen is needed to support the brains normal metabolic functions.

#### **1.4.5 Clinical evidence of brain metabolic defects in LD**

A recent retrospective study and review focused on eight Italian patients genetically confirmed for LD that underwent <sup>18</sup>F-FDG-PET<sup>120</sup>. Though the patient ages, genders, genotypes, and disease severity were mixed in this analysis, a bilateral hypometabolic phenotype was observed in all patients that was more pronounced in advanced disease states. Interestingly, regions with high PGB loads, brainstem, cerebellum, hippocampus, and cerebral cortex, did not directly overlap with the hypometabolic regions that were the temporal (8/8), parietal (7/8), and frontal lobes (7/8), as well as the thalamus (6/8) (**Figure 1.2A**). Further, temporoparietal hypometabolism in patients was worsened in correlation to impaired visual symptoms. In nine additional cases identified from eight publications, <sup>18</sup>F-FDG-PET showed heterogeneous findings, ranging from diffusely decreased cerebral glucose metabolism to unremarkable examinations in two cases. Prospective longitudinal studies are needed to clarify these data, but a regionally specific hypometabolism hallmark is emerging. While these studies are difficult for rare diseases, there is an ongoing natural history study assessing 30 LD patients for two years

at four clinical sites<sup>121</sup>. This study, and others like it, will provide key clinical baselines to assess common features between LD and other neurodegenerative diseases.



## 1.5 Pompe disease - glycogen storage disease type II

### 1.5.1 *Aberrant glycogen in Pompe disease - glycogen storage disease type II (GSD II)*

Pompe disease (GSD II) is a lysosomal storage disorder caused by deficiency of the lysosomal enzyme acid alpha-glucosidase (GAA, alglucosidase alpha). Mutations in the GAA gene lead to excessive accumulation of lysosomal glycogen primarily in the cardiac, skeletal, and smooth muscles. The availability of enzyme replacement therapies (ERTs) for Pompe patients are increasing their lifespans, revealing neurological components initially overshadowed by myopathies. Thus, a CNS phenotype is emerging in Pompe disease provoking a reclassification of the GSD to be attributed to both muscle and nervous system<sup>122</sup>.

The ultimate involvement of the CNS in Pompe disease is not yet clear. However, several observations by EM and PAS indicate that full characterization of Pompe neuropathology is critical to understanding and treating this disease. In the infantile form, glycogen accumulation is seen in neurons of the cortex, midbrain, pons, medulla, and cranial nerve nuclei (**Figure 1.1B**)<sup>123</sup>. Glycogen accumulation is also detected throughout nuclei of the brainstem and cerebellum (**Figure 1.2B**)<sup>124</sup>. Neuronal swelling, or ballooning, is observed in the substantia nigra, dorsal raphe nuclei, pontine nuclei, inferior olivary nuclei, and dentate nucleus<sup>122</sup>. Additionally, Schwann cells of nerve sheaths in the cortex, glial cells and astrocytes of white matter, but rarely Purkinje cells, all accumulate glycogen. Failure to meet myelination milestones at a median age of 6 months in Pompe patients has been suggested to be related to the involvement glycogen accumulation in the CNS<sup>125</sup>. Some studies have indicated that glycogen accumulation in the cerebral cortex is associated with learning difficulties and intellectual disability in type II glycogen storage diseases<sup>126–129</sup>.

Interestingly, glycogen accumulation is more prominent in the infantile onset version of Pompe disease, while late onset Pompe disease glycogen accumulation is observed more rarely<sup>122</sup>. In late onset, the CNS involvement of glycogen has been observed in Schwann cells of the nerve sheaths in the cerebral cortex and spinal cord. Lysosomal glycogen as also been detected in neuronal cell bodies spheroid-shaped structures resembling corpora amylacea are reported in the spinal cord<sup>130</sup>. In large Pompe diseased mammals and birds including cattle, dogs, quails, sheep, and cats, glycogen deposits are shown within brain and spinal cord accumulating in neurons and glial cells<sup>131</sup>. The extent of the CNS involvement in Pompe disease may be elucidated using Pompe disease mouse models with targeted disruption of GAA. Three mouse models with targeted disruption to GAA provide evidence of PAS positive glycogen accumulation in the brain and spinal cord including the cerebral cortex, olfactory bulb, thalamus, hippocampus, hindbrain, cerebellum, and medulla<sup>132</sup>. AAV-mediated gene therapy in GAAKO mice improves neurological defects, but additional research is necessary to understand the clinical translation of these findings<sup>133</sup>.

### 1.5.2 Aberrant metabolism in Pompe disease

Mutations in the gene encoding the lysosomal enzyme GAA prevent Pompe patients from breaking down lysosomal glycogen in the muscle, heart, and CNS<sup>131</sup>. Glycogen accumulates initially in the lysosome and then in the cytoplasm and becomes pathogenic<sup>134</sup>. Subsequently, swelling and rupture of lysosomal membranes releases hydrolytic material causing cellular damage<sup>17</sup>. Clinical severity is predicted based on residual activity of GAA<sup>135</sup>. In the most severe cases, patients undergo progressive myopathy and hypertrophic cardiomyopathy with the main cause of fatality being respiratory failure<sup>131</sup>.

GAA replacement therapy has been useful as both a proof-of-concept for ERTs and in the clinic with two that are currently approved. The current standard ERT (Myozyme and Lumizyme) utilizes a recombinant human GAA (rhGAA) analog that enters cells and lysosomes by the mannose-6-phosphate (M6P) receptor<sup>135</sup>. Both ERTs are created using recombinant DNA technology to produce the human GAA enzyme in Chinese hamster ovary (CHO) cells and are biologically comparable. Myozyme and Lumizyme have been shown to improve patient survival rates, however, manufacturing differences result in differing clinical attributes. Therefore, Myozyme is indicated for infantile-onset Pompe disease while Lumizyme is indicated for patients aged  $\geq 8$  years<sup>136</sup>.

Unfortunately, because rhGAA is exclusively targeted to the lysosome, cytoplasmic glycogen is left to accumulate<sup>135,137</sup>. A newer delivery platform, tested in Pompe mouse models, utilizes an antibody fragment (Fab) fused to GAA called VAL-1221 that allows entry into the lysosome and cytoplasm<sup>137</sup>. This antibody-enzyme fusion (AEF) protein is comprised of the Fab fused to GAA and gains entrance into cells by either the M6P receptor the equilibrative nucleoside transporter 2 (ENT2) receptor and allows for clearance of lysosomal and cytoplasmic glycogen. VAL-1221 completed a Phase I/II clinical trial with promising safety profiles and offers greater potential for clearing both cytoplasmic and lysosomal glycogen.

A pre-clinical study on LD mice has tested an AEF platform, VAL-0417, to deliver amylase to cells in order to degrade pathogenic LBs, rather than replacing an enzyme<sup>118</sup>. The AEF is comprised of the humanized 3E10 Fab fragment and pancreatic  $\alpha$ -amylase. VAL-0417 degrades LBs and reduces LB load *in vitro* and degrades glycogen and polyglucosan *in vivo*. Using VAL-1221 to test LD PGB clearance from the brains of LD mouse models would be useful for discovering if the AEF could enter cells of the CNS as well as fibroblasts. If so, VAL-1221 may have the potential therapeutic application for any of the 17 GSDs (**Table 1.1**). Further, the utility of VAL-1221 within the CNS of Pompe patients would be a useful investigation to further understand the involvement of the CNS and the aberrant glycogen therein to the clinical progression of Pompe disease.

## 1.6 Aging

### 1.6.1 *Aberrant glycogen in aging*

Age-dependent brain PGBs called corpora amylacea were first described in 1837 yet they are an understudied aggregate<sup>21</sup>. Corpora amylacea are PAS+ aggregates that were historically defined as histological features that increased in abundance with age and even more with neurological disease<sup>29</sup>. Corpora amylacea are found largely in glia throughout the brain (**Figure 2C**)<sup>19</sup>. Neurodegenerative diseases in which hyperabundant corpora amylacea have been described include Parkinson's disease, diabetes, vascular dementia, multiple sclerosis, Huntington's disease, Pick's disease, diabetic neuropathy, peripheral neuropathy, motor neuron disease<sup>19,138</sup>. Thus, as aging is inextricably linked with neurodegeneration there is also increased corpora amylacea accumulation. While corpora amylacea are increased in some diseases, it is currently unclear how similar or different diseased corpora amylacea are from disease specific PGBs.

The age-dependent existence of corpora amylacea has been re-confirmed recently in fly models and multiple mouse models, including wildtype C57BL/J6 and the accelerated aging mouse model, senescence accelerated mouse prone 8 (SAMP8)<sup>99</sup>. SAMP8 mice also exhibit reduced lifespan, lordosis, hair loss, and reduced physical activity, similar to human aging<sup>139,140</sup>. Like LD PGBs, corpora amylacea are observed widely in astrocytes and less often in neurons<sup>29</sup>. Corpora amylacea ultrastructure is a spherical body ranging from 2-30  $\mu\text{m}$  that appears as clustered 8-12 nm fibrils that are aggregated or tangled and can be decorated with cell debris<sup>29,100,141</sup>. The fibrils are comprised of glucose polymers as are PAS+ and diastase-resistant and are dependent on the activity of GS in fly and mouse models<sup>99</sup>. Corpora amylacea appear to contain a dense core ranging 50-100 nm in diameter surrounded by concentric rings (**Figure 1C**)<sup>29</sup>.

For nearly 180 years, corpora amylacea were largely ignored and considered benign and/or innocuous aging aggregates<sup>31</sup>. Yet repeated findings by electron microscopy depicted cellular debris, including organelles from neurons, astrocytes, and oligodendrocytes, to be harbored within corpora amylacea<sup>29,100</sup>. Additionally, the presence of the proteasome targeting protein ubiquitin has been an identifying feature of corpora amylacea<sup>100</sup>. Together, these studies implicated corpora amylacea in cellular waste removal and suggested that corpora amylacea may be a vessel in which cell debris could be removed from the cell and eventually degraded. Recent reports corroborate the hypothesis that corpora amylacea may be an integral component of brain waste disposal with corpora amylacea acting as waste containers to protect the cell from damaging residual products<sup>21,31,142</sup>. Naturally occurring IgM antibodies were discovered against corpora amylacea neo-epitopes that detect corpora amylacea and

direct macrophages to phagocytize them<sup>21,31</sup>. Further, data indicating that corpora amylacea exist predominantly in periventricular and subpial regions were intriguing, but no reports identified their existence in the CNS, suggesting that they simply accumulated and remained trapped<sup>19</sup>. Improved methods, which had previously failed to identify corpora amylacea in the cerebral spinal fluid (CSF), were elegantly employed to discover that corpora amylacea are transported through the blood brain barrier, entering the CSF, and are present in lymph nodes<sup>22</sup>. Moreover, these data demonstrate that corpora amylacea can be phagocytosed by macrophages<sup>22</sup>. Thus, corpora amylacea are likely involved in a cellular clearance mechanism.

### **1.6.2 Aberrant metabolism in aging**

Aging is intimately associated with neurological deterioration and is the greatest risk factor for it<sup>143</sup>. There are multiple biomarkers that overlap between aging and neurodegenerative diseases, including the production of cognitive defects like memory loss and learning impairments along with molecular perturbations like reactive oxygen species and mitochondrial defects<sup>3</sup>. <sup>18</sup>F-FDG-PET imaging of age-influenced brain metabolism indicates that the frontal lobes as well as regions within the default mode network, including the temporal and parietal lobes, and prefrontal and posterior cingulate cortex show a strong age-related glucose hypometabolism trend<sup>144</sup>. These data suggest that aging alone could cause a widespread reduction in brain matter and glucose metabolism.

Only a few studies have begun to examine brain metabolism to characterize the role it plays in the CNS during aging. One 2016 study examined the aging metabolic profile of the cortex, hippocampus, and caudoputamen at 12-, 18-, and 24-months of age for normal male C57BL/6 mice using HILIC ESI-Q-TOF/MS<sup>145</sup>. This global-untargeted metabolomics study suggested aging is associated with a significant imbalance of core metabolite levels. Specifically, NAD levels decline, AMP/ATP levels increase, purine/pyrimidine accumulate and there are significantly altered oxidative phosphorylation and nucleotide biosynthesis and degradation. A more recent study determined metabolic fingerprints of brain samples in young (~2-months) and aged (~24-months) normal female C57BL/6J mice using <sup>1</sup>H-NMR spectroscopy<sup>146</sup>. The NMR spectra showed age-dependent changes revealed decreased concentrations of lactate, methionine, N-acetylaspartate, uridine, and inosine. In contrast, concentrations of leucine, isoleucine, valine, glutamine, allantoin, uracil, tyrosine, and phenylalanine were increased in the aged mice. These untargeted global analyses of wildtype aged mice demonstrate that aging is associated with increased metabolite diversity. Several pathways may be involved in these changes as aging metabolic signatures have been associated with carbohydrate, lipids, amino acids, and redox metabolism<sup>147</sup>. Much more

analyses, especially on a longitudinal time frame, is needed to understand the mechanisms that drive metabolic defects in aging.

Understanding the mechanism by which metabolites are dysregulated in the aging brain may uncover the inextricable link between aging and neurodegeneration. A potential link between aging and aberrant brain metabolism are the aging corpora amylacea, which are even more abundant in neurodegenerative diseases<sup>148</sup>. Similarly, the abundance of other neurodegenerative markers like Heat Shock Protein 70 (HSP70), advanced glycation end products (AGEP), and alpha-synuclein increase with age<sup>149–152</sup>. Strikingly, mice lacking GS also lack these markers in all brain regions<sup>99</sup>. While corpora amylacea accumulation disrupts neurological function in aged mice, mice lacking GS exhibit decreased corpora amylacea and increased maximum climbing speeds<sup>99</sup>. Conversely, increased GS activity promotes increased corpora amylacea and progressive degeneration of Purkinje neurons in mice and flies<sup>99</sup>. Thus, neuronal glycogen synthesis contributes to age-related functional decline. These data provide a direct link between glycogen synthesis and the formation of corpora amylacea to age-dependent protein-based aggregates that are well known hallmarks of many neurodegenerative diseases of aging. Furthermore, they indicate that the equilibrium of brain glycogen is critical, and imbalance creates neurodegeneration.

Unfortunately, a direct physiological relationship of glycogen and corpora amylacea to the aging metabolome is not well-defined at this time. The historical assumptions that corpora amylacea are innocuous resulted in limited examination of the relationship between aberrant glycogen metabolism in aging. Data from the recent resurgence in corpora amylacea suggests that progressive accumulation of aberrant glycogen in the brain may contribute to aging-based neurological decline. If so, then interventions that slow this process could be protective against neurological deficits of aging. Glycogen synthesis could be a target to tackle the age-related deterioration of the nervous system.

## 1.7 Temporal lobe epilepsy

### 1.7.1 *Aberrant glycogen in temporal lobe epilepsy*

Greater than 3 million in the US and over 70 million globally suffer from epilepsy<sup>153,154</sup>. Several factors can cause epilepsy including stroke, prenatal damage, CNS infection, head injury, genetics, and brain tumors<sup>155</sup>. For most epileptic patients, the cause is unknown. Seizures are typically diagnosed with electroencephalography (EEG) where “spike and wave” formations coming from specific electrodes map seizure activity to the surface of the brain<sup>156</sup>. These signals can discriminate a focal epilepsy from a generalized one. The chaotic neuronal discharge that defines epilepsy can be dampened with anti-seizure medications, and cocktails of these medications yield diminishing returns with the addition of each one<sup>157</sup>. Available epilepsy medications fail to control seizures in one third of patients including those with the most common focal refractory epilepsy, temporal lobe epilepsy (TLE)<sup>157,158</sup>. Although use of many new antiepileptic drugs with new mechanisms of action has increased, the ability to achieve seizure freedom has not<sup>157</sup>. Therefore, a paradigm shift in research strategies and therapeutic avenues is needed.

For TLE, several different neurological phenotypes are identified, which divide the disease into pathological subgroups. About 30% of TLE patients have identifiable MRI lesions such as tumor, cortical dysplasia, or cavernous hemangioma<sup>159</sup>. Approximately 50% of TLE patients, fall into a pathological subgroup called mesial temporal lobe epilepsy (MTLE) that is classically characterized by hippocampal sclerosis (HS positive) by MRI. Patients with MTLE can suffer from spontaneous recurrent seizures and neuronal loss that originate from mesial temporal lobe structures, such as the hippocampus, parahippocampus, amygdala, entorhinal cortex temporal pole, and the 2 rostral thirds of the superior middle and inferior temporal gyri of the right hemisphere<sup>160–162</sup>. For the remaining portion of TLE patients, MRI cannot identify the brain pathology.

MTLE is particularly interesting with respect to PGBs as they are observed in the temporal regions that are commonly biopsied, and these surgical resections create dramatic reduction in seizure activity (**Figures 1.1D and 1.2D**)<sup>163</sup>. Clinical reports of PGBs in biopsied temporal lobes from patients with TLE began to appear in the early 1990’s and have now become a marker for MTLE<sup>34,163,164</sup>. For MTLE patients, temporal lobectomies are frequently performed for those with partial complex intractable seizures<sup>163</sup>. In most of these resections, the hippocampus reveals neuronal loss especially of the CA1, CA3, and endofolium sectors<sup>161</sup>. These findings overlap with electron microscopy images, as well as PAS+ staining that show a strong presence of PGBs in the pyramidal layer of the hippocampus, primarily the CA1, CA3, CA4, endofolium, and fascia dentata sectors<sup>165,166</sup>. Interestingly, PGBs also appear in the parahippocampal region and the amygdala (**Figure 1.2D**). Within the temporal lobe,

PGBs appear filamentous and amorphous, dominating the white matter and perivascular area, and showing up inside astrocytes and axons<sup>34</sup>. The localized nature of MTLE PGBs has provoked the intriguing possibility that MTLE may be a localized form of a glycogen storage disorder. Now, this concept is gaining traction as studies are demonstrating metabolic links between aberrant glycogen and MTLE<sup>167–169</sup>.

### **1.7.2 *Aberrant metabolism in temporal lobe epilepsy***

Epileptic foci in TLE have been correlated with hypometabolic activity using <sup>18</sup>F-FDG-PET. TLE hypometabolic zones include the contralateral temporal lobe, ipsilateral temporal neocortex, the ipsilateral basal ganglia and thalamus<sup>159</sup>. Interictal glucose hypometabolism is reported in 80% of patients with mesial TLE. Interestingly, even in patients without evidence of hippocampal sclerosis on MRI, the localization of <sup>18</sup>F-FDG PET hypometabolism corresponds to the ictal EEG region. <sup>18</sup>F-FDG-PET can also provide prognostic data based on the extent of initial hypometabolism present<sup>167,170</sup>. A more extensive hypometabolic region can indicate a poor prognosis and a longer duration of epilepsy. Therefore, hypo-glucose metabolism is a clinical biomarker for TLE that is used to determine patient management and surgical decisions. A recent study demonstrated the utility of <sup>18</sup>F-FDG PET in localizing an ictal focus in TLE patients even in those with normal MRI<sup>159</sup>. This study demonstrated that moderate to severe temporal lobe hypometabolism was noted in cases of lesional MRI. Thalamic hypometabolism was associated with moderate to severe rather than mild temporal lobe hypometabolism, suggesting that a hypometabolic thalamus is a marker of temporal dysfunction. Extratemporal hypometabolism was a predictor of poor postsurgical seizure outcome while localized temporal hypometabolism predicted a good outcome<sup>170</sup>. Thus, a hypometabolic assessment is a clinically useful diagnostic and prognostic indicator of TLE.

A hypothesis is emerging that neuronal action potentials are supported by systemic glucose and brain glycogen. Glucose alone is insufficient to support compound action potentials and is supplemented by glycogen<sup>12</sup>. The ANLS hypothesis (see section 1.3.2) suggests that lactate derived from astrocytic glycogen is a major carbohydrate fuel supporting neuronal energetics. Depleting glycogen or interfering with lactate transport results in the loss of the compound action potential<sup>171</sup>. Moreover, glycogen homeostasis is required to control hyperexcitability and seizures<sup>68,79</sup>.

In TLE, K<sup>+</sup> buffering is clearly dysregulated in specimens from TLE patients<sup>172</sup>. One study found that astrocytic K<sub>ir</sub> channels are dysfunctional in sclerotic CA1 hippocampal regions of MTS patients<sup>173</sup>. Using patch clamp, a reduction in astroglial K<sub>ir</sub> currents was observed in sclerotic compared with nonsclerotic hippocampi. These data indicate that dysfunction of astroglial K<sub>ir</sub> channels could underlie impaired K<sup>+</sup> buffering and

contribute to hyperexcitability in epileptic tissue. When and how this dysfunction develops during epileptogenesis is not yet clear. Considering the critical role of astrocytes to maintain interstitial  $K^+$  homeostasis and the connections between astrocytic  $K^+$  buffering and astrocytic glycogen, impairment of astrocyte  $K^+$  uptake should be proconvulsant. Thus, PGB laden sclerotic tissue may be connected to a dysfunction of astrocytic  $K^+$  transporters and  $K^+$  buffering.

Astrocytic  $K^+$  homeostasis and glycogen metabolism are also coupled to glutamate uptake (see section 1.3.2), which is dysregulated in TLE. In TLE patients and in rodent epilepsy models, regions of the hippocampus affected by cell death exhibit a downregulation of glutamine synthetase and an increase in extracellular glutamate concentration, ultimately resulting in neural hyperexcitability, excitotoxicity, and neurodegeneration<sup>168,174</sup>. While glutamate levels are increased, glutamine levels are decreased, and the process of cycling is slower as observed by magnetic resonance spectroscopy<sup>169</sup>. These data pose another route by which the glycogen dysmetabolism and PGBs could upend the foundations of neural homeostasis promoting seizure activity. Glycogenolysis is suggested to yield the ATP supply that maintains the  $Na^+$  gradient that drives glutamate transport<sup>172</sup>. Inhibition of glycogenolysis can raise extracellular glutamate levels<sup>79</sup>. Glutamate transport requires the cotransport of  $Na^+$  and  $H^+$  and the counter transport of  $K^+$ . While, glutamate transporters are expressed on multiple cell types, astrocytes are primarily responsible for glutamate uptake<sup>175</sup>. Thus, suppression of glycogenolysis by PGB accumulation could disrupt the ion gradients required for glutamate uptake by astrocytes. Future studies are needed to clarify the potential mechanism of glycogen dysmetabolism in TLE.



## 1.8 Amyotrophic lateral sclerosis

### 1.8.1 *Aberrant glycogen in amyotrophic lateral sclerosis*

Amyotrophic lateral sclerosis (ALS) is the most common motor neuron disorder<sup>176</sup>. Motor neurons of the corticospinal tract, motor cortex, and motor neurons of the lower brainstem and spinal cord are affected. ALS onset occurs around age 50 with a fatal prognosis in only 3-5 years. Several mechanisms are correlated to ALS onset and progression, including excitotoxicity, oxidative stress, mitochondrial dysfunction, protein aggregation, diminishment in axonal transport, defects in RNA metabolism, and neuroinflammation. Mutant forms of more than 40 genes have been clinically implicated in ALS, including superoxide dismutase 1 (SOD1), TAR DNA-binding protein 43 (TDP-43), and fused in sarcoma (FUS), although most cases are sporadic<sup>177</sup>. Without effective treatment, ALS remains a fatal diagnosis and new hypotheses regarding therapeutic targets are focused on glucose metabolism.

CNS protein misfolding and aggregation is commonly associated with neurodegeneration in ALS. For example, inclusions of human mutant or wild type SOD1 are found at autopsy and in SOD1 overexpressing transgenic mouse models. Recently, glycogen accumulations in ALS and ALS SOD1<sup>G93A</sup> transgenic mice were detected. Strikingly, large PAS+ PGB-like aggregates were observed in cervical spinal cord sections from ALS patients that were absent in age and gender matched donors (**Figure 1.1E and 1.2E**)<sup>32</sup>. ALS PGBs occupied both neurons and glia in the gray matter and only astrocytes in white matter. Biochemical analysis of tissue homogenates confirmed the elevated glycogen in both gray and white matter, yet glucose was only elevated in the gray matter. Glycogen levels were also higher in the brainstem and lumbar spinal cord as well as in the liver and skeletal muscle prior to disease symptom onset.

### 1.8.2 *Aberrant glycogen metabolism in amyotrophic lateral sclerosis*

Altered energy metabolism in ALS correlates to disease progression, suggesting a pathogenic role for energy metabolism in ALS<sup>178</sup>. Nearly two dozen studies have examined ALS patients using <sup>18</sup>F-FDG-PET that has uncovered a diffuse cortical hypometabolic phenotype<sup>179–181</sup>. Therefore, reduced cortical glucose uptake has become a robust early indicator of ALS. Recent studies have described a regional hypermetabolic phenotype localized to the brainstem and both the cortical and dorsal spinal cord. In SOD1<sup>G93A</sup> mice, spinal cord glucose uptake initially increased before symptom onset and subsequently declined during disease progression<sup>182</sup>. Additionally, proteins involved in glycolysis,  $\beta$ -oxidation, and mitochondrial metabolism are altered before disease onset<sup>183</sup>. ALS patients placed on high carbohydrate hypercaloric diets

have displayed increased survival and decreased life-threatening events and hospitalization<sup>184</sup>. Additionally, an ALS fruit fly model overexpressing TDP-43 and phosphofructokinase (PFK), the rate limiting enzyme of glycolysis, in the CNS displayed increased locomotor activity and lifespan<sup>185</sup>. Thus, increased glucose availability may be protective, and the early hypermetabolic activity may be an initial mechanism to compensate for metabolic perturbations.

Recent metabolic observations suggest links between glycogen accumulation and metabolic deficiencies in ALS. In the spinal cords of ALS patients, alpha-glucosidase, the deficient enzyme in Pompe disease, is decreased at the mRNA and protein levels<sup>32,186</sup>. ALS SOD1<sup>G93A</sup> transgenic mice also show a reduction in alpha-glucosidase in the spinal cord, as well as liver and skeletal muscle<sup>32</sup>. In several neuromuscular diseases including ALS, genetic evidence suggests that aberrant metabolism of glycosphingolipids, a subgroup of glycolipids, plays an important role. Glycolipids are lipids attached to a carbohydrate polymer by a glycosidic bond. They are found on the surface of all eukaryotic membranes extending from the cell membrane to the extracellular environment. Glycosphingolipids are formed through the covalent linkage of a glycan moiety to ceramide, a lipid prominently found in the myelin sheath that surrounds axons. In the SOD1<sup>G93A</sup> mouse model, inhibition of glycosphingolipid synthesis exacerbated disease progression, whereas administration of GM3, a subtype of glycosphingolipids, slowed it<sup>187</sup>. Thus, glycosphingolipids may be important players in ALS and their aberrant metabolism may be related to glycogen accumulation. Further investigations are needed to discern the type of glycogen or PGBs that were observed in ALS patients and mice. Crossing ALS mice with a GSKO line would aid in defining the relationship of glycogen accumulation to pathogenesis in ALS.

To further understand the underpinnings of glucose hypometabolism in ALS, polar metabolite changes in ALS in important field of investigation, yet largely unstudied<sup>178</sup>. Though clinical meta-analysis suggests that metabolism does impact ALS, there is not an assertive study to establish any direct link between changes in metabolic parameters and the progression and survival of ALS<sup>176</sup>. Therefore, some pathways may be affected and modulate ALS outcome, but they are not defined. One study has analyzed FUS mutated human derived ALS motor neurons *in vitro* and did not identify alterations to glycolysis or TCA cycle intermediates<sup>188</sup>. Given the recent discovery of glycogen accumulation in the spinal cord, further investigation into the neural and/or glial cell origins may elucidate cell specific metabolic deficiencies. Interestingly, the lactate shuttle has been shown to exist beyond axons and astrocytes in oligodendrocytes and their myelinated axons. Oligodendrocytes have been proposed to perform aerobic glycolysis and give lactate to the myelinated compartments. Though glycogen's role in this process has not been defined, alterations in metabolic support by oligodendrocytes is now expected to underlie various diseases that are psychiatric or physiological like ALS. Further investigation in these areas may provide a clearer

understanding of how different cell types in the CNS contribute to reduced carbohydrate catabolism and new therapeutic opportunities for ALS.

## 1.9 Alzheimer's disease

### 1.9.1 *Aberrant glycogen in Alzheimer's disease*

Alzheimer's disease (AD) is the leading cause of dementia. In 2021, 6.2 million Americans (11.3%) 65 and older are living with AD<sup>189</sup>. Adults younger than 65 can also develop AD, but this prevalence is rarer and number less certain. Like many chronic diseases, AD develops from multiple factors. The greatest risk factor for AD is age and genetics, especially the *E4 APOE* variant, and having a family history of AD<sup>190</sup>. Hallmark clinical symptoms of memory loss and brain atrophy are believed to be driven by senile plaques of  $\beta$ -amyloid and neurofibrillary tangles of hyperphosphorylated-tau<sup>191</sup>. Due to these misfolded aggregates, AD is a proteinopathy<sup>192</sup>. In both sporadic and familial AD, amyloid- $\beta$  oligomers are observed in the cerebral cortex and hippocampus and neurofibrillary tangles of hyperphosphorylated-tau are deposited in soma and processes of neurons<sup>193,194</sup>. Neurofibrillary tangles first develop in the transentorhinal cortex and spread to the entorhinal cortex and hippocampus prior before showing in neocortical regions<sup>193</sup>. A cascade of other symptoms that define AD include, innate immune activation and inflammation, ER stress, ROS, mitochondrial dysfunction, synaptic toxicity, and cell death<sup>192</sup>. Ultimately a combination of some or all of these perturbations cascade to drive neurodegeneration that leads to atrophy of the neocortex, hippocampus, amygdala, basal forebrain, and brainstem. Clearing the plaques or tangles do not prevent or rescue the disease, and the cascade of effects are still undefined as cause or consequence of the proteinopathy. Thus, a new framing of the underlying mechanisms or causes of AD is welcomed<sup>195</sup>.

AD glycogen-like aggregates were first described using light and electron microscopy in 1985 from post-mortem brain and called granular glycogen bodies (**Figure 1.1F**)<sup>148</sup>. While termed granular glycogen bodies, the exact composition and architecture of these aggregates are unknown. EM observations distinguish these glycogen bodies from PGBs in that their ultrastructure appears granular rather than fibrillar as seen in LD and aging (**Figure 1.1A, C, F**). Further, toluidine blue stains these deposits an even dark blue, as opposed to the light blue periphery of CA. Thus, the AD granular glycogen bodies were distinct from visible corpora amylacea yet also observed in proximity to corpora amylacea in AD brains. The AD granular glycogen bodies range 5-50  $\mu\text{m}$  and are found non-membrane bound in the cytoplasm of cellular processes in both gray and white brain matter. While primary neuronal atrophy is observed in the hippocampal and cortical regions, AD glycogen-like aggregates are found more broadly throughout the brain, including the medial frontal, anterior and posterior central, medial temporal, and

lateral occipital gyri (**Figure 1.2F**). Further investigation of the structure of AD granular glycogen and cellular origins is needed.

### **1.9.2 Glycogen metabolism in Alzheimer's disease**

Though direct links between glycogen and AD are currently under investigation, glucose hypometabolism is an established clinical AD hallmark that is especially prominent in *E4 APOE* carriers<sup>196–199</sup>. Another emerging metabolic connection is that astrocyte energetics and metabolism may be a critical factor<sup>200</sup>. In healthy aging, astrocytes support neurons by maintaining neuron homeostasis, maintaining ion gradients and removing excess extracellular glutamate as well as A $\beta$ , the main component of the amyloid plaques found in AD brains<sup>201</sup>.

In the diseased stage, astrocytes show decreased glycolysis<sup>202,203</sup>. The resulting glucose hypometabolism represents a misregulation of nutrient transporters, metabolic enzymes and mitochondrial complexes<sup>200</sup>. This is connected to levels of hyperphosphorylated tau in cerebrospinal fluid (CSF) and impaired cerebral metabolism<sup>204</sup>. The metabolic changes create a cascade of pathological events, leading to oxidative stress and astrogliosis. Reactive astrocytes produce proinflammatory cytokines that activate microglia and amplify neuroinflammation in the brain<sup>205,206</sup>. They produce more reactive oxygen species and their support functions decline<sup>200</sup>. There is a reduction in glutathione, which prevents damage by reactive oxygen species, glutamate uptake, and A $\beta$  clearance, with a concomitant increase in A $\beta$  production. This ultimately results in A $\beta$  deposition in the brain and synaptic dysfunction, causing dementia.

What promotes abnormal glucose metabolism in AD is not known. One hypothesis is that the observed overactivity of glycogen synthase kinase 3 beta (GSK3B) could have the effect of inhibiting GS and starving the cell of glycogen<sup>207</sup>. Another is that soluble glycogen is in limited supply due to the progressive formation of AD granular glycogen. Glycogen breakdown is key to many aspects of brain function, and its tie to learning and memory formation as well as long term memory consolidation (see section 3.1) are particularly interesting in the case of AD. Genetically engineered mice that cannot form glycogen in the brain (GSKO) have defects in long-term potentiation (LTP), which is consistent with their deficits in short-term memory formation and long-term memory consolidation<sup>27</sup>. Also consistent with this hypothesis, feeding AD mice a diet supplemented with pyruvate facilitates increased soluble glycogen stores and improves spatial learning<sup>208</sup>.

Interestingly, cerebral glucose hypometabolism as measured by <sup>18</sup>F-FDG-PET has emerged as a clinical hallmark for AD<sup>196–199</sup>. The degree of glucose hypometabolism has an intimate relationship with AD clinical symptoms and severity. There are multiple clinical and animal studies focused on whether AD cerebral hypometabolism implies general impairment of glucose utilization, i.e., transport deficiencies, or another mechanism specific to glucose. Further, a body of work validating the predictive power

of cerebral hypometabolism, especially in carriers of *E4 APOE*, has raised a “chicken-or-egg” narrative with respect to impaired glucose utilization causing neurodegenerative processes and vice versa<sup>10</sup>.

Cerebral hypometabolism could be part of a vicious cycle, both cause and consequence of AD neurodegeneration<sup>10</sup>. A glycogen dysmetabolism centric view poses the concept that glucose sequestration is a function of glycogen dysmetabolism yielding AD granular glycogen and consequently brain hypometabolism. The creation of AD granular glycogen likely precedes neurodegeneration, however that does not preclude the possibility that it ignites a positive feedback loop wherein the neurodegenerative processes further impose glycogen and/or glucose dysmetabolism.

### **1.10 Conclusions and future directions**

Searching for effective treatments of neurodegenerative diseases is one of the more challenging aspects of neuroscience. Scientists have made significant advancements understanding the range of molecular and cellular pathologies that contribute to neurodegeneration, including protein aggregation, mitochondrial dysfunction, glutamate toxicity, calcium load, proteolytic stress, oxidative stress, neuroinflammation, and aging. Efforts to treat neurodegenerative diseases are often limited by the fact that they tend to address any one of the above pathological changes while ignoring others. Lack of clarity regarding a possible root cause that underlies all the above pathologies poses a significant challenge to the crusade of curing neurodegenerative disease.

Glucose hypometabolism underlies virtually all neurodegenerative diseases. Evidence of glycogen metabolism disruption is a striking similarity between LD and Pompe disease, aging, TLE, AD, and ALS. In this respect, Lafora’s disease offers a helpful model. LD is a fatal neurodegenerative disease, with traditional neurodegenerative disease biomarkers of ROS, inflammation, astrogliosis, hypoxia, and neuronal dysfunction, exacerbated by defined metabolic targets involved in glycogen metabolism. LD is a glycogen storage disorder, defined by PGB aggregation all over the body, driving metabolic defects, CNS deterioration, and fatality. While similar aberrant glycogen accumulation is found in the CNS of Pompe, aging, TLE, AD, and ALS patients, it has not been as well characterized as in LD.

A standard approach to classifying the structure and identity of PGBs will be useful to determine the classifications of these PGBs. Using a published pipeline of methods used to examine the structure and localization of LD PGBs, similar experiments should be performed to understand structural aspects in Pompe disease, aging, TLE, AD, and ALS<sup>15,40,209</sup>. With this knowledge, we may re-group classifications of GSDs and challenge

the classification of neurodegenerative diseases that are not traditionally defined GSDs but diagnosable by glycogen deposits/PGB accumulation. Moreover, due to increased technological advances in glycogen detection, many classical GSDs where a neurological component may be missed should be re-investigated for the influence of CNS PGBs.

There are other neurodegenerative diseases in which to our current understanding, do not develop disease specific PGBs but are afflicted with a gross accumulation of the aging PGB, CA. Exact differences between corpora amylacea and disease PGBs have yet to be extracted beyond aspects observable by microscopy. Astrocytic LD PGBs for example, appear immunologically like corpora amylacea. Molecular and structural differences between corpora amylacea that hyperaccumulates with neurological disease and aging PGBs need to be examined.

Ultimately, the relationship of glycogen deposits/PGBs to upstream and downstream metabolic defects is of interest. Current advances in metabolomics and MALDI to measure glycogen and related metabolic changes may facilitate an understanding of the dysregulated brain energy metabolism underlying neurodegenerative diseases. The possibility of using newly developed methods and technologies to find translational molecular targets is exciting. Given the importance of glycogen synthesis to brain energetics and the succession of multifaceted events detrimental to health that follow its dysmetabolism, glycogen in disease research will be a critical area neuroscience in the years to come.

**Table 1.1 Glycogen storage diseases.**

Disease Name(s)	Gene	Affected enzyme	OMIM
GSD 0a	GYS2	Liver glycogen synthase	240600
GSD 0b	GYS1	Muscle glycogen synthase	611556
GSD 1a, von Gierke	G6PC	Glucose-6-phosphatase $\alpha$	232200
GSD 1b, von Gierke	SLC37A4	Glucose-6-phosphatase transporter	232220
GSD 2, Pompe disease	GAA	Alpha $\alpha$ -glucosidase	232300
GSD 3, Cori/Forbes	AGL	Glycogen debranching enzyme	232400
GSD 4, Anderson, Adult polyglucosan body disease (ABPD)	GBE1	Glycogen branching enzyme	232500
GSD 5, McArdle	PYGM	Muscle phosphorylase	232600
GSD 6, Hers	PYGL	Liver phosphorylase kinase	232700
GSD 7, Tauri	PFKM	Muscle phosphofructokinase	232800
GSD 9a	PHKA2	Phosphorylase b kinase ( $\alpha$ 2 subunit)	236000
GSD 9b	PHKB	Phosphorylase b kinase ( $\beta$ subunit)	261750
GSD 9c	PHKG2	Phosphorylase b kinase ( $\gamma$ subunit)	613027
GSD 9d	PHKA1	Phosphorylase b kinase ( $\alpha$ 1 subunit)	300559
GSD 10	PGAM2	Muscle phosphoglycerate mutase	261670
GSD 11, Fanconi-Bickel	SLC2A2	Glucose transporter 2*	277810
GSD 12	ALDOA	Aldolase A	611881
GSD 13	ENO3	$\beta$ -Enolase	612932
GSD 14	PGM1	Phosphoglucomutase 1	614921
GSD 15	GYG1	Glycogenin-1	603942
Danon disease	LAMP2	Lysosomal-associated membrane protein 2	300257
Lafora disease, 2A	EPM2A	Laforin	254780
Lafora disease, 2B	NHLRC1 (EPM2B)	Malin	254780

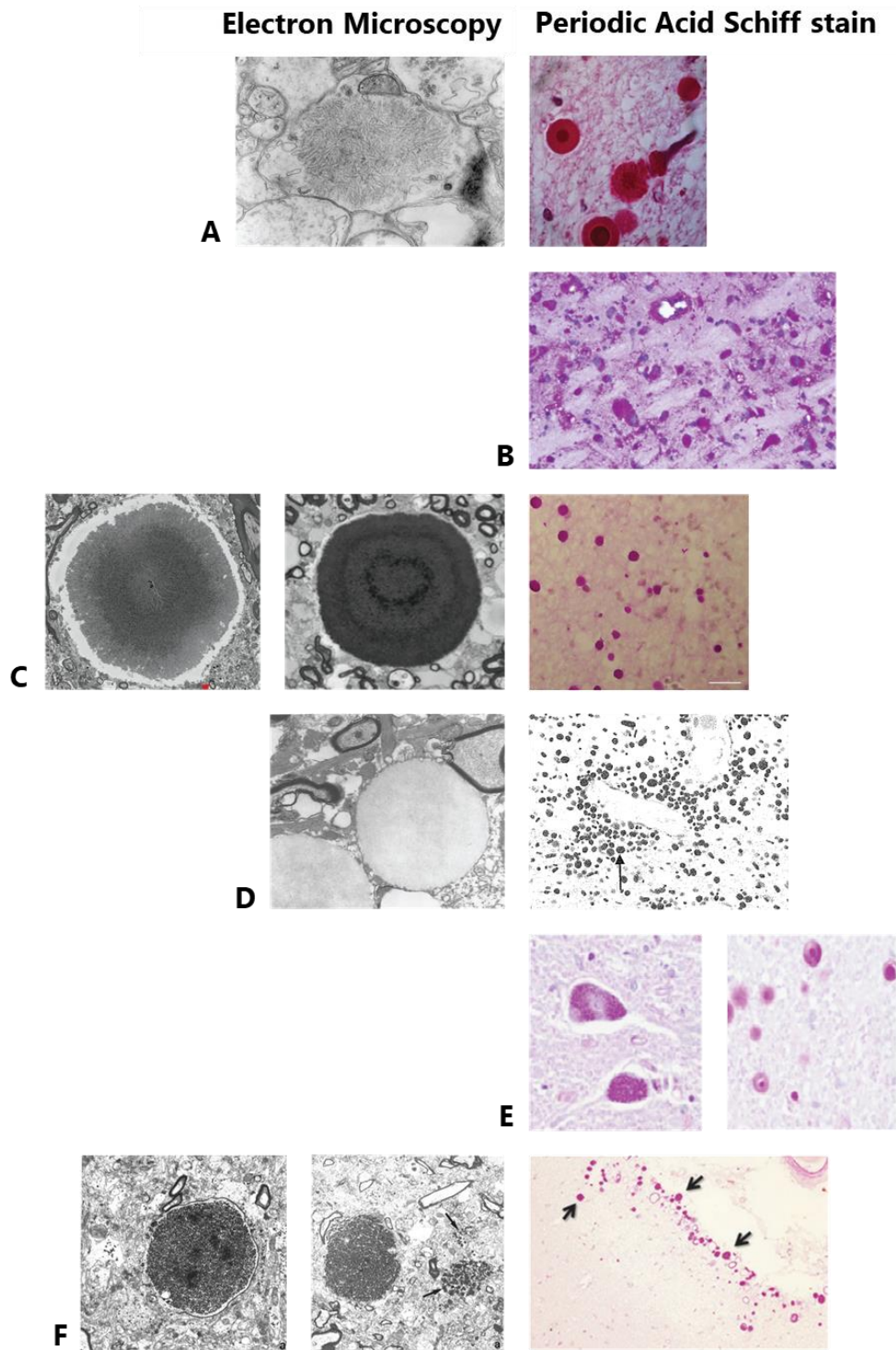


**Figure 1.1 Electron microscopy (EM) and Periodic Acid Schiff stain (PAS) of glycogen deposits/PGBs.**

**A)** Lafora disease (LD) **B)** Pompe disease – glycogen storage disorder type II (GSD II) **C)** Aging **D)** Temporal lobe epilepsy (TLE) **E)** Amyotrophic lateral sclerosis **F)** Alzheimer's disease (AD)

Multiple images in C, E, and F represent different donors.



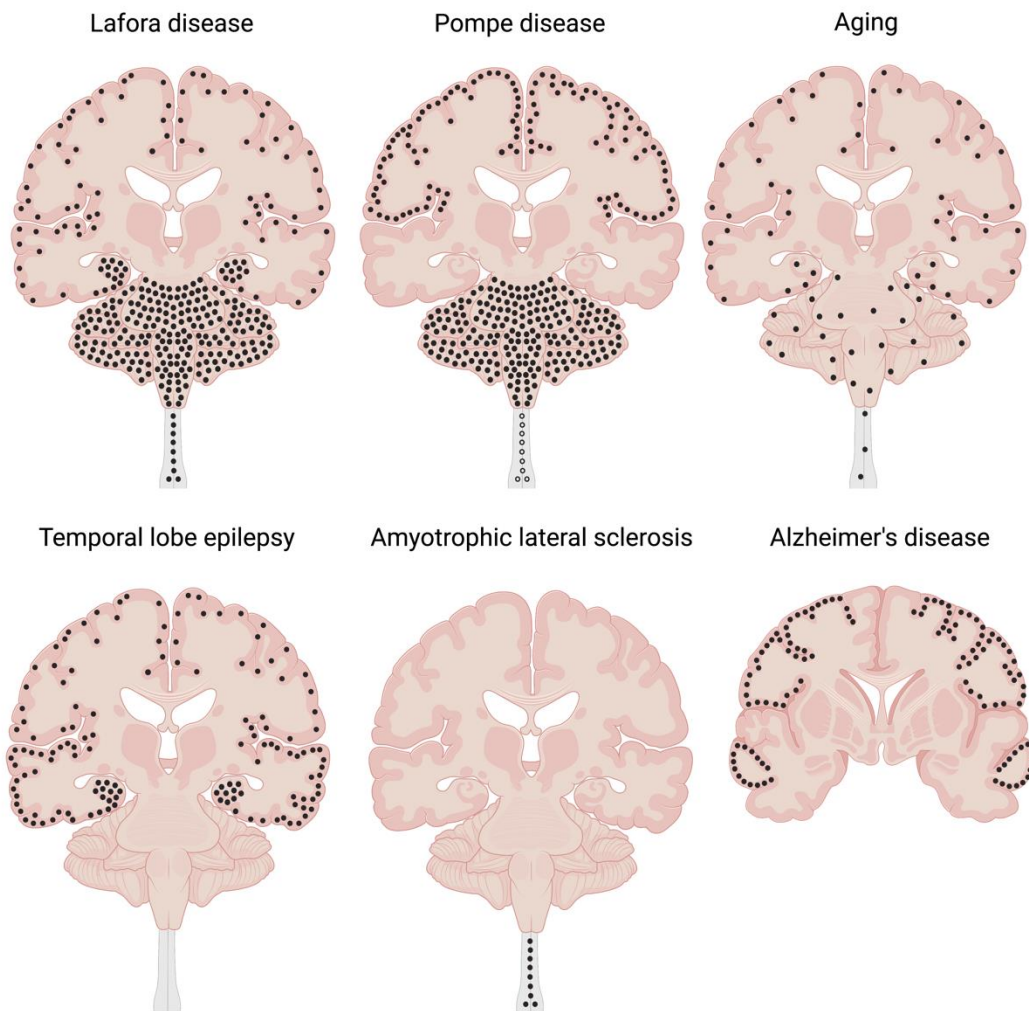


**Figure 1.2 Diagram of glycogen deposits/PGBs in neurodegenerative diseases.** Black dots/circles represent aberrant glycogen accumulations. **A)** Lafora disease (LD) **B)** Pompe disease – glycogen storage disorder type II (GSD II). Black dots represent PGB accumulation in EOPD and black circles represent PGB accumulation in LOPD. **C)** Aging **D)** Temporal lobe epilepsy (TLE) **E)** Amyotrophic lateral sclerosis **F)** Alzheimer's disease (AD).

## CHAPTER 2. Pathological biomarkers of a glycogen metabolism disorder in the aging brain

### 2.1 Introduction

Brain metabolism is the biochemical engine of cognition, memory, and behavior and is ignited and fueled by glucose. The brain accounts for 2% of body mass and 25-40% of total glucose utilization in the resting state and glucose is the pivotal molecule driving brain central carbon metabolism<sup>210-212</sup>. Glucose not only provides bioenergetics for ATP, but also supports nucleotide and neurotransmitter biosynthesis that is important for synaptic communications and normal brain homeostasis. Glucose is stored as the macro-biomolecule glycogen, the majority of which is found in the liver and skeletal muscle. Until recently, glycogen could not be detected in the brain because previous methods were not sensitive enough and failed to preserve glycogen from degradation after euthanasia. Recently improved detection methods and rapid preservation methods have proven successful at preventing glycogen degradation post-euthanasia. These advances led to discoveries of an emerging role for glycogen in synaptic plasticity and memory consolidation<sup>45,52,54</sup>.

Glycogen is comprised of glucose monomers that are linked by  $\alpha$ -1,4-glycosidic linkages into polymers by glycogen synthase (GS). These glucose polymers are branched every ~13 glucose residues by glycogen branching enzyme that generates  $\alpha$ -1,6-glycosidic linkages. Glucose-1-phosphate is released by degrading cytoplasmic glycogen by glycogen debranching enzyme and glycogen phosphorylase. Static analysis of brain glycogen using immunohistochemistry (IHC) reveals region specific and heterogeneous storage patterns<sup>39,213</sup>. However, a dynamic analysis of glycogen in aging and disease is lacking. Mutations in genes encoding glycogen metabolism enzymes cause glycogen storage diseases (GSDs) with severe tissue specific pathogenesis<sup>214</sup>. A hallmark of most GSDs are insoluble glycogen-like aggregates called polyglucosan bodies (PGBs), which vary in cellular location and morphology depending on the molecular defect.

The pathogenicity of brain PGBs is highlighted by the GSD Lafora disease (LD) that also presents as a fatal childhood dementia and progressive myoclonus epilepsy, where LBs are known drivers of the severe disease course. Multiple laboratories using numerous pre-clinical models have demonstrated that LBs drive LD inflammation, neurodegeneration, and epilepsy<sup>25,27,51,92,215-221</sup>. LD patients develop seemingly normal during their first decade of life with epilepsy and myoclonus emerging during adolescence<sup>80</sup>. Patients then experience rapid neurodegeneration, ataxia, dysarthria, and amaurosis that leads to a vegetative state prior death typically within 10 years of onset. LD is an autosomal recessive childhood dementia caused by mutations in either the *Epilepsy Progressive Myoclonus type 2a or 2b (Epm2a or Epm2bB)* gene each accounting for ~50% of cases<sup>46,81-83</sup>. The proteins encoded by *Epm2a* and *Epm2b* are the glycogen phosphatase laforin and the E3 ubiquitin ligase malin, respectively. Loss of function of either protein promotes the generation of aberrantly branched, hyper-phosphorylated, cytoplasmic PGBs called Lafora bodies (LBs) throughout the body and most extensively observed in the skeletal muscle, heart, brain where they are

neurotoxic<sup>78,222</sup>. In the brain, LBs are found in 99% of astrocytes, and <10% of neurons<sup>96</sup>. Multiple independent studies have established that decreasing LB formation or ablating previously established LBs prevents neurodegeneration and epilepsy in LD mouse models while restoring normal brain metabolism<sup>25–28,118,223</sup>. Conversely, overexpression of constitutively active glycogen synthase promotes the accumulation of a PGB that drives neurodegeneration in flies and mice<sup>90</sup>. These studies have elucidated the molecular etiology of LD and established the importance of proper glycogen metabolism in the brain.

Visualizing glycogen is often achieved by using Periodic Acid Schiff staining that was developed in the 1940's<sup>224</sup>. PAS reacts with 1,2-glycol linkages and stains multiple carbohydrate polymers, including glycogen, PGBs, glycoproteins, and proteoglycans<sup>38</sup>. PAS stain is a standard technique for identifying glucose polymers in paraffin embedded tissue, but PAS is limited in both specificity and sensitivity. A more accurate method for quantitation of glucose polymers has been recently established using gas-chromatography coupled mass spectrometry (GCMS)<sup>40</sup>. There are many sources of glucose polymers in tissues beyond glycogen like glycoproteins and proteoglycans, which PAS and GCMS can detect.

LBs can also be detected by an IgM antibody purified from the antisera of rabbits inoculated with the myocardium of a LD patient, designated KM279<sup>217,225,226</sup>. KM279 detects LBs from human brain, skeletal muscle, heart, and liver as well as LBs from other mammals like dogs and mice<sup>225–231</sup>. KM279 also detects other PGBs like those found in GSD IV, hepatocyte “ground-glass” inclusions in livers of alcohol abuse patients, aggregates in a patient with alpha-thalassemia major receiving iron chelation therapy, and aggregates in a patient with trisomy 21 who had undergone a bone marrow transplant for acute myeloid leukemia<sup>232,233</sup>. Importantly, KM279 also detects a PGB found in the aging brain called corpora amylacea, a polyglucosan structure catalyzed by glycogen synthase that accumulates with advancing age<sup>90,225,226,234</sup>. A recent detailed analysis defined that KM279 recognizes aberrant PGBs but does not detect normal glycogen<sup>225</sup>.

An additional anti-carbohydrate antibody is IV58B6. IV58B6 is a robust anti-glycogen antibody that was raised against the mandibular cartilage of a rat<sup>38,225,235,236</sup>. IV58B6 can detect both soluble and insoluble glycogen molecules, like PGBs, as well as mycobacterial polysaccharides and  $\alpha$ -glucans<sup>39,213,226,237–245</sup>. Interestingly, glycogen synthesized *in vitro* either enzymatically or synthetically is not detected by IV58B6 but can be detected by the anti-glycogen antibody ESG1A9, providing a clue that the epitope may be related to branching structure<sup>39</sup>. Several groups have reported that IV58B6 and ESG1A9 have different affinities for varied sizes of glycogen particles<sup>39</sup>. Although the exact epitopes of KM279, IV58B6, and ESG1A9 still need to be defined, these antibodies are powerful tools to visualize and quantify glycogen and glycogen-like aggregates while maintaining spatial information that is lost when glycogen is purified, hydrolyzed, and quantified. The IV58B6 and KM279 antibodies have been used to study healthy and diseased glycogen in the WT and *Epm2a*<sup>-/-</sup> (LKO) mouse brain<sup>15,217</sup>.

In this study, four methods were applied to define the longitudinal patterns of soluble glycogen, corpora amylacea, and LBs in WT and LKO mice. PAS stain, KM279, and

IV58B6 IHC analysis of WT mouse brains, skeletal muscle, and hearts are supported by a recently established and highly robust method for quantifying hydrolyzed glycogen using GCMS. These methods were also used to examine laforin heterozygote mice, a model of healthy carriers of an LD locus.

These methods were used to define a longitudinal analysis of glycogen dynamics in mice with healthy and diseased glycogen metabolism. In doing so, this study contributes to the characterization of the detection specificity of PAS and the glucose polymer detection method by GCMS and the epitopes of IV58B6 and KM279. For sake of clarity, we discuss these techniques with respect to their known specificities for soluble glycogen and/or PGBs. Thus, this longitudinal study is a comprehensive biomarker analysis of the dynamics of glycogen and PGBs. Brain glycogen and LBs are largely found in astrocytes, and glia have been proposed to be involved in an inflammatory response in LD<sup>25,27,118,215,221,223</sup>. Using traditional markers of astrogliosis, Gfap, and microgliosis, Iba1, we also include analyses of glial activation over time. Our analyses collectively describe a plateau effect of total LB accumulation and provide physiological evidence to strongly suggest their propensity to aggregate. We further show that microglia are significantly activated in LKOs compared to laforin heterozygotes, whose microglia activation is the same as in WT mice. These main findings act as a particularly important set of biomarkers highly useful for current and future pre-clinical development of LD therapeutics<sup>118,223</sup>.

## 2.2 Methods

### 2.2.1 *Mouse models and tissue preparation*

Laforin KO (LKO) mice have been described previously and were generated by removing the DSPD exon of *Epm2a*, producing an *Epm2a*-null mutant<sup>217</sup>. Male C57BL/6J LKO, and WT mice were bred to create laforin heterozygotes. The mice were housed in a climate-controlled environment with a 14/10 h light/dark cycle (lights on at 0600 h) with water and solid diet provided *ad libitum* throughout the study. The animal procedures used in this study were approved by the Institutional Animal Care and Use Committee (IACUC) at as specified by the 1985 revision of the Animal Welfare Act. WT, LKO, or laforin heterozygous mice were sacrificed at 1-, 3-, 6-, 9-, 12-months. WT and LKO mice were also sacrificed at 24-months. Mice were sacrificed by cervical dislocation, and decapitation, and tissues were rapidly dissected. One half of the heart, half the quantity of dissected skeletal muscle, and one hemisphere of the brain was fixed with formalin (10% formaldehyde in PBS) for 24 h and exchanged for 70% ethanol after 24 h for immunohistochemistry. The remaining tissue was flash-frozen in liquid nitrogen.

### 2.2.2 *Histology*

Periodic Acid Schiff (PAS) staining was performed per standard protocol on 4  $\mu\text{m}$  sections of formalin fixed brain, skeletal muscle, or heart embedded in paraffin<sup>234</sup>.

IHC was performed on 4  $\mu\text{m}$  sections of brain, heart, or skeletal muscle using IV58B6, Gfap, or Iba1 were de-waxed, rehydrated, and warmed to 37°C for 1 h in Ventana CC2 Standard buffer for antigen retrieval. The antigen retrieval method specific to sections receiving KM279 were [Dako Low pH, 110C, 20', 1 h RT]. The generation of KM279 and IV58B6 primary antibodies has been previously described<sup>225,226,235</sup>. Concentrations of antibodies were as follows: KM279 1:50, IV58B6 1:50, Gfap (Ab7260) 1:2000, Iba1 (ab5076) 1:300. Detection kits used: KM279 Vector MOM (MP-2400), IV58B6 Vector MOM (MP-2400), Gfap Ventana OmniMap Rabbit-HRP (760-4311), Iba1 Ventana OmniMap Goat-HRP (760-182).

### 2.2.3 *Gas-chromatography mass spectrometry (GCMS) analysis of glycogen*

One hemisphere of the brain, half the quantity of dissected skeletal muscle, and one half of the heart was flash-frozen in liquid nitrogen and pulverized into powder (5  $\mu\text{m}$  particles) using a liquid nitrogen Freezer/Mill Cryogenic Grinder (SPEX SamplePrep). Glycogen purification, hydrolysis, derivatization, and quantitation of glycogen by GCMS was performed as described previously<sup>40</sup>. 20 mg of each pulverized tissue was extracted in 1 mL of 50% methanol and separated into polar (aqueous layer) and insoluble fractions containing glycogen/DNA/RNA/protein by centrifugation at 4°C 15,000 rpm for

10 min. The pellet was subsequently washed three times with 50% methanol and once with 100% methanol to remove polar contaminants. The polar fraction was saved for future experiments. The pellet was hydrolyzed by resuspension in 100  $\mu$ L of deionized water followed by addition of an equal part of 6 N HCl. The samples were vortexed thoroughly and incubated at 95 °C for 2 h. The hydrolysis was quenched by adding 100% methanol after which, the samples were incubated on ice for 30 min. The supernatant was collected after centrifugation at 15,000 rpm at 4°C for 10 min and subsequently dried by SpeedVac (Thermo). Derivatization of dried polar samples began with the addition of 70  $\mu$ L of 20 mg/mL methoxylamine hydrochloride in pyridine followed by a 30 °C incubation for 1.5 hr. Then, 50  $\mu$ L was transferred to a V-shaped amber glass chromatography vial and 80  $\mu$ L of trimethylsilylating agent N-methyl-N-trimethylsilyl-trifluoroacetamide (MSTFA) was added. This step was followed by a 30 min incubation at 37 °C. After cooling, the derivatized mixture was analyzed by GCMS. An Agilent 7800B GC coupled to a 5977B MS detector was used in this study. GCMS protocols were similar to those described previously except for a modified source temperature of 280 °C<sup>209</sup>. MassHunter Unknowns Analysis (B.09.00, Agilent Technologies, Santa Clara, CA, USA) software matched to the FiehnLib metabolomics library was utilized for curation of the MS data set with retention time and fragmentation pattern matching. Mass spectra were translated to relative metabolite abundance using MassHunter Quantitative Analysis (TOF) (B08, Agilent Technologies, Santa Clara, CA, USA). Relative abundances were adjusted to protein input.

#### **2.2.4 Quantification and statistical analysis**

PAS staining and IHC quantitation was achieved using HALO analysis software by Indica Labs. PAS, KM279, and IV58B6 analysis (total glycogen) were based on the “Area Quantification” v2.1.11 algorithm. Analysis of IV58B6 regarding nuclear and cytoplasmic glycogen, Gfap, and Iba1 were based on the Multiplex IHC v2.3.4 algorithm. Activated microglia analysis was based on the “Microglial Activation” v1.4 algorithm. Multiple comparison two-way Anova and descriptive statistics were performed using GraphPad Prism software.

## 2.3 Results

### 2.3.1 Longitudinal analysis of glycogen and PGBs in the brain, skeletal muscle, and heart

PAS stain is a historically standard technique for identifying PGBs and glycogen in paraffin embedded tissue<sup>38,142</sup>. A more accurate method for quantitation of glucose polymers has been recently established using GCMS<sup>40</sup>. Using both methods, we analyzed whole brains of 1-, 3-, 6-, 9-, 12-, and 24-month-old WT and laforin knockout (LKO) male mice. To achieve minimal glycogen degradation post-mortem, mice were euthanized by cervical dislocation followed by decapitation and rapidly dissected with tissues submerged in liquid nitrogen or formalin. PAS-stained slides were digitally captured using a ZEISS Axio Scan.Z1 slide scanner and analyzed using the HALO image analysis platform. PAS staining (**Figures 2.1** and **2.2**) and respective area quantitation (**Figure 2.1B**) revealed that the quantity of PAS+ signals in the brain of LKO mice sharply increases between the ages of 1- and 6-months and then plateaus 8-fold higher than WT. Conversely, WT PGBs steadily increased over time though at a dramatically lower level than LKO mice (**Figure 2.1B**).

While PAS reacts with glycogen, glycoproteins and proteoglycans, the GCMS-based method specifically quantifies glucose. Therefore, the GCMS method was utilized to test if the PAS+ quantification was reporting levels of glucose-based polymers. Tissues frozen in liquid nitrogen were pulverized to 5  $\mu\text{m}$  particles using a magnetic assisted tissue-grinding mill while submerged in liquid nitrogen. The free lipids and polar metabolites were removed by the addition of 50% methanol:chloroform (1:1). Glycogen and PGBs were extracted with subsequent methanol and trichloroacetic acid treatment and, resuspended in H<sub>2</sub>O, hydrolyzed to glucose monomers by HCl, derivatized, and analyzed by GCMS<sup>40</sup>. LKO GCMS quantitation revealed a dramatic increase between 1- and 3-months that plateaus after 6-months and is 5-fold higher than WT (**Figure 2.1C**).

Adjacent slices from the same animals were analyzed by immunohistochemistry (IHC) using the IV58B6 antibody that has been demonstrated to detect both glycogen and PGBs and the KM279 antibody that detects PGBs (**Figure 2.3A**)<sup>225,226,235</sup>. By 12-months, LKO whole brain KM279 detection signals reached an amplitude that is higher than WT by 15-fold (**Figures 2.3B-C** and **2.4**). Importantly, WT whole brain KM279 detection is identical to that seen in laforin heterozygotes suggesting that healthy LD carriers do not accumulate LBs (**Figures 2.27A-B** and **2.4**). Analysis and quantitation of IV58B6 detection closely match the total glucose polymers detected by GCMS (**Figures 2.3D-E**, **2.5** and **2.1B**). IV58B6 detection signals dramatically increased between 1- and 3-months and plateaued after 6-months 2-fold higher than WT. Conversely, there is no statistical difference in IV58B6 glycogen levels in aged WT mice. Interestingly, a study examining glycogen in young versus old mice using IV58B6 IHC demonstrated patchy glycogen that diminished over time as corpora amylacea accumulate, resulting in glycogen intensity levels remaining the same<sup>39</sup>. The same change in glycogen

morphology is observed and quantified by IV58B6 and GCMS in the WT and laforin heterozygous mice (**Figures 2.3D-E** and **2.28A-C**).

On the corresponding WT and LKO skeletal muscle and heart tissues, we performed a similar longitudinal PAS stain, KM279 IHC, and GCMS analysis. Unlike the rapid accumulation and plateau with PAS+ and KM279 staining observed in the LKO brain, a continuous increase was observed from 1-month to 24-months for both signals in the LKO skeletal muscle and heart (**Figures 2.6A-F, 2.7, 2.8, 2.9, and 2.10**). WT KM279 signals increased in skeletal muscle and heart tissues over time, but the increase was dramatically more blunted than in the age-matched LKO tissues (**Figures 2.6A-C, 2.7, 2.8, 2.9, and 2.10**). These data illustrate that the rate of LB accumulation in skeletal muscle and heart is constant and is not like the rapid and then plateaued accumulation in the brain. GCMS analysis on LKO skeletal muscle supported the KM279 detection findings exhibiting an increase in glucose polymers over time and reaching a level 5-fold higher than WT by 12-months (**Figure 2.29A**). The same analyses performed on LKO hearts indicates that glucose polymers are 8-fold higher than WT by 12-months (**Figure 2.29B**). GCMS analysis of WT and laforin heterozygous skeletal muscle shows that glycogen levels remain constant between 1- and 12-months while increasing in heart (**Figure 2.29C-D**). Interestingly, KM279 detection is also observed to increase in the heart of laforin heterozygotes but not in WT (**Figure 2.10**). These results contribute to the characterization of tissue specific glucose polymer dynamics.



### **2.3.2 Longitudinal analysis of glycogen and PGBs in the hippocampus, cerebellum, and brainstem**

In LD patients and mice, PGBs are predominately observed in the hippocampus, brainstem, and cerebellum<sup>218</sup>. Therefore, we defined these regions-of-interest (ROIs) and performed regional “Area Quantification” analysis of the KM279 detection signal by using the HALO image analysis platform. In each of the ROIs, the LKO KM279 detection signal increases rapidly before 6-months and plateaus after 6-months of age (**Figures 2.11A-C, 2.12, 2.13, and 2.14**), which is the same pattern observed in whole brain analysis (**Figure 2.3B-C**). During the plateau, hippocampus and cerebellum LKO KM279 detection signals are each 30-times higher than WT (**Figure 2.11A, C**). The brainstem LKO KM279 detection signal is 15-times higher than WT (**Figure 2.11B**). Therefore, LBs are highest in the hippocampus and cerebellum. The WT KM279 detection signal shows an expected age dependent upward trend that is matched by laforin heterozygotes, suggesting that healthy carriers of an LD locus do not have LBs (**Figures 2.11A-C, 2.12, 2.13, 2.14, and 2.27C**).

Between 1- and 6-months, the rate of KM279 detection signal increases most rapidly in the cerebellum, with a rate of increase that is 10-times faster than in the hippocampus and 5-times faster than in the brainstem (**Figure 2.11A-C**). Within this same time frame, KM279 detection in the brainstem increases 2-times faster than in the hippocampus (**Figure 2.11A, C**). Taken together, these results suggest that LB onset and accumulation rate is highest in the cerebellum, followed by brainstem, and lastly in the hippocampus.

A similar ROI analysis was performed to quantitate the IV58B6 detection signal. Like whole brain analysis, regional IV58B6 detection on LKO mice indicates that the IV58B6 detection signal increases steeply between 1- and 6-months and then plateaus (**Figures 2.11D-F, 2.15, 2.16, 2.17**). The LKO IV58B6 detection signal is highest in the hippocampus followed by the cerebellum and the brainstem, where total glycogen is 5-times, 3-times, and 2-2.5-times higher, respectively, than in WT mice (**Figure 2.11D-F**). The WT IV58B6 detection signal is approximately equal between the hippocampus and cerebellum and does not increase with age, which agrees with previous reports (**Figure 2.11D, F**)<sup>15</sup>. The IV58B6 detection signal in the brainstem is less than in the hippocampus or cerebellum and shows an increasing trend over time (**Figure 2.11E**). The laforin heterozygote hippocampus IV58B6 detection signal is almost 2-times as much as WT and decreases overtime (**Figure 2.12D-F**). This finding may be suggestive of a region dependent regulation of laforin expression. Observational analysis of the WT and laforin heterozygote hippocampus exhibits a morphological change in IV58B6 detection patterns between the two genotypes over time, moving from a disperse to clustered arrangement (**Figure 2.12A**). These data emphasize results from the whole brain analysis in which IV58B6 detection and GCMS detection of carbohydrate polymers remains constant over time while changes in IV58B6 detection patterns are observed (**Figures 2.1C, 2.3D-E, 2.5, 2.15, 2.16, and 2.17**).

### 2.3.3 Average size and size variation of LD and aging PGBs in the hippocampus

Both PAS staining and KM279 IHC detect PGBs. Interestingly, PAS staining yields uniform signals while KM279 IHC yields light and dark staining as well as uniform versus punctate patterns. Therefore, we studied these signal attributes to characterize LBs and corpora amylacea. We first measured the diameters and calculated descriptive statistics of PAS+ signals from the hippocampus of WT and LKO mice during 6-, 9-, 12-, and 24-months, i.e., the age range where the PAS+ signal “Area Quantification” plateaus. The PAS+ signal coefficient of variation increases in LKO mice from 42% to 61% between 6- and 12-months, while in WT mice it does not change over time and is on average 43% (**Table 2.1**). These statistical measures indicate that PAS+ signal diameters vary significantly in both LKO and WT and that the variation increases with age in LKO mice. The average diameters of LKO PAS+ signals increase from 1.4-3.2  $\mu\text{m}$ , and range from 4.5-14.6  $\mu\text{m}$ , while neither the average diameter nor range of WT PAS+ signals change with age (**Figure 2.1D** and **Table 2.1**). Importantly, the LKO PAS+ signals described in the 75<sup>th</sup> percentile increase more dramatically over time than those within the 25<sup>th</sup> percentile, while neither value changes over time in WT mice (**Table 2.1**). These data indicate that the size of PAS+ signals become larger with time while PAS+ “Area Quantification” stays the same. Furthermore, the increase in LB size variation is driven by the higher abundance of larger signals. Collectively, these data strongly suggest that LBs aggregate.

A similar analysis was performed on KM279 detection signals using adjacent brain slices. The KM279 detection signal reveals two structures in the brains of WT and LKO mice. One structure appears uniform, looking dense, dark brown, and circular (**Figure 2.30A, B**). The other is a non-uniform structure, appearing uncondensed and light brown and encircling the uniform structure (**Figure 2.30A-D**). These structures were separately quantified using the “Area Quantification” analysis tool (**Figure 2.30C, D**). Between 1- and 24-months, the accumulation of the “uncondensed” material paralleled the accumulation of the uniform dark brown circular aggregates with almost 2-times the abundance (**Figure 2.30C**). To measure the diameters of KM279 detection signals we measured the uniformly detected structures because the boundaries are clearly defined and excluded the non-uniform appearing material (**Figure 2.30A-B**). The calculated coefficient of variation of the of WT uniform KM279 detection signals does not change over time and is on average 52%. In LKO mice, an increase in the coefficient of variation of the uniform KM279 signals is only significant between 12- and 24-months and is on average 33%. Thus, the average variation of uniform KM279 detection signals in WT mice is significantly higher than in LKOs (**Table 2.1** and **Figure 2.30E**). Further, the WT KM279 detection signal variation is the same in laforin heterozygote mice (**Figure 2.11C**). In contrast to the PAS+ signals, the average diameters of the LKO 6-, 9-, 12-, and 24-month-old uniform KM279 signals did not change with age, which is also seen in WT mice (**Table 2.1**). However, the average diameter of the uniform KM279 signals in LKOs is larger than in WT, averaging 3.7  $\mu\text{m}$  versus 2.9  $\mu\text{m}$  (**Table 2.1**). These collective findings indicate that the average diameter of the LKO uniform KM279 signals is larger than WT, while WT uniform KM279 signals exhibit larger diameter variation than LKOs.

Further, in both WT and LKO mice, the average diameter of the uniform KM279 signals is larger on average than PAS+ signals (**Figure 2.1D, 2.30E, and Table 2.1**). Thus, analysis of PAS+ and KM279 detection signals indicate diverging characteristics between the LKO and aging PGB. Furthermore, PAS+ and KM279 detection signals exhibit a divergence in PGB detection specificity.

#### **2.3.4 Longitudinal analysis of Gfap and Iba1 inflammatory markers**

Astrocytes and microglia play complementary roles in building and maintaining the brain, especially with respect to their proinflammatory reactions to neurodegeneration<sup>246</sup>. These glial cells also have an emerging relationship to glycogen and aberrant PGBs. Astrocytes are the main cells that accumulate glycogen in the brain and two recent independent studies demonstrated that glycogen inclusions within LKO or malin knockout (MKO) mouse brains were found in 99% of astrocytes and only 4% of neurons<sup>96</sup>. Glycogen inclusions were also found within microglia, suggesting a role for both astrocytes and microglia in LD<sup>96</sup>. Further, some recent studies have pointed to the possibility that the glycogen inclusions that accumulate in glia may promote irregular functionality of their inflammatory responses, which may be an important biomarker of LD<sup>96,97</sup>. Gfap-immunoreactive astrocytes and Iba1-immunoreactive microglia have previously been quantified at 3-4-months and 12-months in LKO and MKO mice showing increased cell count or activation at the latter time point<sup>25,28,221,247,248</sup>. For a more complete assessment of the inflammatory response in LD we performed a longitudinal analysis of Gfap expressing astrocyte and Iba1 expressing microglia activation in the LKO mouse brains and compared them to WT and laforin heterozygous aging mouse brains.

Using “Multiplex IHC” analysis of Gfap reactive astrocytes, we first quantitated the number of these glial cells over time. Whole brain quantitation indicates that the number of Gfap positive astrocytes in LKO mice is the same as WT animals until 12-months (**Figure 2.31A**). A similar trend is observed in the brainstem and cerebellum (**Figure 2.31C, D**). In the hippocampus, Gfap positive astrocytes increase in quantity from 6- to 24-months (**Figure 2.31B**). Since reactive astrocytes are scored by quantifying the area of hypertrophy and elongated protractions, we next measured reactive astrocytes by Gfap “Area Quantitation”. No difference in astrocyte activation is detected between WT and LKO mice in any region before 12-months (**Figures 2.18A, 2.19, 2.20, 2.21, and 2.22**). Since no change in astrocyte number or activation is seen for the first year of life in the LKO mice, the late stage or “middle-aged” emergence of astrocyte activation may be more related to aging than LD pathology. Interestingly, at 6-months and after, the laforin heterozygote mice exhibit an increase in Gfap expressing astrocyte count and area quantitation compared to WT (**Figure 2.32**). Why laforin heterozygotes have increased number and activation of Gfap astrocytes is unclear, however this finding is in opposition to what is seen in LKO mice, further supporting the hypothesis that astrocyte reactivity in LKO mice is defective.

Performing a similar analysis on Iba1-immunoreactive microglia, we used “Multiplex IHC” analysis to measure any change in the number of these cells over time. We find that the quantity of Iba1 reactive microglia significantly increases in the hippocampus of LKO mice between 6- and 24-months (**Figure 2.31F and Figure 2.23**). No difference is seen in whole brain analysis or in the other ROIs (**Figure 2.31E, G-H, 2.24, 2.25, and 2.26**). To perform a microglia activation analysis, we used the HALO tissue analysis software “Microglial Activation” quantification method in which Iba1 positive cells completely lacking protractions are scored as active. Unlike astrocyte activation, the morphology of microglia activation is defined by a full retraction of microglia

protractions. Using this specified method, we find that LKO microglia activation is 2 times higher than WT within the whole brain, brainstem, and cerebellum and less prominent in the hippocampus (**Figure 2.18B**). Importantly, no difference in whole brain or any ROI is observed in microglia cell count or activation between WT and laforin heterozygotes (**Figure 2.33**). These analyses show that microglia, not astrocytes, are activated throughout the lifespan of the LKO mouse.

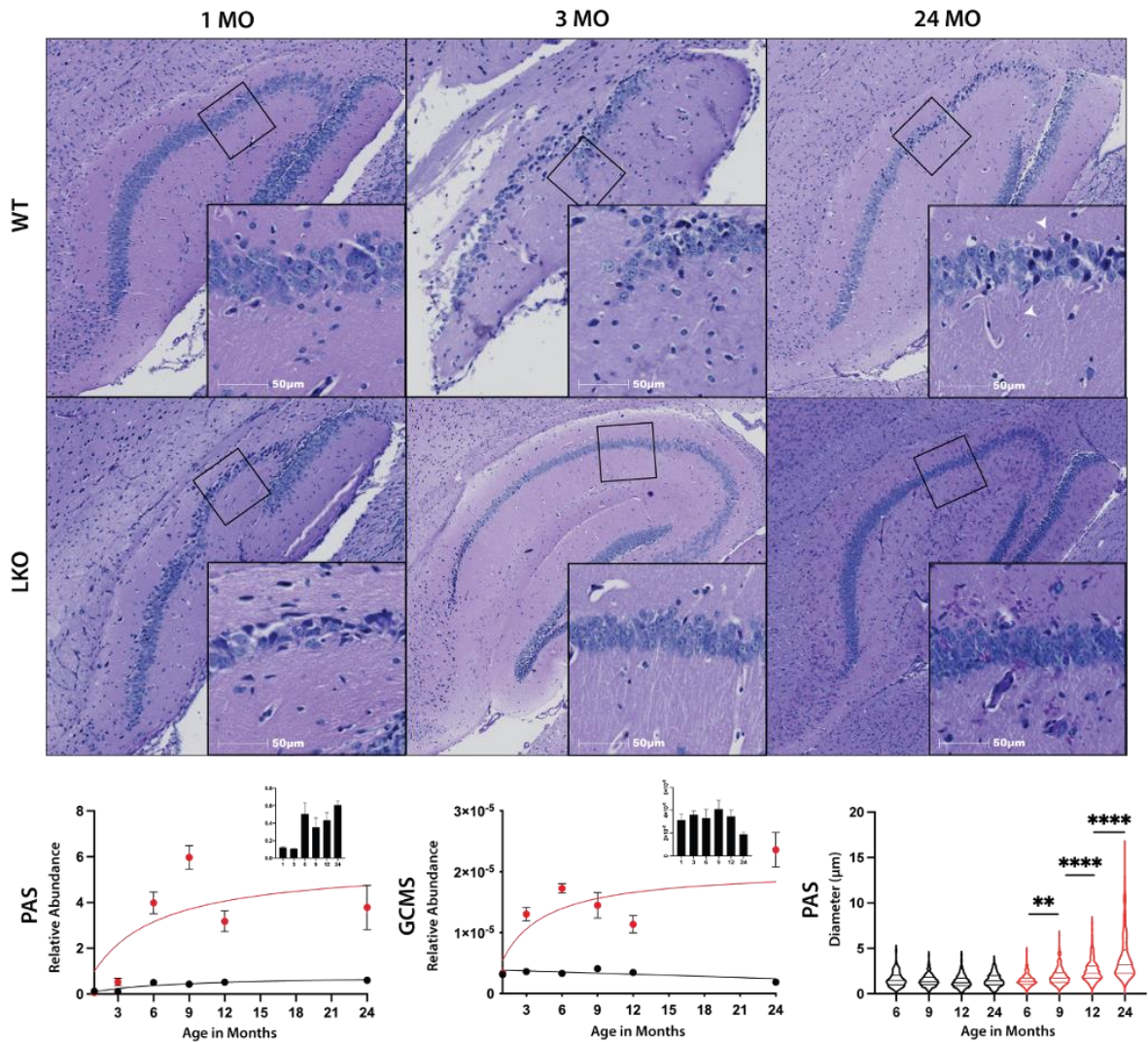


**Figure 2.1 Whole brain PAS stain and GCMS analysis of glucose polymers on WT and LKO mice aged 1-, 3-, 6-, 9-, 12-, and 24-months.** IHC analysis was performed using Indica labs software (HALO) "Area Quantification". **A)** Representative IHC images of PAS staining. **B)** Quantitation of PAS positive inclusions. **C)** Quantitation of acid-hydrolyzed glucose polymers by GCMS analysis. **D)** Quantitation of PAS+ signal diameters within the hippocampi of 6-, 9-, 12-, and 24-month-old WT and LKO mice. Black = WT, red = LKO. Pop-out column graphs are WT data. \*\*\*\* = ( $p < 0.0001$ ) \*\* = ( $p = 0.0064$ )

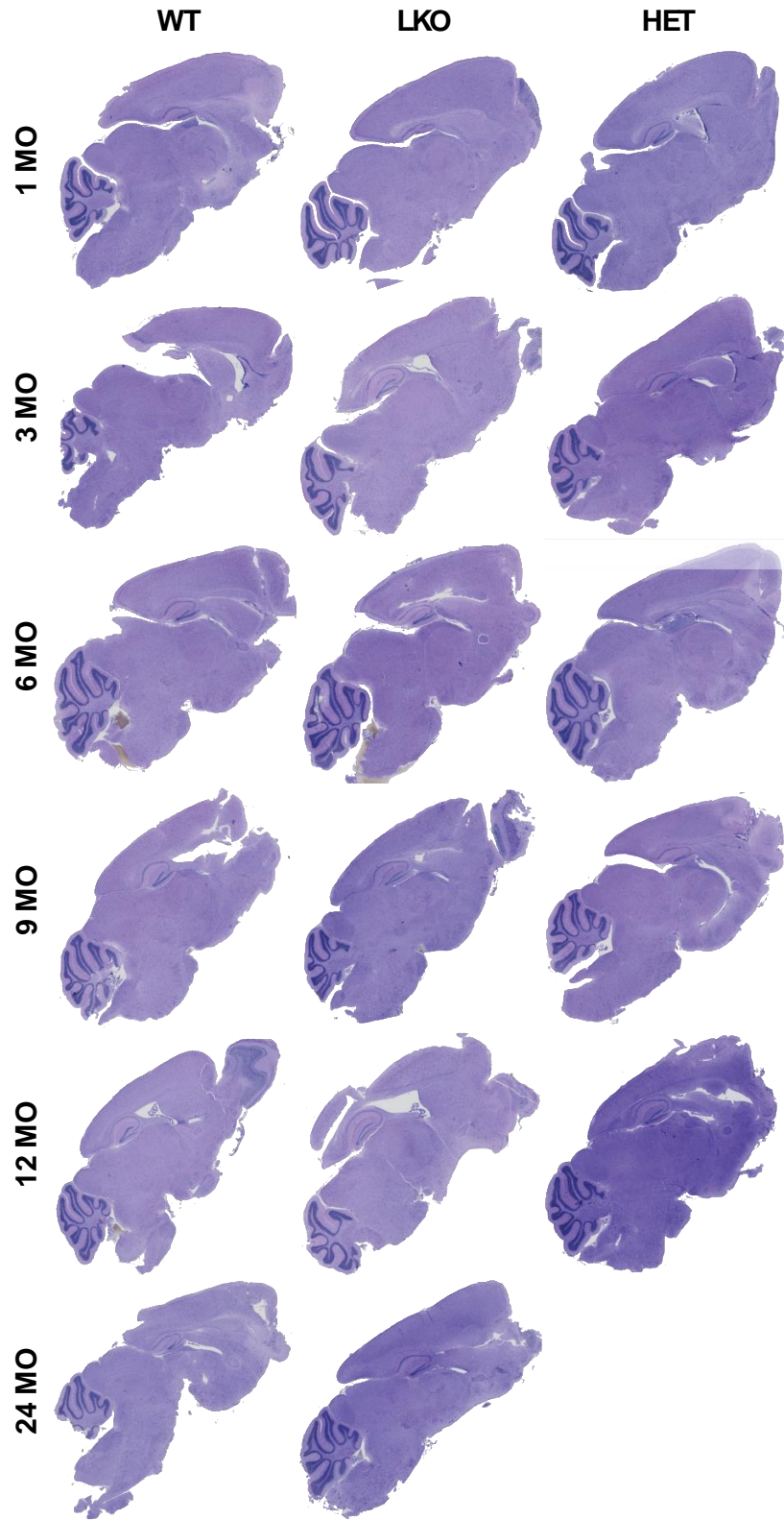
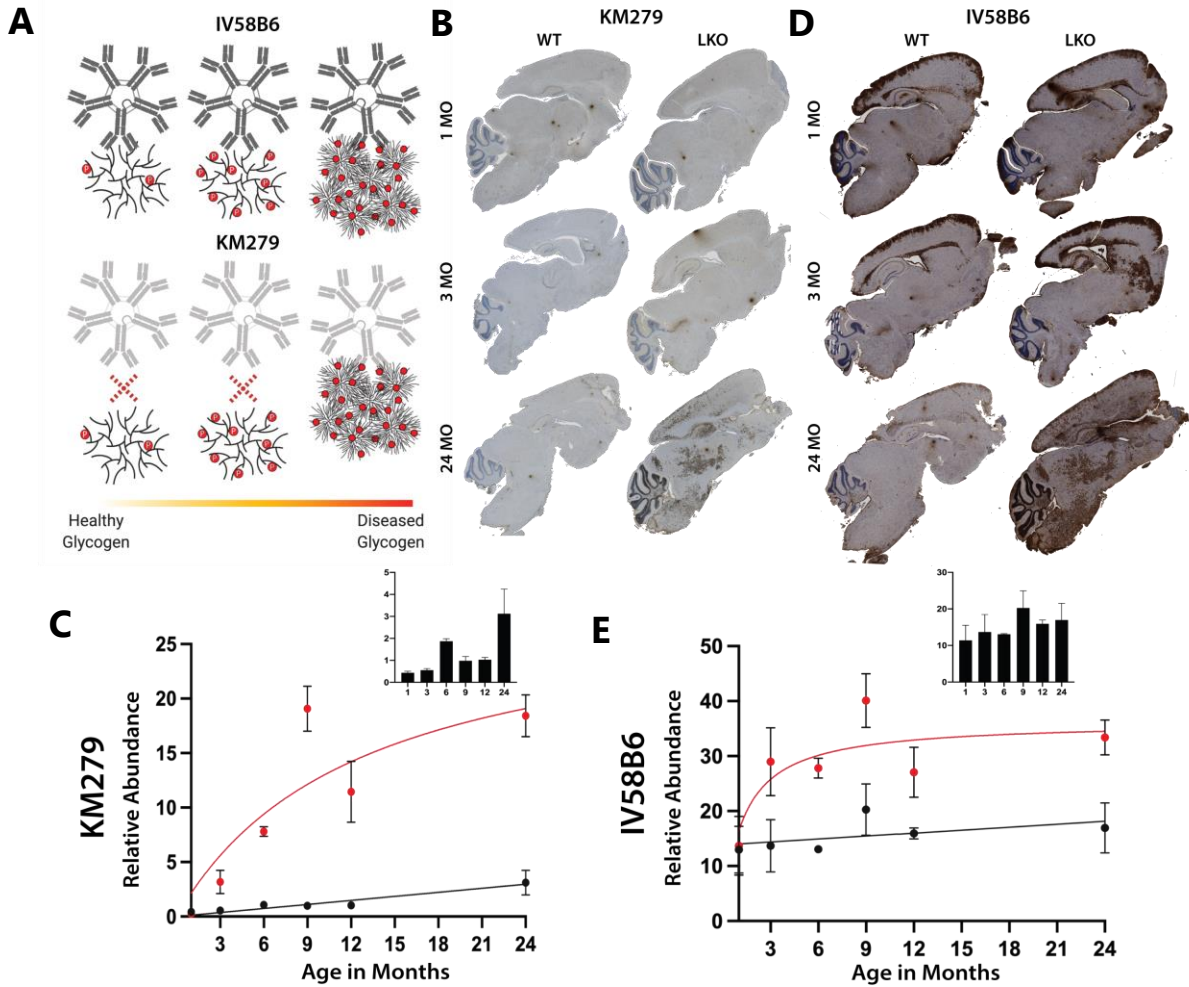


Figure 2.2 Whole brain Periodic Acid Schiff (PAS) staining.





**Figure 2.3 Whole brain KM279 and IV58B6 IHC analysis of WT and LKO mice aged 1-, 3-, 6-, 9-, 12-, and 24-months.**

IHC analysis was performed using Indica labs software (HALO) "Area Quantification". **A)** Schematic illustration of IV58B6 and KM279 antibody affinity to healthy and diseased glycogen. **B, D)** Representative IHC images of KM279 and IV58B6 quantitated in C and E, respectively. **C, E)** Quantitation of KM279 and IV58B6 IHC analysis, respectively. Black = WT, red = LKO. Pop-out column graphs are WT data.



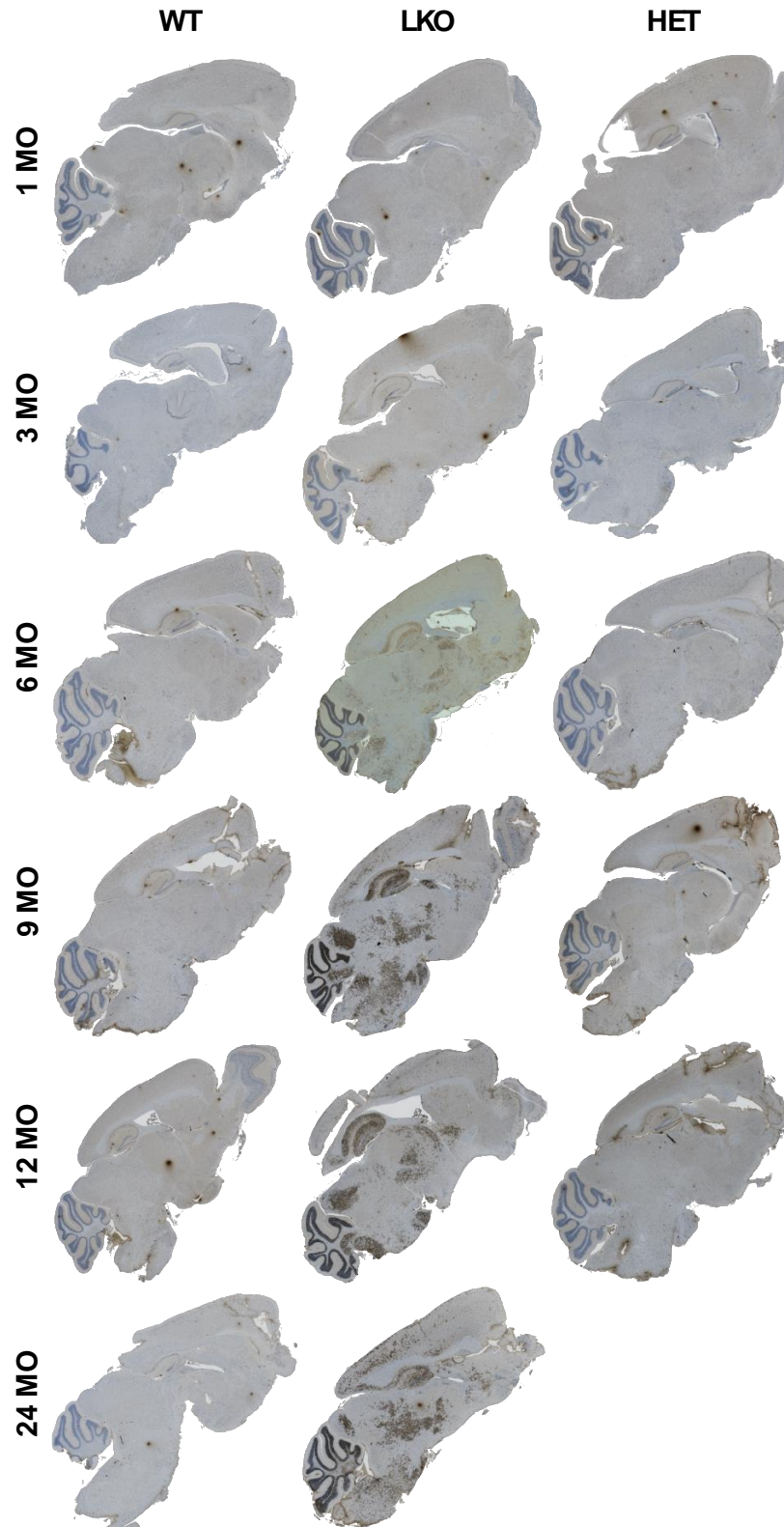


Figure 2.4 Whole brain KM279 IHC.

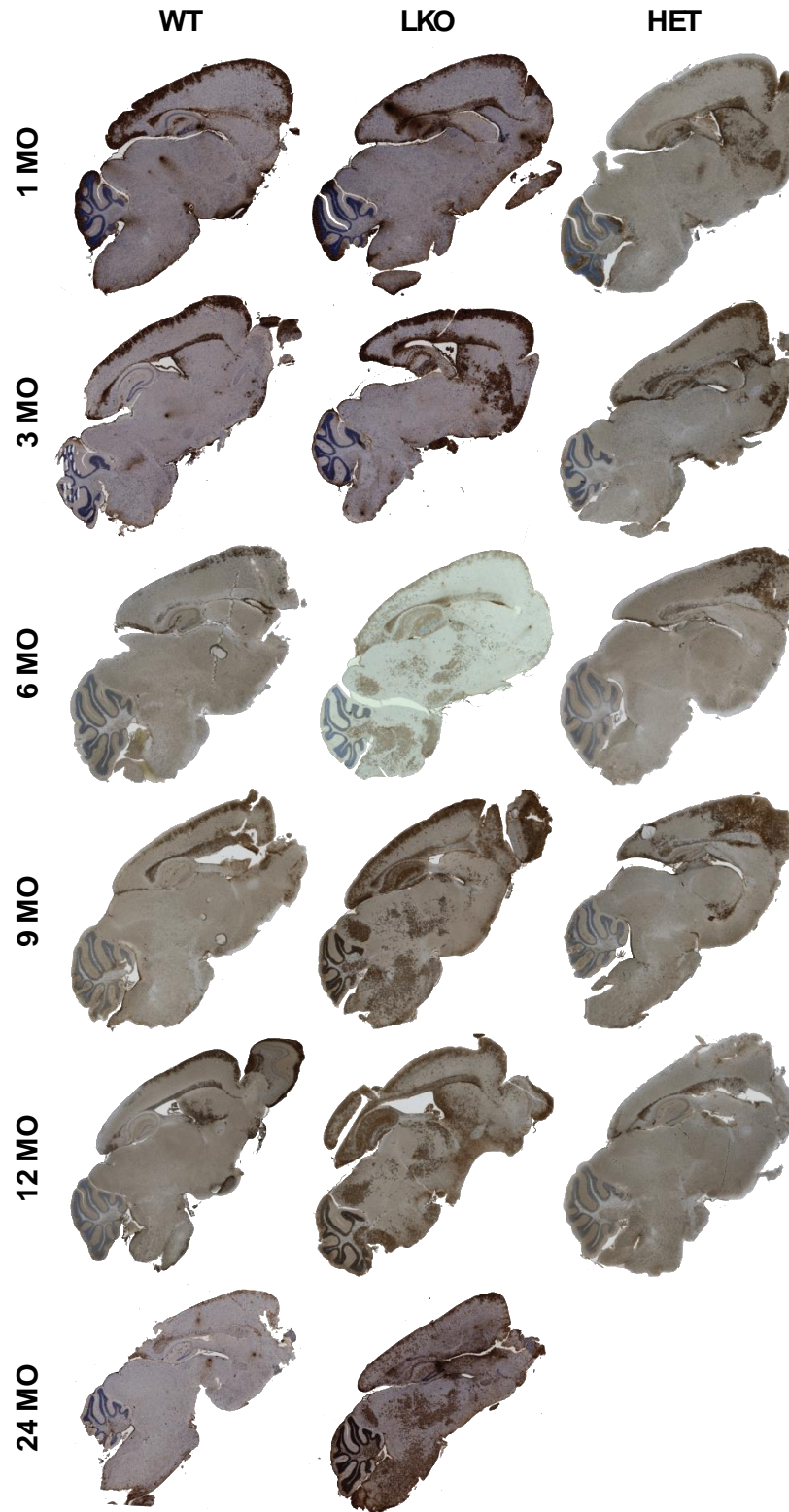
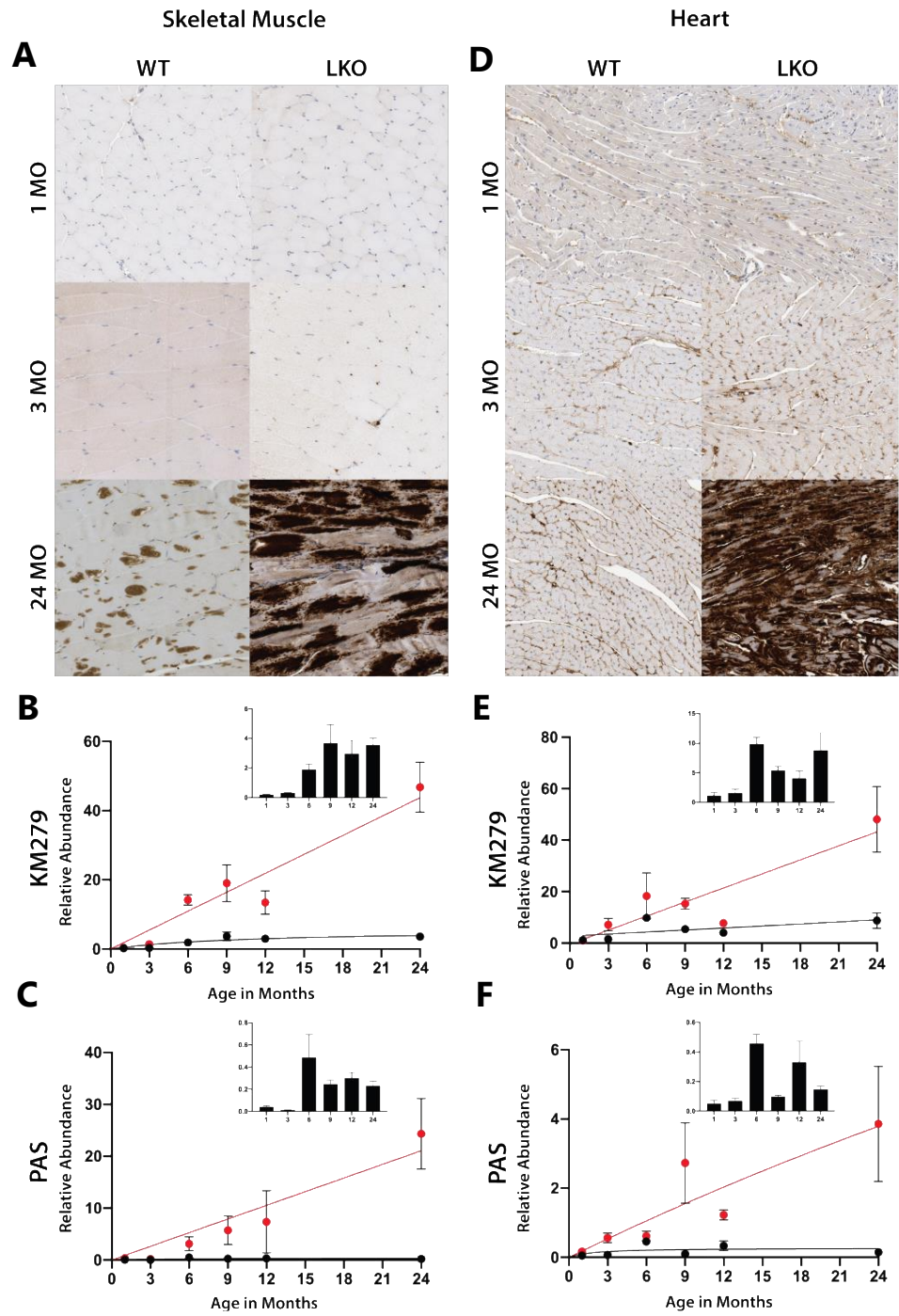


Figure 2.5 Whole brain IV58B6 IHC.



**Figure 2.6 Skeletal muscle and heart PAS stain and KM279 IHC analysis of WT and LKO mice aged 1-, 3-, 6-, 9-, 12-, 24-months.**

IHC analysis was performed using Indica labs tissue analysis software (HALO) "Area Quantification". **A, D)** Representative KM279 IHC analysis on skeletal muscle and heart quantified in **B, E**, respectively. **B, C)** Quantitation of KM279 IHC and PAS stain analysis on skeletal muscle, respectively. **E, F)** Quantitation of KM279 IHC and PAS stain analysis on heart, respectively. Black = WT, red = LKO. Pop-out column graphs are WT data.



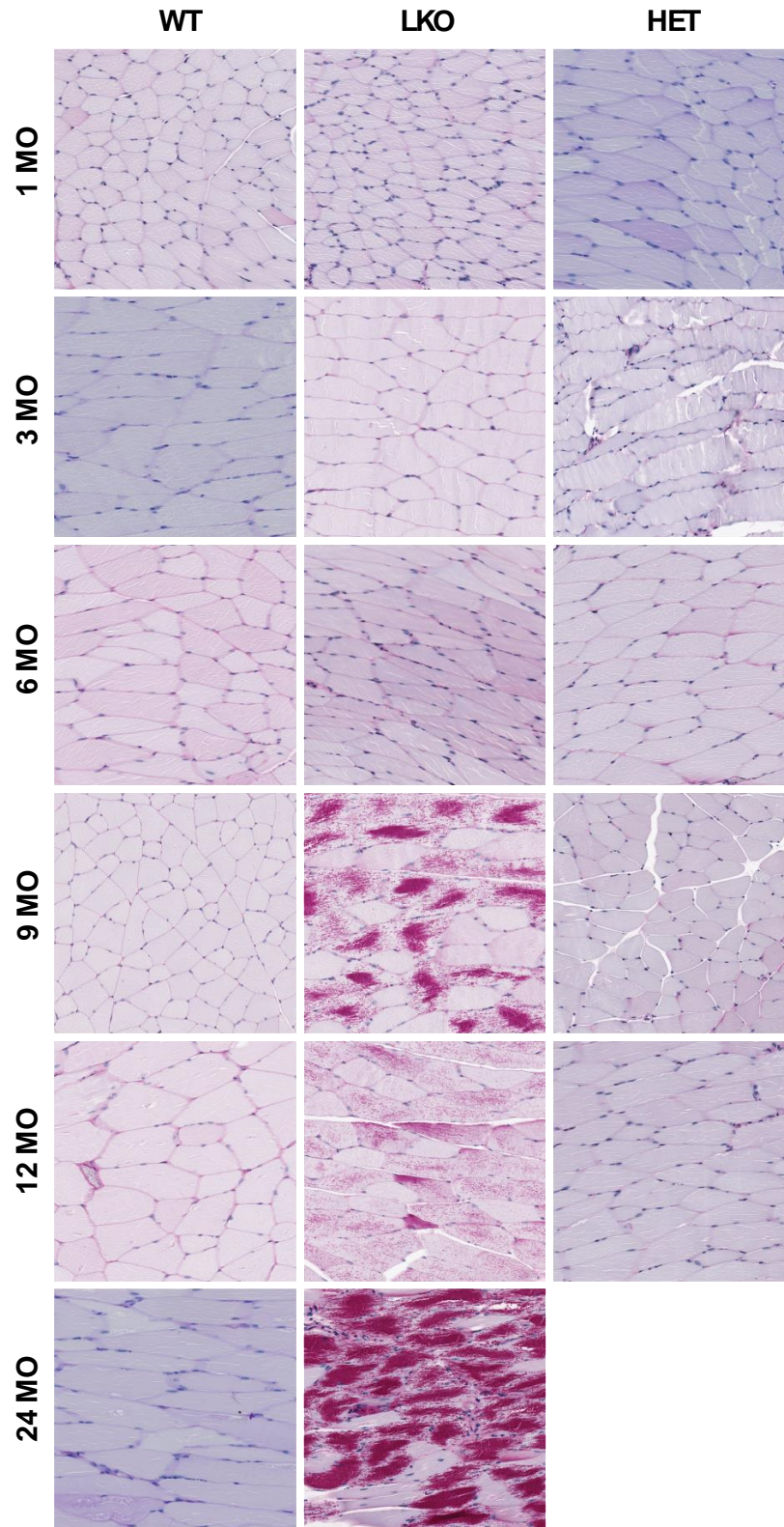


Figure 2.7 Skeletal muscle Periodic Acid Schiff (PAS) staining.

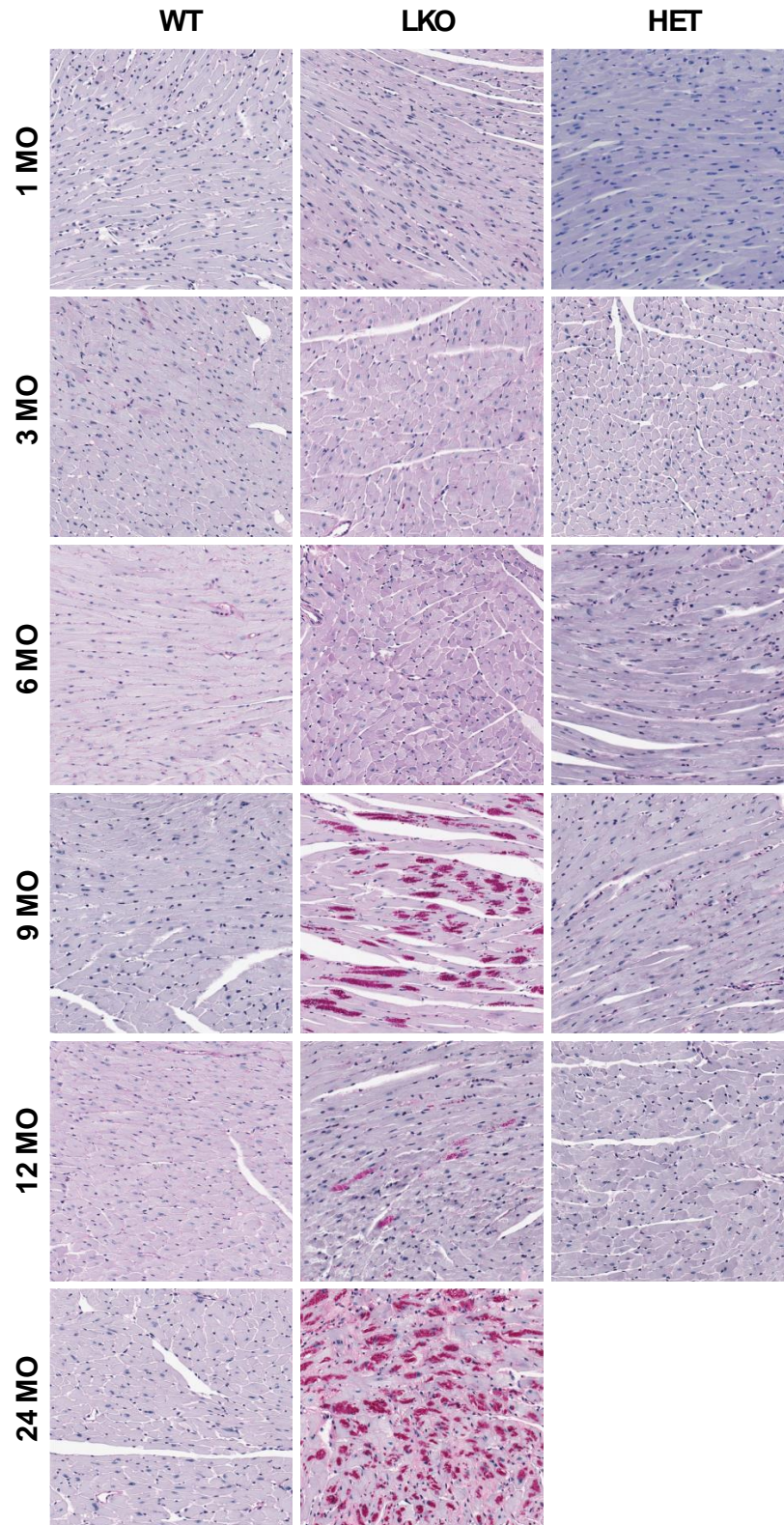


Figure 2.8 Heart Periodic Acid Schiff (PAS) staining.



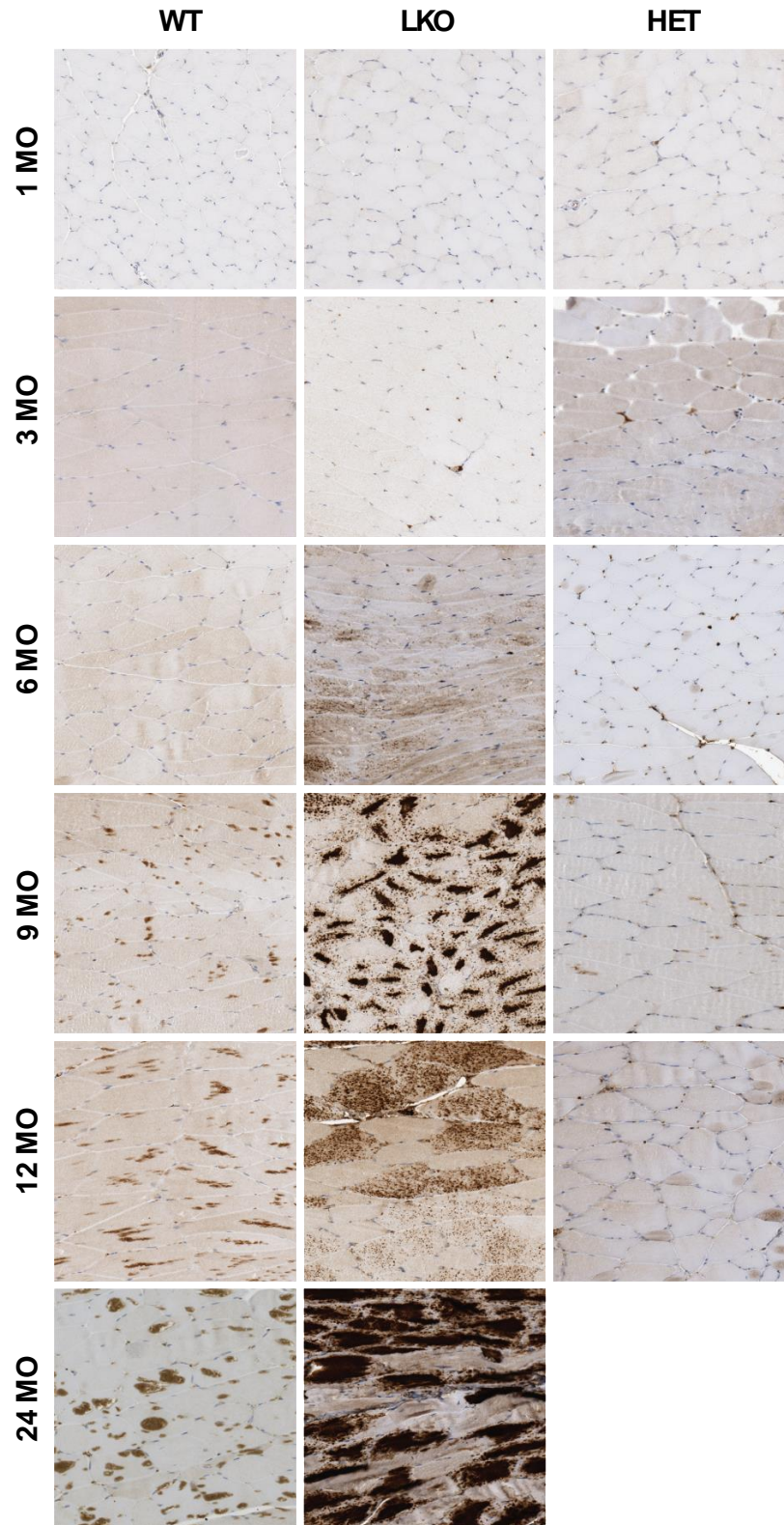


Figure 2.9 Skeletal muscle KM279 IHC.

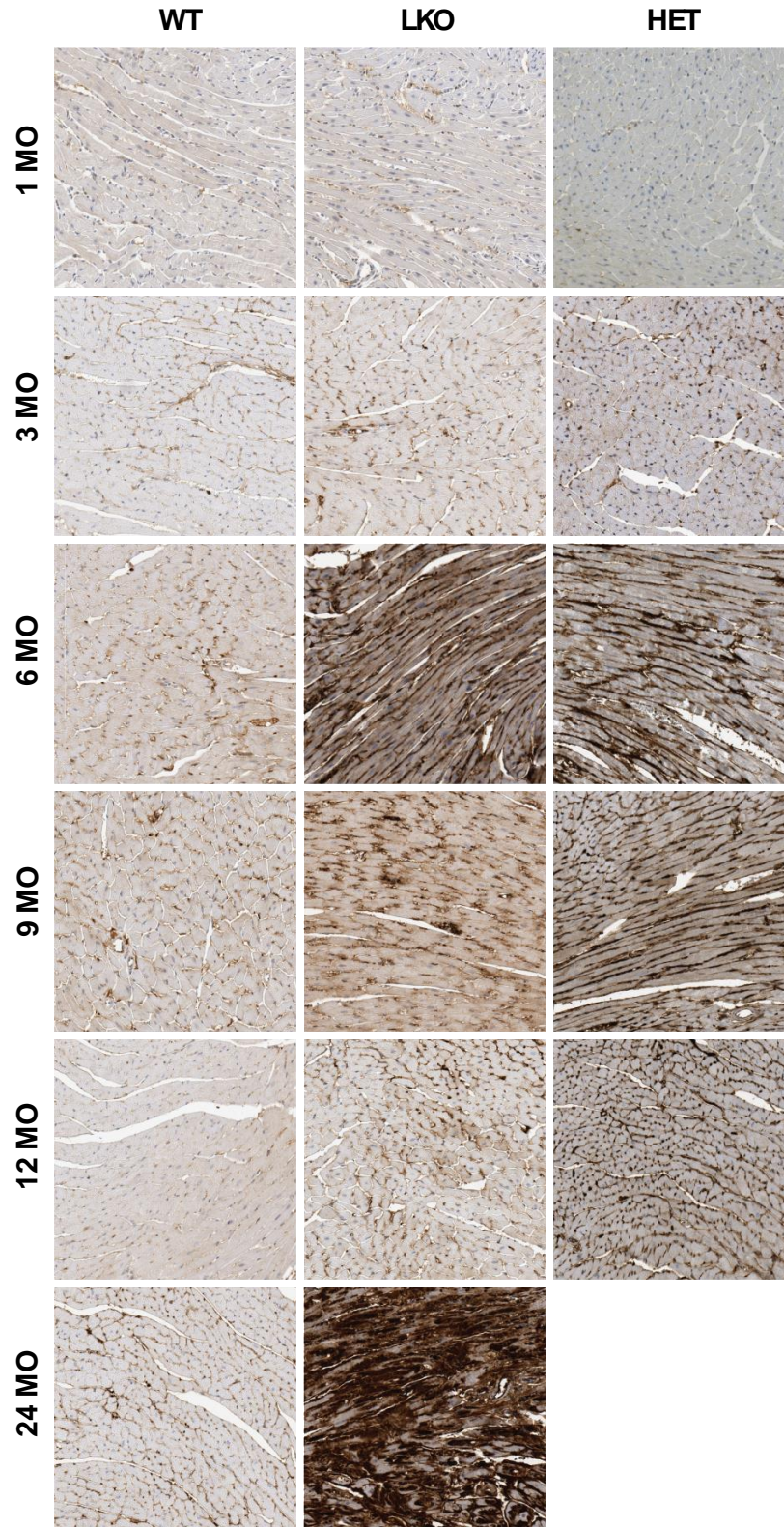
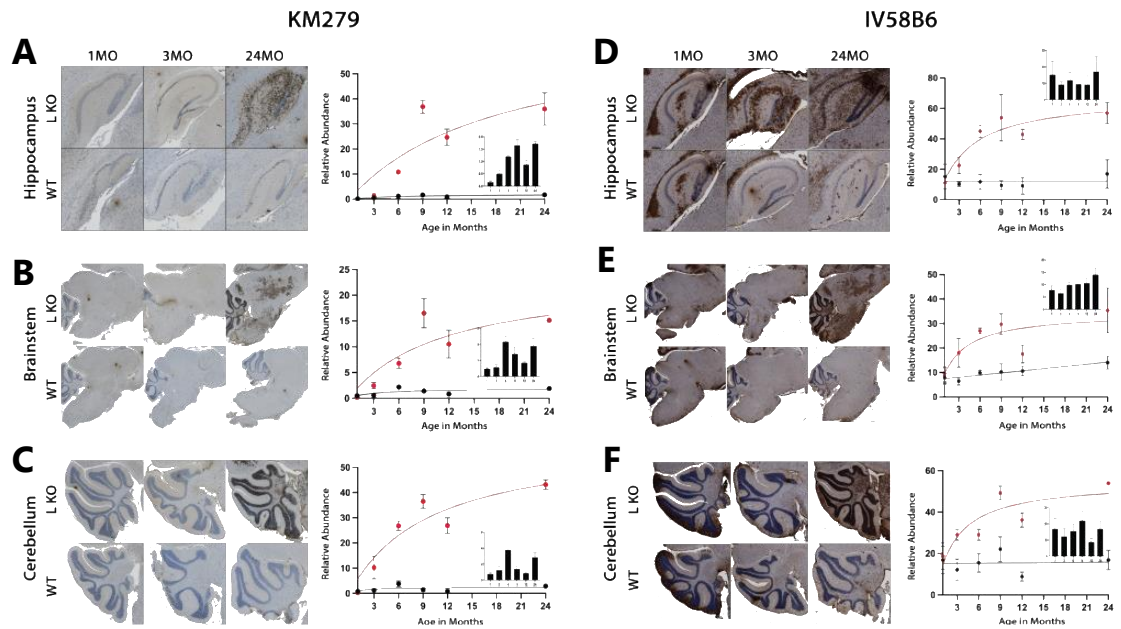


Figure 2.10 Heart KM279 IHC.





**Figure 2.11 Brain region-of-interest KM279 and IV58B6 IHC analysis of WT and LKO mice aged 1-, 3-, 6-, 9-, 12-, 24-months.**

IHC regional analysis on hippocampus (top row), brainstem (middle row), and cerebellum (bottom row) was performed using Indica labs software (HALO) "Area Quantification". **A-C)** Representative region-of-interest IHC analysis of KM279 (mainly diseased glycogen) (left) and quantitation (right). **D-F)** Representative region-of-interest IHC analysis of IV58B6 (total glycogen, diseased and non-diseased) (left) and quantitation (right). Black = WT, red = LKO. Pop-out column graphs are WT data.



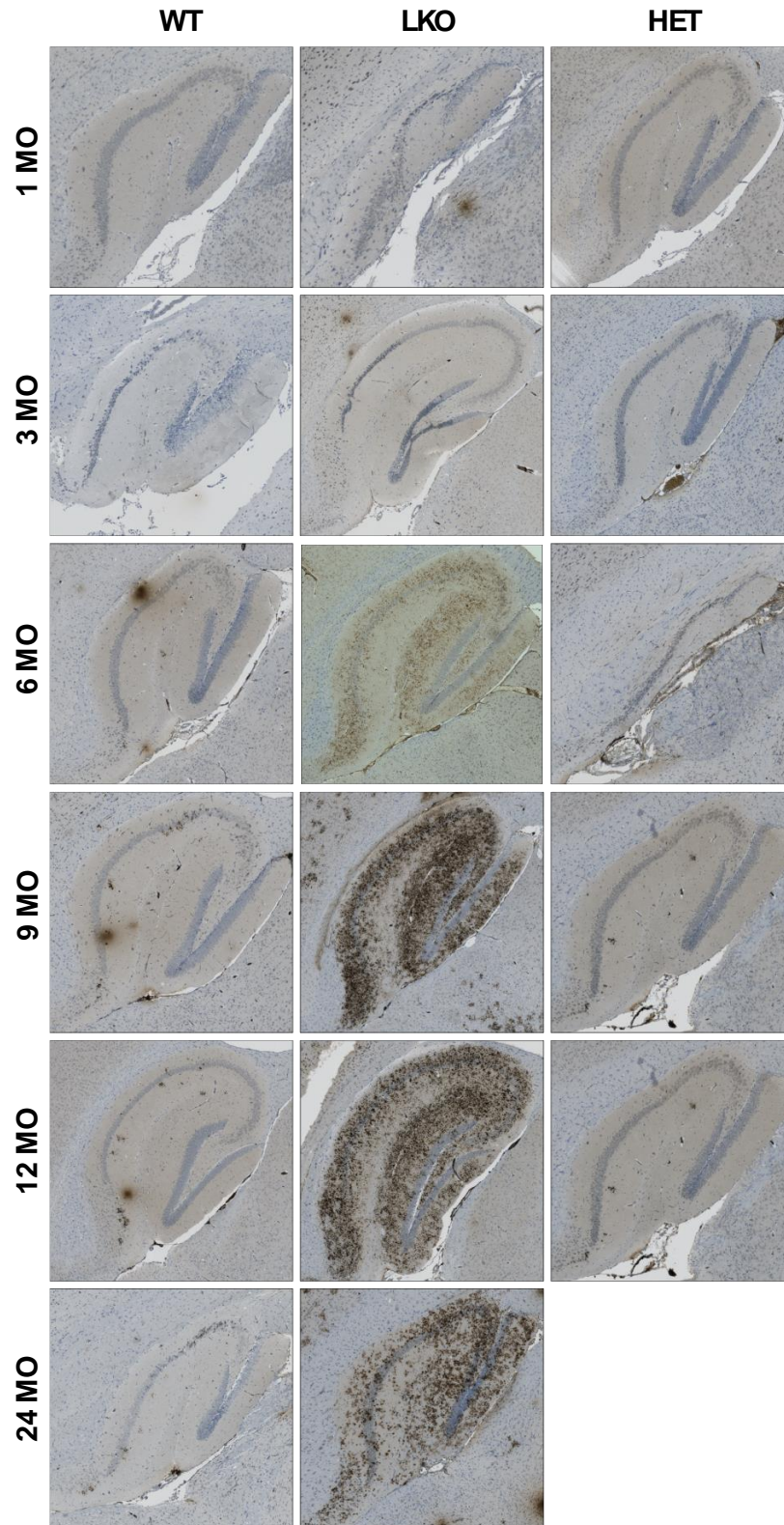


Figure 2.12 Hippocampus KM279 IHC.

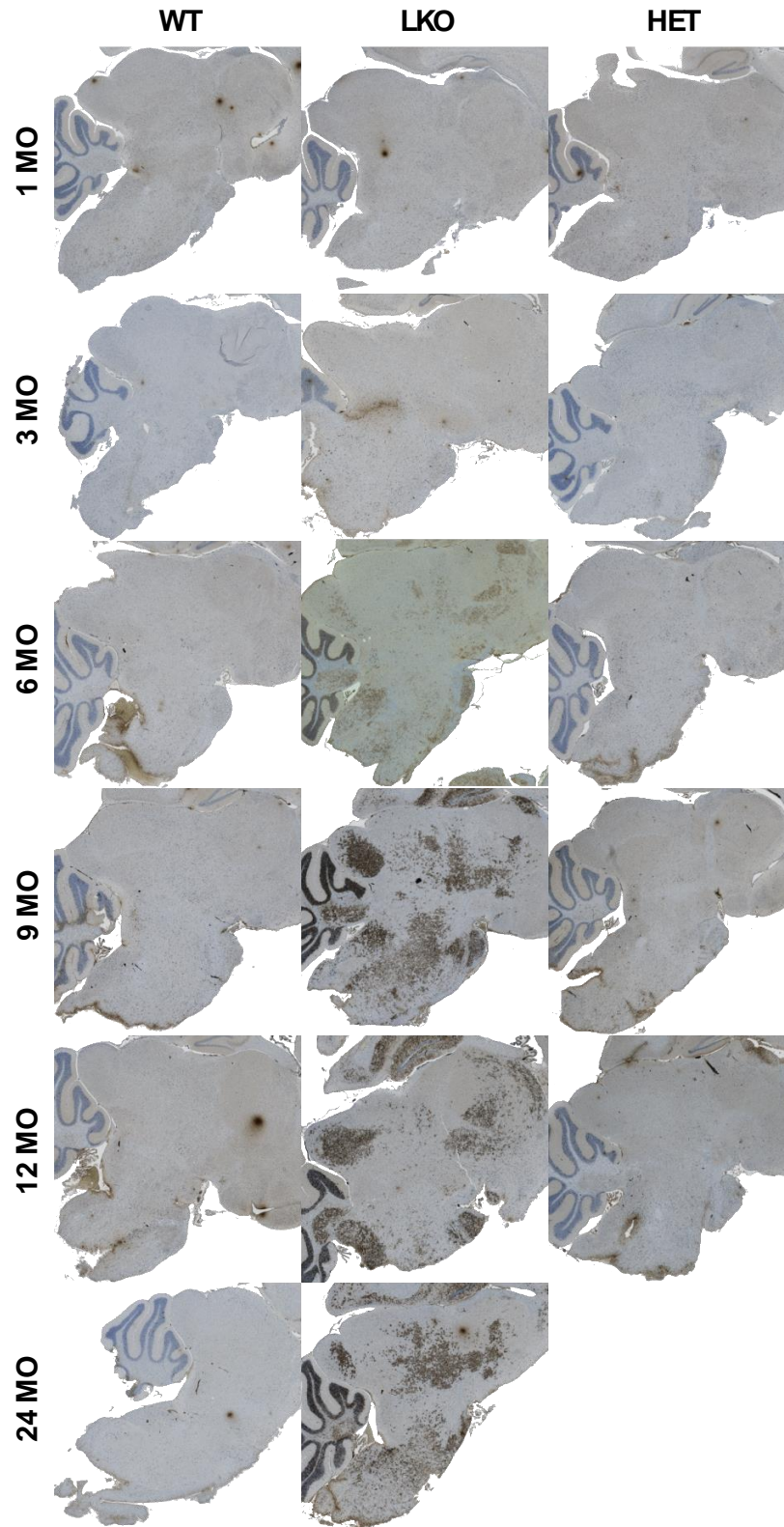


Figure 2.13 Brainstem KM279 IHC.



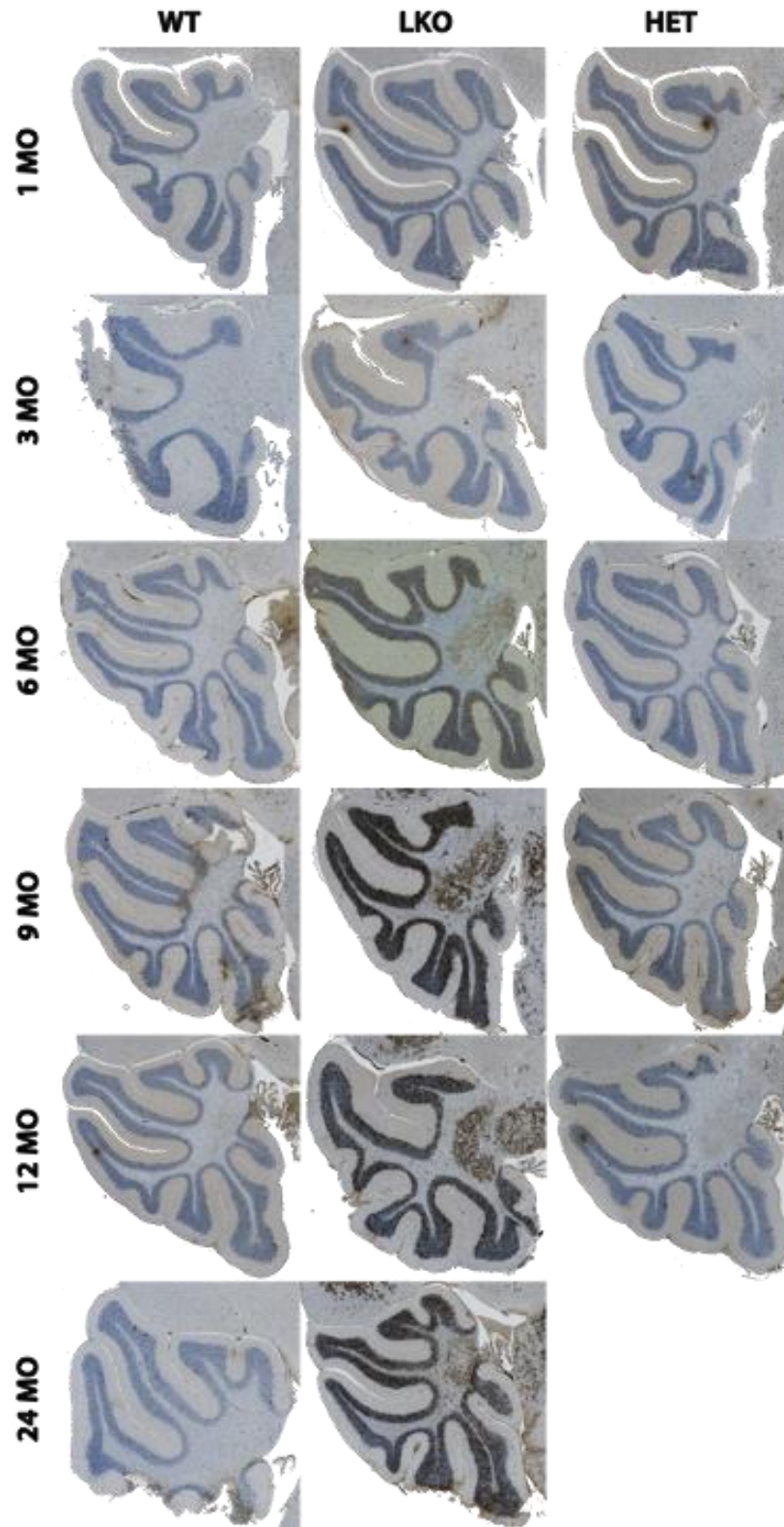


Figure 2.14 Cerebellum KM279 IHC.

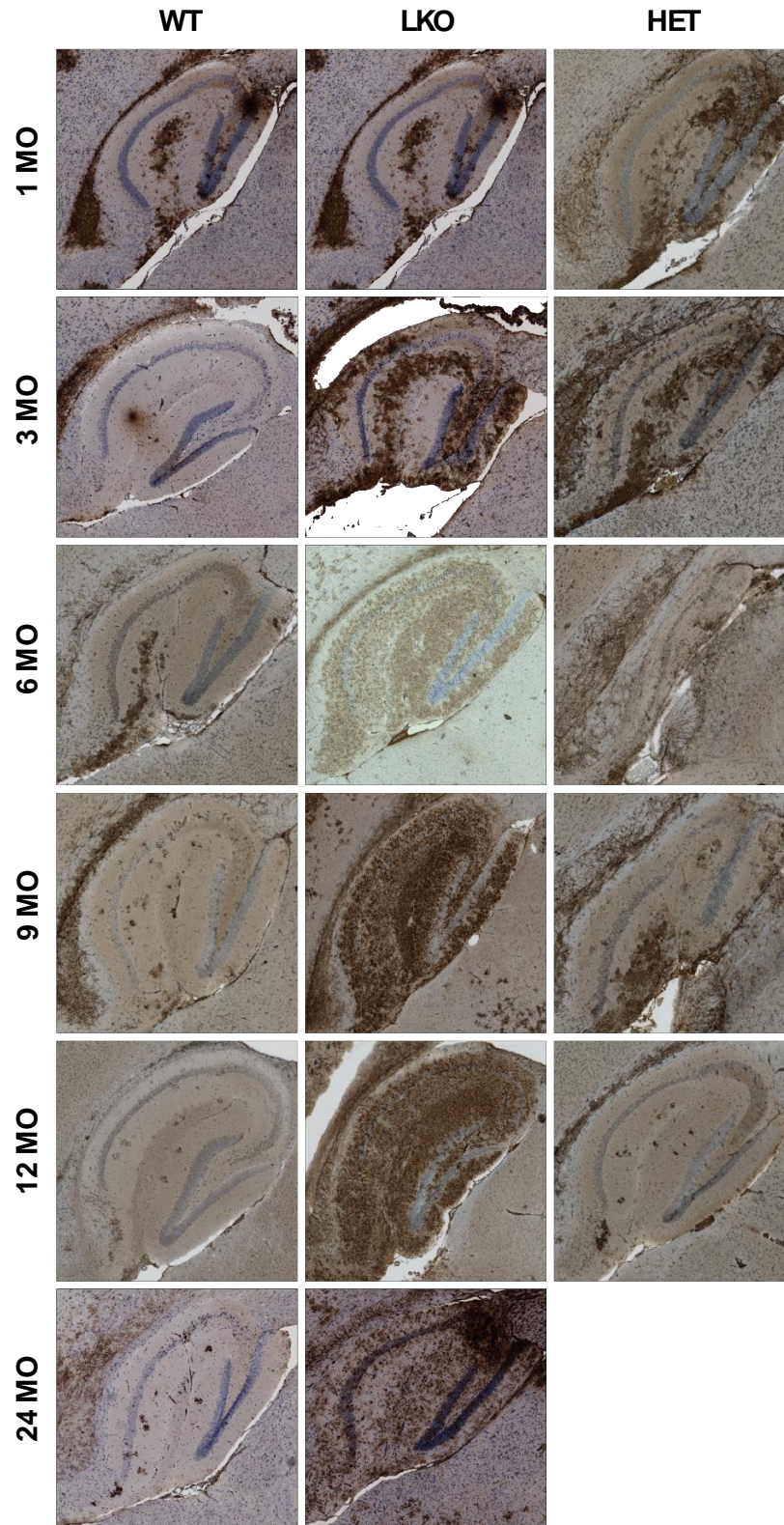


Figure 2.15 Hippocampus IV58B6 IHC.



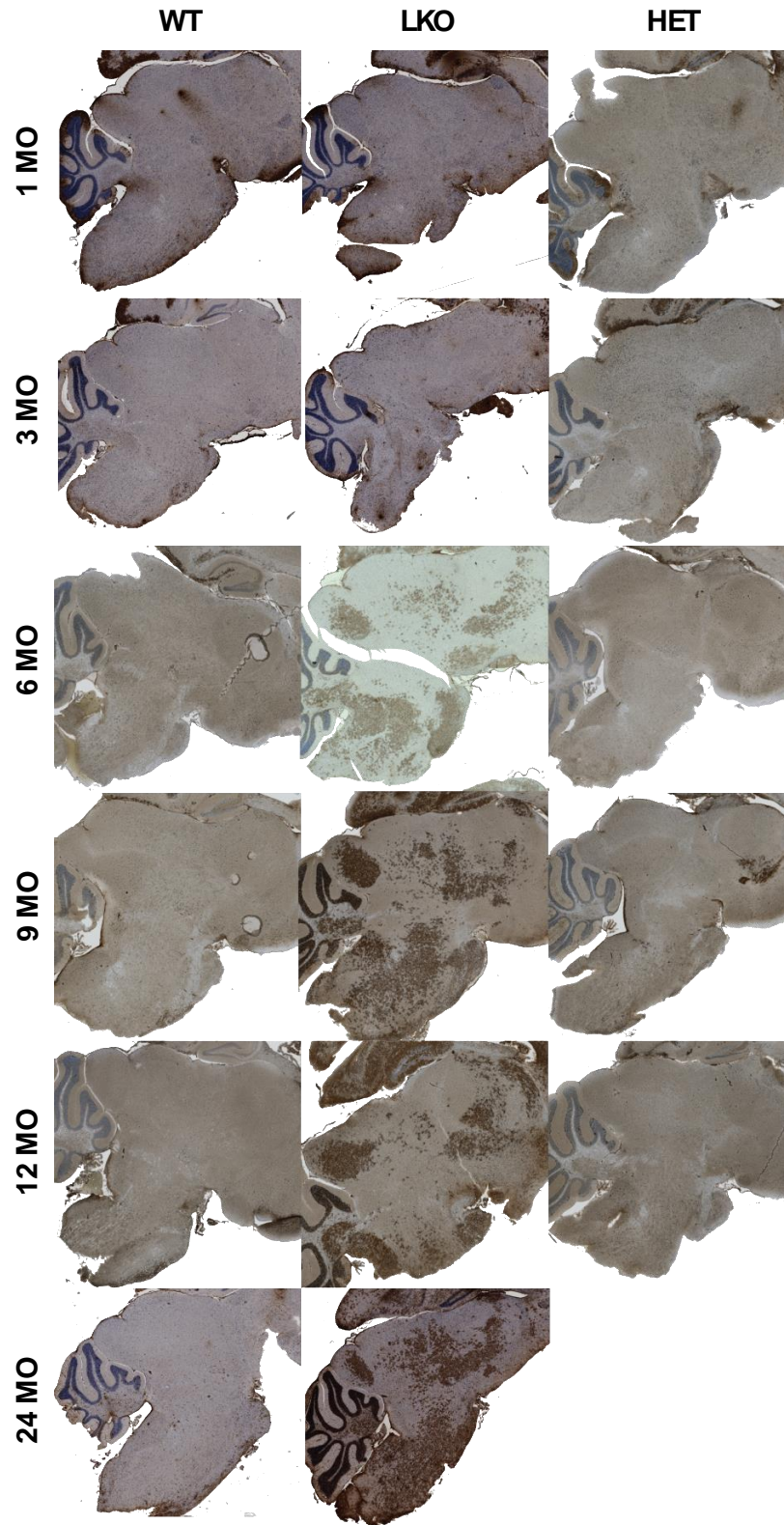


Figure 2.16 Brainstem IV58B6 IHC.

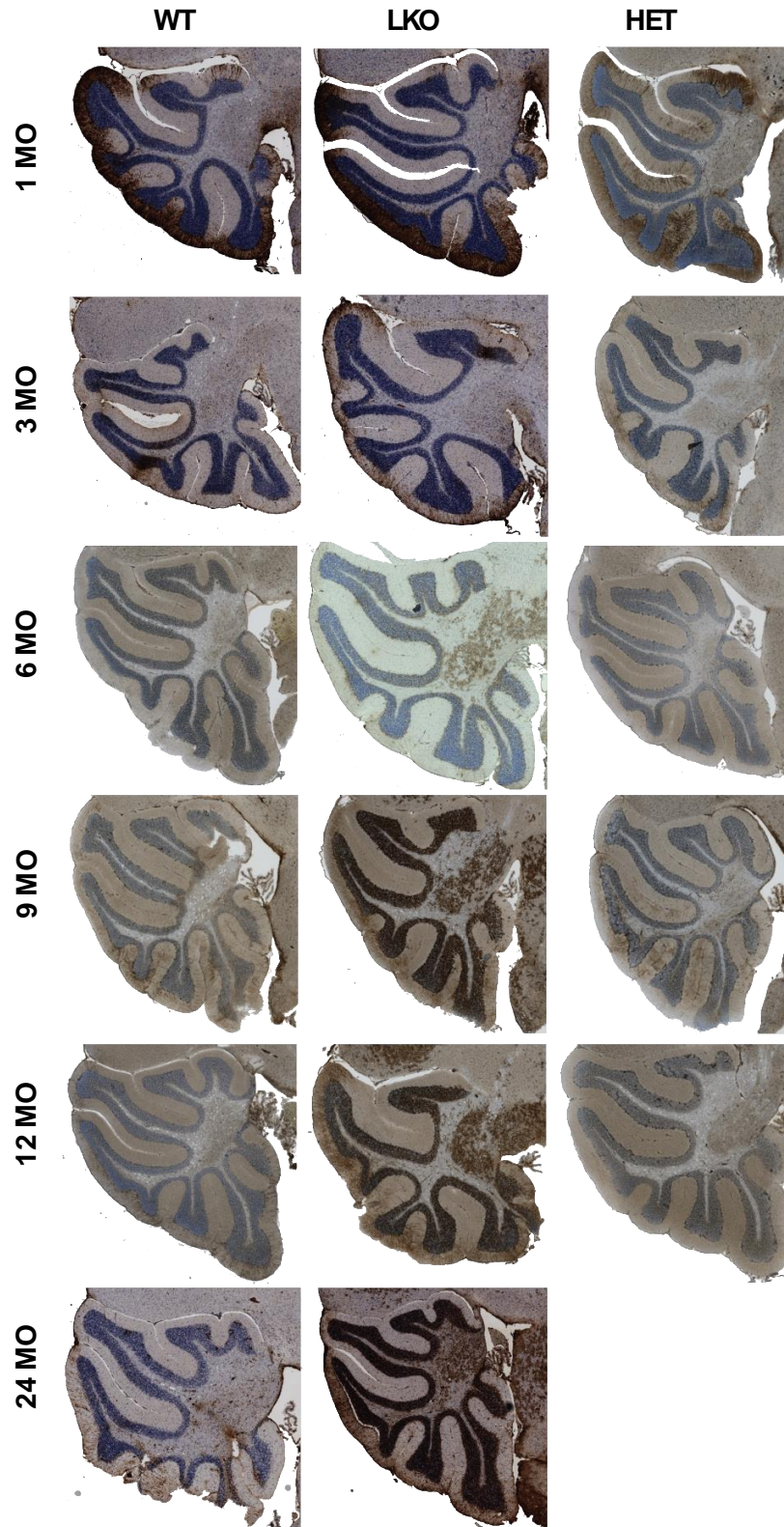
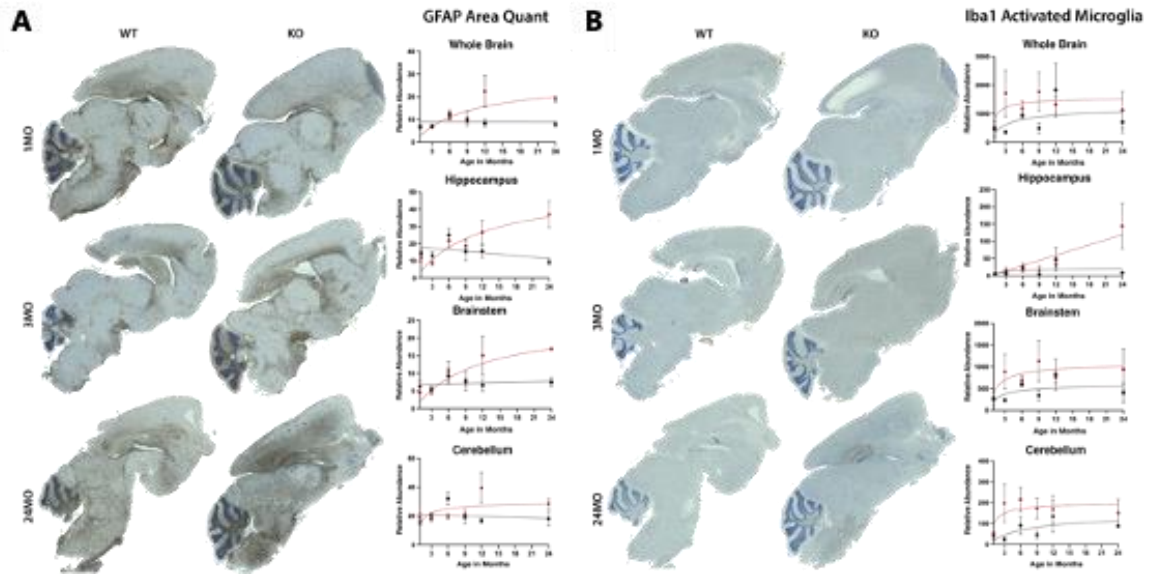


Figure 2.17 Cerebellum IV58B6 IHC.

**Table 2.1 Descriptive statistics of PGB diameters.**

PGB diameter measurements were taken from 200 PGBs per hippocampus using Indica labs software (HALO). Average diameter, 25% percentile, 75% percentile, range, and coefficient of variation were calculated using Prism 9. Color gradients were produced using 2 color conditional formatting in Excel.

		LKO				WT			
		6	9	12	24	6	9	12	24
Age (months)									
Average Diameter (μm)	PAS	1.4	1.7	2.3	3.2	1.6	1.5	1.4	1.5
	KM279	3.5	3.7	3.6	4.0	2.7	2.7	3.2	3.0
25% Percentile	PAS	1.1	1.3	1.7	2.3	1.0	1.0	0.9	1.0
	KM279	2.7	3.0	2.8	3.0	1.8	1.6	2.2	2.1
75% Percentile	PAS	1.7	2.3	3.0	4.9	2.0	1.8	1.7	2.0
	KM279	4.2	4.3	4.3	4.8	3.7	3.8	4.2	3.9
Range (μm)	PAS	4.5	6.0	7.5	14.6	4.4	4.0	4.0	3.5
	KM279	7.4	5.8	6.0	11.1	52.2	56.6	53.6	47.7
Coefficient of variation (%)	PAS	42	48	49	61	49	25	51	47
	KM279	35	26	31	38	52	56	53	47



**Figure 18. Whole brain activated astrocyte (GFAP) and microglia (Iba1) analysis of WT and LKO mice aged 1-, 3-, 6-, 9-, 12-, 24-months.** IHC analysis was performed using the Indica labs tissue analysis software (HALO) "Area Quantification" of GFAP IHC and "Microglia" activation of Iba1 IHC. **A)** Representative GFAP IHC (left) and area quantitation (right). **B)** Representative Iba1 IHC (left) and area quantitation (right). Black = WT, red = LKO.



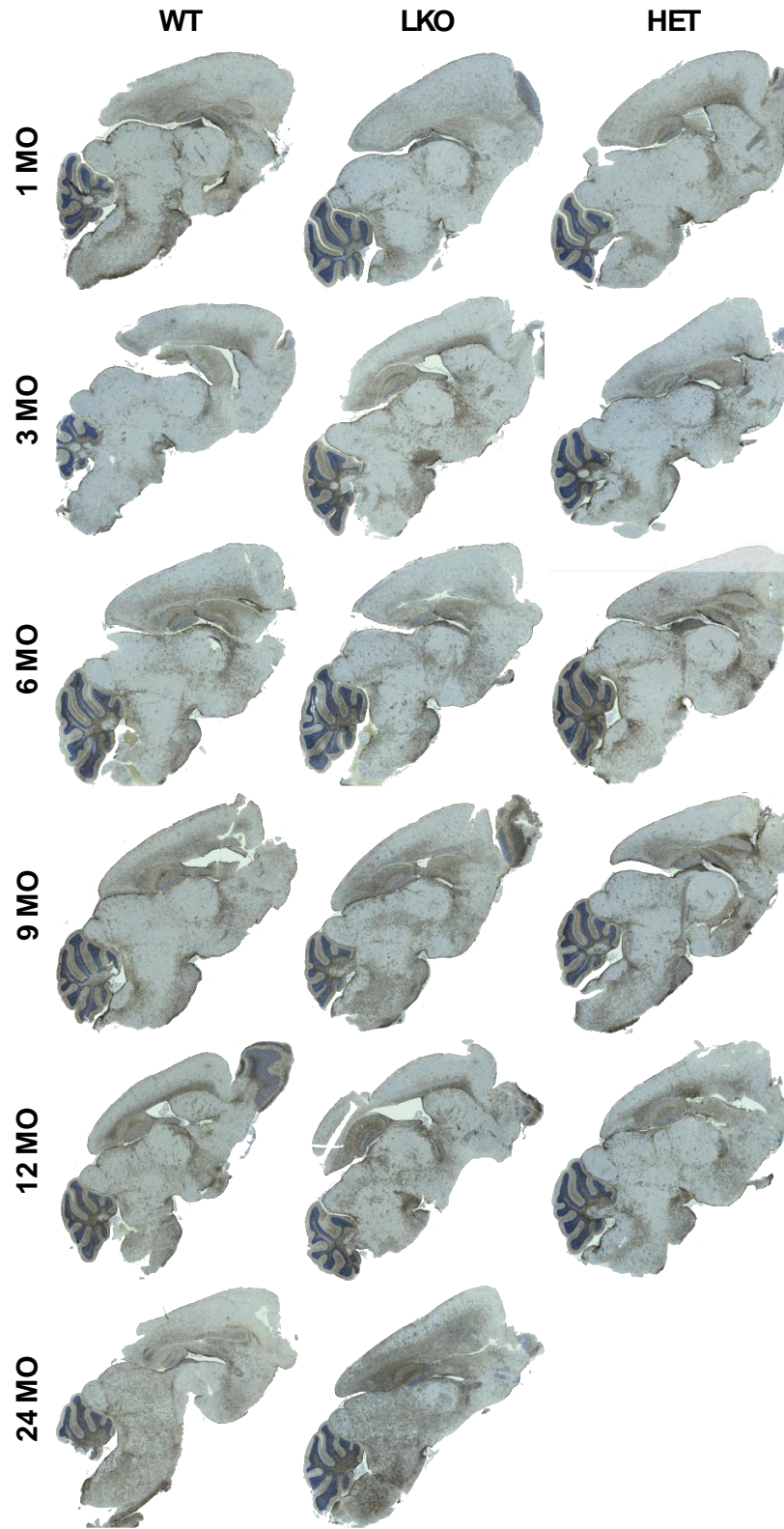


Figure 2.18 Whole brain GFAP IHC.

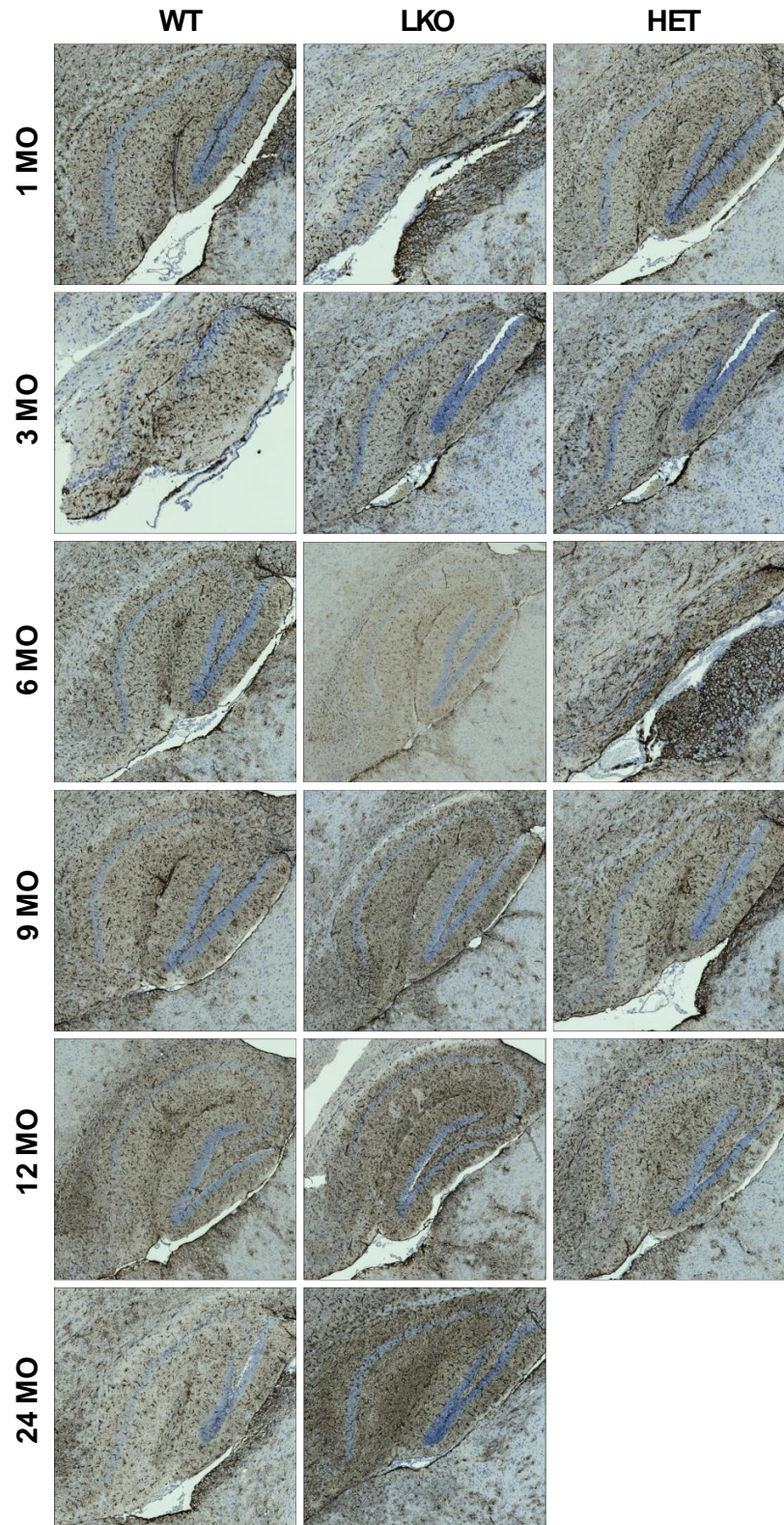


Figure 2.19 Hippocampus GFAP IHC.



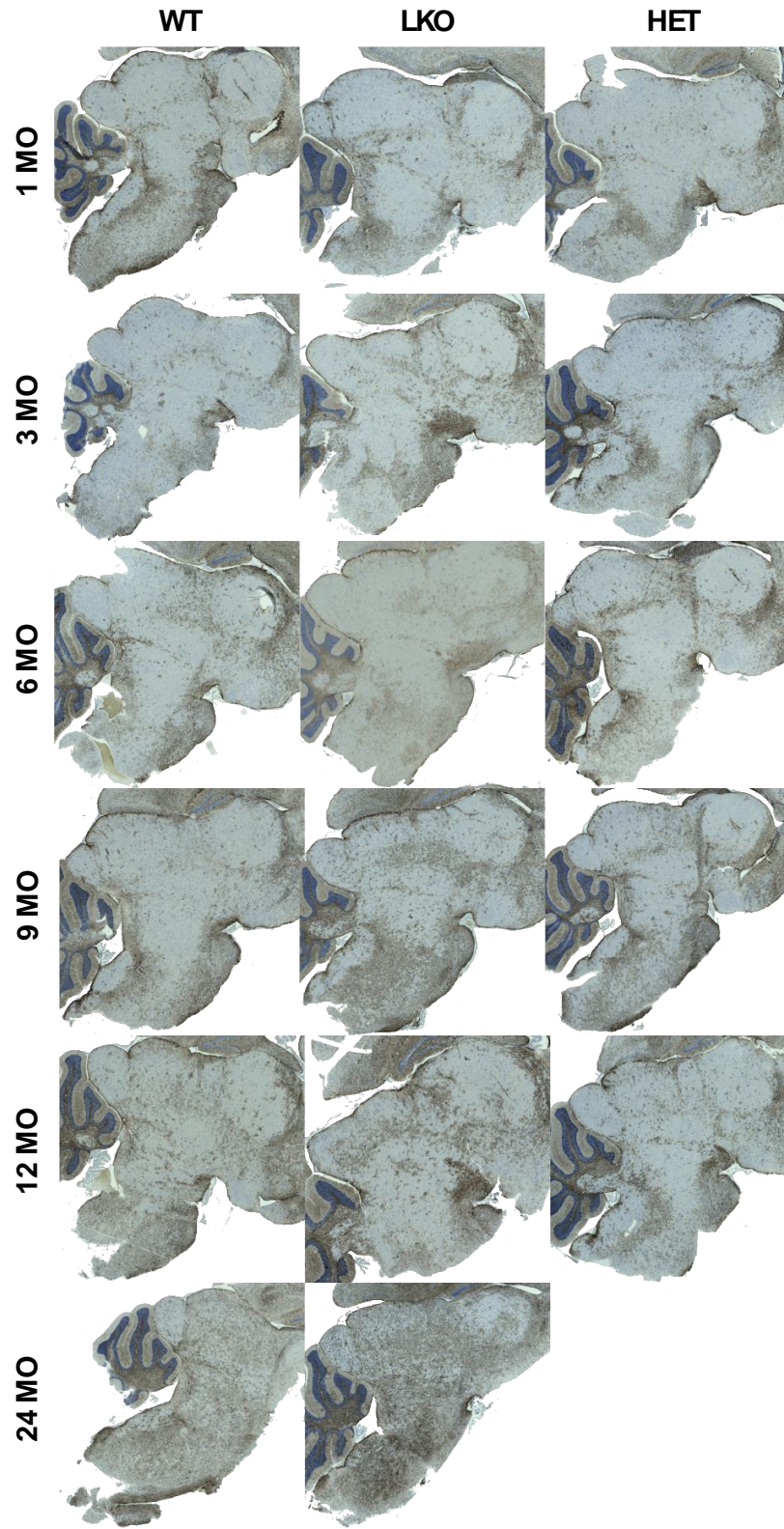


Figure 2.20 Brainstem GFAP IHC.

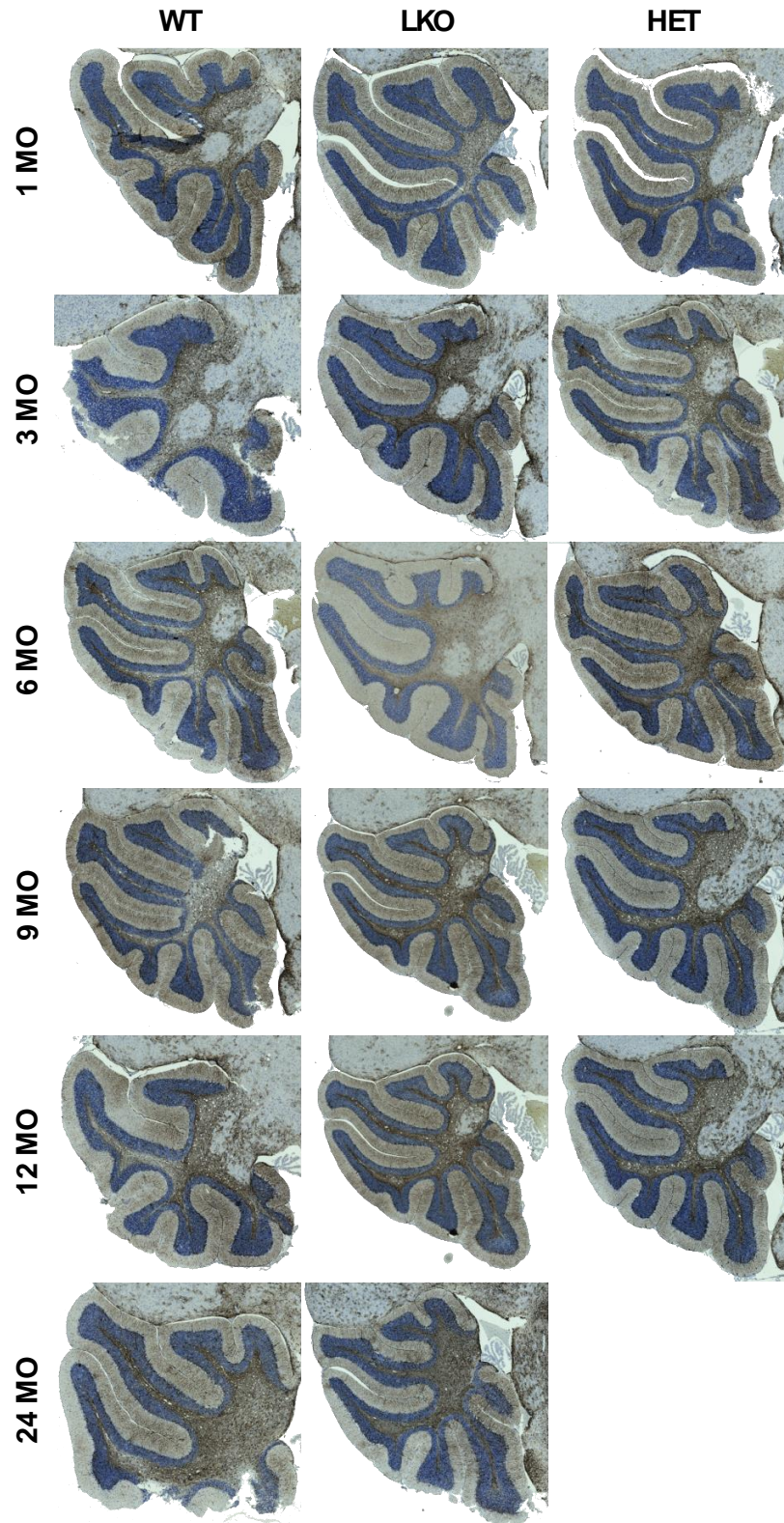


Figure 2.21 Cerebellum GFAP IHC.



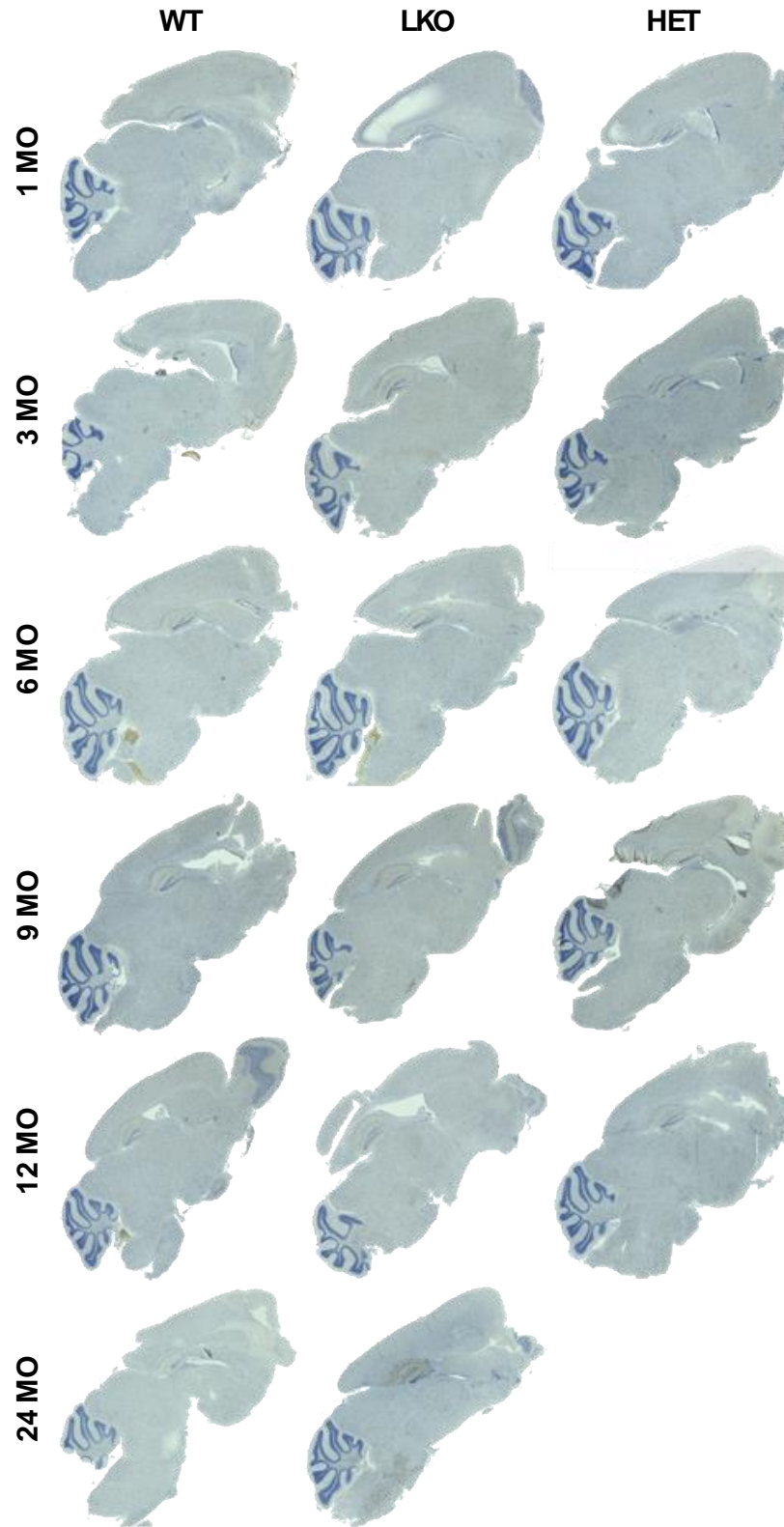


Figure 2.22 Whole Brain Iba1 IHC.

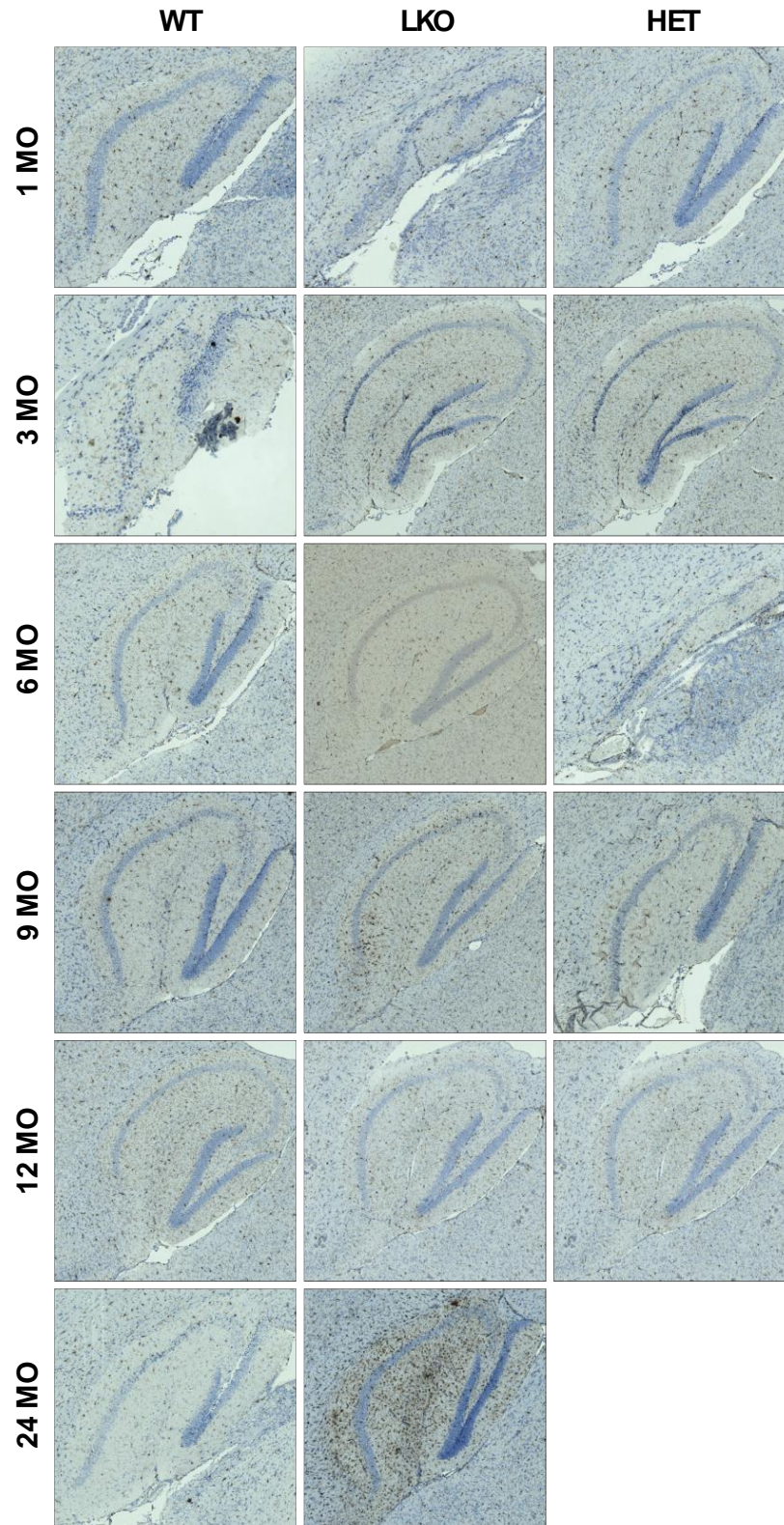


Figure 2.23 Whole brain Iba1 IHC.

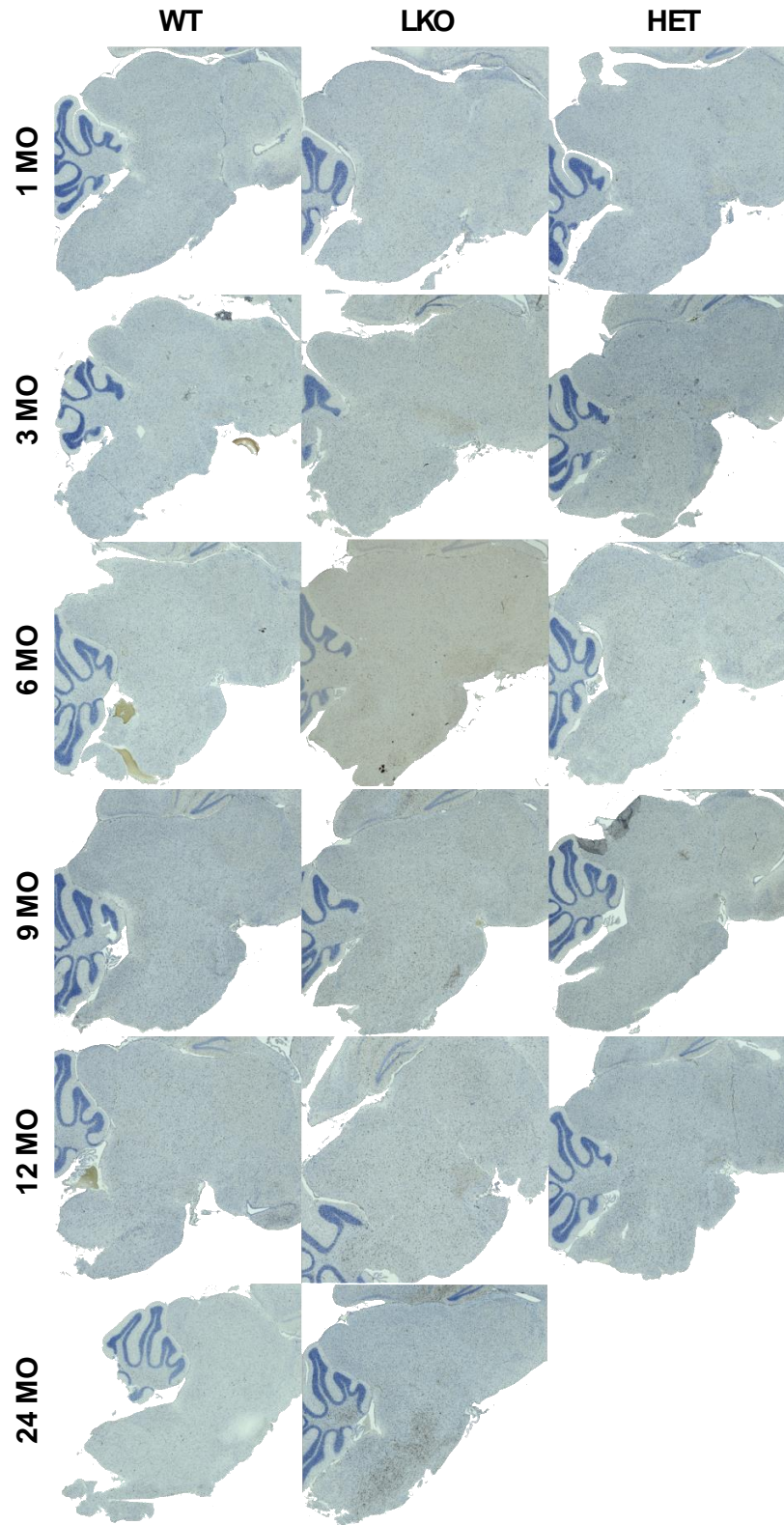


Figure 2.24 Brainstem Iba1 IHC.



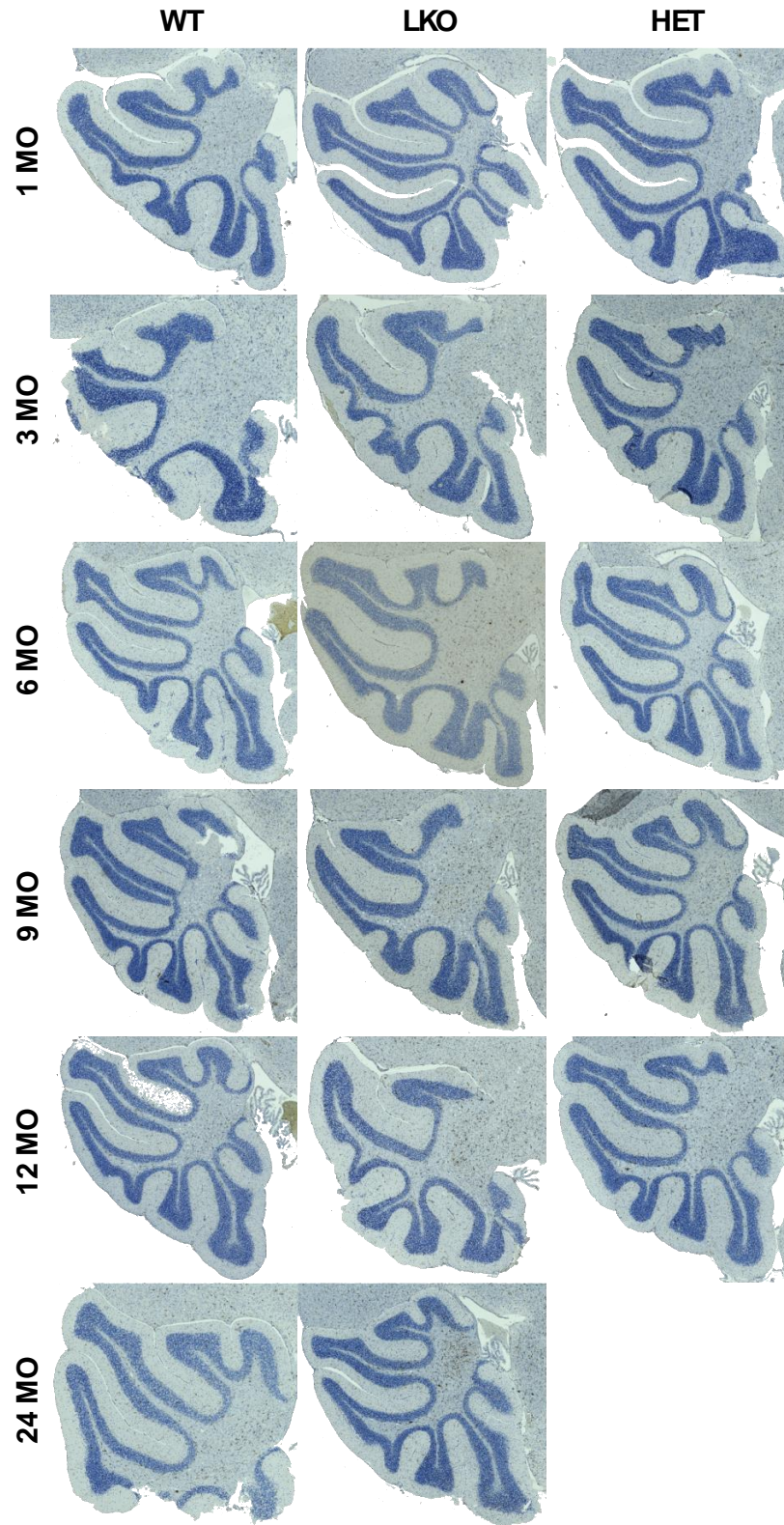
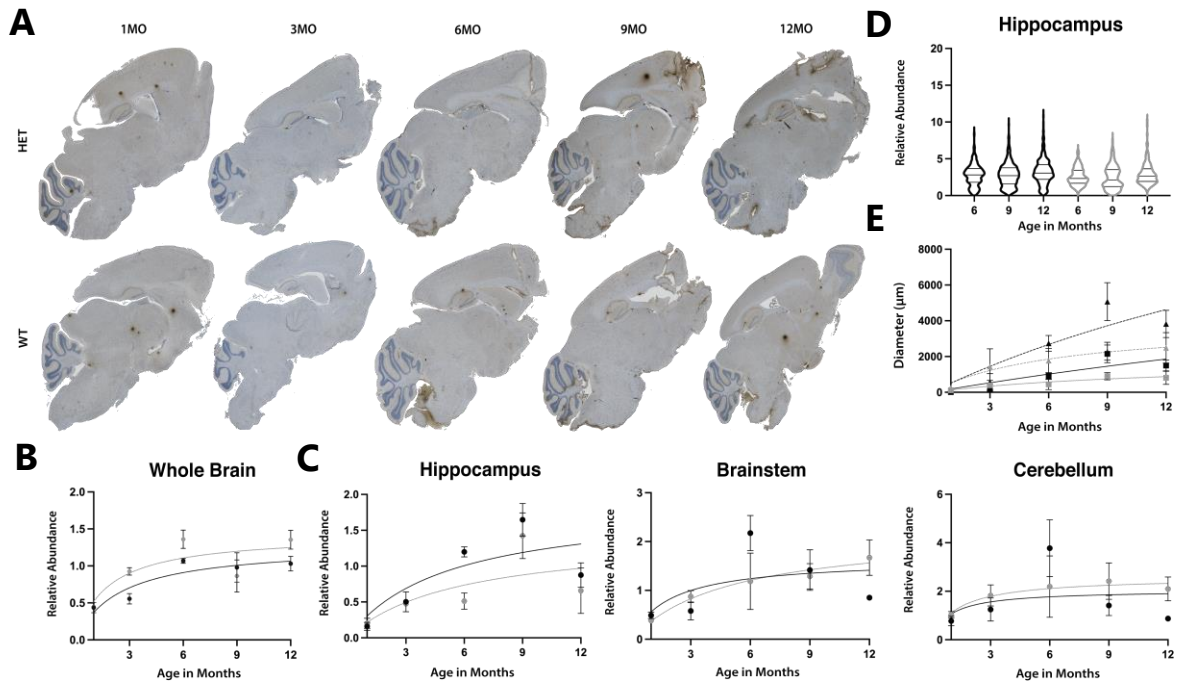


Figure 2.25 Cerebellum Iba1 IHC.





**Figure 2.27 Whole brain and region-of-interest KM279 IHC analysis of WT and laforin heterozygote brains aged 1, 3, 6, 9, 12-months.**

IHC analysis was performed using Indica labs software (HALO) "Area Quantification" and ruler tool. **A)** Representative IHC images quantitated in B. **B)** Whole brain quantitation of KM279 IHC. **C)** ROI quantitation of KM279 IHC. **D)** Violin plots of dense dark brown circular aggregate diameters. **E)** "Area Quantification" of WT and heterozygote dense dark brown circular aggregates and light brown uncondensed material. Black = WT, gray = laforin heterozygotes. Squares and solid line = dense dark brown circular aggregates, triangles and broken line = light brown uncondensed material. WT data is previously shown.

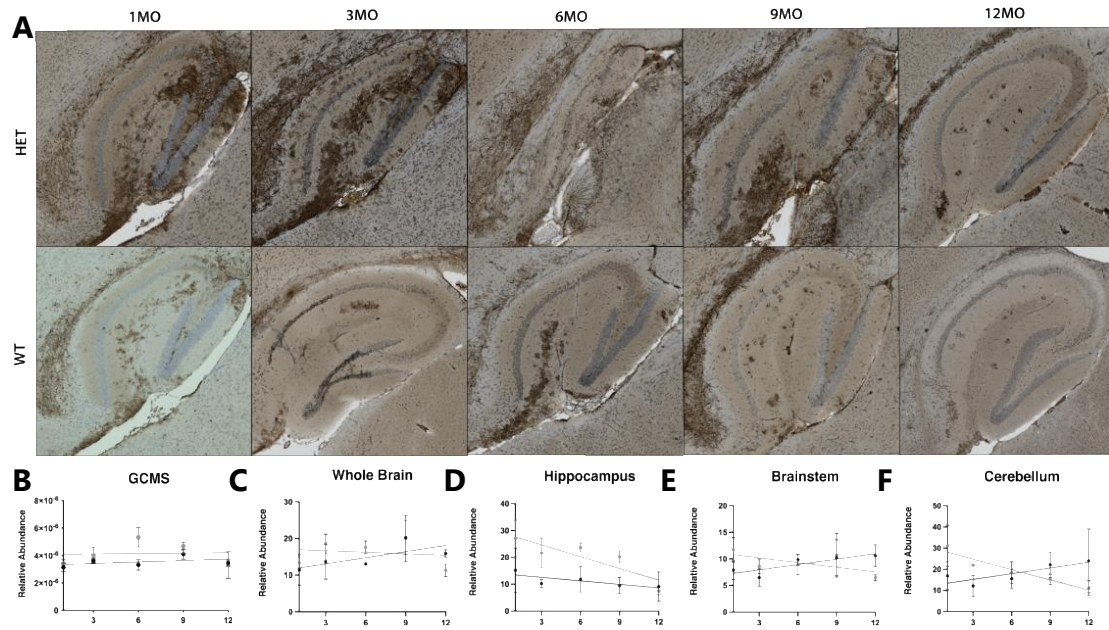


**Figure 2.28 Whole brain IV58B6 IHC and GCMS analysis of glucose polymers on WT and laforin heterozygote mice aged 1, 3, 6, 9, 12-months.**

IHC analysis was performed using Indica labs software (HALO) “Area Quantification”.

**A)** Representative IHC images quantitated in **D**. **B)** Quantitation of acid hydrolyzed glucose polymers by GCMS. **C)** Whole brain quantitation of IV58B6. **D, E, F)** ROI

quantitation of IV58B6 in hippocampus, brainstem, and cerebellum, respectively. Black = WT, gray = laforin heterozygotes. WT data is previously shown.

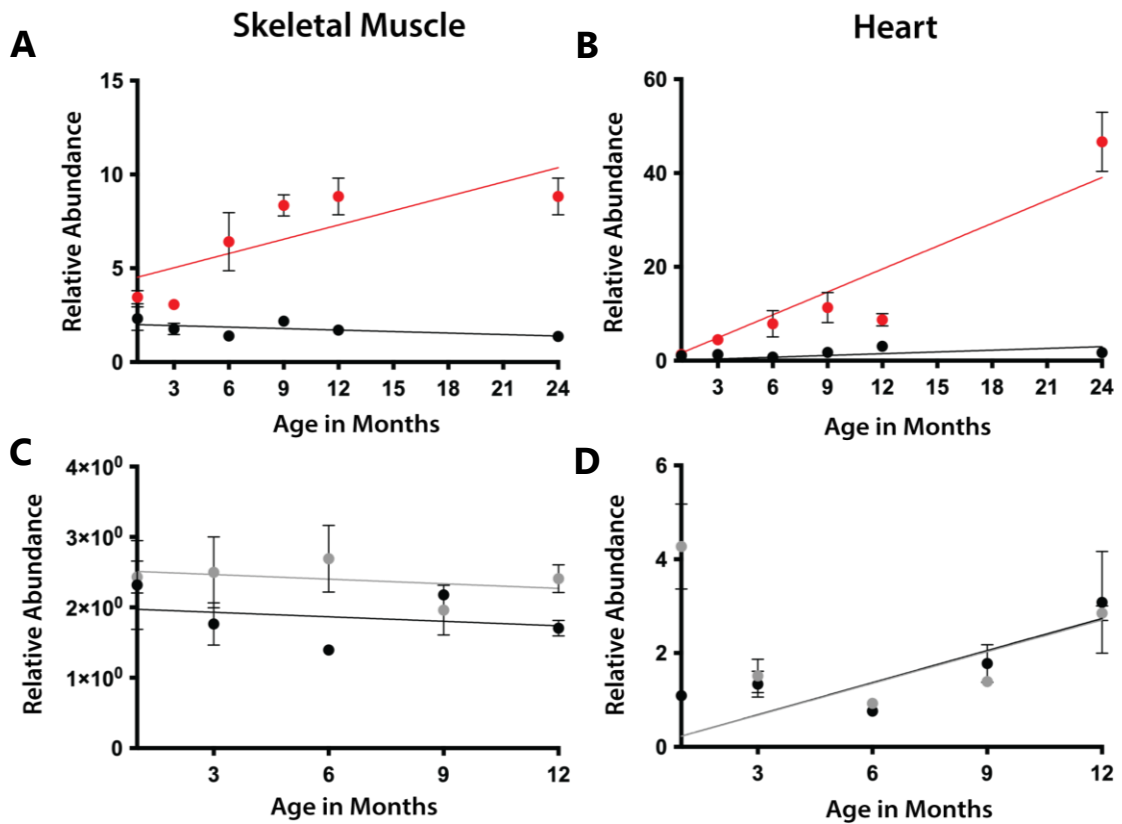


**Figure 2.29 Skeletal muscle and heart GCMS analysis of glucose polymers of WT and LKO mice aged 1-, 3-, 6-, 9-, 12-, and 24-months.**

**A)** Quantitation of GCMS analysis of glucose polymers from skeletal muscle **B)** Quantitation of GCMS analysis of glucose polymers from heart. Black = WT, red = LKO.

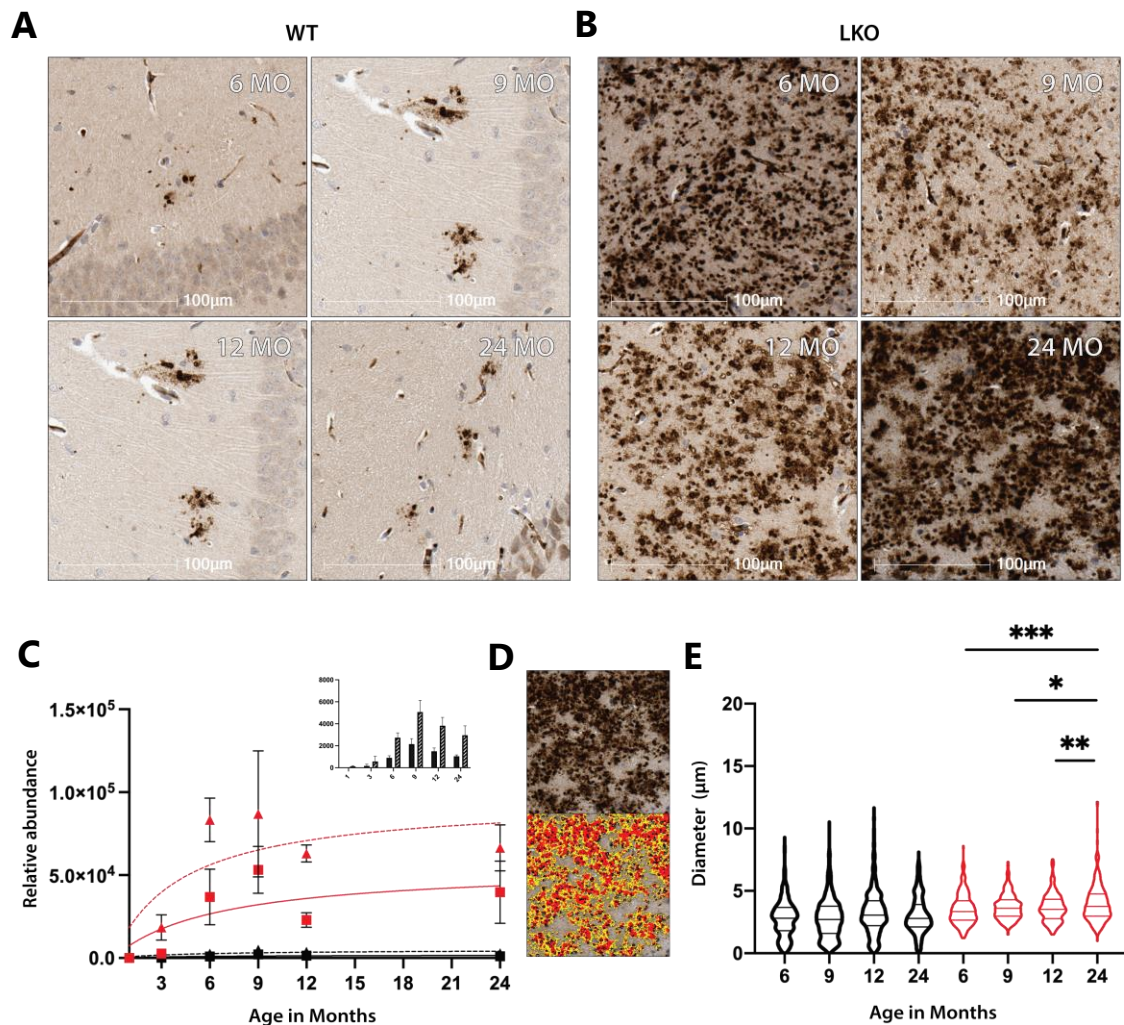


**Figure 2.26 Quantitative and qualitative analysis of KM279 IHC on WT and LKO hippocampus of 6, 9, 12, 24-month-old mice. IHC analysis was performed using the Indica labs tissue analysis software (HALO) "Area Quantification" and ruler tool. A, B) Qualitative representation of uniform dark brown circular aggregates and uncondensed light brown material detected by KM279 on WT and LKO brains, respectively. C) Hippocampus quantitation of WT and LKO uniform and uncondensed material. Pop-out column graph is WT data. WT = black, LKO = red. Squares and solid line/bar = uniform material, triangles and broken line/bar = uncondensed material. D) Representation of "Area Quantification" analysis in C. Red = "uniform" material, yellow = "uncondensed" material. E) Violin plots of "uniform" material diameters. WT = black, LKO = red. \*\*\* = (p = 0.0002), \*\* = (p = 0.0021), \* = (p = 0.0209)**

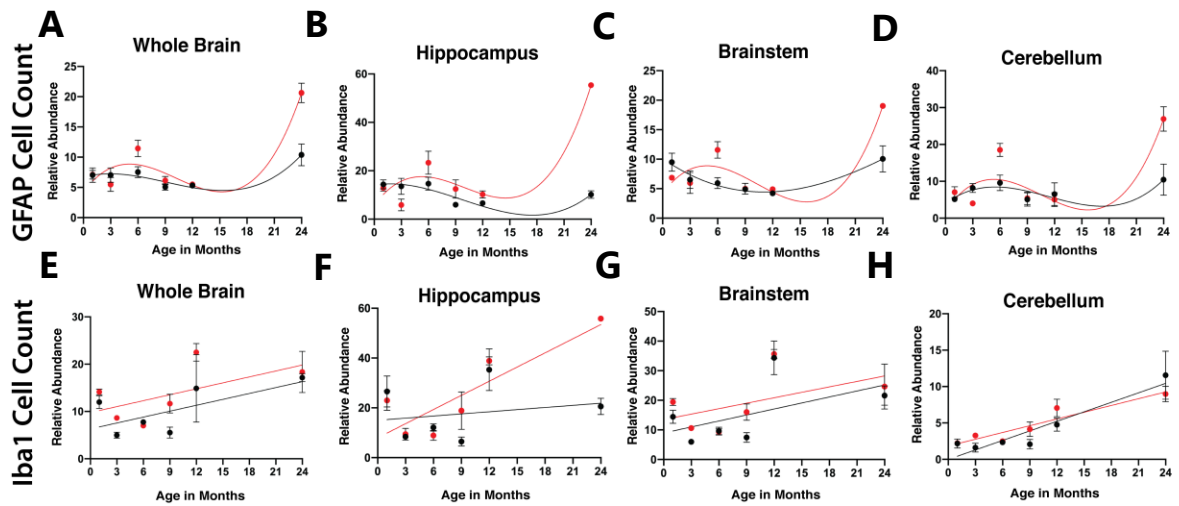


**Figure 2.27 Whole brain and region-of-interest cell count analysis of GFAP expressing astrocytes and Iba1 expressing microglia of 1, 3, 6, 9, 12-month-old-mice.**

IHC analysis was performed using the Indica labs tissue analysis software (HALO

"Multiplex IHC". **A-D)** Quantitation of whole brain and region-of-interest analysis of GFAP. **E-H)** Quantitation of whole brain and region-of-interest analysis of Iba1. Black =

WT, red = LKO



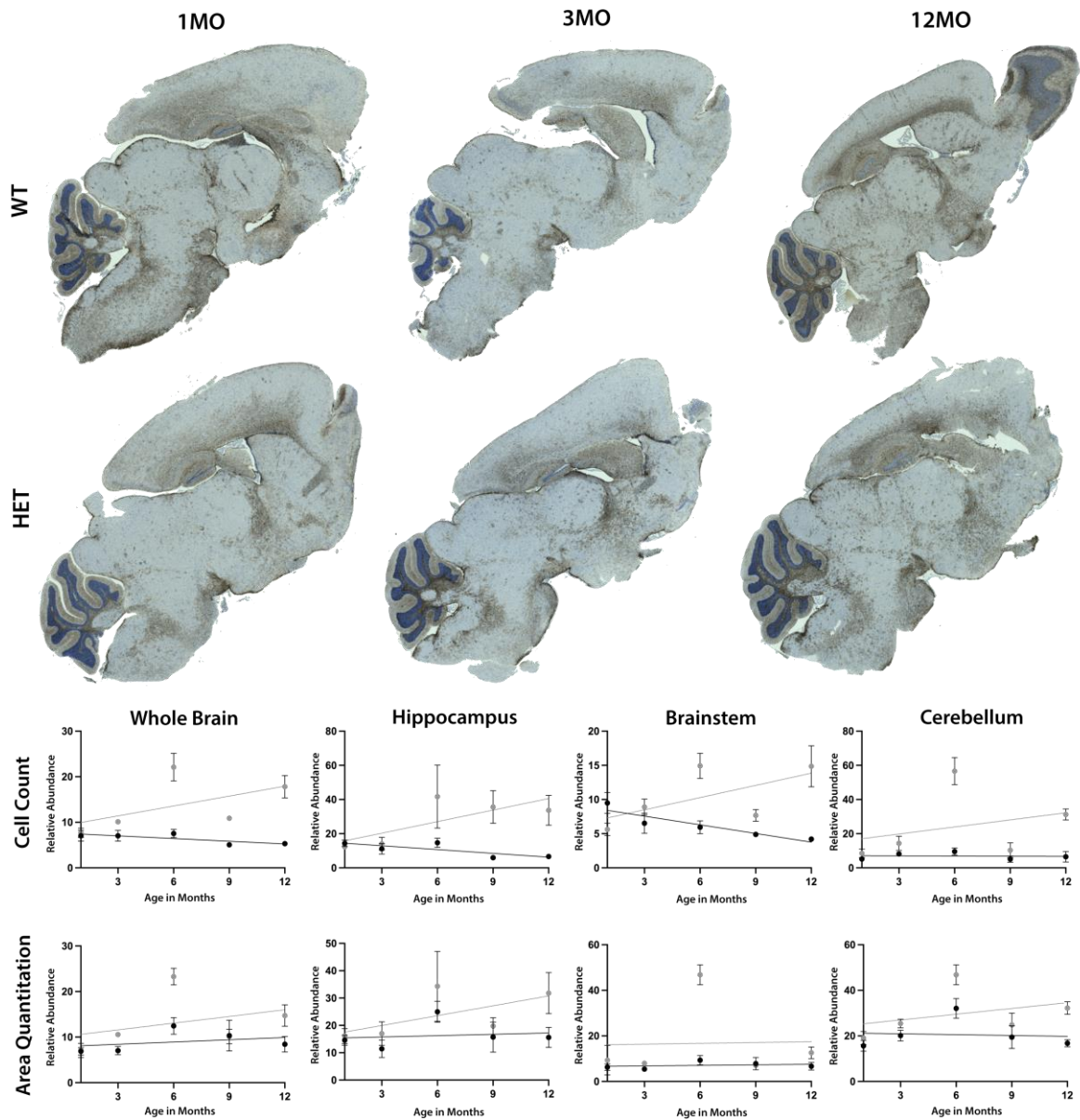


**Figure 2.28** Whole brain GFAP IHC analysis on WT and laforin heterozygote brains aged 1, 3, 6, 9, 12-months. IHC analysis was performed using the Indica labs tissue analysis software (HALO) "Multiplex IHC" and "Area Quantification".

**A)** Representative GFAP IHC quantitated in B and C. **B)** Astrocyte cell count. **C)** GFAP "Area Quantification". Black = WT, gray = laforin heterozygotes. Black = WT, gray = laforin heterozygotes. WT data is previously shown.

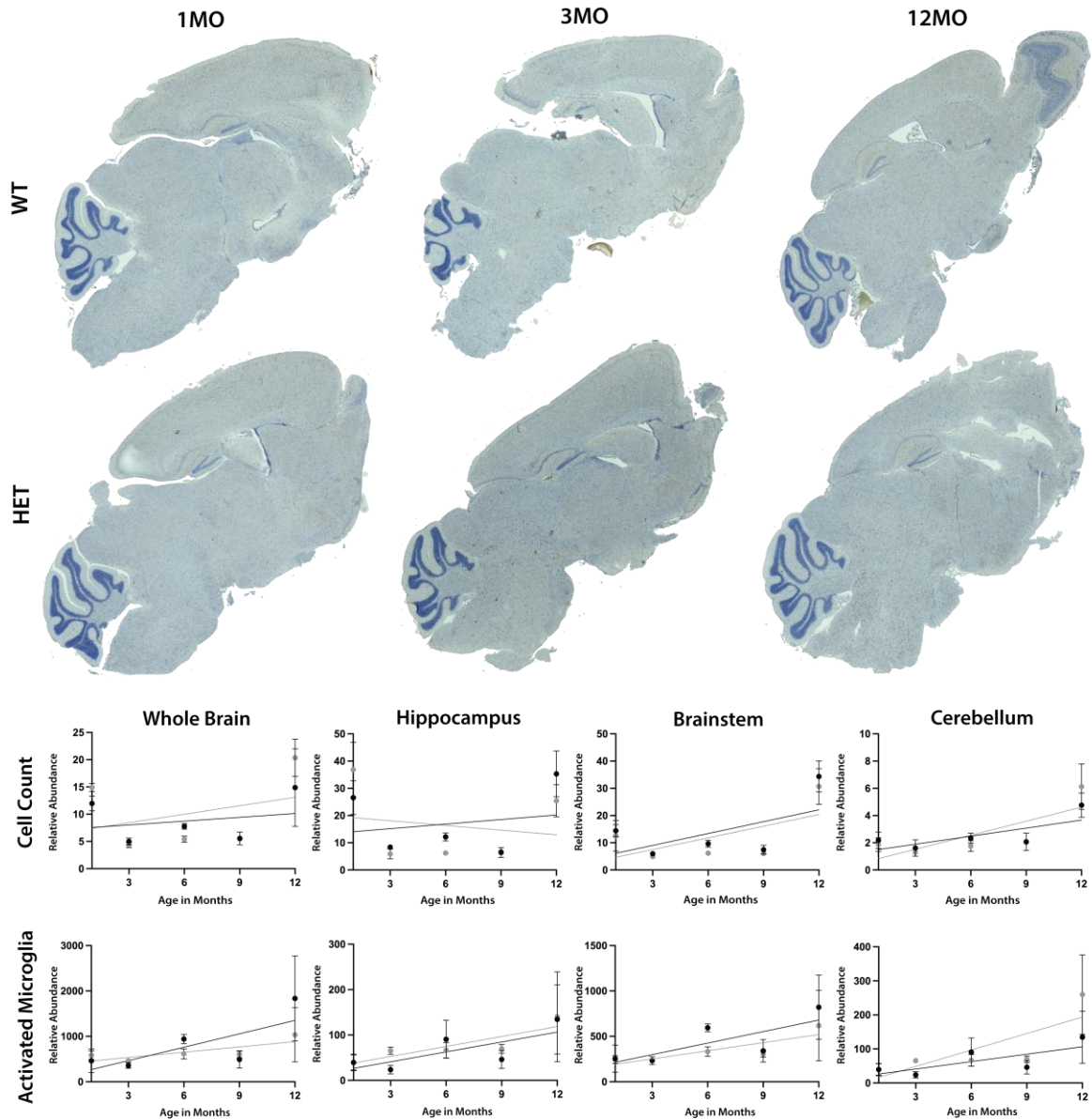


**Figure 2.29 Whole brain Iba1 IHC analysis on WT and laforin heterozygote brains aged 1, 3, 6, 9, 12-months. IHC analysis was performed using the Indica labs tissue analysis software (HALO) "Multiplex IHC" and "Area Quantification".**

**A) Representative Iba1 IHC quantitated in B and C. B) Microglia cell count. C) Iba1 "Area Quantification".** Black = WT, gray = laforin heterozygotes. Black = WT, gray = laforin heterozygotes. WT data is previously shown.

## 2.4 Discussion

This study uses four complementary methods and a longitudinal analysis approach to fill in knowledge gaps regarding normal and diseased glycogen dynamics. This longitudinal analysis was performed using C57BL/6J WT, LKO, laforin heterozygous mice, and a digital pathology workflow to produce rigorous and reproducible data that is supported by GCMS. Our results form a more complete characterization of the LKO mouse that models LD pathophysiology. These characterizations lead to a model of LD pathophysiology in which LB accumulation begins in the cerebellum, then the brainstem, and last the hippocampus, increasing in number to a height that is most egregious in the hippocampus. Current therapeutic approaches that aim to limit the production of glycogen or degrade LBs will benefit from the discovery that brain LBs stop accumulating and begin to form aggregations at 6-months of age. Furthermore, LD inflammation rescue is widely assessed by reversing the quantity of Gfap expressing astrocytes in older mice<sup>95,215,247,249–252</sup>. Our results indicate that microglia, but not astrocytes, are activated over the entire lifespan of the LKO mouse. Therefore, microgliosis is the more likely driver of inflammation in LD. These findings among others discussed below will be highly informative guides for current and future pre-clinical therapeutic development.

### 2.4.1 Soluble versus insoluble glycogen in the LKO mouse

The water-soluble quality of glycogen provides cells with carbon and energy<sup>105</sup>. Pathogenic buildup of insoluble glycogen defines glycogen storage diseases<sup>253</sup>. Previous reports have measured the ratio of soluble to insoluble glycogen in LKO, MKO, and WT age matched mice. One study on 10-13-month LKO and 15-month MKO mice indicated that skeletal muscle total glycogen (soluble and insoluble) is 2-times higher in both genotypes compared to WT<sup>106</sup>. To uncouple the quantities of soluble glycogen to PGBs, they used centrifugation to separate the soluble from insoluble glycogen fractions. WT soluble glycogen levels were the same as in the LKOs and the WT insoluble fraction was nominal. Since the soluble and insoluble fractions of the LKO mice were approximately equal, the 2-fold increase in total glycogen in the LKO mice was a result of the insoluble fraction. The same analysis has been published on the brain tissue from 11-month-old MKO mice<sup>51</sup>. These data indicated that total WT glycogen is equal parts soluble and insoluble. WT and MKO soluble glycogen levels are the same, but MKO insoluble glycogen is 3-times higher than WT, bringing the total increase in glycogen to ~2.5-times higher than WT. In both LD models using skeletal muscle or brain tissues, the increase in total glycogen is driven by LBs while soluble glycogen is unchanged from normal conditions. These reported findings fall in line with our total glycogen and LB analysis using IHC.

Using both KM279 IHC and IV58B6 IHC on adjacent tissue sections we were also able to separate LB accumulation from total glycogen load. Total LKO brain glycogen measured by IV58B6 IHC is 2-fold higher than WT or laforin heterozygotes. Total LKO



brain LBs measured by KM279 IHC is half the amount of total glycogen detected by IV58B6 IHC. Given the preceding studies quantifying soluble and insoluble glycogen in these mouse models we may infer that the 2-fold increase in IV58B6 detection compared to WT or laforin heterozygotes is driven by LBs. Importantly, our GCMS analysis measures total LKO glucose polymers to be 5-fold higher than WT, and 3-times higher than analyzed by IV58B6 IHC. This result is likely explained by more sugars being broken down by acid hydrolysis required for GCMS analysis than are detected by the anti-glycogen antibody IV58B6.

#### **2.4.2 LB aggregation and diverging characteristics of corpora amylacea**

Varied sizes of LBs have been previously categorized as type I and II/III<sup>80</sup>. Type I refers to smaller dust-like inclusions that are most abundant and type II/III refers to larger and more rare inclusions<sup>254</sup>. These characteristics are captured by our measurements and statistical analyses of PAS+ signal size and variation. The LBs we categorized in the 25<sup>th</sup> and 75<sup>th</sup> percentile represent type I and II/III respectively. Recent studies have indicated that type I inclusions are exclusive to astrocytes and type II/III to neurons, even in old age<sup>96</sup>. Our results show that type I and type II/III, both increase in size after 6-months of age while total PAS+ signal “Area Quantification” rises quickly between 1- and 6-months and is unchanged thereafter. Furthermore, the increased variation of LB sizes is driven by the appearance of type II/III. Collectively, these analyses suggest that LBs accumulate and then aggregate. Furthermore, neuronal LBs, not astrocytic, have been recently suggested to be the main contributors of increased susceptibility to kainate-induced epilepsy in LD mice<sup>98</sup>. If so, neuron specific LB (type II/III) aggregation may be driving epilepsy in LD.

Our diameter measurements and statistical analysis of WT PAS+ signals indicate that average LB average size and range is larger than corpora amylacea. Furthermore, corpora amylacea size variation is unchanged with time while LB variation increases and is driven by the increasing size of type II/III LBs. Thus, these statistics describe innate differences between corpora amylacea and type II LBs. The same analysis performed on the uniform material detected by KM279 reveal the opposite, LKO uniform KM279 signals do not increase in variation and the variation of WT uniform KM279 signals is larger than in LKOs. Collectively, these results suggest innate differences between corpora amylacea and any type of LB. This is an important distinction considering recent published data that showcased a common epitope of type I inclusions and corpora amylacea not shared by type II/III, thus naming the type I inclusions corpora amylacea-like bodies (CAL)<sup>96</sup>. Indeed, CAL and corpora amylacea have structural similarities and our results contribute to this comparative analysis indicating that corpora amylacea and CAL are not exactly the same.

KM279 IHC analysis further led to differentiating characterizations between the detection specificities of KM279 IHC and PAS+ staining. Unlike PAS staining, the anti-PGB antibody detection signals reveal an uncondensed material encircling a uniform material. These findings create the impression that the structure of corpora amylacea

and LBs contains a dense core surrounded by an uncondensed network of particles made of the same material. These findings are intriguing considering a recently published model of spontaneous *in vitro* LB aggregation. In this model, polyglucosan particles spontaneously aggregate to form networks and active cellular sequestration of these polyglucosan networks creates tissue specific morphologies<sup>20</sup>. The uncondensed material detected by KM279 may be the physiological representation of polyglucosan networks.

Characterizing the aggregation behavior of LBs is important for informing the efficacy of the therapeutics in development that aim to decrease LB load by either reducing and/or breaking down LBs. According to our finding that LBs aggregate in the brain in combination with the *in vitro* model of spontaneous LB aggregation, incomplete destruction or removal of LBs in late-stage LD represented after the 6-month mark in LKO mice may result in re-aggregation and unsuccessful therapeutic intervention.

### **2.4.3 Inflammation markers of LD**

To assess inflammatory brain damage in LD, two histological markers are widely used. Gfap for astrogliosis and Iba1 for microgliosis. Previous studies have quantified Gfap expressing astrocytes in LKO mice at 12-months and 20- to 26-months<sup>25,28,221,247,248</sup>. Our longitudinal analysis indicates that before 12-months the number or “Area Quantification” of reactive Gfap expressing astrocytes does not increase above normal levels. Therefore, astrogliosis occurs well after the PGBs have infiltrated. Conversely, we show that activated microglia, the synergistic inflammatory signaling companion of astrocytes, are significantly higher throughout the lifespan of LKO mice compared to WT and laforin heterozygotes.

Compared to LKOs, the laforin heterozygote mice show a reverse inflammatory response in terms of astrocyte and microglia reactivity despite regional increases in reactive astrocyte levels. This may be accounted for by increased soluble glycogen in the hippocampus as laforin heterozygotes do not have LBs. Further study is needed to determine the reason for laforin heterozygous hippocampal glycogen. It may be possible that there are regional differences in the ability to compensate for laforin expression that is not accounted for in our whole brain analysis.

Why astrocyte activation is delayed in the LKO mouse model is unclear. One aspect to consider is that since Gfap is an intermediate filament protein that outlines the cytoskeletal profile of astrocytes’ somata and main branches, the entire astrocytic morphology cannot be evaluated by Gfap staining, and thus astrocytic activation may not be properly captured by “Area Quantification” of Gfap density. On the other hand, considering the damage inflicted to the brain in LD, the unresponsiveness of astrocytes may simply be a consequence of their inundation with LBs. CAL is demonstrated to accumulate in astrocytes and makes up the majority of brain LBs, while only minor quantities exist in microglia<sup>97</sup>. Therefore, the possibility that CAL accumulation affects astrocyte health and compromises the astrocyte’s ability to become activated in LD is intriguing. The increase in activated Gfap expressing astrocytes seen after 1 year may be

a delayed response or more related to aging than LD pathology. Taken together, activated microglia are more likely important to the driving mechanism of inflammation in LD than activated astrocytes and should be more heavily considered as an important biomarker for therapeutic development.

## **2.5 Final conclusions**

In this study we confirm and expand on previously published data describing pathological LD biomarkers. Our analysis of astrogliosis and microgliosis challenges assumptions about inflammatory drivers. These results redirect the focus of inflammatory biomarkers and putative therapeutic targets from astrocytes to microglia. Our longitudinal analysis illustrates the progressive pathology of both LD and WT aging mice. This thorough analysis will be a highly beneficial benchmark reference for all pre-clinical therapeutic development approaches to prevent or reverse LD.

## CHAPTER 3. Metabolic changes during aging compared with a neurodegenerative disease

### 3.1 Introduction

Aging is a universal human condition that is harmful and likened to disease and the main risk factor for neurodegenerative disease<sup>3</sup>. The progressive nature of neurodegeneration further intertwines neurodegenerative disease with an age-dependent dimension<sup>5</sup>. Central nervous system (CNS) metabolic defects have been proposed to be an important underlying feature of both aging and neurodegenerative disease<sup>1,3</sup>. Thus, it is not only important to understand the metabolism of aging for the potential to enhance quality of life, but to also establish a metabolic baseline for studying neurodegenerative disorders. In fact, many aging metabolism studies have emerged as a consequence of the problem of subtracting the influence of age from metabolism studies of neurodegenerative diseases<sup>144</sup>. In aging and neurodegenerative diseases, a progression of glucose hypometabolism emerges by Fluorodeoxyglucose <sup>18</sup>F Positron Emission Tomography (<sup>18</sup>F-FDG-PET)<sup>10,255</sup>. Targeting brain glucose metabolism has been proposed as one of five ‘brain energy rescue’ strategies to provide significant symptom relief and disease modification in neurodegenerative disorders<sup>7</sup>.

Mammalian brain energy consumes 20% of total body energy, and glucose is the major substrate of brain energy metabolism<sup>256</sup>. Glycogen can store ~50,000 glucose molecules that when released can fuel the TCA cycle, making glycogen an important energy cache<sup>257</sup>. To form this macromolecule, linear glucose polymers are synthesized by glycogen synthase (GS) and branched every ~13 residues by glycogen branching enzyme<sup>258</sup>. Breakdown is achieved by glycogen debranching enzyme and glycogen phosphorylase<sup>17</sup>. Glycogen is well-studied in the liver and muscle where liver glycogen is catabolized to provide systemic glucose, and muscle glycogen is catabolized to meet local energy demands during exercise<sup>13</sup>. The role of glycogen in the heart is suggested to be an ‘energy buffer’ where glycogen catabolism is titrated relative to glucose uptake and liberated only during times of ‘anoxaemic emergencies’<sup>259</sup>.

The role of glycogen in the brain is an emerging field. Historically, glycogen was not detected in the brain due to issues with euthanasia that triggered glycogen degradation and lack of sensitivity<sup>260,261</sup>. Brain glycogen is critical for long-term potentiation and memory formation, and impairments to these processes characterize neurocognitive aging<sup>45,55</sup>. Further, brain glycogen metabolism has been recently linked to proteostasis, a common feature of aging and neurodegenerative disease<sup>262</sup>. Additionally, 25% of brain glycogen is comprised of the sugar monomer glucosamine, which is incorporated into and released from glycogen by the same enzymes that incorporate and release glucose<sup>16</sup>. In two GSD mouse models, brain regions affected by PGBs have impaired protein N-glycosylation<sup>16</sup>. If glucosamine sequestration is driven by the formation of PGBs, thereby limiting the production of UDP-GlcNAc, the fundamental building block of N-glycans, this would lead to dire consequences of proteostasis and cellular function. Interestingly, targeted reduction in glycogen synthase improves neuronal function with

age and extends lifespan in mice<sup>99</sup>. With reduction in glycogen synthase, an age-related aberrant glycogen-aggregate known as corpora amylacea is also reduced in mice and flies<sup>99</sup>. These data are strong evidence that the development of corpora amylacea depends on the synthesis of glycogen and that their formation is an evolutionarily conserved process. The underlying cause of corpora amylacea formation and whether corpora amylacea is protective, pathological, or both is still under investigation.

Similar cellular origins and morphological characteristics of corpora amylacea have been reported in the highly pathological glycogen-like aggregates called Lafora bodies (LBs), found in the childhood dementia Lafora disease (LD)<sup>96</sup>. LD is a neurodegenerative glycogen storage disorder, as well as a fatal myoclonic epilepsy and childhood dementia where seizures and cognitive symptoms emerge around the age of ten and patients typically die in their early to mid-twenties (OMIM: 254780). LBs are the result of a molecular deficit in glycogen metabolism and drive the severe clinical course by depriving the brain of access to its normal glycogen derived glucose cache<sup>118</sup>. LD is caused by autosomal recessive mutations in the epilepsy progressive myoclonus type 2a or 2b (*Epm2a* or *Epm2b*) gene<sup>46</sup>. The proteins encoded by *Epm2a* and *Epm2b* are the glucan phosphatase laforin, and the E3 ubiquitin ligase malin respectively, and each account for ~50% of cases<sup>46</sup>. Loss of function of either protein promotes the generation of the pathogenic, cytoplasmic, LBs throughout the body and most extensively in skeletal muscle, the heart, and the brain where they are neurotoxic<sup>20</sup>. Multiple laboratories utilizing different pre-clinical models have demonstrated that LBs drive neurodegeneration, synaptic dysfunction, susceptibility to seizure activity, and changes to long-term potentiation (the process required for memory storage)<sup>51,55,92,216,217,263</sup>.

To explore the relationship between brain glycogen metabolism and aging, we utilized the power of metabolomics. Metabolomics has emerged as the latest 'omics' technology that is powerful in creating a comprehensive profile of global or systemic metabolite changes in biological systems at a specific time and condition<sup>264</sup>. Though the metabolomics field is new compared to other 'omics' fields like, genomics, transcriptomics, and proteomics, metabolomics has already shown significant potential for novel biomarker discovery and enhancing our understanding of underlying biological mechanisms<sup>264</sup>. Over the last decade, a few global-untargeted metabolomics studies of the aging murine brain have emerged<sup>145,146,265,266</sup>. As cross-sectional studies, they are limited in capturing the real age-related phenomenon. Therefore, there is a need to incorporate longitudinal measures in aging studies to fill in significant gaps in our knowledge about metabolite stability over time. This research is important for accurate identification of age-related biomarkers and biologically relevant metabolic targets.

We designed a unique opportunity to study the effects of aberrant glycogen metabolism in aging and disease by performing a longitudinal metabolomics analysis on laforin KO (LKO) and WT mice. The LKO mouse is a monogenetic model of aggressive neurodegeneration, inflammation, decreased proteostasis, cellular stress response, and mitochondrial dysregulation caused by aberrant glycogen metabolism<sup>267</sup>. These pathologies are also well-established symptoms of aging and aging mice<sup>147</sup>. An important common feature of LD and the LKO mouse to aging is the accumulation of insoluble glycogen-like aggregates (LBs and corpora amylacea, respectively), which both

depend on glycogen synthase<sup>99</sup>. One differing characteristic is that LB accumulation is rapid in comparison to the slowly accumulating corpora amylacea<sup>99</sup>. To study the longitudinal metabolic relationship between age and glycogen utilization, we focused our investigations on central carbon metabolism, hypothesizing that aberrant glycogen metabolism in the LKO mouse causes changes to TCA cycle metabolism. We performed this study using LKO and WT C57BL/6J mice aged to be 1-, 3-, 6-, 9-, 12-, and 24-months. We examined the brain, skeletal muscle, and heart tissues and used an additional genotype, *Epm2a*<sup>+/+</sup> (laforin heterozygotes), to represent healthy carriers of an LD locus.

We report the TCA metabolite signature of the aging WT mouse and show relative differences in the metabolic signature in the LKO mouse that are met by the aging WT mouse in older age. Our data show that defective glycogen metabolism is correlated with changes to cellular respiration and that with normal aging, similar changes to cellular respiration are seen. Using a statistical biomarker detection tool, we confirm recent findings that glucosamine depletion is a likely driving feature of feature of LD and show a similar pattern in WT aging. Collectively, our findings begin to uncover the impact of glycogen metabolism on neural energetics and suggest an underlying metabolic signature common to aging and a mouse model of childhood dementia. These results have allowed us to form a new hypothesis that glucosamine is depleted by the formation of corpora amylacea, as it is in LD mice, thereby driving cognitive aging.



## 3.2 Methods

### 3.2.1 *Mouse models and tissue preparation*

Laforin KO (LKO) mice have been described previously and were generated by removing the DSPD exon of *Epm2a*, producing an *Epm2a*-null mutant<sup>217</sup>. Male C57BL/6J WT, and LKO mice were bred to birth laforin heterozygotes. All mice were housed in a climate-controlled environment with a 14/10 h light/dark cycle (lights on at 0600 h) with water and solid diet provided *ad libitum* throughout the study. The Institutional Animal Care and Use Committee (IACUC) at the University of Kentucky approved the animal procedures used in this study as specified by the 1985 revision of the Animal Welfare Act. WT, LKO, or laforin heterozygous mice were aged to be 1-, 3-, 6-, 9-, 12-months. WT and LKO mice were also aged to be 24-months old. Mice were sacrificed by cervical dislocation and tissues were rapidly dissected. One half of the heart, half the quantity of dissected skeletal muscle, and one hemisphere of the brain was flash-frozen in liquid nitrogen and pulverized into powder (5  $\mu$ m particles) using a liquid nitrogen Freezer/Mill Cryogenic Grinder (SPEX SamplePrep) for glycogen quantification using gas-chromatography mass spectrometry analysis<sup>40</sup>. The remaining halves were formalin fixed and set aside for other experiments.

### 3.2.2 *Gas Chromatography-Mass Spectrometry (GC-MS) analysis*

#### 3.2.2.1 *Extraction*

20 mg of each pulverized tissue was extracted in 1mL of 50% methanol. 250  $\mu$ L of the polar fraction was transferred to another eppi-tube and dried at  $10^{-3}$  mBar using SpeedVac (Thermo), derivatized, and analyzed by GCMS. The remaining 750  $\mu$ L was stored at -80°C for experimental replicates. Derivatization of dried polar samples began with the addition of 70  $\mu$ L of 20 mg/mL methoxylamine hydrochloride in pyridine followed by a 30°C incubation for 1.5 hr. Then, 50  $\mu$ L was transferred to a V-shaped amber glass chromatography vial and 80  $\mu$ L of trimethylsilylating agent N-methyl-N-trimethylsilyl-trifluoroacetamide (MSTFA) was added. This step was followed by a 30 min incubation at 37°C. After cooling, the derivatized mixture was analyzed by a Triple Quadrupole GCMS (TQMS) (Agilent 7010). GCMS protocols were similar to those described previously except for a modified source temperature of 280°C<sup>209</sup>. Data processing was performed using MassHunter Unknowns Analysis (B.09.00, Agilent Technologies, Santa Clara, CA, USA) software matched to the FiehnLib metabolomics library. Mass spectra were translated to relative metabolite abundance using MassHunter Quantitative Analysis (TOF) (B08, Agilent Technologies, Santa Clara, CA, USA). Relative polar metabolite abundances were adjusted to protein input.

### 3.2.2.2 *Quantification and statistical analysis*

Statistical analysis was carried out using GraphPad Prism9. All data are presented as means  $\pm$  S.E. One-way ANOVA was used to compare each set of age groups or two genotypes from the same age group. Up to 5 biological replicates were used for each age group. Protein normalized metabolites were uploaded to MetaboAnalyst and run through principal component analysis (PCA) and receiver operating characteristic analysis (ROC).

### 3.3 Results

Glucose derived from glycogen catabolism is used for cellular respiration in a tissue dependent manner. Thus, we hypothesized that LKO glycogen dysmetabolism promotes changes to the TCA cycle that are tissue dependent. To test this hypothesis, we compared the longitudinal TCA signatures of WT mice to LKO mice and laforin heterozygote mice, which represent a healthy model of a LD caring locus. All mice were aged 1-, 3-, 6-, 9-, and 12-months, and WT and LKO mice were aged an additional year to model old-age. These age intervals represent young (1-month), mature adult (3-6-months), middle age (9-12-months), and old age (24-months) of the mouse lifespan. We focused our comparisons on brain, skeletal muscle, and heart, as LBs dominate these tissues in LKOs. Tissues were rapidly dissected, submerged into liquid nitrogen. Using a magnetic assisted tissue-grinding mill, tissues were ground into 5  $\mu\text{m}$  while remaining submerged in liquid nitrogen. Free polar metabolites were removed by the addition of 50% methanol. Each sample set containing 210 polar fractions each and up to 5 biological replicates per age group was derivatized and analyzed by TQMS in a randomly generated order (**Figure 3.1A-B**). The 210 pellet fractions containing protein/DNA/RNA were analyzed simultaneously using GCMS and quantitated protein input was used to normalize the polar metabolite quantitation (**Figure 3.1A, C**). Each tissue sample set was analyzed by the TQMS or GCMS in a single sequence and metabolites were assigned blindly to decrease the possibility of instrument drift.

#### 3.3.1 TCA metabolite signatures of the aging WT and LKO brain

To establish a TCA cycle signature of the aging brain, we first analyzed WT brain TCA cycle metabolites that included glucose, fructose, lactate, pyruvate, citrate, glutamate, succinate, fumarate, and malate. Consistent among each of these metabolites in WT mice is an increase in metabolite load observed after 1-month that decreases after 6-months and increases again between 9- and 24-months (**Figure 3.2**). Therefore, the aging brain TCA cycle metabolite load appears dynamic, despite no observable difference between adult and old-aged mice (3- and 24-months) for glucose, fructose, lactate, citrate, glutamate, or malate.

We then compared the LKO TCA cycle metabolite signatures to WT. The WT aging TCA cycle metabolite signature among 1-, 9-, 12-, and 24-month-olds is similar to the brain TCA cycle signature of LKO mice (**Figure 3.3**). However, mature adult LKO mice, 3-6-months, showed a decreased metabolite load for glucose, fructose, lactate, citrate, glutamate, succinate, fumarate, and malate. The decrease is statistically significant in 6-month-olds, where fructose is 3-fold lower than WT, lactate is 2-fold lower than WT, malate is 2-fold lower than WT, and glutamate is 2-fold lower than WT. Thus, for all observable TCA cycle metabolites except for pyruvate, LKO TCA cycle metabolite load

was lower than WT at 3- and 6-months. These results indicate a glycogen metabolism dependent effect on TCA cycle metabolism in the brain.

### **3.3.2 TCA metabolite signatures of the aging WT and LKO skeletal muscle and heart**

To establish the TCA signature of aging in skeletal muscle, we analyzed TCA cycle metabolites that included lactate, pyruvate, citrate, succinate, fumarate, and malate. No change over time is observed in lactate, pyruvate, or citrate levels with WT skeletal muscle aging (**Figure 3.4**). A non-significant age dependent trend in WT mice skeletal muscle can be seen in succinate, fumarate, and malate, where metabolite load decreases after 1-month, increases after 6-months and decreases again between 9- and 24-months. These results are consistent with previous reports indicating that old age does not impose significant changes to skeletal muscle TCA cycle metabolite load<sup>146,266</sup>. Quantitation of TCA cycle intermediates in LKO skeletal muscle indicates no trend or significant differences between WT and LKO metabolite load at any age (**Figure 3.5**). Therefore, unlike in brain, accumulation of LBs in the skeletal muscle does not appear to impose changes to TCA cycle metabolite load.

Lastly, we defined the TCA cycle signature of the aging heart. WT heart TCA metabolite spectra included glucose, lactate, pyruvate, citrate, glutamine, succinate, fumarate, and malate. Except for glucose, no difference is measured between heart TCA cycle metabolites of different age groups (**Figure 3.6**). These data support previous findings suggesting that unlike glucose, glycogen load in the heart is stable<sup>259</sup>. Quantitation of TCA cycle intermediates in LKO heart tissue indicates no trend or significant differences between WT and LKO metabolite load at any age (**Figure 3.7**). Thus, like skeletal muscle, accumulation of LBs in the heart does not appear to create changes to TCA cycle metabolite load. Our analysis of longitudinal WT and LKO TCA cycle metabolite loads support our hypothesis that the influence of aberrant glycogen metabolism on TCA cycle metabolite loads is tissue dependent.

### **3.3.3 TCA metabolite signatures of laforin heterozygote aging mice**

To further determine the influence of LB accumulation on TCA cycle metabolite signatures, we analyzed these signatures in the laforin heterozygote mice. Using laforin heterozygote mice to model healthy carriers of an LD locus, we see that no trend or significant change exists between laforin heterozygotes and WT mice in the brain, skeletal muscle, or heart (**Figures 3.8, 3.9, and 3.10**). Thus, the aging trends between WT are supported by the parallel longitudinal TCA metabolite signatures of the laforin heterozygotes in all three tissues. These data further suggest that brain TCA metabolism defects seen in the LKO mice at 3- and 6-months can be corrected with one functional copy of *Epm2a*.

### **3.3.4 Statistical analysis of TCA metabolite profile variation in aging WT, LKO, and laforin heterozygotes and biomarker prediction of LD and aging**

To examine why TCA metabolite load differs between LKO and WT mice at 3- and 6-months but not at older ages, we used principal component analysis (PCA) to describe metabolite variation at each age interval. Through PCA we see that the brain TCA metabolite profile of LKO mice increasingly separates from WT and laforin heterozygotes during 1-, 3- and 6-months of age (**Figure 3.11A-C**). At 9-months, the metabolite profile of all three genotypes begins to overlap and by 12-months little variance exists between any of the metabolite profiles until 24-months (**Figure 3.11D-F**). No separation occurs in skeletal muscle or heart except at 24-months (**Figure 3.12A-F, and 3.13A-F**). This suggests that natural aging results in similar metabolic pathway changes as LD. Therefore, we predicted that similar predicted biomarkers of aging and LD should be observed using a receiver operating characteristic (ROC) curve-based approach for biomarker prediction. As expected, we identified glucosamine and its derivative galactosamine as molecular drivers of the LKO metabolic signature in 6-, 9-, and 12-month-olds (**Figure 3.14A-D**). Using the same approach to identify biomarkers of aging, glucosamine also emerged as a metabolite that differentiates young mice from aging mice (**Figure 3.14E-H**). These results suggest that glucosamine may be a driver of both LKO and aging pathology.

### 3.4 Discussion

Cognitive decline and neurodegeneration, as well as metabolic changes related to mitochondrial activity, reactive oxidative stress, proteolytic stress, and hypoxia, are known phenotypes of normal aging and neurodegenerative diseases of aging<sup>3</sup>. Glycogen metabolism has been shown or proposed to underly all of these features, which are exasperated in the glycogen storage disease and childhood dementia LD<sup>267</sup>. To explore our hypothesis that aberrant glycogen metabolism impacts TCA cycle cellular respiration in LD, we first analyzed a longitudinal model of WT aging TCA cycle metabolism of brain, skeletal muscle, and heart tissues. We then compared the WT aging signature to LKO and laforin heterozygote aging to define the age dependent influence progressive LB accumulation on the TCA cycle.

In the brain of WT mice, there is evidence of a consistent time-dependent trend in metabolite load that increases after 1-month, decreases after 6-months, and increases again between 9-and 24-months, such that no observable difference is seen between the metabolite load of 24- and 3-month-olds. These trends are supported by the laforin heterozygote mice, as no difference is observed between the laforin heterozygote and WT mice in any tissue. Our WT aging data is consistent with previously published cross-sectional analyses on brain, skeletal muscle, and heart indicating that no TCA cycle dysregulation is seen in old-aged (24-month-old) mice compared to young adult mice (3-month-olds)<sup>145,146,266</sup>. Consistent with our hypothesis, TCA cycle metabolite load is decreased in LKOs as adults (3-6-months) which correlates with the time frame in which significant emergence of LBs is seen. Further, by PCA the LKO brain TCA metabolite variation diverges from WT, increasing in separation from 1 to 6 months of age. Interestingly, the TCA metabolome divergence is not seen in older ages, instead the aged-matched WT TCA metabolome signature increasingly overlaps between 9 and 12-months of age. One interpretation of this finding is that the aging TCA metabolome may be shifting with age such that it progressively resembles the TCA signature of LKO mice. A similar phenomenon was recently reported in an Alzheimer's mouse model, wherein the WT brain metabolome begins to overlap with the AD metabolome at 24-months<sup>268</sup>. In support of this interpretation is our predicted biomarker analysis in which we found that a known biomarker of LD, glucosamine sequestration, is also predicted to be implicated in WT aging<sup>16</sup>.

Sequestration of glucosamine in PGBs is a recently published LD phenomenon, which has been shown to create major downstream infarctions to cellular function largely involving glycosylation<sup>16</sup>. Thus, considering the well documented aging and glycogen dependent progressive accumulation of corpora amylacea, glucosamine sequestration may be a reasonable target of investigation for the downstream neural dysfunctions of aging<sup>19,138</sup>. Further, the lesser degree of glucosamine sequestration by corpora amylacea may explain the lesser degree of neurocognitive and molecular insults in aging compared to LD. The overlapping brain cellular respiration signatures between the WT an LKO mouse models in older age may be further explained by the fact that the LKO mouse model has a less severe disease progression than LD in humans<sup>118</sup>. The LD mouse



model lives until old-age, where LD patients typically die just as they reach adulthood in their early 20's<sup>215,217-219</sup>. As no differences at any age are observed between the LKO and WT genotype in skeletal muscle or heart tissues, these collective findings contribute to a growing body of data characterizing unique roles for glycogen that are specific to the brain. These results suggest that LBs and their metabolic consequences are more detrimental to the CNS than in the skeletal muscle or heart where they also heavily accumulate, further supporting previous indications that LBs are neurotoxic<sup>78,222</sup>.

The extent to which glycogen supports brain energy metabolism requires continued investigation. Glycogen is required for a healthy cognitive functioning and its accessibility is critical, as demonstrated in LD<sup>118</sup>. Glycogen-like aggregations and/or corpora amylacea hyper-accumulation have been documented in other neurodegenerative diseases e.g., Alzheimer's disease, amyotrophic lateral sclerosis (ALS), temporal lobe epilepsy (TLE), Parkinson's disease, diabetic neuropathy, peripheral neuropathy, and motor neuron disease<sup>19,138</sup>. As compromised energy metabolism is a known underlying factor of neurodegenerative disease and aging, glycogen dysmetabolism may be an underlying cause in not only LD and aging, but of many other neurodegenerative diseases not currently classified as glycogen storage disorders. A similar analysis of the influence of glycogen on these diseases may be modeled by the present study. Further, flux analysis on TCA cycle metabolites and glucosamine should be considered in aging, LD, and other dementias where aberrant glycogen-like aggregates and glycosylation defects have been reported<sup>269,270</sup>.

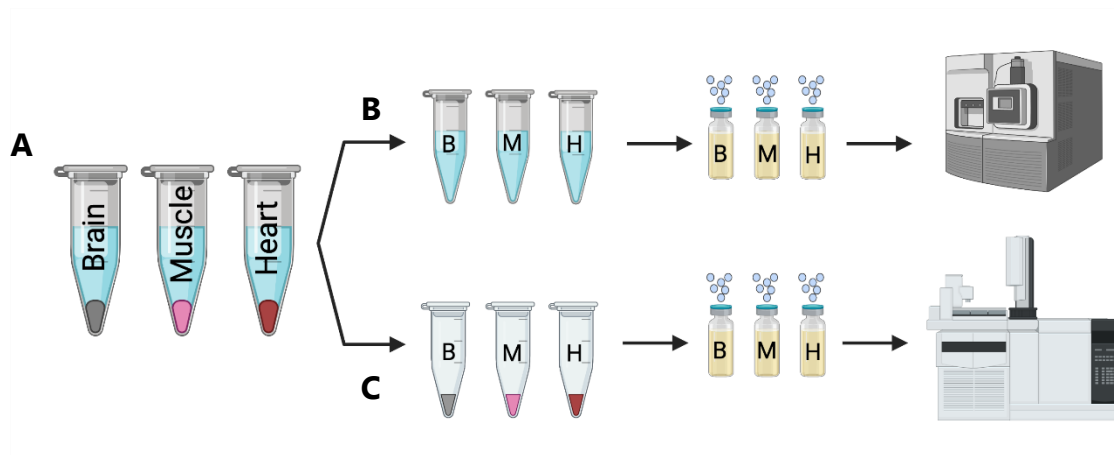


**Figure 3.1 Metabolomics workflow.**

**A)** Polar metabolites from brain, skeletal muscle, and heart tissue were extracted and separated from the tissue pellet containing protein/DNA/RNA. **B)** (Top) Polar metabolites from each tissue were derivatized and analyzed by TQMS. **C)** (Bottom) protein in the tissue pellet was analyzed by GCMS.

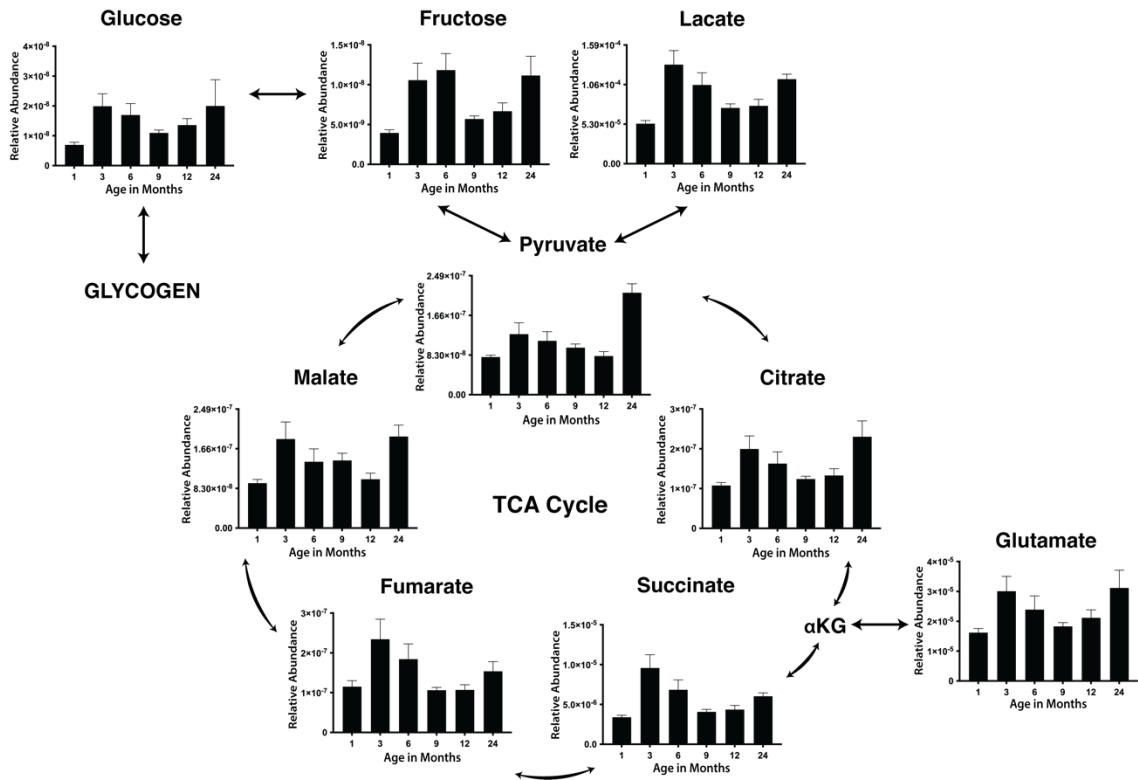


**Figure 3.2 WT brain TCA metabolites.**

Mass spectra were translated to relative metabolite abundance normalized to protein input. Statistical analysis using one-way ANOVA comparing each set of age groups or genotypes was performed using GraphPad Prism9. All data are presented as means  $\pm$  S.E. In each age group, up to 5 biological replicates were used.

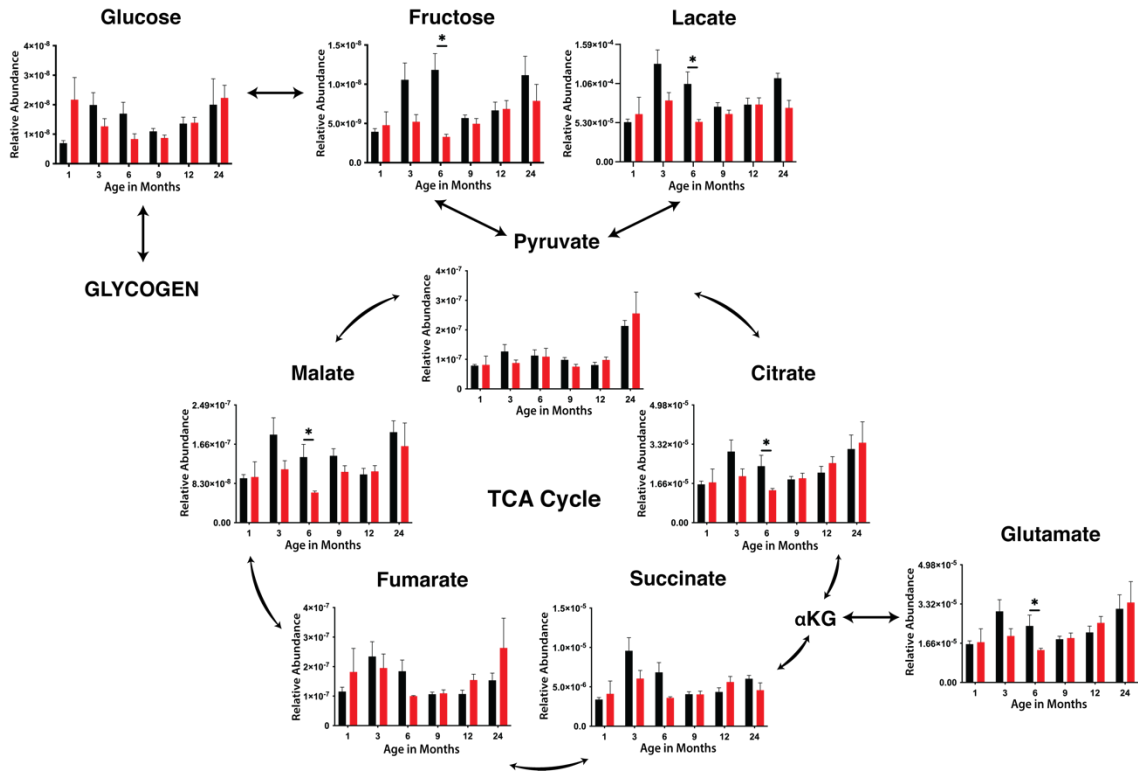


**Figure 3.3 WT versus LKO brain TCA metabolites.**

Mass spectra were translated to relative metabolite abundance normalized to protein input. Statistical analysis using one-way ANOVA comparing each set of age groups or genotypes was performed using GraphPad Prism9. All data are presented as means  $\pm$  S.E. In each age group, up to 5 biological replicates were used.

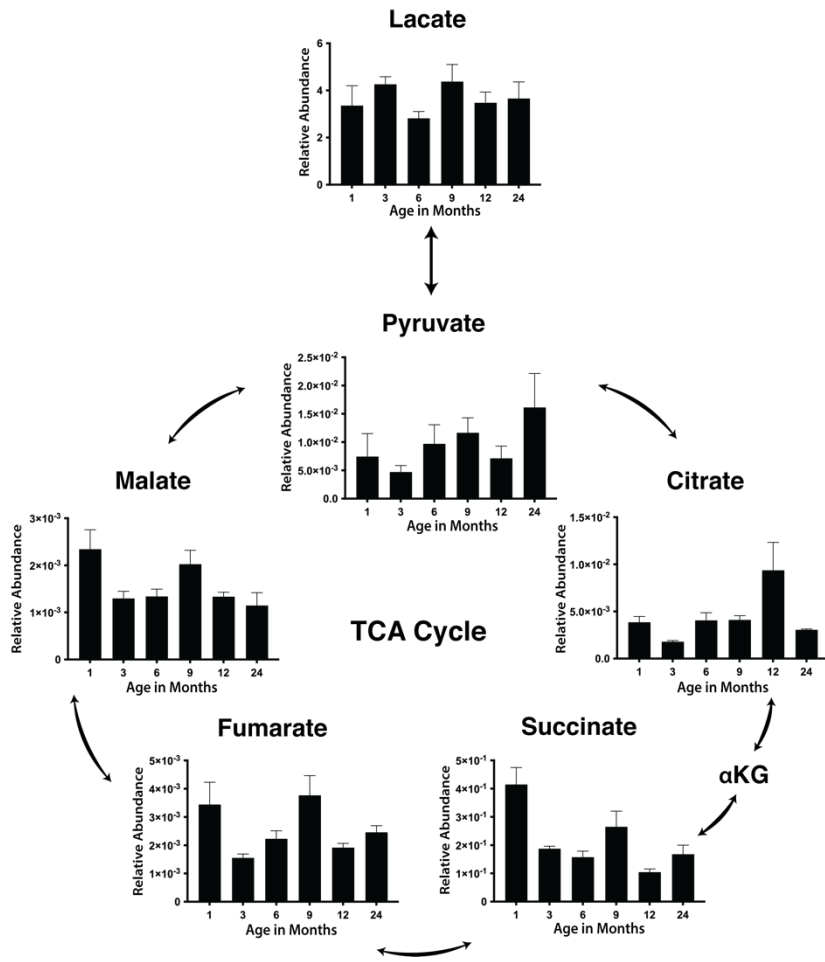


**Figure 3.4 WT skeletal muscle TCA metabolites.**

Mass spectra were translated to relative metabolite abundance normalized to protein input. Statistical analysis using one-way ANOVA comparing each set of age groups or genotypes was performed using GraphPad Prism9. All data are presented as means ± S.E. In each age group, up to 5 biological replicates were used.

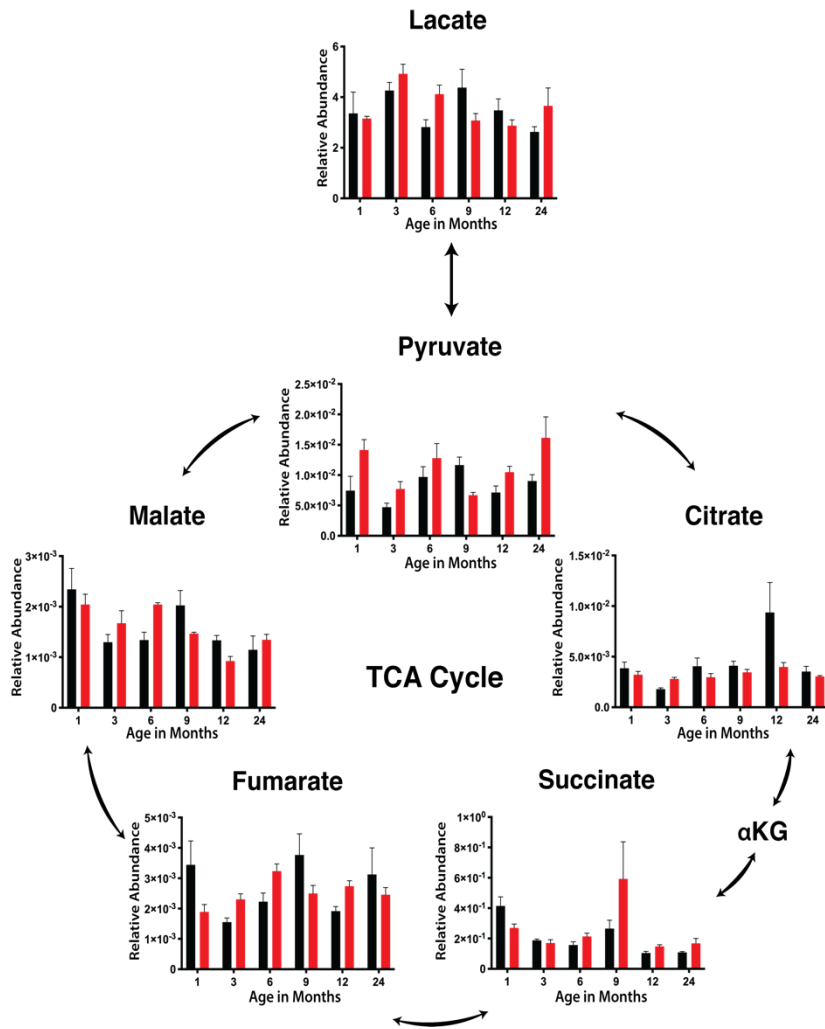


**Figure 3.5 WT versus LKO skeletal muscle TCA metabolites.**

Mass spectra were translated to relative metabolite abundance normalized to protein input. Statistical analysis using one-way ANOVA comparing each set of age groups or genotypes was performed using GraphPad Prism9. All data are presented as means  $\pm$  S.E. In each age group, up to 5 biological replicates were used.

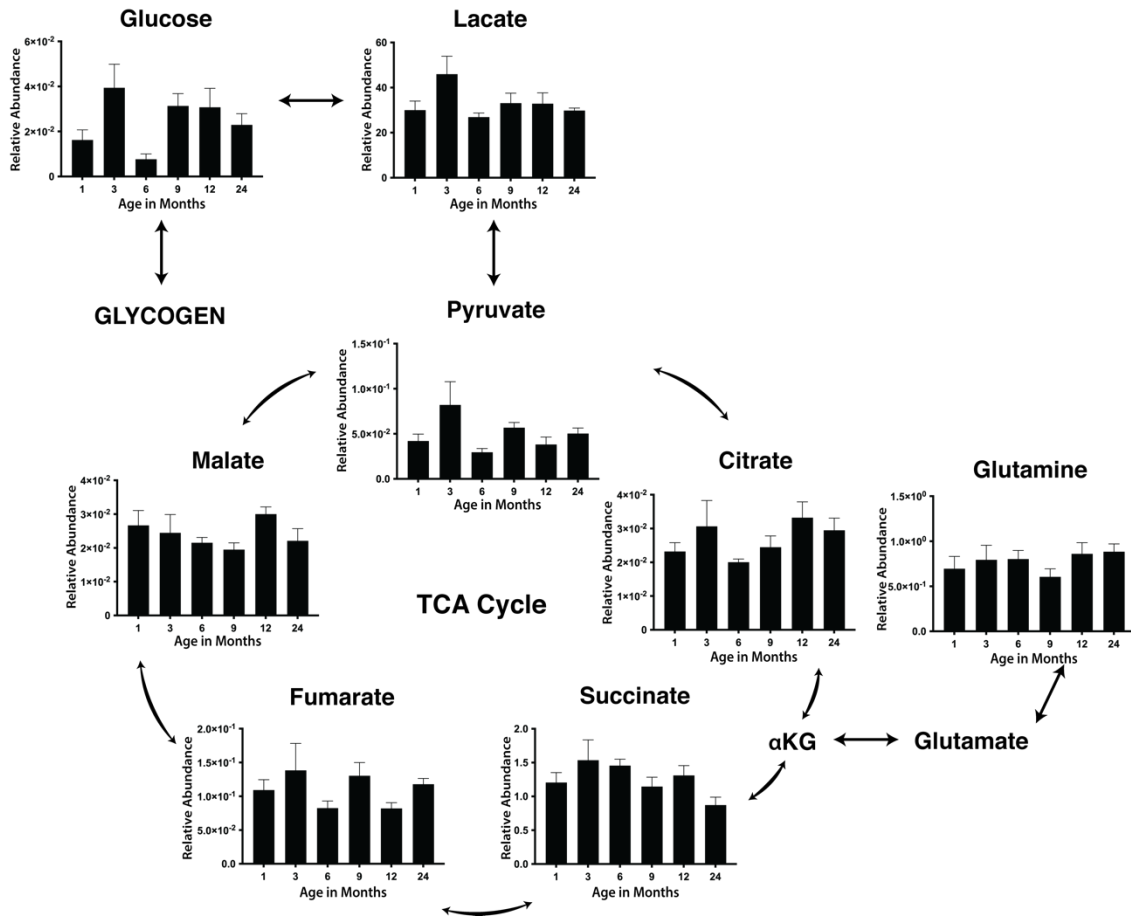


**Figure 3.6 WT heart TCA metabolites**

Mass spectra were translated to relative metabolite abundance normalized to protein input. Statistical analysis using one-way ANOVA comparing each set of age groups or genotypes was performed using GraphPad Prism9. All data are presented as means  $\pm$  S.E. In each age group, up to 5 biological replicates were used.



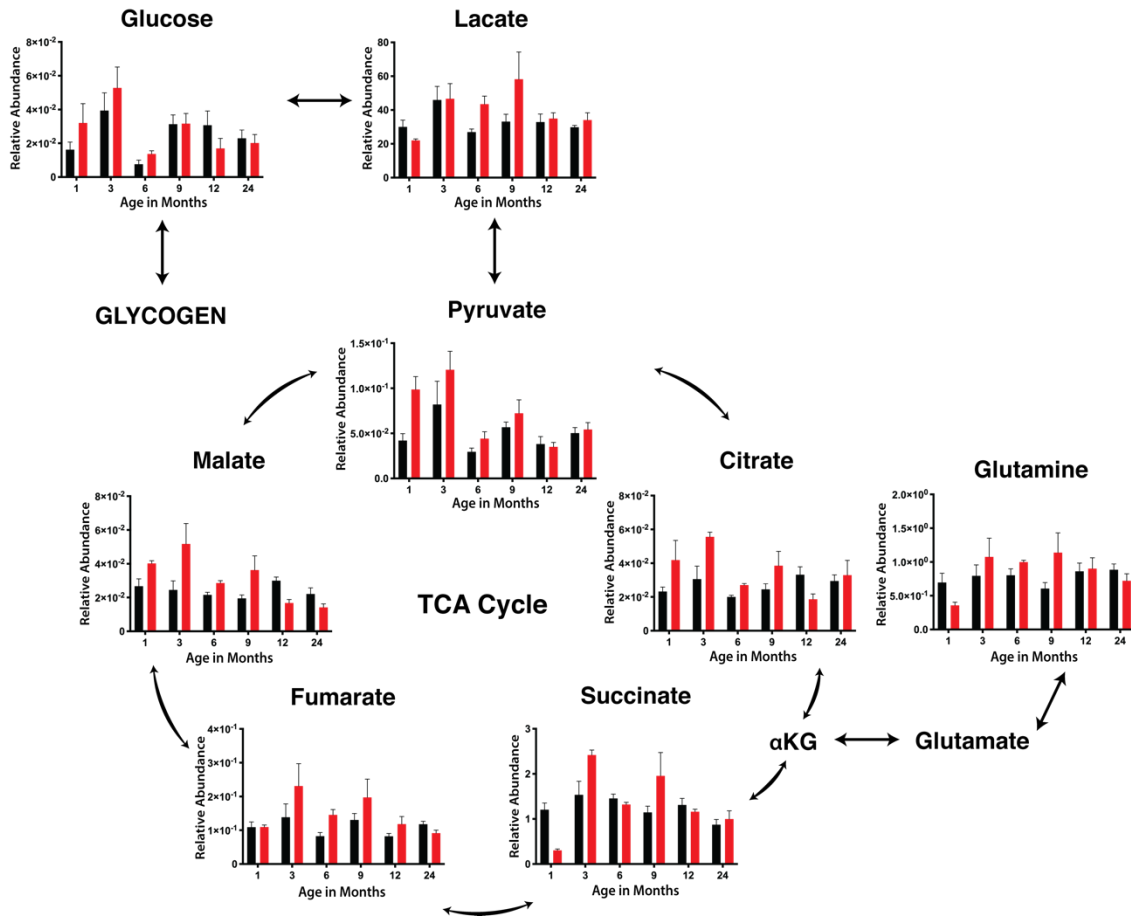


**Figure 3.7 WT versus LKO heart TCA metabolites.**

Mass spectra were translated to relative metabolite abundance normalized to protein input. Statistical analysis using one-way ANOVA comparing each set of age groups or genotypes was performed using GraphPad Prism9. All data are presented as means  $\pm$  S.E. In each age group, up to 5 biological replicates were used.

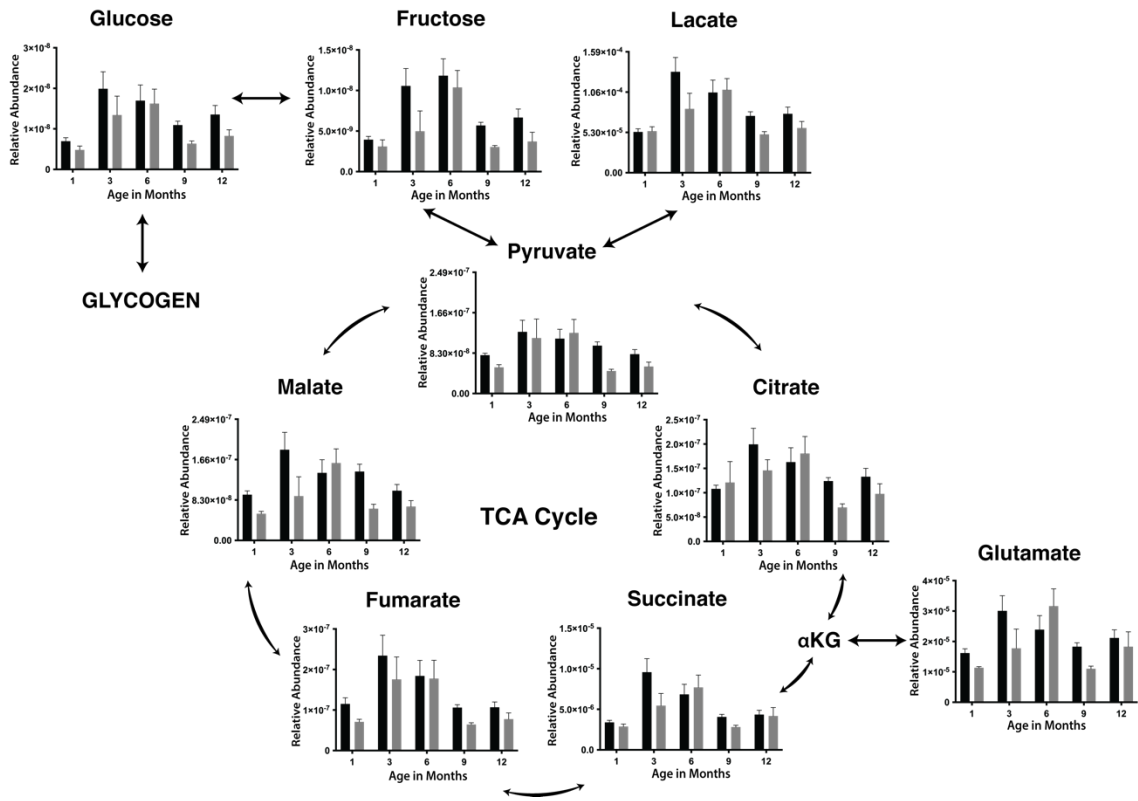


**Figure 3.8 WT versus laforin heterozygote brain TCA metabolites.**

Mass spectra were translated to relative metabolite abundance normalized to protein input. Statistical analysis using one-way ANOVA comparing each set of age groups or genotypes was performed using GraphPad Prism9. All data are presented as means  $\pm$  S.E. In each age group, up to 5 biological replicates were used.

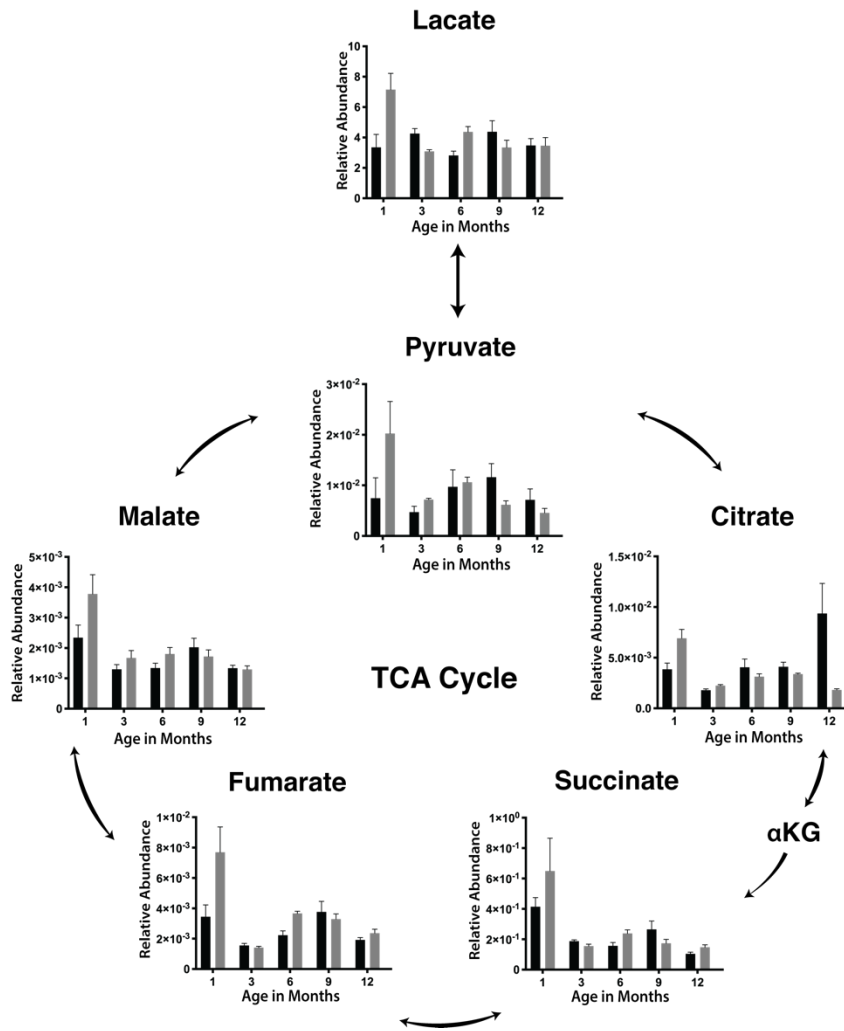


**Figure 3.9 WT versus laforin heterozygote skeletal muscle TCA metabolites.** Mass spectra were translated to relative metabolite abundance normalized to protein input. Statistical analysis using one-way ANOVA comparing each set of age groups or genotypes was performed using GraphPad Prism9. All data are presented as means  $\pm$  S.E. In each age group, up to 5 biological replicates were used.

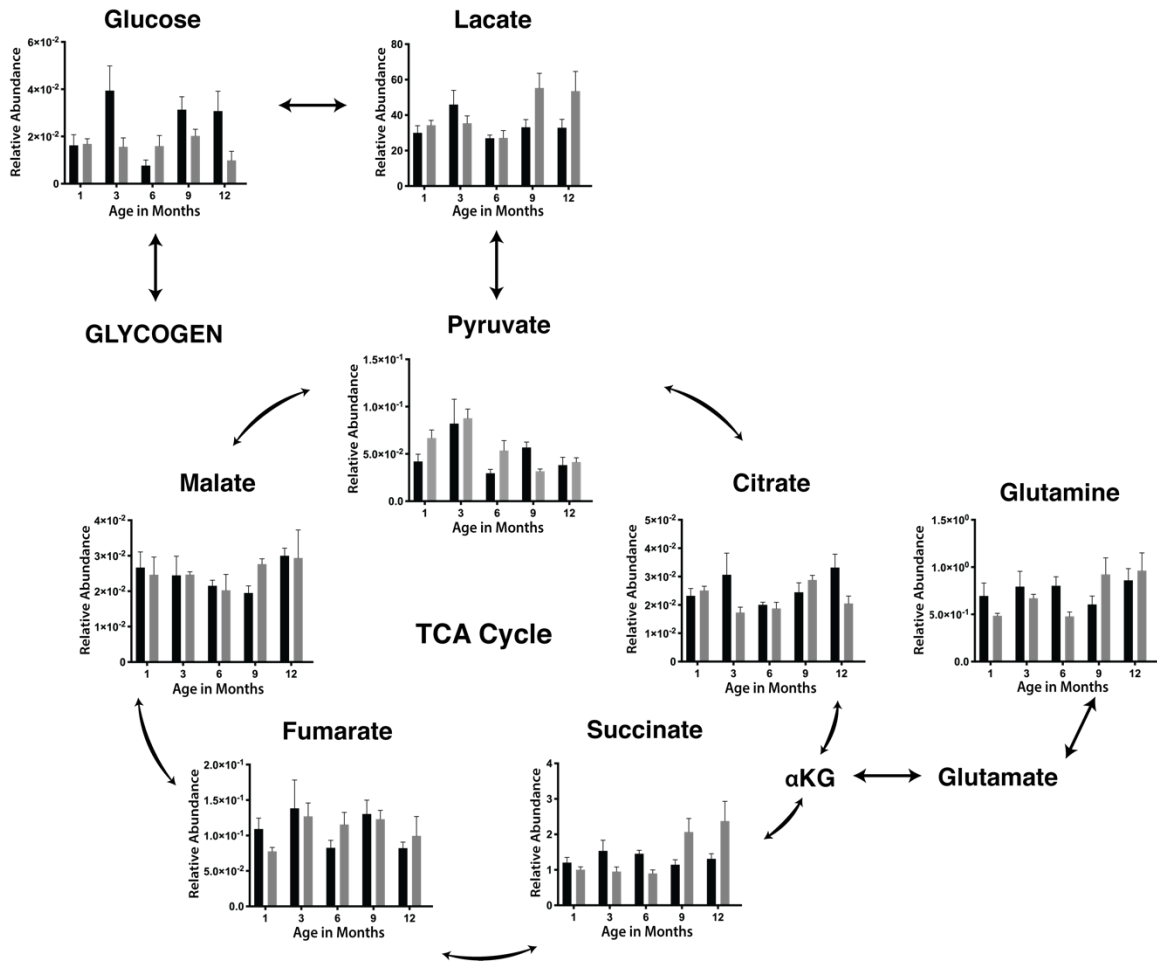


**Figure 3.10 WT versus laforin heterozygote heart TCA metabolites.**

Mass spectra were translated to relative metabolite abundance normalized to protein input. Statistical analysis using one-way ANOVA comparing each set of age groups or genotypes was performed using GraphPad Prism9. All data are presented as means  $\pm$  S.E. In each age group, up to 5 biological replicates were used.

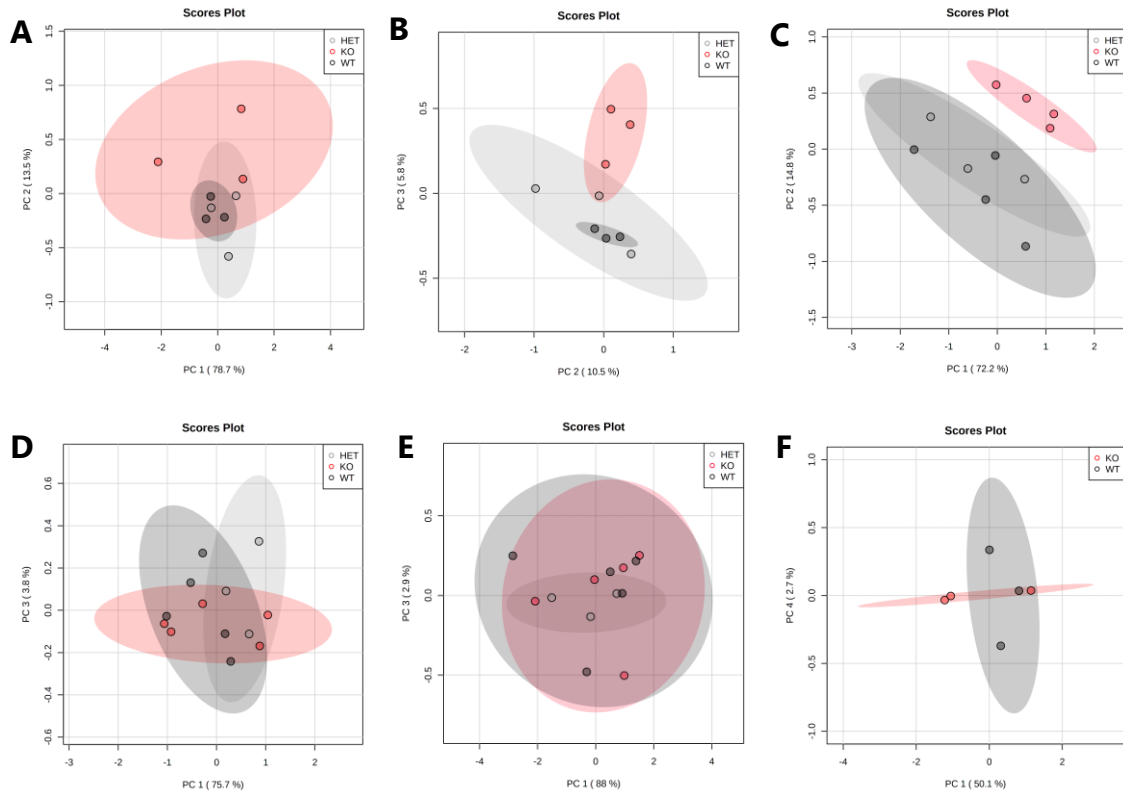


**Figure 3.11 PCA plots of brain TCA metabolites.**

Mass spectra were translated to relative metabolite abundance normalized to protein input. Statistical analysis using one-way ANOVA comparing each set of age groups or genotypes was performed using GraphPad Prism9. All data are presented as means  $\pm$  S.E. In each age group, up to 5 biological replicates were used. Protein normalized metabolites were uploaded to MetaboAnalyst and run through principal component analysis (PCA).

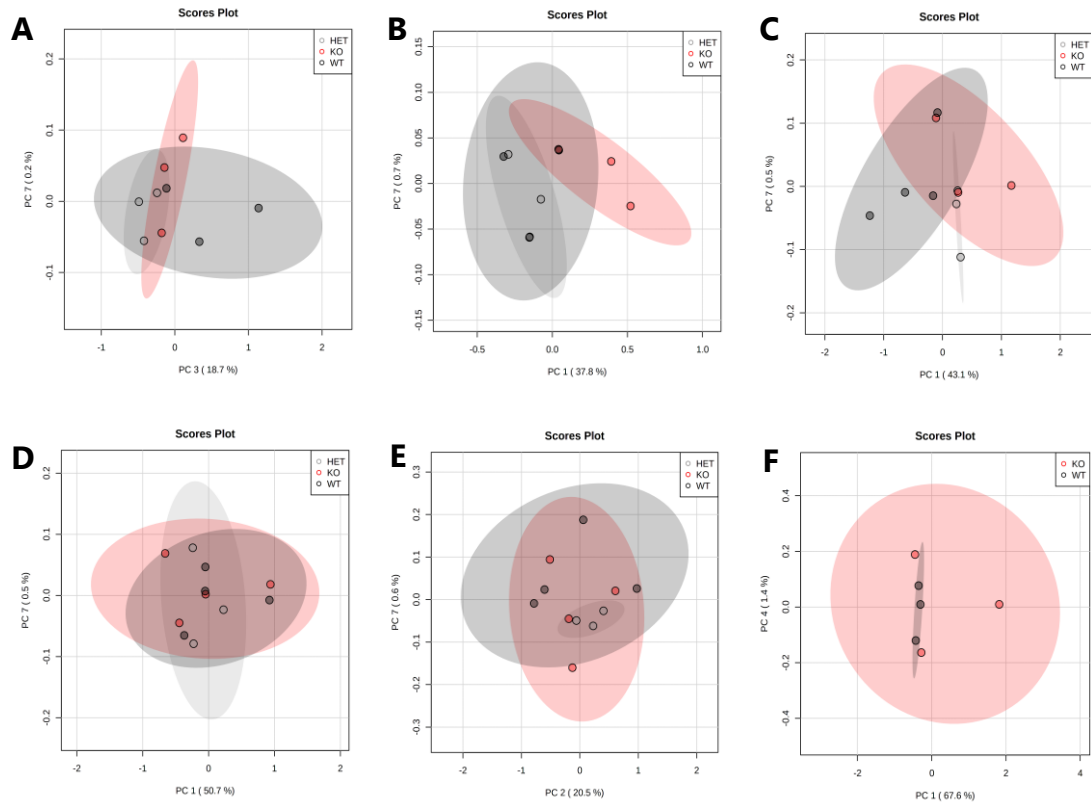


**Figure 3.12 PCA plots of skeletal muscle TCA metabolites.**

Mass spectra were translated to relative metabolite abundance normalized to protein input. Statistical analysis using one-way ANOVA comparing each set of age groups or genotypes was performed using GraphPad Prism9. All data are presented as means  $\pm$  S.E. In each age group, up to 5 biological replicates were used. Protein normalized metabolites were uploaded to MetaboAnalyst and run through principal component analysis (PCA).

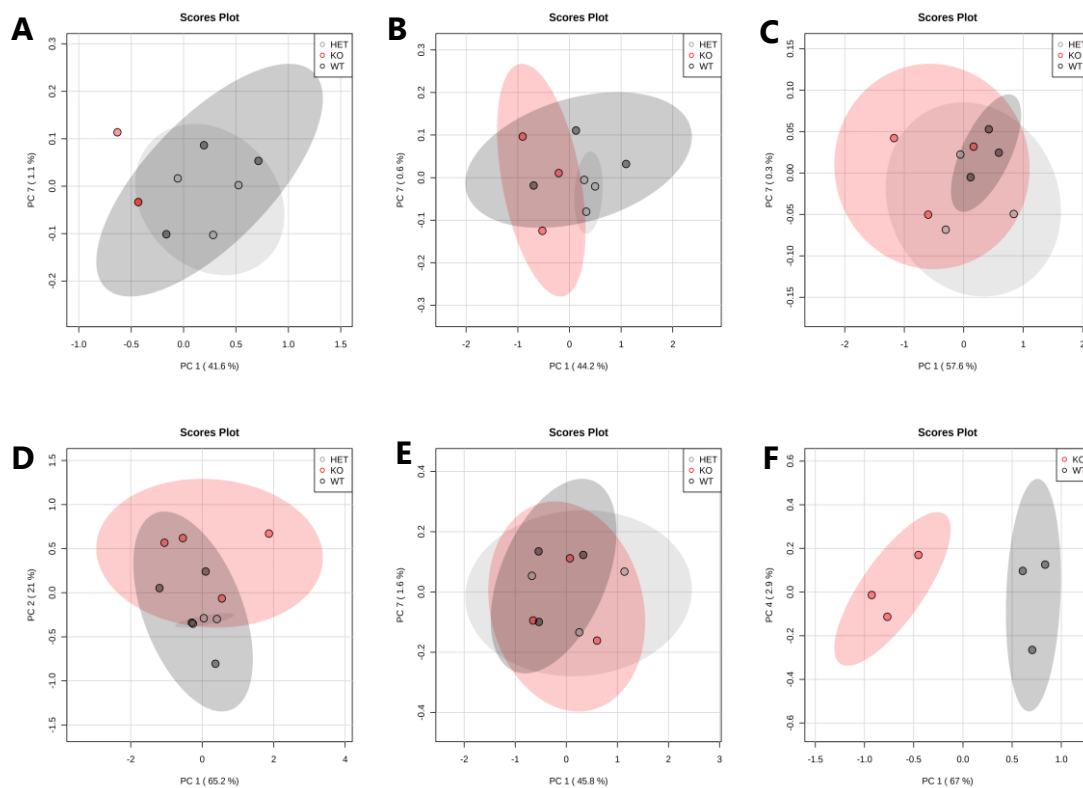


**Figure 3.13 PCA plots of heart TCA metabolites.**

Mass spectra were translated to relative metabolite abundance normalized to protein input. Statistical analysis using one-way ANOVA comparing each set of age groups or genotypes was performed using GraphPad Prism9. All data are presented as means  $\pm$  S.E. In each age group, up to 5 biological replicates were used. Protein normalized metabolites were uploaded to MetaboAnalyst and run through principal component analysis (PCA).



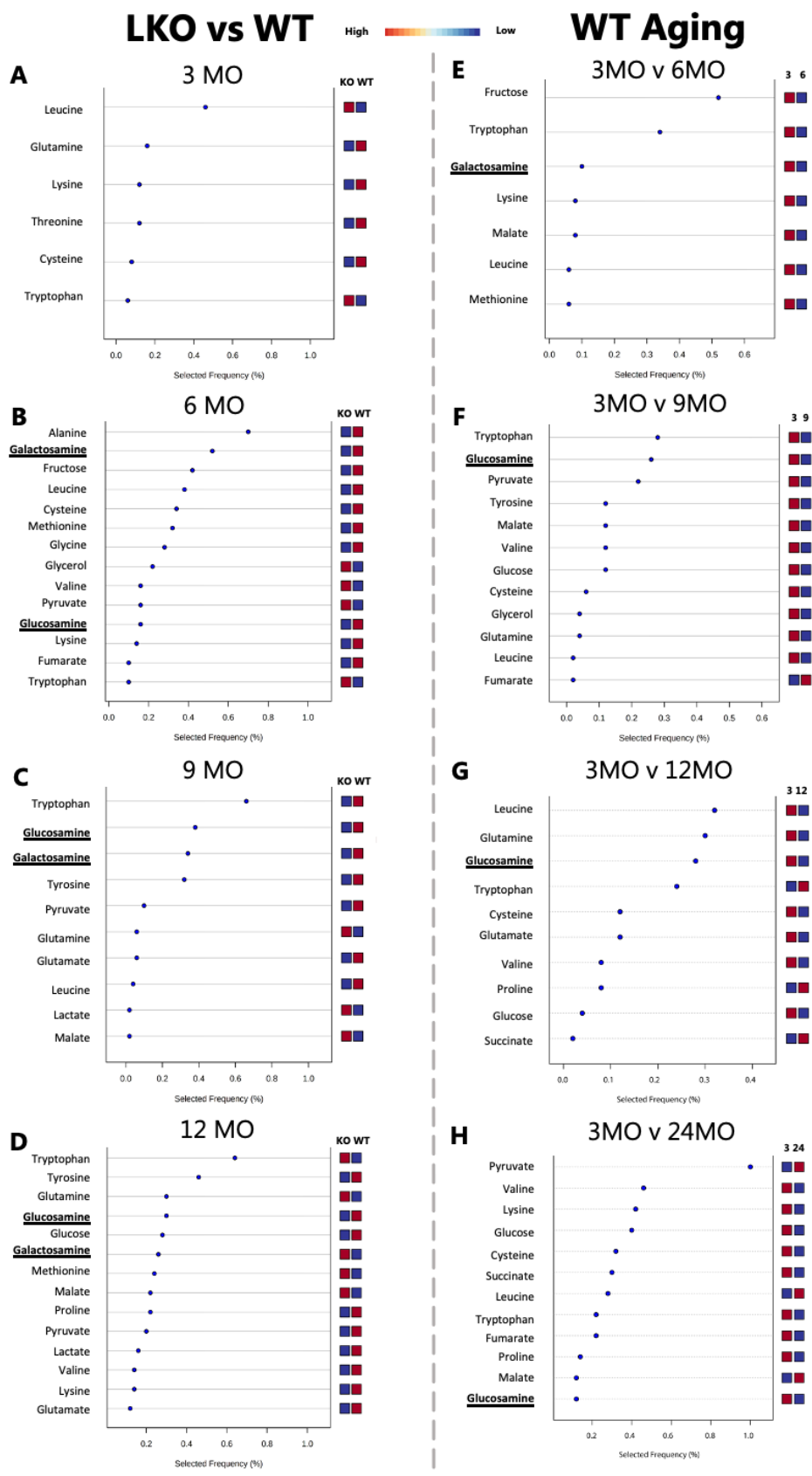


**Figure 3.14 Biomarkers of LD and aging.**

Mass spectra were translated to relative metabolite abundance normalized to protein input. Statistical analysis using one-way ANOVA comparing each set of age groups or genotypes was performed using GraphPad Prism9. All data are presented as means  $\pm$  S.E. In each age group, up to 5 biological replicates were used. Protein normalized metabolites were uploaded to MetaboAnalyst and run through receiver operating characteristic analysis (ROC).

## CHAPTER 4. Generation and characterization of a laforin nanobody inhibitor

### 4.1 Introduction

Glycogen is the storage form of glucose and a highly important substrate for cellular metabolism<sup>271</sup>. Nearly all tissues metabolize glycogen and recent work has focused on the importance of glycogen metabolism in the brain<sup>14</sup>. Characterization of the enzymes and mechanisms of glycogen metabolism began over 70 years ago and include: synthesis by glycogen synthase, branching via glycogen branching enzyme, hydrolysis by glycogen phosphorylase, and debranching via glycogen debranching enzyme<sup>13</sup>. Over the last 20 years, a previously unknown protein called laforin has emerged as an important contributor to glycogen metabolism homeostasis.

Multiple labs demonstrated that laforin is a glycogen phosphatase and mutations in the gene encoding laforin cause the formation of aberrant glycogen-like aggregates called Lafora bodies (LBs)<sup>86,89,272</sup>. LBs are cytoplasmic, water-insoluble aggregates more similar to plant starch than human glycogen<sup>20,103,104,273</sup>. The LBs form in cells from nearly all tissues and are the pathological agent driving neurodegeneration and death in Lafora disease (LD) patients<sup>25–28</sup>. LD is autosomal recessive and classified as both a progressive myoclonus epilepsy and glycogen storage disease. The direct relationship between mutated laforin, LB formation, and LB neurotoxicity highlights the importance of glycogen metabolism in the brain. While laforin removes phosphate from glycogen, how phosphate impacts normal glycogen homeostasis or how hyper-phosphorylation is detrimental to glycogen homeostasis and LB formation remains under investigation.

Based on sequence and structural conservation, laforin is classified in the protein tyrosine phosphatase superfamily and the dual specificity phosphatase clade<sup>274</sup>. Laforin is the only known human glycogen phosphatase and is comprised of a dual-specificity phosphatase (DSP) domain and a carbohydrate binding module (CBM). Like all DSPs, laforin contains a protein-tyrosine phosphatase catalytic loop that includes a CX<sub>5</sub>R motif (CNAGVGR, residues 266–272) at the base of the active site<sup>115</sup>. The architecture and depth of this active site allow laforin to dephosphorylate glycogen<sup>274–276</sup>. The laforin CBM belongs to CBM family 20 and allows laforin to bind glycogen as well as other complex carbohydrates *in vitro* and *in vivo*, like LBs, amylopectin, and maltodextrins<sup>20,222,276</sup>. Key structural aspects of laforin that promote glucan-specific phosphatase activity are: closely integrated CBM-DSP domains, an anti-parallel dimerization, and a signature DSP sequence within the active site channel<sup>274</sup>.

In addition to being a glycogen phosphatase, laforin interacts with several proteins involved in glycogen metabolism, including the E3 ubiquitin ligase malin<sup>84</sup>. Approximately 50% of LD patients have mutations in the gene encoding malin and ~50% have mutations in the gene encoding laforin. Malin polyubiquitinates a number of proteins involved in glycogen metabolism, including both laforin and glycogen phosphorylase<sup>84,114,277</sup>. The consequences of malin-directed ubiquitination are still being elucidated. LD mouse models with a mutation in either gene form hyperphosphorylated

LBs and display neurodegeneration<sup>88,89</sup>. However, the relationship between phosphorylation and LD progression remains an unresolved and critical issue<sup>78,107,278</sup>.

Recombinant antigen-specific, single-domain antibodies, often referred to as nanobodies (Nb), are increasingly used for modulating protein properties for the purpose of elucidating function<sup>279</sup>. While canonical antibodies are comprised of two heavy chains and two light chains, nanobodies are derived from the antigen binding domain of heavy-chain antibodies, produced in camelids and select other organisms. Thus, nanobodies are monomers with a dedicated variable domain, also referred to as VHH, and are ten times smaller than a canonical IgG, i.e. ~15 kDa. Their small size promotes their high propensity for binding unique structural features of proteins, otherwise unreachable by conventional immunoglobulins and capable of manipulating protein conformation linked to function<sup>279–281</sup>. Nanobodies contain three complementary determining regions (CDRs) that are primary determinants of specific antigen binding. Similar affinities between VHHs and conventional antibodies are generally attributed to elongated CDR3 loops in VHH domains, which provide a paratope formed by a single entity<sup>282</sup>.

In this study, we present the characterization of six laforin nanobodies, consisting of five unique CDR3 regions. Two llamas were immunized with recombinant human laforin, 74 potential VHH anti-laforin candidates were screened, and six stably binding anti-laforin nanobodies were characterized. Epitope mapping of the six laforin nanobodies established three general epitopes, one that spans both the CBM and DSP on the opposite side of the DSP active site, one that lies on the CBM, partially covering regions that bind glycogen, and one that covers the DSP active site. Secondary structure epitope mapping established that nanobody Nb72 binds the PTP-loop of the laforin DSP domain. Utilizing three *in vitro* assays, we demonstrate that Nb72 inhibits the phosphatase activity of laforin. These laforin nanobodies are a novel set of molecular tools for defining the role of laforin in glycogen metabolism and disease.

## 4.2 Methods

### 4.2.1 VHH library generation

#### 4.2.1.1 Purification of Laforin

*H. sapiens* (Hs) Laforin residues 1-328 was expressed from pET28b (Novagen) as an N-terminal His<sub>6</sub> tagged protein, as previously described<sup>283</sup>. Briefly, laforin was expressed in BL21 (DE3) (Novagen) *E. coli* cells grown in 2xYT media at 37°C until OD<sub>600</sub> = 0.6, culture flasks were placed on ice for 20 min, induced with 1 mM (final) isopropyl thio-β-D-galactopyranoside (IPTG), grown for an additional 14h at 20°C, and harvested by centrifugation. Cells were resuspended and lysed in buffer A (20 mM Tris-HCl, 100 mM NaCl, 10% glycerol, 2 mM DTT, pH 7.5), centrifuged, and the proteins were purified using a Profinia immobilized metal affinity chromatography (IMAC) column with Ni<sup>2+</sup> beads (Bio-Rad) and a Profinia protein purification system (Bio-Rad) using wash (buffer A) and elution buffer (300mM imidazole, 20 mM Tris-HCl, 100 mM NaCl, 10% glycerol, 2 mM DTT, pH 7.5). The desalted elution fraction was further purified using fast protein liquid chromatography (FPLC) with a HiLoad 16/60 Superdex 200 size exclusion column (GE Healthcare). The buffer used for laforin purification for the small-scale pulldowns described in methods 2.3.2 was (50 mM HEPES, 100 mM NaCl, 10% glycerol, 2 mM DTT, pH 7.5. For all other experiments, laforin was purified in 20 mM Tris-HCl, 100 mM NaCl, 10% glycerol, 2 mM DTT, pH 7.5.

#### 4.2.1.2 Immunizations

Inoculation, construction of the VHH libraries, panning, and cloning was performed by the VIB Nanobody Core (Vrije Universiteit Brussel, Brussels). Two llamas were subcutaneously injected on days 0, 7, 14, 21, 28 and 35 with 250 µg/animal of recombinant laforin emulsified with Gerbu adjuvant P. On day 40, anticoagulated blood was collected for lymphocyte preparation.

#### 4.2.1.3 Construction of the VHH libraries

A VHH library was constructed from each llama to screen for the presence of laforin specific nanobodies. First strand cDNA synthesis was achieved using an oligo(dT) primer and total RNA from peripheral blood lymphocytes as a template. The VHH encoding cDNA sequences were amplified by PCR, digested with PstI and NotI, and cloned into the PstI and NotI sites of the phagemid vector pMECS.

#### **4.2.2 Isolation of laforin specific nanobodies**

Each library was panned individually for three rounds on solid-phase coated antigen (200 µg/mL in 100 mM NaHCO<sub>3</sub>, pH 9.3). After each round of panning, the enrichment for laforin-specific phages was assessed by comparing the number of phagemid particles eluted from antigen-coated wells with the number of phagemid particles eluted from negative control (uncoated blocked) wells. In total, 950 colonies (475 colonies for each library: 95 from panning round one, 285 from round two, and 95 from round three) were randomly selected and analyzed by ELISA for the presence of laforin specific nanobodies in their periplasmic extracts. The antigen used for panning and ELISA screening was the same as the one used for immunization, using uncoated blocked wells as negative control. Out of these 950 colonies, 138 colonies scored positive in this assay. Based on sequence data of the positive colonies, 74 different full-length nanobody candidates were distinguished based on complementary determining regions.

#### **4.2.3 Sequence verification, alignment, and evolutionary analysis**

Nanobody sequences were verified using the primer: 5' TTA TGC TTC CGG CTC GTA TG 3' and the six direct laforin binding nanobody plasmids will be deposited to <https://www.addgene.org/>. All sequence alignments were performed using Clustal-Omega available on the European Bioinformatics Institute's server <http://www.ebi.ac.uk/>. The evolutionary tree was calculated from the alignment using neighbor-joining clustering implemented in the Clustal-Omega package<sup>284</sup>. The guide tree was displayed with the program iTOL (<http://itol.embl.de/>)<sup>285</sup>.

#### **4.2.4 Screening for VHH expression**

74 potential VHH candidates were transformed into BL21 (DE3) *E. coli* cells (MilliporeSigma) and expression levels were analyzed by Western analysis. Nanobodies were expressed from pMECS as a C-terminal HA and His<sub>6</sub> fusion in 10 mL cultures grown in 2xYT until OD<sub>600</sub> = 0.6. 100 µL of each culture was aliquoted, centrifuged, air dried, and stored at -20°C while protein expression was induced in the remaining cultures using 1 mM IPTG (final concentration). Induced cultures grew for 3.5h, 80 µL of the induced cultures were pelleted, air dried and stored at -20°C. The 100 µL uninduced and 80 µL induced culture pellets were lysed with 75 µL of 50 mM TRIS, 8M urea by vortexing. Total proteins from the bacteria culture lysate were resolved by stain-free gel SDS-PAGE (Bio-Rad). Nanobody expression was visualized by Western analysis using an anti-6xHis antibody (1:1000) (NeuroMab #75-169) and goat anti-mouse secondary (1:3000) (Invitrogen #62-6520).

## **4.2.5 Small scale pulldowns**

### *4.2.5.1 Small scale nanobody purification*

Nanobodies screened for expression were purified using the remaining 9.82 mL of induced culture, which was pelleted and frozen at -20°C. Nanobodies were purified from the *E. coli* pellets with Ni-NTA resin. *E. coli* cell lysates were centrifuged to separate soluble protein which was incubated with Ni-NTA agarose beads for 1 h at 4°C in 1 mL bind buffer (20 mM Tris-HCL, 100 mM NaCl, 15 mM Imidazole, pH 8.0). The samples were washed three times in bind buffer and eluted in 100 µL of 300 mM imidazole, 100 mM NaCl, pH 8.0 and used for small scale pulldowns.

### *4.2.5.2 Antigen affinity pulldown*

Primary screening for nanobody binding was achieved by a small-scale pulldown method in which Affi-gel 10 affinity resin (Bio-Rad) was bound to laforin and subsequently to each purified VHH clone<sup>286</sup>. Expression and purification of laforin was performed as described above in 50 mM HEPES, 100 mM NaCl, 10% glycerol, 2 mM DTT, pH 7.5. 50 µL Affi-gel (100 µL slurry) per pulldown was washed and resuspended in cold PBS per manufacturer's directions. The washed Affi-gel was saturated with laforin in 50 mM HEPES, 100 mM NaCl, 10% glycerol, 2 mM DTT, (final volume 500 µL) and incubated with rocking for 1 h at 4°C. The laforin bound Affi-gel resin was spun down at 300 rpm for 2 min and washed with cold PBS two times. Affi-gel alone was used as a control. Then, the laforin bound or unbound Affi-gel was blocked with cold 1X TBS for 1 h at 4°C. The samples were spun down, supernatant was removed, and 75 µL (~4-12 µg) of small batch Ni<sup>2+</sup> purified nanobodies were added. Pulldowns were washed three times with 1X PBS, and the supernatant was removed. Bound proteins were denatured in Laemmli's buffer, and ~12 µL of each sample was loaded per well of a stain free SDS-PAGE gel and imaged.

## **4.2.6 Nanobody purification**

Larger concentrations of purified nanobodies were achieved by scaling up methods described in 2.2 and 2.3.1. Nanobodies were expressed in BL21 (DE3) *E. coli* cells grown in 2xYT at 37°C to OD<sub>600</sub> = 0.9. 15 mL of pre-culture was used per L culture. Cultures were induced with 1 mM IPTG (final) and incubated for ~16-18 h at 25°C after which, pellets were harvested by centrifugation. Nanobodies were purified from the *E. coli* pellets with Ni-NTA resin. *E. coli* cell lysates were centrifuged to separate soluble protein which was incubated with Ni-NTA agarose beads for 1 h at 4°C in 30 mL bind buffer (20 mM Tris-HCL, 100 mM NaCl, 15 mM Imidazole, pH 8.0). The samples were washed three times in bind buffer and eluted in 300 mM imidazole, 100 mM NaCl, pH 8.0. Eluted



samples were separated from the Ni-NTA beads by filtering through a 25 mM syringe filter and then buffer exchanged with 20 mM Tris-HCl pH 7.5, 100 mM NaCl using FPLC with a HiLoad 16/60 Superdex 75 column (GE Healthcare).

#### **4.2.7 Size exclusion analysis of VHH-laforin complexes**

Laforin and VHH were combined in molar ratio (~1:1.1) and resolved by size exclusion chromatography (SEC) using a HiLoad 10/300 Superdex 200 size exclusion column and 100 mM NaCl, 20 mM Tris, 10% glycerol, 0.35 mM  $\beta$ -mercaptoethanol (BME), pH 7.5. WT laforin alone was utilized as a control. Fractions were collected in 500  $\mu$ L volumes and visualized by loading 20  $\mu$ L of each fraction onto a stain-free gel SDS-PAGE (Bio-Rad) and imaged.

#### **4.2.8 Hydrogen Deuterium Exchange Mass Spectrometry (HDX)**

HDX experiments were performed as previously described<sup>276,287</sup>. The optimal peptide coverage map of laforin was obtained using a quench solution containing 0.08 M GuHCl, 0.1 M Glycine, 16.6% glycerol, pH 2.4. To initiate HDX experiments, 3  $\mu$ L of stock solution (laforin or laforin-nanobody complex at 1 mg/mL) was mixed with 9  $\mu$ L of D<sub>2</sub>O buffer (8.3 mM Tris, 50 mM NaCl, pD<sub>READ</sub> 7.2) and incubated at 0°C for 10, 100, 1000 and 10,000 sec. The exchange reaction was quenched by adding 18  $\mu$ L of the above quench solution, and the quenched samples were flash frozen with dry ice. All frozen samples, including un-deuterated and equilibrium-deuterated control samples, were passed over an immobilized pepsin column (16  $\mu$ L) at a flow rate of 25  $\mu$ L/min and digested peptides were collected on a C18 trap column (Optimize Tech, Opti-trap, 0.2x2 mm) for desalting. The peptide separation was performed on a C18 reverse phase column (Agilent, Poroshell 120, 0.3x35 mm, 2.7  $\mu$ L) with a linear gradient of 8-48% B over 30 min (A: 0.05% TFA in H<sub>2</sub>O; B: 80% acetonitrile, 0.01% TFA, and 20% (H<sub>2</sub>O)). Mass spectrometry (MS) analysis was performed on the Orbitrap Elite mass spectrometer (Thermo Fisher Sci), which was adjusted for HDX experiments<sup>288</sup>. The resolution of the instrument was set at 120,000 at m/z 400. Proteome Discoverer software (v1.3, Thermo Scientific) was used to identify the sequence of the digested peptide ions from their MS/MS data. HDXaminer (Sierra Analytics, Modesto, CA) was utilized to confirm the peptide identification and calculate the centroids of isotopic envelopes of all the peptides. The level of deuterium incorporation of each peptide was calculated by applying back-exchange correction<sup>289</sup>. The ribbon maps were generated from deuteration level of overlapping peptides to improve the resolution of the HDX data.

## 4.2.9 Phosphatase assays

### 4.2.9.1 *Para-Nitrophenyl Phosphate (pNPP) assay*

Generic phosphatase activity assays were performed using *para*-Nitrophenyl Phosphate (pNPP) as previously described<sup>86,290</sup>. Assays were performed using 96 well plates in 50  $\mu$ L reactions containing 1X phosphatase buffer (0.1 M sodium acetate, 0.05 M Bis-Tris, 0.05 M Tris-HCl, pH 5.0), 2 mM dithiothreitol (DTT), and 50 mM pNPP. To maintain reactions in the linear phase, 250, 500, or 1000 ng of laforin pre-bound to an equal molar quantity of nanobody were added to the reaction in triplicates and incubated in a 37°C water bath for 10 minutes. The reaction was terminated by the addition of 200  $\mu$ L of 0.25 M NaOH and absorbance was measured at 410 nm.

### 4.2.9.2 *Glucan dephosphorylation assays*

Glucan phosphatase activity assays were performed as previously described<sup>86,290</sup>. Assays were performed using 96 well plates in 100  $\mu$ L reactions containing 1X phosphatase buffer (100 mM sodium acetate, 50 mM bis-Tris, 50 mM Tris-HCl, pH 7.0) and 2 mM DTT, and 10mg/mL rabbit skeletal muscle glycogen or 1 mg/mL potato amylopectin (MilliporeSigma). To maintain enzymatic activity in the linear phase, every 10 seconds, 250, 500, or 1000 ng of laforin pre-bound to an equal molar quantity of nanobody were added to the reaction mixture in quadruplicates and incubated for 30 min at RT. The reaction was stopped by the addition of 25  $\mu$ L of malachite gold reagent mix added every 10 sec. Once each well was given the malachite gold reagent mix, stabilizer was added to each well in intervals of 10 seconds. Absorbance was measured at 635 nm.

### 4.2.9.3 *Statistical analysis*

Two-way ANOVA was performed using GraphPad Prism version 9.0.0 for Mac, GraphPad Software, San Diego, California USA, [www.graphpad.com](http://www.graphpad.com)

## 4.3 Results

### 4.3.1 *Anti-laforin nanobody primary screen*

Two llamas were immunized with purified recombinant human laforin. Lymphocytes were isolated, and the VHH coding sequences were cloned into a phagemid vector. After three rounds of panning and ELISA screens using recombinant laforin protein, a total of 74 clones scored positive and were sequenced, revealing 37 different CDR3 groups (**Figure 4.6**). A sequence similarity tree reveals the presence of two nanobody groups in which 35 clones are found in one and 39 are found in the other (**Figure 4.1**). All 74 clones were transformed into BL21 *E. coli* cells and VHH expression was determined by western analysis using an anti-HIS antibody. Approximately 50% of the clones were eliminated due to lack of expression in BL21 cells (data not shown). The expressing clones were each purified on a small scale and screened for their capacity to bind laforin by a pulldown method using affinity resin.

To identify nanobodies that form a stable complex with laforin, the ability of purified nanobodies to be precipitated by laforin affinity resin was assessed. Laforin coupled resin was incubated individually with each of the purified VHH clones, the resin was washed, and bound proteins were eluted and analyzed by SDS-PAGE. This primary screen identified six clones as having direct antigen binding (**Figure 4.2A**).

The six identified anti-laforin nanobodies are: Nb40, Nb41, Nb50, Nb57, Nb72, and Nb73. Based on phylogenetic analysis and sequence alignment (**Figures 4.1** and **Figure 4.2B**), the six identified nanobodies that bind laforin exhibit sequence diversity and contain five different CDR3 regions. Complete DNA sequences of the six laforin nanobodies are provided in **Table 4.1**.

### 4.3.2 *Size-exclusion analysis of anti-laforin nanobodies complexed to laforin*

Size-exclusion chromatography (SEC) was utilized to detect and characterize the laforin-nanobody complexes. Each nanobody was incubated with laforin in ~10% molar excess, samples were subjected to SEC, fractions were collected, and analyzed by SDS-PAGE (**Figure 4.3**). The laforin-nanobody complexes eluted between 12.11-14.51 mL, laforin alone eluted at 15.40 mL, and the nanobodies alone eluted between 18.08-19.53 mL. All six laforin-nanobody complexes eluted prior to laforin or the nanobody alone, indicating a higher molecular weight and supporting the results of the primary screen. Similarly, SDS-PAGE analyses of the fractions demonstrate co-elution of the laforin-nanobody complexes. Nb40 and Nb73 complexed with laforin eluted earlier than others (**Figure 4.3**). These supershifted complexes may indicate an increase in nanobody to laforin stoichiometry. Alternatively, Nb40 and Nb73 may interfere with the laforin CBM binding to the carbohydrate-based resin. Laforin CBM mutations have been shown to interrupt this interaction and change the elution time<sup>291</sup>.

### **4.3.3 Nanobody epitope mapping via Hydrogen-Deuterium Exchange Mass Spectrometry (HDX)**

Epitope mapping can be accomplished using hydrogen-deuterium exchange (HDX) mass spectrometry. HDX quantifies protein surfaces that are solvent accessible. When a nanobody binds a protein, the surface of the protein becomes less solvent accessible. This decrease in solvent accessibility can be quantified by HDX.

Each laforin-nanobody complex and laforin alone were incubated in deuterated buffer for 10, 100, 1,000, and 10,000 seconds (**Figures 4.4** and **4.7**). A decrease in laforin deuteration ( $\geq 15\%$  decrease in deuteration compared to WT) emerged with Nb40 and Nb41 (**Figures 4.4A** and **4.7A**), Nb50 and Nb57 (**Figures 4.4B** and **4.7B**), and Nb72 and Nb73 (**Figures 4.4C** and **4.7C**). Nb40 and Nb41 differ by only one amino acid within CDR2, with an alanine in Nb40 replaced with a valine in Nb41. Given this high degree of sequence similarity, their shared epitope was expected. Their epitope partially maps across the CBM (residues 60-66, 120-124, and 126-129) with the majority spanning across the recognition domain of the DSP (residues 139-145, 148-161, 163-169, and 171-186). The epitope of Nb41 extends further on the DSP (residues 193-197). Sequence homology between Nb40 and Nb41 is 99.2% (**Figure 4.8**). Nb50 and Nb57 share a similar epitope that encompasses most of the CBM (residues 30-33, 35-41, 43-52, 60-66, 120-124) and partially across the DSP (residues 287-291). Nb57 extends further on the CBM (residues 43-56, 58-66, and 126-129). Sequence homology between Nb50 and Nb57 is 66.2% (**Figure 4.8**). Nb50 and Nb57 share a partial CBM epitope with Nb40 and Nb41. The DSP epitope of Nb40 and Nb41 partially overlaps with Nb72 and Nb73. The epitopes of Nb72 and Nb73 are mapped solely on the DSP and overlap with the recognition domain (residues 139-145, 148-155, 193-197, 236-242). Importantly, Nb72 includes the PTP-loop (residues 267-275). Intriguingly, the sequence homology between Nb72 and Nb73 is 70.6% and no sequence homology exists between their CDR3 regions (**Figure 4.8**).

These results indicate that three general binding regions exist among the six laforin nanobodies. Nb40 and Nb41 span both the CBM and DSP on the opposite side of the DSP active site (**Figures 4.4D** and **4.7D**). Nb50 and Nb57 span the CBM, partially covering regions that bind glycogen (**Figures 4.4E** and **4.7E**). Nb72 and Nb73 bind a region near the DSP active site and Nb72, but not Nb73, overlaps with the PTP-loop (**Figures 4.4F** and **4.7F**).

### **4.3.4 Nb72 inhibits the general phosphatase activity of laforin**

Given the binding site of Nb72, we predicted that this nanobody would decrease or inhibit the phosphatase activity of laforin. To assess laforin's general phosphatase activity, we utilized the phosphatase substrate *para*-nitrophenyl phosphate (pNPP). Protein tyrosine phosphatases, including laforin, can convert pNPP to *para*-nitrophenyl

(pNP) that results in a colorimetric change that can be quantified at OD<sub>410</sub>. Three concentrations of recombinant laforin were incubated with a respective and ~1:1 molar ratio of nanobody Nb72 or Nb23, a nanobody that did not co-precipitate with laforin (**Figure 4.2A**) As controls, recombinant laforin was also pre-incubated in buffer lacking a nanobody, and nanobodies were tested in the absence of laforin. The pNPP substrate was added to each combination using previously defined optimal conditions, reactions were quenched with sodium hydroxide, and dephosphorylation levels were quantified at OD<sub>410</sub>. Laforin incubated with Nb23 yielded similar levels of pNPP dephosphorylation as laforin alone, indicating that Nb23 did not inhibit laforin phosphatase activity (**Figure 4.5A**). Conversely, laforin incubated with Nb72 displayed a dramatic 85% reduction in pNPP phosphatase activity (**Figure 4.5A**).

#### **4.3.5 Nb72 inhibits the glycogen phosphatase activity of laforin**

The small molecule pNPP is a readout for general phosphatase activity. However, pNPP can integrate into the DSP active site independent of the laforin CBM to be converted into pNP. In cells, laforin binds glycogen via its CBM and engages the phospho-glucose substrate with its DSP active site to dephosphorylate the substrate. Therefore, we sought to determine if Nb72 binding to laforin inhibits its specific glucan phosphatase activity.

Glycogen dephosphorylation can be assessed by quantifying phosphate release using a malachite gold colorimetric assay. Three concentrations of recombinant laforin were incubated with nanobody Nb72 or the negative control nanobody Nb23 in a respective and ~1:1 molar ratio. As a control, recombinant laforin was also pre-incubated in buffer lacking a nanobody. Then, rabbit skeletal muscle glycogen was added as the substrate using previously defined optimal conditions. Reactions were incubated at 20° C for 30 min and then quenched with the phosphatase inhibitor N-ethylmaleimide. Malachite gold solutions were added, and dephosphorylation levels were quantified at OD<sub>635</sub>. Laforin incubated with Nb72 yielded a dramatic 95% reduction in laforin's glycogen phosphatase activity while Nb23 did not reduce the activity (**Figure 4.5B**). No other nanobody showed a robust inhibitory effect on laforin's phosphatase activity towards amylopectin (**Figure 4.9**).

Laforin's endogenous substrate is glycogen<sup>86,272,292</sup>. However, laforin has a higher binding affinity for LBs<sup>222,293</sup>. While glycogen is water-soluble, the glucose chains of LBs are longer and predicted to form helical structures making LBs more water-insoluble<sup>20,104,273</sup>. Plant amylopectin is also a water-insoluble glucan that has covalently attached phosphate and has been utilized as a LB proxy<sup>20,86,292,294</sup>. Therefore, we performed a similar assay as above utilizing malachite gold, laforin, and the nanobodies with amylopectin as the substrate. Overall, laforin released ~10-fold more phosphate from amylopectin than glycogen, which is as expected given the higher level of phosphate in amylopectin<sup>105,295</sup>. Nb72 was observed to significantly inhibit laforin phosphatase activity by 55% against amylopectin (**Figure 4.5C**). These data further

strengthen a growing body of results suggesting that laforin has a higher degree of binding and/or activity towards insoluble substrates.

## 4.4 Discussion

The glycogen phosphatase laforin is critical for brain glycogen metabolism. Mutations in the laforin gene promote the formation of cytoplasmic, insoluble glycogen-like aggregates that are the pathological agent of LD<sup>46,49,118,272</sup>. The mechanism by which laforin influences the solubility of glycogen is still unknown, and progress in this discovery could be accelerated with additional tools. The current study showcases the generation of six laforin nanobodies, mapping of the nanobody epitopes by HDX, and three *in vitro* assays demonstrating that nanobody Nb72 inhibits laforin's phosphatase activity.

HDX nanobody epitope mapping revealed that one nanobody, Nb72, decreased deuterium exchange within the laforin PTP-loop, implying that Nb72 could inhibit the laforin phosphatase activity. Three *in vitro* phosphatase activity assays established that binding Nb72 to laforin markedly reduces the phosphatase activity of laforin. The first assay employed a non-specific substrate, *para*-nitrophenyl phosphate (pNPP), to assess the inhibitory activity of Nb72. The pNPP assay quantifies laforin phosphatase activity independent of glycogen binding. Nb72 decreased laforin phosphatase activity by 85%. Using more biologically relevant substrates, we discovered that Nb72 diminishes laforin phosphatase activity against skeletal muscle glycogen by 95%, and amylopectin by 55%. Thus, Nb72 is more effective at inhibiting laforin's phosphatase activity directed towards glycogen. These data are consistent with published reports demonstrating that laforin preferentially binds more water-insoluble substrates like amylopectin and LBs<sup>222,296</sup>. The reason for this preference has been proposed to be that the CBM domain has an enhanced contribution to phosphatase activity as the carbohydrate increases in complexity and/or insolubility<sup>294</sup>. Laforin is dramatically stabilized in the presence of a longer chain length oligosaccharide compared to a shorter chain length oligosaccharide. Further, the presence of the longer chain length oligosaccharide promotes cooperativity in binding between the dimers of laforin that is not observed with a shorter chain length sugar substrate<sup>276</sup>. These data are further supported by our findings that more phosphate is released from amylopectin than glycogen in the presence of laforin. The ~10-fold difference in phosphate release can be accounted for by the ~10-fold difference in total phosphate contained in amylopectin versus glycogen. Glycogen contains 1 phosphate per 1,000-10,000 glucose residues and amylopectin contains 1 phosphate per ~300 glucose residues<sup>89,106,258,294,297,298</sup>.

Nanobodies are a rapidly growing technology that are being utilized in novel ways to refine a wide variety of traditional techniques such as crystallization chaperoning, affinity purification, immunoprecipitation, super-resolution microscopy, confocal microscopy, flow cytometry, cell delivery, radiolabeling, and modulating protein function and interactions in cells<sup>299,300</sup>. An immediate opportunity to utilize the laforin nanobodies is with respect to modulating laforin's phosphatase activity, glycogen binding, and interactions. Nb72 clearly inhibits the glycogen phosphatase activity of laforin *in vitro*. Nb50 and Nb57, CBM-binding nanobodies, may modulate laforin's



catalytic activity (**Figure 4.9**) by altering carbohydrate binding in cell culture. These nanobodies could be expressed in cells as intrabodies to probe the relationship between glycogen phosphate with glycogen metabolism, central carbon metabolism, and metabolic signaling events without imposing structural mutations to laforin.

Another opportunity to use the laforin nanobodies is protein crystallography. The only full-length laforin structure to date is the catalytically inactive human Laforin-C266S<sup>276</sup>. While this structure has provided key insights, as described above, a structure of the wildtype and patient mutations is needed to fully define the catalytic cycle and resolve why laforin mutations cause LD. This work has been hampered due to the extensive conformational dynamics of laforin. Crystallizing laforin with the nanobodies could permit capturing additional conformational states<sup>299</sup> that are important for its biological function. Additional panning of the nanobody library using either laforin mutants with distinct conformational states or laforin bound to substrate or partner protein could allow identification of additional unique conformation-specific nanobodies.

Multiple groups have demonstrated that laforin and malin physically interact and form a complex<sup>301</sup>. Additionally, the *in vivo* function of laforin likely includes a sophisticated scaffolding and/or signaling role because multiple studies have found that laforin interacts with several glycogen metabolism related proteins<sup>86,116,117</sup>. In fact, many laforin protein interactions are both involved in glycogen metabolism and are putative substrates of malin, including the protein phosphatase 1 regulatory subunits GL, R5 and R6/PTG; glycogen synthase, the pyruvate kinase isoforms PKM1 and PKM2; and AMP-activated protein kinase  $\beta$  subunits<sup>49,111,301,302</sup>. Due to these interactions, the laforin-malin complex has been suggested to participate in protein degradation, oxidative stress, and the unfolded protein response<sup>117</sup>. Therefore, LD pathology could arise from mutations that affect the specific activity of laforin and/or malin, and also from mutations that impair the interaction of both proteins to form a complex.

Moreover, laforin has potentially pleiotropic roles associated with dynamic cellular localization changes<sup>303,304</sup>. Laforin has been shown to translocate to the nucleus under nutrient or heat stress and can return to the cytoplasm once the stress conditions cease<sup>50</sup>. Interestingly, malin has recently been shown to ubiquitinate glycogen phosphorylase and translocate it to the nucleus thereby promoting nuclear glycogen catabolism. The released glucose 1-phosphate is utilized for histone acetylation to regulate transcriptional profiles<sup>114</sup>. Therefore, the nuclear localization of malin and, under certain conditions, of laforin suggests a regulatory function of both proteins in the nucleus. Furthermore, a natural mutation in laforin causes it to lose ER localization<sup>303</sup>. Fluorescent nanobody fusions, sometimes called chromobodies, are useful markers to track and visualize dynamic changes without disturbing other cellular functions<sup>279,305–307</sup>. To date, most assays detecting laforin localization have probed for a tagged version of laforin that is often over-expressed<sup>50</sup>. Anti-laforin nanobodies as intrabodies and/or chromobodies could be useful tools for defining both laforin dynamic localization and physical interactions. Overall, these nanobodies represent an important set of tools that will open new avenues to illuminate the mechanism of laforin's role in normal glycogen metabolism and LD.

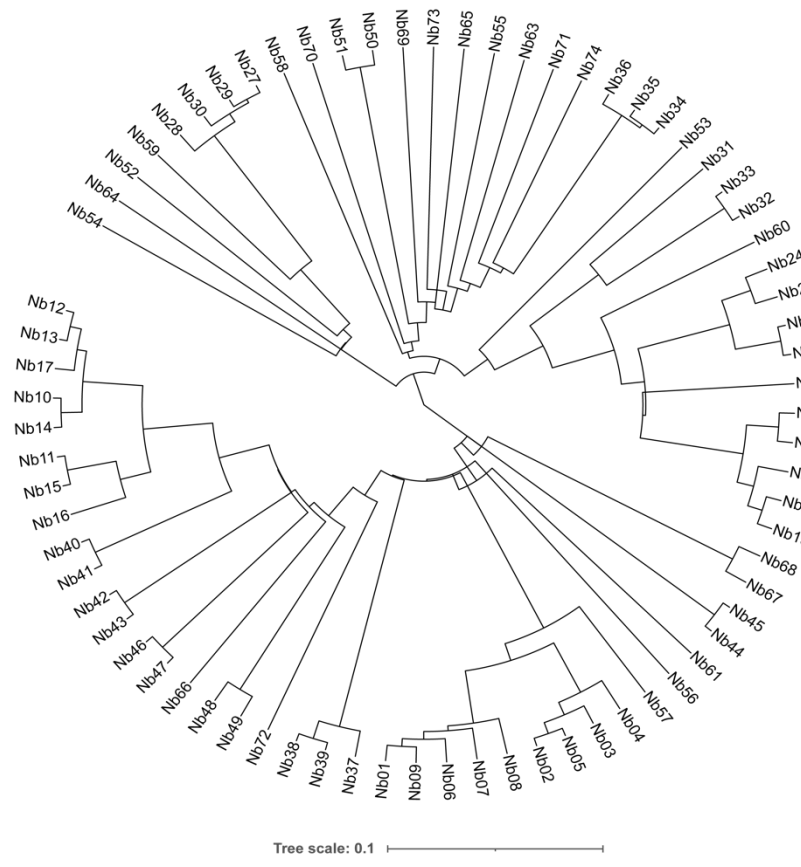


**Figure 4.1 Anti-laforin nanobody guide tree.**

A binary tree was generated from a sequence alignment and subsequent tree generation of the 74 generated laforin nanobody clones using Clustal-Omega.

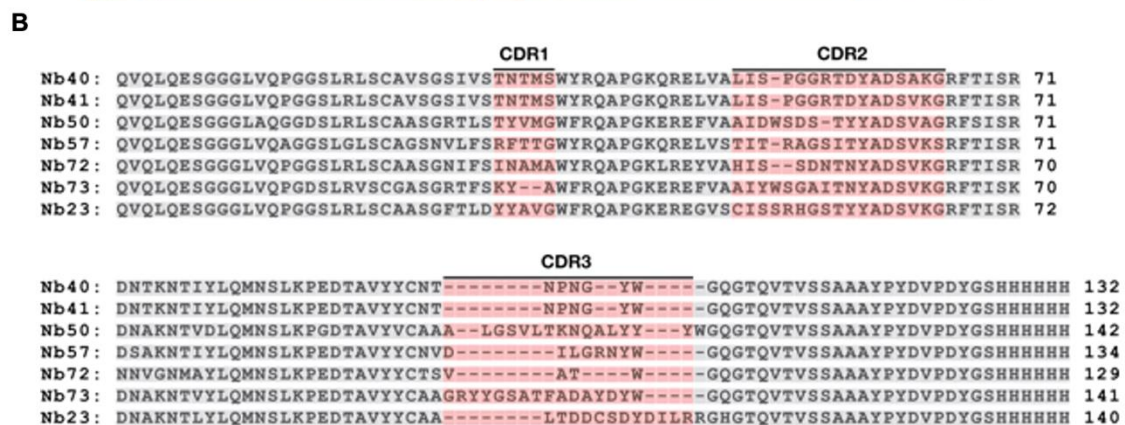
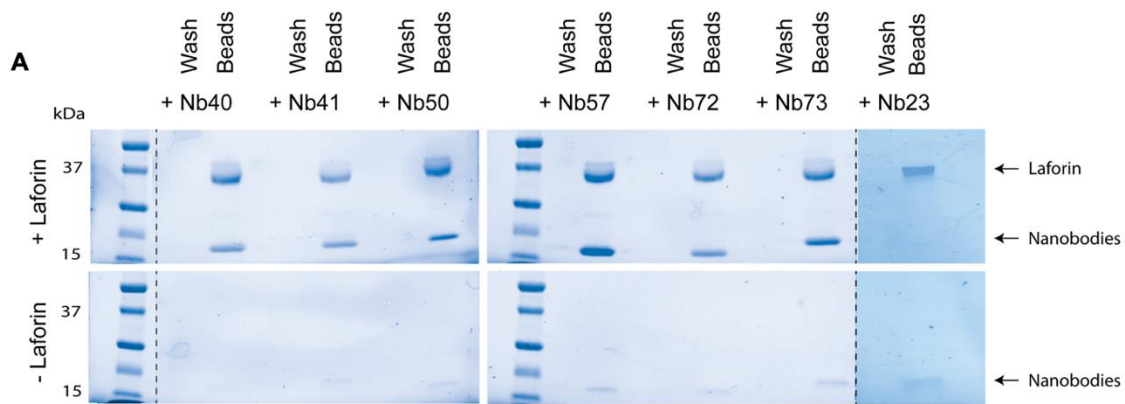


**Figure 4.2 Direct antigen binding nanobodies and comparison of their sequences.** (A) Primary screening for nanobody binding was achieved by incubating laforin with affinity resin, washing the resin, blocking the resin with TBS, incubating the laforin bound affinity resin with a nanobody, and washing the resin before the laforin-nanobody complex was eluted. Free (wash) and bead bound laforin and/or nanobody was loaded onto an SDS-PAGE stain-free gel and imaged (top). As a control, affinity resin without bound laforin was blocked and then incubated with nanobody (bottom). (B) Sequence alignment of nanobodies in A. Sequence homology is 55.9% identical. Complementary determining regions are highlighted in red and framework regions are highlighted in gray (Kabat).

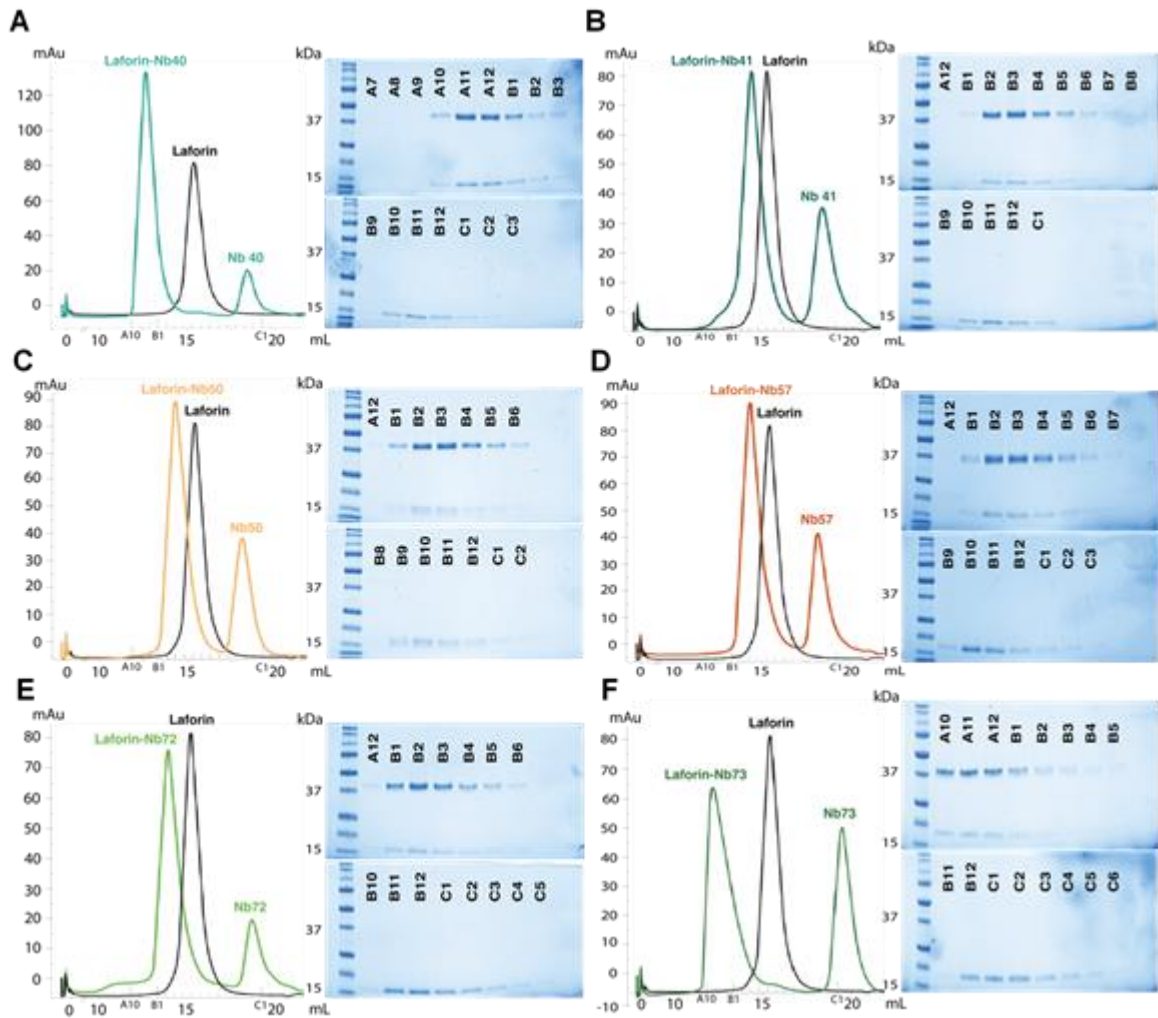


**Figure 4.3 Size-exclusion (SEC) analysis of anti-laforin nanobodies complexed to laforin.**

For each SEC analysis of the laforin-nanobody complex, the respective fractions are visualized by an SDS-PAGE stain-free gel shown to the right. **A-F)** SEC analysis of the laforin dimer alone is shown in black (15.4mL). **A)** Nb40 (18.45mL) complexed to laforin in light teal (12.65mL). **B)** Nb41 (18.58mL) complexed to laforin in dark teal (14.51mL). **C)** Nb50 (18.08mL) complexed to laforin in light orange (14.28mL). **D)** Nb57 (18.19mL) complexed to laforin in dark orange (14.3mL). **E)** Nb72 (18.89mL) complexed to laforin in light green (14.12mL). **F)** Nb73 (19.53mL) complexed to laforin in dark green (12.11mL).

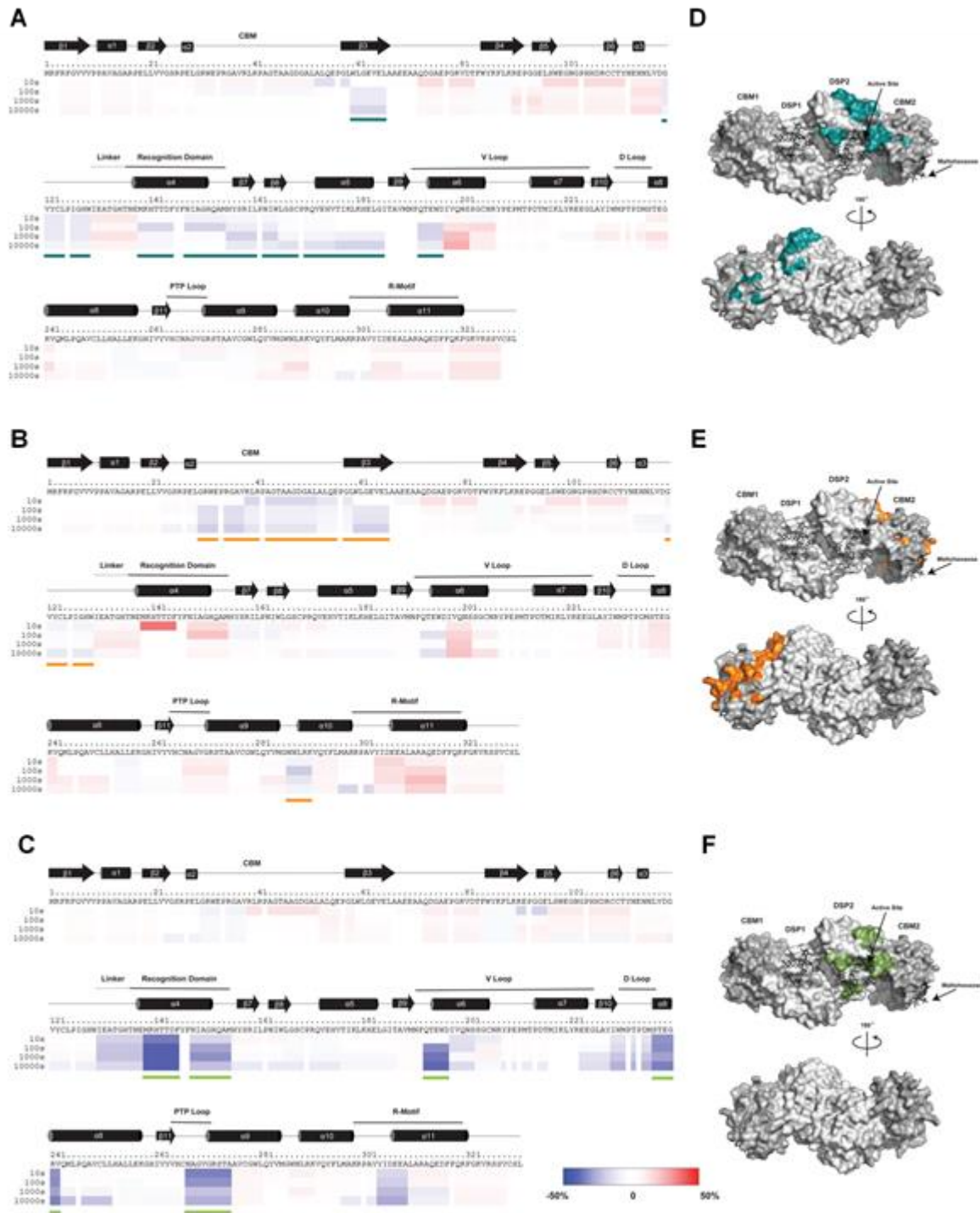


**Figure 4.4 HDX analysis of anti-laforin nanobody binding of Nb41, Nb57, and Nb72.**

Fractions of each nanobody bound to laforin (Figure 4.3) were analyzed by hydrogen deuterium exchange mass-spectrometry (HDX) and the deuteration level was compared to laforin alone. The percent difference in deuteration between the nanobody complex versus laforin alone is represented with a negative percent change in blue to a positive percent change in red. Each colored bar below the primary sequence represents percent change in deuteration at one of four time points. Secondary structure elements are depicted above the primary sequence with the CBM and DSP motifs labeled. Regions where the nanobody caused a  $\geq 15\%$  change in deuteration are highlighted with a colored line. **A)** The Nb41 epitope on laforin spans  $\beta 3$ ,  $\beta 7$  and  $\beta 8$  sheets,  $\alpha 4$ ,  $\alpha 5$ , and partially  $\alpha 6$  helices. Highlighted with a dark teal line. **B)** The Nb57 epitope on laforin includes the  $\beta 3$  sheet and partially covers the  $\alpha 10$  helix. Highlighted with a dark orange line. **C)** The Nb72 epitope on laforin covers the  $\alpha 4$  helix, and partially spans the  $\alpha 6$ ,  $\alpha 8$ , and  $\alpha 9$  helices. Highlighted with a light green line. **D-F)** The identified epitope for each nanobody was modeled onto the surface map of the laforin structure (PDB: 4RKK). Nb41 (dark teal), Nb57 (dark orange), and Nb72 (light green) respectively mapped on laforin. The CBM and DSP of laforin are colored dark gray and light gray respectively.

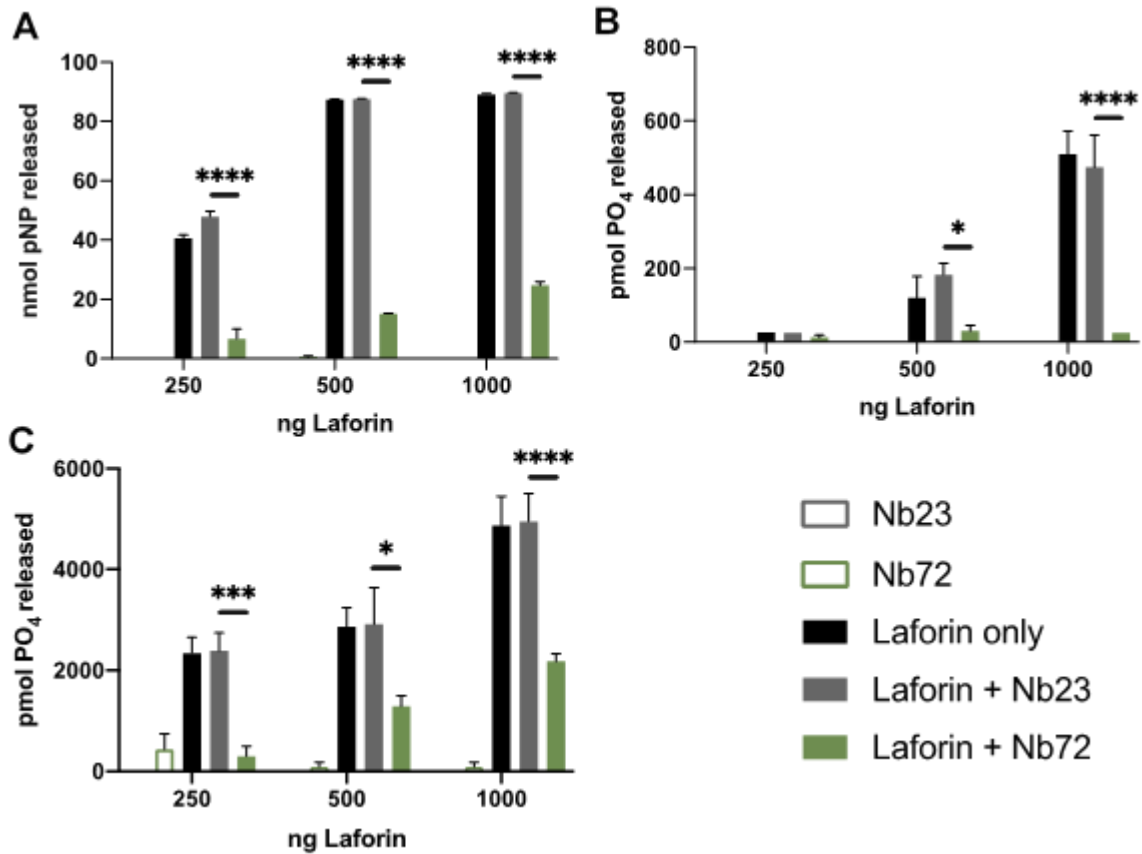


**Figure 4.5 Laforin activity in the presence of Nb72.**

**A)** The specific activity of laforin against pNPP in the presence and absence of nanobodies. **B)** The specific activity of laforin against rabbit skeletal muscle glycogen in the presence and absence of nanobodies. **C)** The specific activity of laforin against potato amylopectin in the presence and absence of nanobodies. Each bar is the mean  $\pm$ SEM of 4 replicates. \*  $p < 0.0301$ , \*\*\*  $p = 0.0007$ , \*\*\*\*  $p < 0.0001$ .

Table 4.1 DNA sequences of the six laforin binding nanobodies.

<p><b>Nb40</b></p>	<p>CAGGTGCAGCTGCAGGAGTCTGGGGGAGGCTTGGTGCAGCCTGGGGGGTCTCTGAGACTCTCCTGTGCAGTCTCTGGAAGCATCGTCAGTACGAATACTATGAGCTGGTACCGCCAGGCTCCAGGGAACAGCGCGAGTTGGTCGCACCTTATTTGCCTGGTGGTAGGACAGACTATGCAGACTCCGCGAAGGGCCGATTACCATCTCCAGAGACAACACCAAGAACACGATTTATCTCAAATGAACAGCCTGAAGCCTGAGGACACGGCCGTCTATTACTGTAATACTAATCCTAACGGCTACTGGGGCCAGGGGACCCAGGTCACCGTCTCCTCAGCGGCCGCATACCCGTACGACGTTCCGGACTACGGTTCACCACCACCATCACCATCACTAG</p>
<p><b>Nb41</b></p>	<p>CAGGTGCAGCTGCAGGAGTCTGGGGGAGGTTTGGTGCAGCCTGGGGGGTCTCTGAGACTCTCCTGTGCAGTCTCTGGAAGCATCGTCAGTACGAATACTATGAGCTGGTACCGCCAGGCTCCAGGGAACAGCGCGAGTTGGTCGCACCTTATTTGCCTGGTGGTAGGACAGATTATGCAGACTCCGTGAAGGGCCGATTACCATCTCCAGAGACAACACCAAGAACACGATTTATCTCAAATGAACAGCCTGAAGCCTGAGGACACGGCCGTCTATTACTGTAATACTAATCCTAACGGCTACTGGGGCCAGGGGACCCAGGTCACCGTCTCCTCAGCGGCCGCATACCCGTACGACGTTCCGGACTACGGTTCACCACCACCATCACCATCACTAG</p>
<p><b>Nb50</b></p>	<p>CAGGTGCAGCTGCAGGAGTCTGGGGGAGGATTGGCGCAGGGTGGGGACTCTCTGAGACTCTCCTGTGCAGCTCTGGACGCACCTTAAGTACGTATGTCATGGGCTGGTTCCGCCAGGCTCCAGGGAAGGAGCGTGAATTTGTAGCAGCTATTGACTGGAGTGATAGCACATAATTATGCAGACTCCGTGGCGGGCCGATTACCATCTCCAGGAGACAACGCCAAGAACACGGTGGATCTGCAAATGAACAGCCTGAAACCTGGGGACACGGCCGTTTATGTCTGTGACAGCAGCTTTAGGGTCTGTACTAACGAAGAATCAAGCCCTGTATTACTACTGGGGCCAAGGGACCCAGGTCACCGTCTCCTCAGCGGCCGCATACCCGTACGACGTTCCGGACTACGGTTCACCACCACCATCACCATCACTAG</p>
<p><b>Nb57</b></p>	<p>CAGGTGCAGCTGCAGGAGTCTGGAGGAGGCTTGGTGCAGGCTGGGGGGTCTCTAGGACTCTCCTGTGCAGGCTCTAACGTACTCTTCAGTCGCTTTACCACGGCTGGTACCGCCAGGCTCCAGGGAAGCAGCGCGAATTGGTCTCAACGATTACTCGTGCGGGTAGTATAACGTATGCAGACTCCGTGAAGAGCCGATTACCATCTCACGAGACAGCGCCAAGAACACGATTTATCTGCAAATGAACAGCCTGAAACCTGAGGACACGGCCGTCTATTACTGTAATGTGGATATATTAGGCCGGAACACTACTGGGGCCAGGGGACCCAGGTCACCGTCTCCTCAGCGGCCGCATACCCGTACGACGTTCCGGACTACGGTTCACCACCACCATCACCATCACTAG</p>
<p><b>Nb72</b></p>	<p>CAGGTGCAGCTGCAGGAGTCTGGGGGAGGCTTGGTGCAGCCTGGGGGGTCTTTGAGACTTTTCTGTGCAGCTCTGGAATATCTTCAGTATCAATGCCATGGCCTGGTACCGACAGGCTCCAGGGAACAGCGCGAGTATGTCGCACATATTTCTAGTGATAACACAAACTATGCAGACTCCGTGAAGGGCCGATTACCATCTCCAGAAACAAACGTCGGGAATATGGCGTATCTGCAAATGAACAGCCTGAAACCTGAAGACACAGCCGTCTATTATTGTACATCTGTGCGAACCTGGGGCCAGGGGACCCAGGTCACCGTCTCCTCAGCGGCCGCATACCCGTACGACGTTCCGGACTACGGTTCACCACCACCATCACCATCACTAG</p>
<p><b>Nb73</b></p>	<p>CAGGTGCAGCTGCAGGAGTCTGGGGGAGGCTTGGTGCAGCCTGGGGACTCTCTAAGAGTTTCTGTGGAGCTCTGGACGCACCTTCAGTAAATATGCTTGGTTCCGCCAGGCTCCAGGGAAGGAGCGTGAGTTTGTGTCAGCTATTTACTGGAGTGGTGTCTATTACGAACATGCGGACTCCGTGAAGGGCCGATTACCATCTCCAAAGACAACGCCAAGAACACGGTGTATCTGCAGATGAACAGCCTGAAACCTGAGGACACGGCCGTTTATTACTGTGAGCCGGCCGATACTATGGTAGTGCTACCTTCGCGGATGCATATGACTATTGGGGCCAGGGGACCCAGGTCACCGTCTCCTCAGCGGCCGCATACCCGTACGACGTTCCGGACTACGGTTCACCACCACCATCACCATCACTAG</p>







**Figure 4.7 HDX analysis of anti-laforin nanobody binding of Nb40, Nb50, and Nb73.**

Fractions of each nanobody bound to laforin (Figure 4.3) were analyzed by hydrogen deuterium exchange mass-spectrometry (HDX) and the deuteration level was compared to laforin alone. The percent difference in deuteration between the nanobody complex versus laforin alone is represented with a negative percent change in blue to a positive percent change in red. Each colored bar below the primary sequence represents percent change in deuteration at one of four time points. Secondary structure elements are depicted above the primary sequence with the CBM and DSP motifs labeled. Regions where the nanobody caused a  $\geq 15\%$  change in deuteration are highlighted with a colored line. **A)** Laforin-Nb40 epitope spans  $\beta 3$ ,  $\beta 7$  and  $\beta 8$  pleated sheets and  $\alpha 4$  and  $\alpha 5$  helices. Highlighted with a light teal line. **B)** Laforin-Nb50 epitope includes the  $\beta 3$  pleated sheet and partially covers the  $\alpha 10$  helix. Highlighted with a light orange line. **C)** Laforin-Nb73 epitope covers the  $\alpha 4$  helix, and partially covers the  $\alpha 6$  and  $\alpha 8$  helices. Highlighted with a dark green line. **D-F)** The identified epitope for each nanobody was modeled onto the surface map of the laforin structure (PDB: 4RKK). Nb40 (light teal), Nb50 (light orange), and Nb73 (dark green) respectively mapped on laforin. The CBM and DSP of laforin are colored dark gray and light gray respectively.

```

                                CDR1                                CDR2
Nb40: QVQLQESGGGLVQPGGSLRLSCAVSGSIVS TNTMSWYRQAPGKQRELVALISPGGRTDYADSAKGRFTISR 71
Nb41: QVQLQESGGGLVQPGGSLRLSCAVSGSIVS TNTMSWYRQAPGKQRELVALISPGGRTDYADSVKGRFTISR 71
*****

                                CDR3
Nb40: DNTKNTIY LQMNSLKPEDTAVYYC NTNPNGYWGQGTQVTVSSAAAYPYDVPDYGSHHHHHH 132
Nb41: DNTKNTIY LQMNSLKPEDTAVYYC NTNPNGYWGQGTQVTVSSAAAYPYDVPDYGSHHHHHH 132
*****

                                CDR1                                CDR2
Nb50: QVQLQESGGGLAQGGDSLRLS CAASGR TLS TYVMGWFRQAPGKERE FVA AIDWSDSTYYADSVAGRFSISR 71
Nb57: QVQLQESGGGLVQAGGSLGLSCAGSNVLF SRFTTGWYRQAPGKQRELVS TITRAGSITYADSVKSRFTISR 71
*****

                                CDR3
Nb50: DNAKNTVDLQMNLSLKPEDTAVYYCAA ALGSVLTKNQALYYWGQGTQVTVSSAAAYPYDVPDYGSHHHHHH 142
Nb57: DSAKNTIY LQMNSLKPEDTAVYYC NVDIL-----GRNYWGQGTQVTVSSAAAYPYDVPDYGSHHHHHH 134
*****

                                CDR1                                CDR2
Nb72: QVQLQESGGGLVQPGGSLRLS CAASGN IFS INAMAWYRQAPGKLREYVAHIS--SDNTNYADSVKGRFTISR 70
Nb73: QVQLQESGGGLVQPGDSLRLVSCGASGR TFS --KYAWFRQAPGKERE FVA AIYWSGAITNYADSVKGRFTISK 70
*****

                                CDR3
Nb72: NNVGNMAYLQMNLSLKPEDTAVYYCTS -----VATWGQGTQVTVSSAAAYPYDVPDYGSHHHHHH 129
Nb73: DNAKNTVY LQMNSLKPEDTAVYYCAA GRYYSATFADAYDYWGQGTQVTVSSAAAYPYDVPDYGSHHHHHH 141
*****

```

**Figure 4.8 Anti-laforin nanobody sequence alignments.**

Sequence homology between Nb40 and Nb41 is 99.2%, Nb50 and Nb57 is 66.2%, and Nb72 and Nb73 is 70.6% (Clustal-Omega). CDRs highlighted in red, framework highlighted in gray.

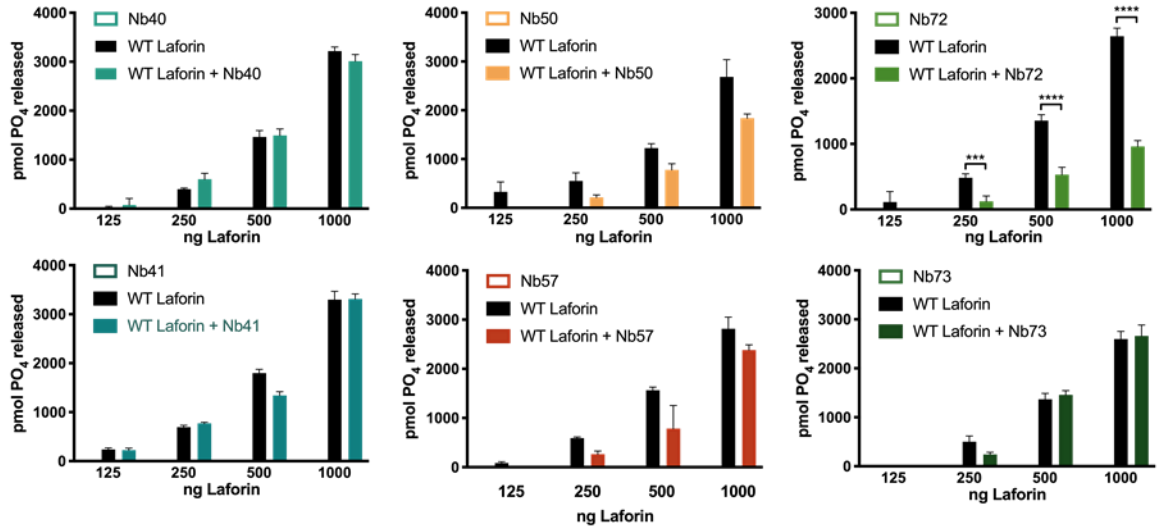


**Figure 4.9 Laforin-nanobody activity assays.**

The specific activity of laforin against potato amylopectin in the presence and absence of nanobodies. Only Nb72 inhibits laforin's phosphatase activity. Each bar is the mean ±SEM of 4 replicates. \*\*\*\* p < 0.0001.



## 5.1 Introduction

Over 8,000 rare genetic diseases have been described and most are without therapeutic options<sup>308</sup>. Underlying ~12% of rare genetic disease mutations are nonsense mutations/STOP mutations/premature termination codons (PTCs)<sup>309</sup>. PTC mutations transcribed in frame into mRNA result in truncated protein translation<sup>310</sup>. Excitingly, repurposed small molecules have shown promising results in correcting PTC mutations to generate full-length proteins<sup>311,312</sup>.

The first pharmaceutical agents tested to suppress PTC mutations therapeutically were aminoglycosides (AGs)<sup>313</sup>. AGs are primarily used as antibacterial agents that inhibit bacterial protein synthesis<sup>314</sup>. Translational inhibition occurs because AGs prevent ribosome mRNA translocation by binding the 50S ribosomal subunit and the bacterial aminoacyl site of the 16S ribosomal mRNA. In eukaryote cells, AGs do not inhibit translation and can promote misincorporation of near-cognate aminoacyl-tRNA at the site of the PTC mutation<sup>310,315</sup>. Therefore, AGs can promote full length translation of PTC mutated mRNA. The precise mechanism of PTC readthrough is not yet well understood. However, a recent study indicated that geneticin (G418), the best characterized PTC readthrough AG, may interfere with tRNA due to tight binding of the ribosome's decoding center, like that observed for bacterial ribosomes<sup>316</sup>.

AGs have been tested for their ability to promote readthrough in over 100 tissue-culture and mouse models for multiple diseases, including Duchenne Muscular Dystrophy (DMD) and Cystic Fibrosis (CF)<sup>317</sup>. These studies demonstrated that AGs like G418 and gentamicin can promote readthrough of the PTC mutations, however, their clinical application is limited due to ototoxicity and contribution to superbug evolution. Therefore, the application of AGs is better suited for proof-of-concept experiments *in vitro*.

The search for non-toxic, well-characterized compounds that safely confer readthrough activity in humans led to the first bench to bedside translation of a PTC readthrough therapy. The non-aminoglycoside molecule ataluren (PTC124) produced full readthrough of the most common PTC mutation found in patients with DMD and is approved for clinical use by the European Commission<sup>318</sup>. However, The Food and Drug Administration denied approval for PTC124 in the United States because the provided data, including a safety evaluation, was inadequate<sup>319</sup>. Interestingly, the mechanism of action for PTC124 is suggested to diverge from G418 and is derived exclusively from its ability to inhibit release factor activity<sup>316</sup>. Unfortunately, a recent meta-analysis of PTC124 clinical trials in DMD patients determined that PTC124 provided only a mild slowing of DMD disease progression compared with placebo<sup>320</sup>. Furthermore, PTC124 has not yet proven to be an effective readthrough drug for any other genetic disease.

These outcomes have been attributed to the repeated finding that nucleotide sequence regulates suppression of PTCs and no one drug suppresses two PTCs to the same extent<sup>321</sup>. Further, no algorithms can predict how the genetic context influences the readthrough ability of a given PTC. The CF field recently discovered the readthrough properties of escin, a non-toxic herbal supplement, by using an enzymatic assay to screen 1600 small molecules<sup>311</sup>. Therefore, the development of a high throughput drug screening approach designed for discovering PTC specific readthrough compounds among clinically approved drug libraries may be required to achieve therapeutic and translational potential.

An ideal disease to develop a PTC readthrough high throughput screening assay is one that is monogenetic where mutations result in aberrant protein function that drive disease. Lafora disease (LD) is an autosomal recessive childhood dementia resulting from mutations in the *Epm2a* gene<sup>322,323</sup>. *Epm2a* mutations, of which 15% are PTCs, result in the loss-of-function of laforin, the glycogen phosphatase<sup>324</sup>. Sequence and structural conservation classifies laforin in the protein tyrosine phosphatase superfamily and the dual specificity phosphatase clade<sup>274</sup>. Laforin is the only known human glycogen phosphatase and is comprised of a dual-specificity phosphatase (DSP) domain and a carbohydrate binding module (CBM)<sup>274</sup>. Laforin loss-of-function results in the production of aberrant glycogen-like aggregates in the cytoplasm called Lafora bodies (LBs)<sup>81,324</sup>. The LBs are found in the cytoplasm of cells from most tissues, including patient skin biopsies and post-mortem brain tissue<sup>80</sup>. Using multiple mouse and fly models, independent investigators have determined that LBs drive pathophysiology<sup>25,26,28,81</sup>. No treatment exists for this fatal disease, but recent pre-clinical work suggests that rescuing normal laforin expression leads to the ablation of LBs<sup>325,326</sup>. Thus, rescuing laforin expression may be an attractive avenue for therapeutic development.

In this study, we explored three cell culture approaches for screening the readthrough efficiencies of small molecules against the 12 clinically known *Epm2a* PTC mutations. We generated a Western blot assay, an enzymatic assay, and a laforin nanobody-based ELISA to test readthrough. Using these assays, we tested gentamicin, G418, and escin for readthrough. PTC124 was excluded from this study as prior work determined that it was unsuccessful at promoting readthrough of *Epm2a* PTC mutations. The Western blot and enzymatic assay are widely used low-throughput approaches for PTC readthrough screening that we modified for *Epm2a*<sup>309–312,322,323</sup>. The results of these screens proved that gentamicin and G418 can induce readthrough of *Epm2a* PTC mutations *in vitro*. However, they are limited in their potential to be adapted for high throughput screening due to demanding technical requirements.

For a third screening approach with potential for scale, we designed a novel nanobody based sandwich ELISA. Nanobodies are antibodies naturally produced the camelid family<sup>327</sup>. Nanobodies consist of a single monomeric variable domain (VHH) with a complete antigen binding site. Nanobodies can be readily selected and produced in *E. coli*, ensuring their supply and consistent quality<sup>328</sup>. In contrast to conventional antibodies, nanobodies are exceptionally stable, withstanding fluctuations in temperature and pH<sup>281,282</sup>. These advantages make nanobodies ideal for high throughput use and clinical environments. Using alpaca (*Vicugna pacos*)

generated nanobodies raised against human recombinant laforin, we developed highly specific monoclonal antibodies to replace the polyclonal anti-laforin antibodies currently used to isolate laforin<sup>329</sup>. Our nanobody based ELISA system is a unique readthrough screening system in which full-length laforin, but not truncated laforin, can be detected by a CBM binding anti-laforin nanobody. This same system can be used to determine phosphatase activity by interchanging the addition of the CBM binding detection nanobody with the phosphorylated substrate *para*-nitryl phenyl phosphate. Therefore, the nanobody based ELISA readthrough screening system has two possible outputs, quantitation of laforin full length translation and resulting phosphatase activity. The laforin nanobody ELISA may be a scalable option for high throughput analysis of *Epm2a* readthrough drugs.



## 5.2 Methods

### 5.2.1 cDNA generation and sequencing

Primary fibroblasts were grown using Fibrolife S2 Cell Culture Medium supplemented with Fibrolife S2 Lifefactors LS-1038 (Lifeline Cell Technology). 1% Penstrep was substituted for gentamicin for suppression of bacterial growth. To extract genomic DNA, 20  $\mu$ l of ThermoPol Buffer (New England Biolabs) was added to the samples, boiled for 5 min and digested with Proteinase K (10 mg/mL) for 2 h at 55°C. Then, Proteinase K was inactivated by boiling for 10 min. Total RNA was isolated using PureZOL/Aurum Total RNA Isolation Kit (Bio-Rad) according to the manufacturer's instructions. The RNA quality for RNA-seq was tested using an Agilent Bioanalyzer 2100. Quantitative RT-PCR was performed using SoAdvanced SYBR<sup>®</sup> Green supermix. The cDNA and a 207 bp sequence of the genomic DNA was amplified using PCR. PCR was carried out in a 25  $\mu$ l reaction solution containing 1  $\mu$ l of 10 mM dNTP, 1  $\mu$ l of 10 mM forward and reverse primer, 2.5  $\mu$ l of 1 $\times$  ThermoPol Buffer (New England Biolabs), and 0.5 units of Pfu Polymerase (New England Biolabs). Amplicons were purified and subcloned into a pJET1.2/blunt vector using the CloneJET PCR Cloning Kit (ThermoFisher Scientific). Plasmids were transformed into *E. coli* and the DNA was sequenced.

### 5.2.2 Reporter plasmid cloning

Three sets of reporter plasmids were generated for this study. For the enzyme assays, complementary oligonucleotides were generated, annealed, and ligated into a pAC99 reporter plasmid, as previously described<sup>323</sup>. This plasmid contains a unique Msc1 cloning site between *lacZ* and *luc* genes coding for  $\beta$ -galactosidase and luciferase, respectively.  $\beta$ -galactosidase and luciferase coding sequences are separated by an in-frame stop codon corresponding to the mutation found in a patient, flanked by four codons in 5' and 3', respectively.

The reporter plasmids generated for the Western blots were generated using site directed mutagenesis to insert an *Epm2a* PTC mutation into WT laforin cDNA flanked by a 5' Flag tag and 3' Myc tag. Each mutated amplicon was inserted into a pcDNA 3.1+ Amp/Zeocin cloning plasmid (ThermoFisher Scientific) using the BamHI and NotI restriction sites. Because the Flag and Myc tags could interfere with laforin nanobody capture and detection in the ELISA screening system, a similar set of plasmids without tags was created. PCR amplification of the previously generated PTC mutated laforin cDNA was inserted into a pcDNA 3.1+ Amp/Zeocin (ThermoFisher Scientific) cloning plasmid using the BamHI and NotI restriction sites.

### **5.2.3 Cell culture transfections and drug treatments**

HEK293 cells were grown in DMEM (ThermoFisher Scientific) containing 10% fetal bovine serum. Reporter plasmids were transfected for 24 h using FuGene according to the manufacturer's instructions. For drug treatments, 2 mL of multiple concentrations of Geneticin (G418), Gentamicin, or 0.04% DMSO in media was added per well of a 6-well plate and left to incubate overnight (~24 h). Cells were harvested using trypsin, prepared for Western blots or ELISAs, and flash frozen. Cells harvested for Western blots were lysed in RIPA buffer (0.5% deoxycholate, 1% IGEPAL-CA630, 0.1% sodium dodecyl sulfate, 150 mM NaCl, 50 mM Tris-8.1). Cells harvested for ELISAs were lysed in PLC-lysis buffer (50 mM Tris pH 7.4, 150 mM NaCl, 10% (v/v) glycerol, 1% (v/v) NP-40, 1 mM EGTA, 10 mM NaPP<sub>i</sub>, 100 mM NaF<sub>i</sub>, supplemented with protease inhibitor cocktail).

For the enzymatic assays, HeLa cells were seeded in the wells of 6 well plates and left to grow overnight (~24 h). Then, 3 h before transfection, the cell medium was removed, and 2 mL of fresh medium was added. During the 3 h incubation, the transfections were prepared using 18 µL at 1 µg/µL of DNA in 600 µL of NaCl and vortexed. In a separate tube, 36 µL of JetPei in 600 µL of NaCl was mixed by vortexing. Then, the JetPei mixture was added to the DNA mixture and incubated for 30 min at RT. Next, 200 µL of the transfection mixture was added to each well of the 6-well plate. Because the precipitate can be toxic to these cells, transfections were performed close to the end of the day and cell treatment was performed in the morning ~16 h later. Drug treatment consisted of aspirating the media from the 6-well plates and adding 2 mL of either 2.5 mM Gentamicin, 2.5 mM Geneticin, 10 µM Escin, or 0.4% DMSO in media and incubating overnight (~24 h). Finally, the cells were harvested by trypsin and added to respective epi-tubes for enzyme assay preparation.

### **5.2.4 SDS-PAGE and Western Blot**

Protein concentrations were determined using the Pierce BCA Protein Assay Kit (Thermo Scientific 2327) according to the manufacturer's protocol. Sodium dodecyl sulfate polyacrylamide gel electrophoresis (SDS-PAGE) and Western blots were run using TGX stain free pre-case 12% gels (Bio-Rad). Western transfers were performed using a semidry turbo-transfer system onto PVDF membranes (Bio-Rad). The membranes were blocked with 5% nonfat milk and probed with primary antibodies [mouse anti-FLAG M2 (Sigma-Aldrich) and rabbit anti-MYC (Origene)] at a 1:1000 dilution. The membranes were incubated with the secondary antibodies [goat anti-rabbit IgG, HRP-linked antibody and goat anti-mouse IgG, HRP-linked antibody (Invitrogen)] at a 1:3000 dilution. The membranes were developed using chemiluminescence followed by fluorescence. Gels and membranes were imaged on a ChemiDoc MP imaging system (BioRad).

### 5.2.5 Enzyme assays

Luciferase was assayed by following the protocol of Nguyen, with a Berthold LUMAT LB 95501 luminometer for light detection<sup>330</sup>. Chloramphenicol acetyltransferase (CAT) activity was determined in accordance with the two-phase partition method<sup>331</sup>.  $\beta$ -galactosidase was assayed in accordance with the classical method of Miller<sup>332</sup>.

### 5.2.6 Laforin purification

*H. sapiens* (Hs) laforin residues 1–328 was expressed from pET28b (Novagen) as an N-terminal His6 tagged protein, as previously described<sup>329</sup>. Briefly, laforin was expressed in BL21 (DE3) (Novagen) *E. coli* cells grown in 2xYT media at 37°C until OD<sub>600</sub> = 0.6, culture flasks were placed on ice for 20 min, induced with 1 mM (final) isopropyl thio- $\beta$ -D-galactopyranoside (IPTG), grown for an additional 14 h at 20°C, and harvested by centrifugation. Cells were resuspended and lysed in buffer A (20 mM Tris-HCl, 100 mM NaCl, 10% glycerol, 2 mM DTT, pH 7.5), centrifuged, and the proteins were purified using a Profinia immobilized metal affinity chromatography (IMAC) column with Ni<sup>2+</sup> beads (Bio- Rad) and a Profinia protein purification system (Bio-Rad) using wash (buffer A) and elution buffer (300 mM imidazole, 20 mM Tris-HCl, 100 mM NaCl, 10% glycerol, 2 mM DTT, pH 7.5). The desalted elution fraction was further purified using fast protein liquid chromatography (FPLC) with a HiLoad 16/60 Superdex 200 size exclusion column (GE Healthcare). Laforin was purified in 20 mM Tris-HCl, 100 mM NaCl, 10% glycerol, 2 mM DTT, pH 7.5).

### 5.2.7 Nanobody purification and HRP-conjugation

Nanobodies were purified as previously described<sup>329</sup>. Nanobodies were expressed in BL21 (DE3) *E. coli* cells grown in 2xYT at 37°C to OD<sub>600</sub> = 0.9. 15 mL of pre-culture was used per L culture. Cultures were induced with 1 mM IPTG (final) and incubated for ~16–18 h at 25°C after which, pellets were harvested by centrifugation. Nanobodies were purified from the *E. coli* pellets with Ni-NTA resin. *E. coli* cell lysates were centrifuged to separate soluble protein which was incubated with Ni-NTA agarose beads for 1 h at 4°C in 30 mL bind buffer (20 mM Tris- Hcl, 100 mM NaCl, 15 mM imidazole, pH 8.0). The samples were washed three times in bind buffer and eluted in 300 mM imidazole, 100 mM NaCl, pH 8.0. Eluted samples were separated from the Ni-NTA beads by filtering through a 25 mM syringe filter and then buffer exchanged with 20 mM Tris-Hcl pH 7.5, 100 mM NaCl using FPLC with a HiLoad 16/60 Superdex 75 column (GE Healthcare). Nanobodies being screened for their use as detection nanobodies were conjugated to HRP (Abcam) according to the manufacturer's protocol.

### **5.2.8 Enzyme-Linked Immunosorbent Assay (ELISA)**

Wells of a Corning 9018 96-well plate were incubated with 100  $\mu$ L of capture nanobody (Nb41) overnight (~16 h) at a final concentration of 0.18  $\mu$ L/mL in 1X Tris-buffered saline (TBS) at 4 °C with a plate cover. Wells were then rinsed three times with 200  $\mu$ L 1X TBS followed by incubation for 1 h with 200  $\mu$ L of blocking solution (1% BSA in 1X TBS) at RT followed by wells being rinsed three times with 200  $\mu$ L 1X TBS. The sample (100  $\mu$ L; recombinant *H. sapiens* (Hs) laforin 329X or whole cell lysate diluted to 100  $\mu$ L in 1X TBS, 1mM DTT) was added and incubated for 1 h at RT, the wells were rinsed three times with 200  $\mu$ L of 1X TBS, and 100  $\mu$ L of primary HRP-conjugated nanobody was added in 1X PBS in 1% BSA, 1mM DTT and incubated for 1 h at RT. The wells were then washed three times with 200  $\mu$ L TBS and 100 of TMB substrate (Thermo Fisher) was added and developed according to the manufacturer's instructions. The reaction was terminated by adding 100 of stopping solution (0.18 M H<sub>2</sub>SO<sub>4</sub>). Absorbance was quantified at 450 nm using a BioTek Epoch2 microplate reader. To quantify the saturation curves for putative capture nanobodies bound to the plate, the anti-Camelid IgG, HRP-linked antibody was used at a 1:5000 dilution and developed using TMB substrate (Thermo Fisher).

### **5.2.9 *para*-Nitrophenyl phosphate (pNPP) assay**

Generic phosphatase activity assays were performed using *para*-nitrophenyl phosphatase (pNPP) as previously described<sup>329</sup>. Assays were performed using 96 well plates in 50  $\mu$ L containing 1X phosphatase buffer (0.1 M sodium acetate, 0.05 M Bis-Tris, 0.05 M Tris- HCl, pH 5.0), 2 mM dithiothreitol (DTT), and 50 mM pNPP). Wells of a 96-well plate were incubated capture nanobody (Nb41) overnight (~16 h), rinsed three times with 1X TBS, by incubating with blocking solution (1% BSA in 1X TBS) at RT, followed by wells being rinsed three times with 200  $\mu$ L 1X TBS. 100  $\mu$ L recombinant laforin in 1X TBS, 1mM DTT was added and incubated for 1 h at RT, the wells were rinsed three times with 200  $\mu$ L of 1X TBS, and 100  $\mu$ L of 1X phosphatase buffer containing 50mM pNPP was added to the wells and incubated in a 30°C water bath for 10 min. The reaction was terminated by the addition of 100  $\mu$ L of 1 M NaOH.

## 5.3 Results

### 5.3.1 PTC mutations in *Epm2a*

An important consideration before developing PTC readthrough screening assays is whether the PTC in question is transcribed in frame into mRNA. PTC mutations located near splice sites may not be transcribed in frame and instead result in alternatively spliced mRNA or trigger nonsense mediated decay of the pre-mRNA transcript<sup>333</sup>. These PTC mutations are not candidates for readthrough therapy.

Twelve *Epm2a* LD PTC mutations have been reported with R241X being the most common mutation in LD (**Figure 5.1A** and **Table 5.1**)<sup>81,296,334–339</sup>. The point mutation underlying R241X is a g.113165 C>T mutation that results in a premature TGA stop codon (**Figure 5.1A** and **Table 5.1**). The C>T point mutation is located three nucleotides from the 5' end of the fourth exon and not predicted to trigger nonsense mediated decay, which typically requires a PTC to be at least 50-55 nucleotides upstream of an exon-exon junction (**Figure 5.1A**)<sup>333</sup>. However, the C>T placement could induce variance in pre-mRNA splicing. To assess whether the g.113165 C>T mutation is transcribed in frame, we obtained primary skin fibroblasts from a patient homozygous for g.113165 C>T. After confirming the genetic mutation by gene sequencing, we performed an RNA prep from the same primary fibroblasts followed by RT-PCR to determine in frame transcription (**Figure 5.1B-C**). The cDNA was isolated and sequenced to determine that the R241X mutation is not alternatively spliced and results in the c.721 C>T point mutation (**Figure 5.1C**). This result implies that the resulting translated protein will be truncated at R241 and the R241X *Epm2a* PTC mutation is a candidate for readthrough therapy.

### 5.3.2 A Western blot assay for screening PTCs

A traditional approach for determining readthrough expression involves overexpressing PTC mutated cDNA in HEK293 cells, incubating the cells with a readthrough drug, and determining total expression levels via Western blot analysis. To adapt this system for *Epm2a* R241X, we utilized the *MeCP2* R294X PTC mutation implicated in Rett syndrome as an experimental control. Readthrough expression of *MeCP2* R294X has been previously shown using gentamicin<sup>340</sup>. Thus, two similar plasmids were made, one containing *MeCP2* R294X cDNA and the other containing *Epm2a* R241X cDNA, each joined to a 5' Flag-tag sequence. A third construct was made in the same way, except it contained the WT *Epm2a* cDNA. The WT cDNA allowed us to control for change in translation levels independent of readthrough. After incubating the HEK293 cells with increasing concentrations of gentamicin (0-3.5 mM), cells were harvested, total protein extracts were generated, and WBs were performed to detect the Flag-tag. We determined that readthrough expression of both *Epm2a* and *MeCP2*

increases in concentration, while WT laforin levels do not change (**Figure 5.2A**). These are encouraging results, but not definitive results of readthrough as they do not normalize for basal levels of readthrough. Additionally, aminoglycosides have been shown to stabilize PTC mutated mRNA, potentially promoting variation in mRNA stability between the WT and PTC targets analyzed<sup>310</sup>.

Therefore, we generated a dual reporter system also detectable by Western blot. The benefit of a dual gene reporter system is that both reporter proteins are expressed from the same mRNA, eliminating potential variation in mRNA stability between the different targets. We developed this system by flanking the PTC mutated *Epm2a* cDNA by a 5' Flag-tag and a 3' Myc-tag. HEK293 cells were transfected with 2 µg/mL of DNA and incubated with 0-2 mM G418 for 24 hr. Cells were harvested, total protein extracts were generated, and WBs were performed to detect the Flag- or Myc-tag. After overexpression of the test plasmid in HEK293 cells and incubation with G418, we ran a Western blot and detected the Flag-tag with a fluorescent secondary antibody, and the Myc-tag with a chemiluminescent secondary antibody (**Figure 5.2B**). Thus, translation levels of the truncated laforin peptide are detected by the anti-Flag antibody and readthrough is measured by the anti-Myc antibody on the same blot. As expected, Western blot analysis indicated that WT expression levels as detected by either anti-Flag or anti-Myc are not changed with increasing concentrations of G418. Conversely, increased expression of the R241X mutated cDNA is detected by the anti-Myc antibody at 1 mM G418 indicating readthrough. Using the anti-Flag antibody, we also observed increased expression of laforin at 1 mM G418. Furthermore, we detected a protein with at 29 kD upon G418 addition. This protein may be the result of expression of the truncated form of laforin R241X, which is calculated to have a molecular weight of 29 kD. Interestingly, higher concentrations of G418 did not result in readthrough. This result is likely explained by the fact that G418 is often used as a cell selection reagent and high concentrations of G418 can compromise cell vitality. This result supports the notion that the toxicity of G418 limits its use to preliminary pre-clinical studies in low doses. These data suggest that the Flag/Myc reporter system is useful as a readthrough screening system. However, due to Western blot limitations, like technical demand, time, and off-target antibody detection, this screening assay is not practical for a quick and streamlined analysis of readthrough compound libraries.

### **5.3.3 An enzymatic assay for screening PTCs**

To examine readthrough across the 12 *Epm2a* PTC mutations, we employed a widely cited cell culture-based assay optimized for higher throughput compared to Western blot analysis<sup>309–312,322,323</sup>. The basic mechanics of this assay involve the overexpression of a plasmid containing two enzyme reporter genes, *LacZ* and *Luc*, that flank a 9-codon sequence containing a PTC mutation at codon 5 (**Figure 5.3**). This plasmid is transfected into HeLa cells, optimal for their fast growth, that are then incubated with a readthrough drug. When partial protein expression is generated in the cells, the 5' reporter gene, *LacZ*, will express β-galactosidase attached to the partial protein

sequence. If readthrough of the PTC mutation occurs, then the full dual reporter fusion protein will be expressed containing an N-terminal  $\beta$ -galactosidase and the C-terminal luciferase (expressed from *luc*), linked together by the 9 amino acid protein sequence. Therefore, readthrough efficiency is estimated by normalizing luciferase activity to  $\beta$ -galactosidase activity.

HeLa cells were transfected with 1  $\mu\text{g}/\mu\text{L}$  of DNA and incubated with each 0.04% DMSO, 2.5 mM gentamicin, 2.5 mM G418, or 10  $\mu\text{M}$  escin for 24 hours. Cells were harvested and added to respective epi-tubes for enzyme assay preparation. Using the enzymatic assay, we first determined the readthrough expression of each of the 12 *Epm2a* PTC mutations, grouped by PTC codon, using 2.5 mM gentamicin versus DMSO. There was an increase in expression for all of the mutants with W165X, R241X, and E158X expression being statistically significant with gentamicin versus DMSO. These results indicated that gentamicin could produce readthrough of each *Epm2a* PTC mutations to varying degrees above the DMSO control with a 2-6-fold increase observed (**Figure 5.4A-B**). Interestingly, there was some level of readthrough for each of the mutants in the presence of DMSO, indicating basal readthrough, with R241X exhibiting the highest level of basal readthrough in this system (**Figure 5.4A**). This result is encouraging because basal readthrough levels are suggested in the literature to be an indicator of best responders to drug induced readthrough<sup>323</sup>. Additionally, R241X is the most common LD mutation. Next, we tested G418 to establish its usefulness as a positive control, and escin as a possible clinically relevant drug candidate. G418 typically produced readthrough expression levels higher than that of gentamicin (**Figure 5.5A**). Like gentamicin, G418 yielded statistically significant readthrough in W165X, R241X, and E158X as well as two additional PTCs, W287X, E138X. These results demonstrate that G418 is a more potent readthrough compound than gentamicin for the *Epm2a* mutations and align with published reports testing G418 on other genes<sup>316</sup>. For both AGs, *Epm2a* TAG mutations yielded the highest level of readthrough and TGA the lowest (**Figure 5.4A, 5.5A**). In contrast, escin did not produce readthrough expression above basal DMSO-treated levels (**Figure 5.5B**). Therefore, gentamicin and G418, but not escin, can be used to promote readthrough of *Epm2a* PTCs in cell culture.

Commercial gentamicin is not a pure compound and is majorly composed of gentamicins C1, C1a, C2, and C2a constituting 92–99% of the mixture. Of the minor components, gentamicin B constitutes 0.8–5.3%, and C2b between 1.3–2.1%. Occasionally, sisomisin is found, comprising only 0.4–0.6%. Additionally, gentamicin A and X2 (also known as gentamicin X) together comprise between 1.1–7.8%. Other components in the complex include gentamicin B1 and garamine. Recent work showed that despite gentamicin X2 and B1 being minor components they are potent readthrough inducers<sup>341,342</sup>. Since their levels can vary by lot, this variation may impact readthrough expression. To determine the effect of drug batch on readthrough variability we tested 9 batches of gentamicin on the R241X mutation. HeLa cells were transfected with 1  $\mu\text{g}/\mu\text{L}$  of DNA and incubated with each 0.04% DMSO, 2.5 mM G418, or 2.5 mM gentamicin from 9 different batches for 24 hours. Cells were harvested and added to respective epi-tubes for enzyme assay preparation. While there was some minor readthrough variation, there was no significant differences of induced

readthrough between batches (**Figure 5.6**). Thus, despite some variability, lot should not greatly affect the accuracy of readthrough measurements.

Lastly, we considered the role of cell type on readthrough expression variability. While HeLa cells are more optimal for higher throughput screening than slower growing cells like NIH3T3 or HEK293, HeLa cells may not necessarily be optimal for highest expression of readthrough. HeLa, NIH3T3, or HEK293 cells were transfected with 1  $\mu\text{g}/\mu\text{L}$  of DNA and incubated with each 0.04% DMSO, or 2.5 mM gentamicin. Cells were harvested and added to respective epi-tubes for enzyme assay preparation. Interestingly, gentamicin promoted statistically significant readthrough of R241X in HeLa and NIH3T3 cells but the increased readthrough in HEK293 cells was not statistically significant (**Figure 5.7A-C**). These results suggest that HeLa cells in comparison to NIH3T3 or HEK293 are an optimal cell line because they grow faster and can yield statistically significant effects of readthrough. The enzymatic assay established *in vitro* proof that readthrough of all 12 *Epm2a* PTC mutations is possible. However, the technical requirements, though easier than Western blot analysis, are still too time consuming and prone to human error for efficient screening of large drug libraries.

#### **5.3.4 A nanobody based ELISA screening approach**

We recently developed six laforin nanobodies and characterized their binding affinity and the laforin epitope. The six laforin nanobodies were categorized into three groups that shared epitopes. One epitope spans both the CBM and DSP on the opposite side of the DSP active site and is bound by nanobodies 40 and 41 (Nb40 and Nb41). The second epitope spans the CBM, partially covering regions that bind glycogen and is bound by nanobodies 50 and 57 (Nb50 and Nb57). The third epitope overlaps with a region near the laforin DSP active site, and is bound by nanobodies 72 and 73 (Nb72 and Nb73), but only Nb72 inhibits laforin phosphatase activity<sup>329</sup>. Based on these known epitopes, we hypothesized that a pair of nanobodies could be used to generate a sandwich ELISA for detecting and quantifying laforin readthrough.

We first determined the optimal plate saturation concentrations of the nanobodies that primarily bind the DSP. We excluded the use of Nb72 since it inhibits laforin enzymatic activity and we wanted to use phosphatase activity as a potential readout. Therefore, we examined Nb40, Nb41, and Nb73. We first plated 100  $\mu\text{L}$  per well of increasing concentrations of Nb40 (0–30  $\mu\text{g}/\text{mL}$ ), Nb41 (0–70  $\mu\text{g}/\text{mL}$ ), and Nb73 (0–150  $\mu\text{g}/\text{mL}$ ) and detected the saturation curves with an HRP conjugated anti-Camelid antibody, developed using TMB substrate and read at OD<sub>450</sub> using a microplate reader. The results indicated that Nb40, Nb41, and Nb73 each displayed a different pre-saturating concentration of 3  $\mu\text{g}/\text{mL}$ , 8  $\mu\text{g}/\text{mL}$ , and 11  $\mu\text{g}/\text{mL}$ , respectively (**Figure 5.8A-C**). To determine which of these nanobodies was useful as a capture nanobody, we tested each nanobody by plating the respective pre-saturating concentration and subsequently binding 100  $\mu\text{L}$  of increasing concentrations (0–20  $\mu\text{g}/\text{mL}$ ) of purified recombinant human laforin. As a readout of laforin phosphatase activity, we incubated laforin with the generic phosphatase substrate, *para*-nitrophenyl phosphate and



performed pNPP assays. Protein tyrosine phosphatases, including laforin, can convert pNPP to *para*-nitrophenyl (pNP) and the colorimetric change is quantified at OD<sub>410</sub>. By performing pNPP assays, Nb41 was identified as a useful capture antibody that allows the DSP of laforin to remain active (**Figure 5.8D**, data not shown for Nb40, and Nb73)). The linear range of captured laforin was within the known linear range of detection by the pNPP assay. Based on the pNPP assay results, the saturation concentration of recombinant laforin is 20 µg/mL.

We then determined which CBM binding nanobody was most optimal for laforin detection. In each well, we plated 100 µL of Nb41 at 8 µg/mL and bound 100 µL purified recombinant human laforin at 20 µg/mL. After washing, capture nanobody saturation curves were generated using increasing concentrations of Nb50, or Nb57, at 0–2 µg/mL each conjugated to HRP (**Figure 5.8E-F**). Wells were then washed and developed using TMB substrate and read at OD<sub>450</sub> using a microplate reader. Nb57-HRP exhibited a robust saturation curve with a higher specificity than Nb50-HRP (**Figure 5.8E-F**). Pre-saturating concentrations were indicated to be 0.18 µg/mL for Nb57-HRP and 1 µg/mL for #113.

Currently, the polyclonal anti-laforin antibody #113 is utilized to immunoprecipitate laforin as it demonstrated the most robust ability to capture laforin from cell lysate<sup>290</sup>. We sought to determine whether Nb57-HRP provided higher specificity than polyclonal anti-laforin antibody #113. To generate and compare the saturation curves using Nb57-HRP and #113, we plated 100 µL of Nb41 at 8 µg/mL and bound 100 µL purified recombinant human laforin at 20 µg/mL. After washing, we bound of 100 µL of Nb57-HRP at 0.18 µg/mL, or 100 µL of #113 at 1 µg/mL (**Figure 5.9A-B**)<sup>343</sup>. Bound #113 was subsequently washed and bound with a secondary antibody. A

After washing the Nb57-HRP bound and #113 and secondary bound plates, the assays were developed using TMB substrate and read at OD<sub>450</sub> using a microplate reader. Comparing the standard curves generated by Nb57-HRP or #113, Nb-57-HRP signals appeared in closer alignment with the four-parameter logistic (FPL) model. Thus, the monoclonal Nb57-HRP detected laforin with higher specificity than the polyclonal anti-laforin antibody.

To determine the assay efficiency, the percent recovery of Nb57-HRP was determined by generating a 22-point standard curve of recombinant laforin and analyzing the linear range using a four-parameter logistic (FPL) model (**Figure 5.10A-B**). 100 µL of Nb41 at 8 µg/mL was plated and bound 100 µL purified recombinant human laforin at 20 µg/mL. After washing, 100 µL of Nb57-HRP at 0.18 µg/mL was bound. A second wash performed before the assays was developed using TMB substrate and read at OD<sub>450</sub> using a microplate reader. The FPL model was selected because it provides a better fit (percent recovery) to all of the data compared to linear models, even under circumstances where the linear model lack-of-fit value ( $R^2$ ) is equal or greater than 0.99<sup>344</sup>.

$$Y = \text{top} + \frac{\text{bottom} - \text{top}}{1 + \left(\frac{x}{\text{EC}_{50}}\right)^{\text{slope}}}$$

In the FPL mode, Y is the output value, absorbance in this case, which is 450 nm for the pNPP assay. “Top” is the upper asymptote and “bottom” is the lower asymptote. X is the concentration of recombinant laforin in the well, EC<sub>50</sub> is the concentration with 50% maximum response, and slope is the Hill coefficient. Evaluation of the percent recovery of each point with the concentration calculated by the FPL curve established that the lowest concentration measured within 20% of the FPL curve and that is significantly higher than background, which is 2 µg/mL recombinant laforin (**Figure 5.10A-B**). The upper limit is 10 µg/mL, indicating that the range for accurate quantification of laforin is between 20-1000 ng (**Figure 5.10A**).

A final experiment concluded preliminary development of the nanobody-based laforin ELISA for the purpose of screening laforin PTC readthrough. Plasmids containing WT *Epm2a*, R241X *Epm2a* or an empty vector were transfected into HEK293 cells. After transfection, whole cell lysates were then prepared using native PLC-lysis buffer. Increasing concentrations of whole cell lysates were incubated in the wells of a 96-well plate saturated with Nb41. Subsequent detection of laforin was performed using 0.18 µg/mL of Nb57-HRP (**Figure 5.11**). The signal of WT laforin detection exceeded the signal produced in the wells containing laforin R241X or empty vector by 10-fold. Therefore, these data indicate that this nanobody based ELISA may be used to screen readthrough of R241X *Epm2a*.

## 5.4 Discussion

To date, more than 100 studies have shown that the stimulation of PTC readthrough may result in the partial restoration of the expression of deficient proteins that underlie ~40 different genetic diseases<sup>317</sup>. However, no study has demonstrated a remarkable improvement in patient health or a significant alleviation of the disease phenotype. The establishment of a truly efficient PTC readthrough based therapy requires new, more potent compounds with less toxicity. This goal may be achieved by scanning drug libraries to repurpose and/or modify compounds to achieve efficient nonsense suppression. To effectively implement this strategy, high throughput testing is needed to screen drugs against specific PTC mutations.

LD is an ideal disease to model a high throughput screening approach for PTC readthrough as PTC mutations in a single gene result in loss-of-function at the protein level that directly causes LD pathophysiology<sup>25,26,28,81</sup>. Furthermore, a simple and cost-effective *in vitro* assay has been previously developed to establish the presence or absence of glucan phosphatase activity<sup>290</sup>. To explore high throughput assay development for *Epm2a* PTCs we first adapted two traditional low-throughput screening approaches, a Western blot assay and an enzymatic assay, to test two AGs and the non-toxic herbal anti-inflammatory compound escin, that had been reported to promote readthrough in some systems, to establish a proof-of-concept for *Epm2a* readthrough. Using these dual gene reporter assays we determined that readthrough is possible for all 12 *Epm2a* PTC mutations using gentamicin. Gentamicin and G418 are the most commonly used pre-clinical aminoglycosides in PTC readthrough studies, with G418 promoting readthrough at lower concentrations and higher efficiencies than gentamicin and other aminoglycosides such as amikacin, paromomycin, and tobramycin<sup>321</sup>. As expected, G418 proved to be a more potent readthrough compound for *Epm2a* PTCs than gentamicin and may serve as a robust positive control for future studies.

A known factor of readthrough efficiency variation is the PTC mutation and surrounding nucleotide sequence<sup>321</sup>. Though there is no absolute rule to predict PTC mutation readthrough efficiencies, TAA are often reported as the PTC mutations most recalcitrant to readthrough, followed by TGA with TAG exhibiting the highest level of readthrough<sup>315,323</sup>. For the *Epm2a* PTC mutations, TAG mutations yielded the highest level of readthrough and TAA the lowest. Interestingly, *Epm2a* PTC readthrough in TGA and TAA PTCs using either gentamicin or G418 was more frequent. Therefore, the surrounding *Epm2a* nucleotide context may be uniquely modulating ease of readthrough. TGA and TAA PTC mutations exhibited higher readthrough by gentamicin than TAG. These results are inconsistent with other disease models and suggest that the surrounding nucleotides may be a more important factor in modulating PTC readthrough. Encouragingly, the TGA mutation R241X, the most common mutation in LD, shows a significant amount of basal readthrough, which has prevalue for its potential to be readthrough by small molecules.

Using the dual reporter enzymatic assay, all 12 PTC mutations were screened for readthrough with three compounds and a control and analyzed within the span of 15 days. Therefore, this enzymatic assay proved to be higher throughput than the Western blot assay. As a dual reporter assay, the enzymatic assay provides similar benefits as the Western blot but is a much more quantitative approach. The fluorescent nature of the internal control ( $\beta$ -galactosidase) permits accurate calibration of individual experiments for the overall expression level of each construct (vector stability, transfection efficiency, transcriptional and translation rates). However, limitations still exist in this assay as luciferase was shown to have off-target interactions with small molecules. Thus, the possibility of readthrough drug interaction and attenuation of excitation or emission light is an important consideration with this assay. A more ideal screening method would include the benefits of a fast-growing cell culture system, a dual reporter system, and an absence of off target drug interaction.

To generate the proof-of-concept for a such an approach, we generated a novel nanobody based ELISA. We used previously generated anti-laforin nanobodies to construct an ELISA that can capture laforin without inhibiting its phosphatase activity and subsequently detect the full-length product. With nanobody epitopes previously defined, we chose a pair of nanobodies with different binding sites, such that the capture nanobody (Nb41) binds the DSP, and the detection nanobody (Nb57) binds the CBM<sup>329</sup>. We first developed a recombinant laforin standard curve by capturing with Nb41 and detecting with Nb57-HRP. We also determined that the generic phosphatase activity of recombinant laforin captured by Nb41 can be tested using *para*-nitrophenyl phosphate in a pNPP assay. These results provided the proof-of-concept that laforin recovered from cell lysate or human tissue may be quantified and assessed for phosphatase activity in parallel assays. To test the laforin nanobody ELISA using whole cell lysate, we used Nb41 to capture laforin from cell culture previously overexpressed with WT laforin, laforin R241X, or EV. We discovered the encouraging results that Nb57-HRP can detect WT laforin at 10-times the concentration found in the cell lysates compared to empty vector. Importantly, Nb57-HRP does not detect the truncated laforin peptide generated from transcribing laforin R241X in the absence of readthrough compounds. These data suggest that the overexpressed truncated form has competed for binding to Nb41 but is not subsequently detected by Nb57-HRP because it lacks a CBM. These results suggest that the nanobody based ELISA using Nb41 and Nb57-HRP can be used to detect readthrough of R241X.

Continued development of our nanobody based ELISA screening strategy is needed to verify this hypothesis. Theoretically, the combination of Nb41 and Nb57-HRP should be able to detect the full readthrough products of any laforin PTC mutation. However, detection of basal readthrough for internal control may be limited depending on the PTC mutation or require different sets of nanobodies. Of note, the pre-clinical development for therapy aiming to recover laforin protein expression, like adeno-associated viral vector (AAV) therapy, may use the laforin nanobody ELISA to quantitate and assess the quality of laforin phosphatase activity<sup>326</sup>. Moreover, the long shelf life of nanobodies, low technical requirements, and ease of reproducibility when performing an ELISA provide the possibility of using the laforin nanobody ELISA in clinical settings.

Further development of the nanobody based ELISA for PTC readthrough may act as a blue-print for creating similar assays for screening PTCs specific to other diseases, helping to alleviate the bottleneck of bench-to-bedside translation of PTC readthrough therapy.

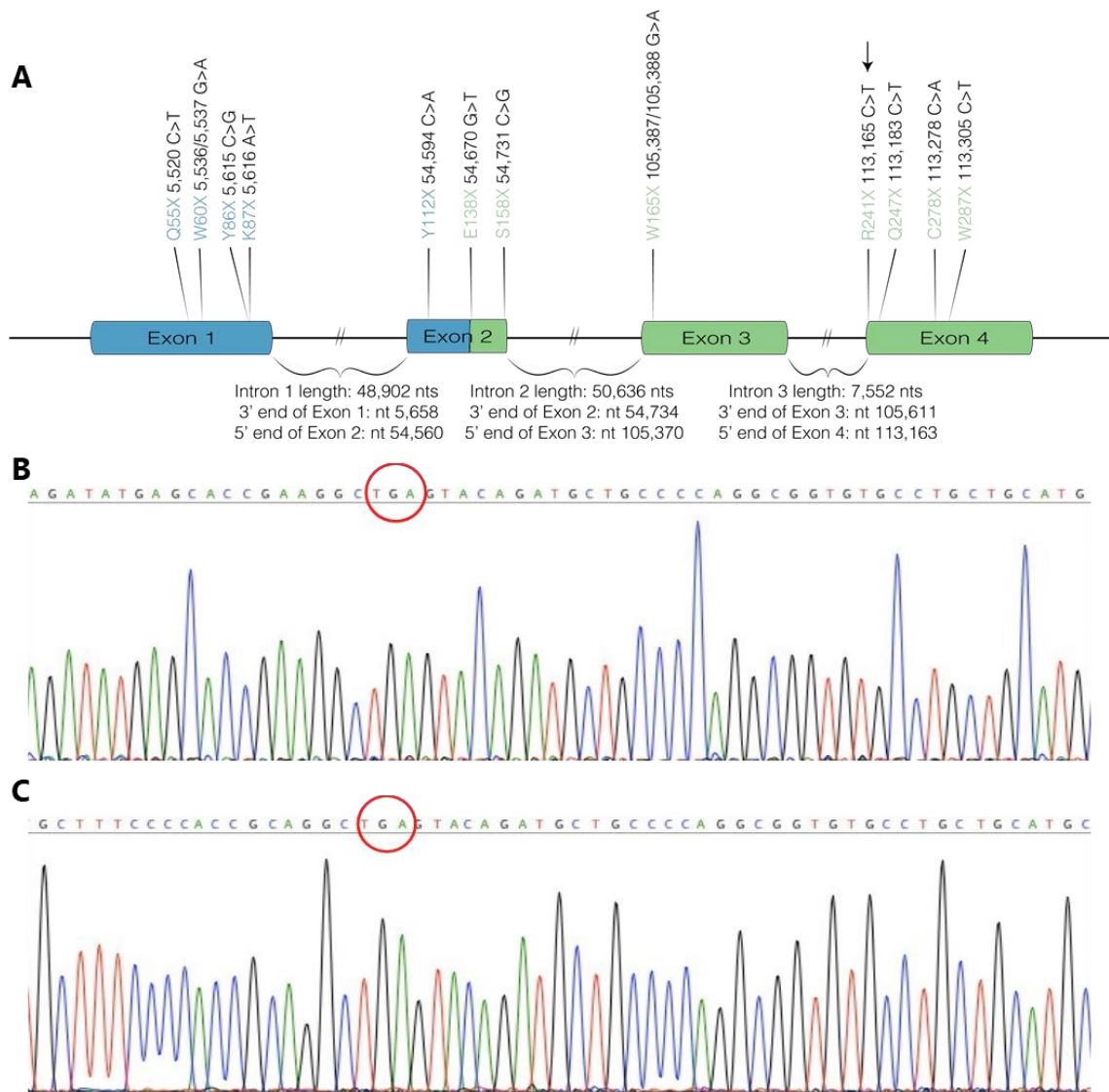


**Figure 5.1 12 PTC mutations in *Epm2a* cause Lafora disease.**

**A)** Location of LD PTCs mapped to *Epm2a*. Blue = Carbohydrate Binding Module, Green = Dual Specificity Phosphatase Domain. Arrow is pointing to R241X, the most common mutation in LD. **B)** Gene sequencing of patient fibroblasts **C)** cDNA was generated from patient fibroblasts and sequenced. The g.113165 C > T and corresponding c.721 C > T C>T point mutation is found, indicating that the R241X PTC mutation is transcribed in frame from gene to mRNA.

**Table 5.1 *Epm2a* PTC mutations and corresponding nucleotide changes at the mRNA and gene level.**

Underscored nucleotides indicate the position in the gene codon that is mutated and results in a PTC.

<b>Protein</b>	<b>mRNA</b>	<b>Gene</b>
p.Q55X	c.163 C > T	g.5520 C > T; <u>C</u> AG
p.W60X	c.179 G > A	g.5536 G > A; T <u>G</u> G
p.Y86X	c.258 C > G	g.5615 C > G; T <u>A</u> C
p.Y87X	c.259 A > T	g.5616 A > T; <u>A</u> AG
p.Y112X	c.336 C > A	g.54594 C > A; T <u>A</u> C
p.E138X	c.412 G > T	g.54670 G > T; <u>G</u> AA
p.S158X	c.473 C > G	g.54731 C > G; T <u>C</u> A
p.W165X	c.495 G > A	g.105388 G > A; T <u>G</u> G
p.R241X	c.721 C > T	g.113165 C > T; <u>C</u> GA
p.Q247X	c.739 C > T	g.113183 C > T; <u>C</u> AG
p.C278X	c.834 C > A	g.113278 C > A; T <u>G</u> C
p.W287X	c.861 G > A	g.113305 G > A; T <u>G</u> G

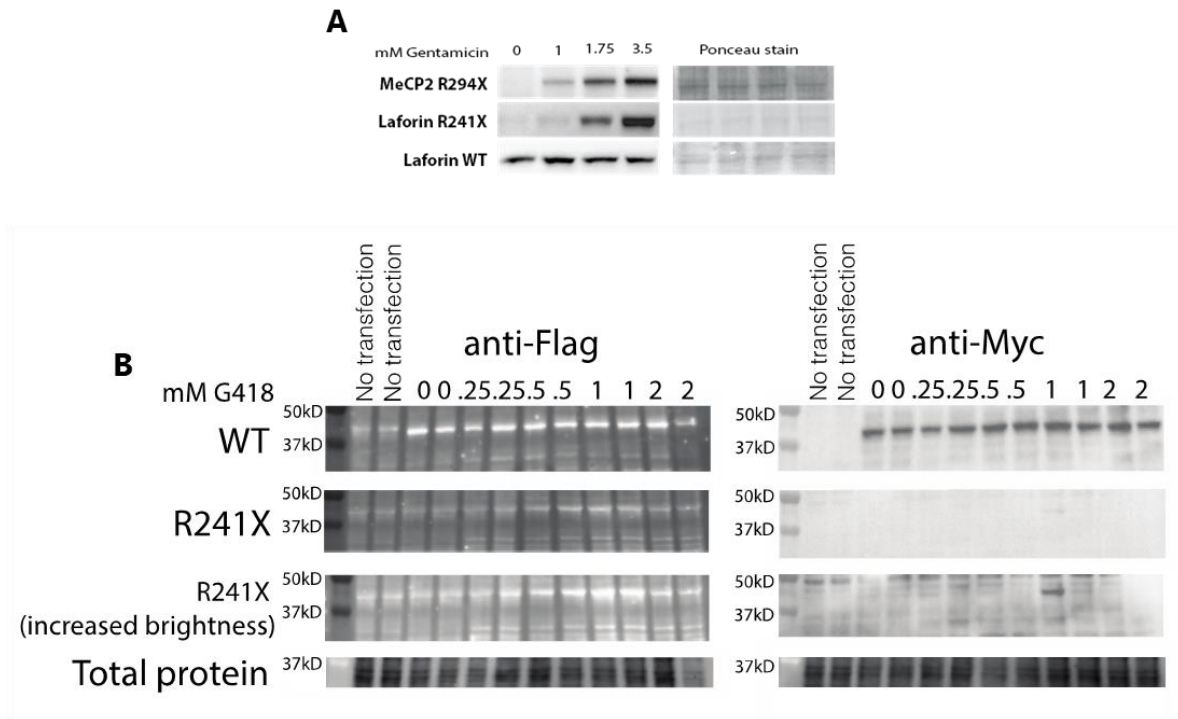


**Figure 5.2 Western blot screening of aminoglycoside induced readthrough of R241X.**  
**A)** HEK293 cells were transfected with *MeCP2* R241X, R241X, or WT NT-Flag construct and treated with increasing concentrations of gentamicin for 48 h. Laforin or MeCP2 levels were assessed by western analysis with anti-Flag antibody. **B)** HEK293 cells were transfected with R241X, or WT NT-Flag and CT-Myc construct, treated with increasing concentrations of G418 for 48h. Laforin levels were assessed by western analysis using anti-Flag and anti-Myc antibodies.



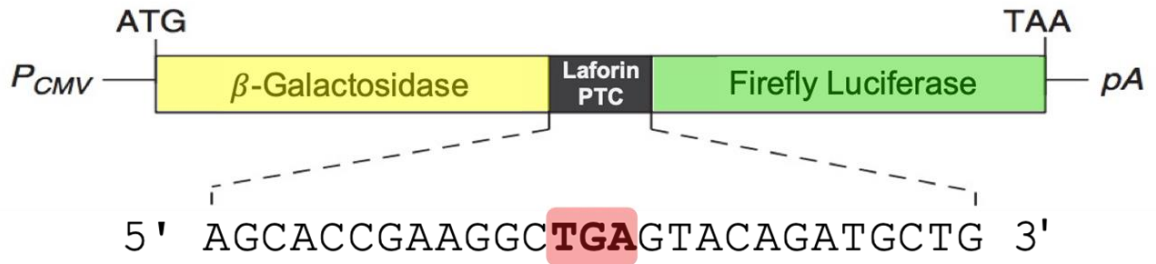


**Figure 5.3 Description of the dual gene reporter system.**

For quantification in HeLa cells,  $\beta$ -galactosidase and firefly luciferase coding sequences, flanked an oligonucleotide that included a PTC mutation. Their expression is driven by the SV40 promoter (pAC99 vectors). The construction of the oligonucleotides was performed by surrounding the PTC mutation of interest by four codons and cloned in-frame between  $\beta$ -galactosidase and firefly luciferase coding sequences. Readthrough was determined by normalizing the expression of firefly luciferase to the expression of  $\beta$ -galactosidase obtained for each nonsense mutation.

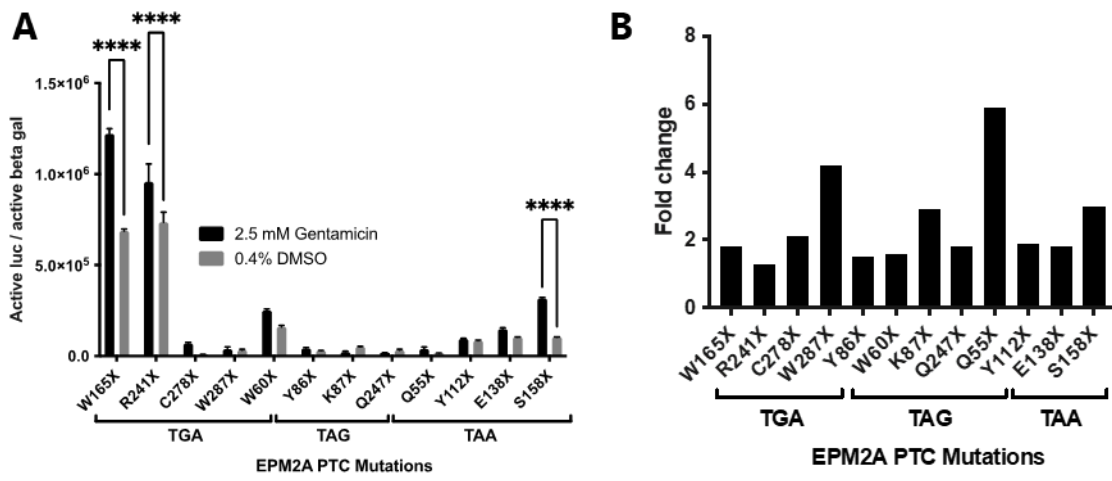


**Figure 5.4. Enzymatic screening for identifying nonsense mutations responsive to aminoglycoside treatment.**

**A)** Readthrough of 12 PTC mutations in *Epm2a* was measured in HeLa cells with and without gentamicin (2.5 mM) treatment for 24 h. **B)** Foldchange of readthrough from gentamicin treatment compared to DMSO. Mean values are presented together with the standard error of the mean (SEM) (n=5).

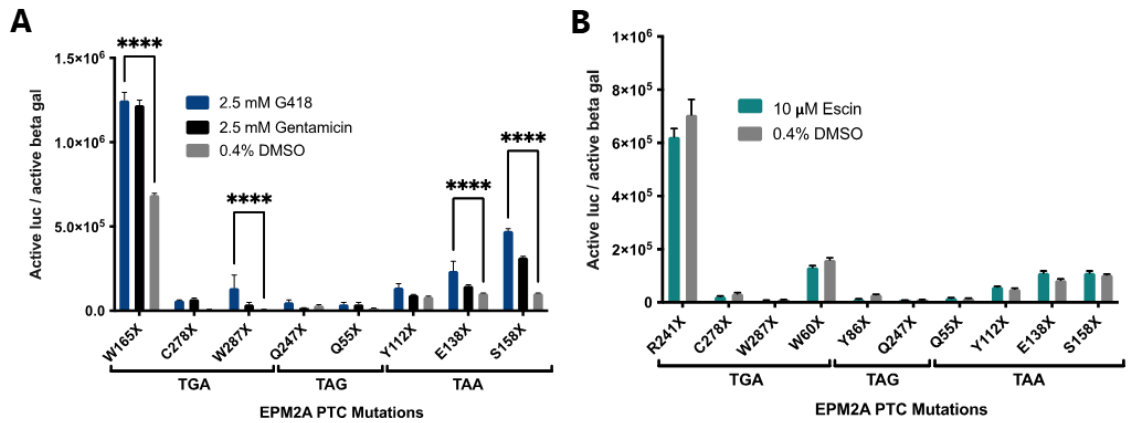


**Figure 5.5 Enzymatic screening for identifying nonsense mutations responsive to G418 or escin treatment.**

**A)** Readthrough of 8 PTC mutations in *Epm2a* was measured in HeLa cells with and without G418 (2.5 mM) compared to gentamicin (2.5 mM) treatment for 24 h. Gentamicin and DMSO data is previously shown. **B)** Readthrough efficiencies of 10 PTC mutations in *Epm2a* were measured in HeLa cells with and without escin (10 μM) for 24 h. DMSO data is previously shown. Mean values are presented together with the standard error of the mean (SEM) (n=5).

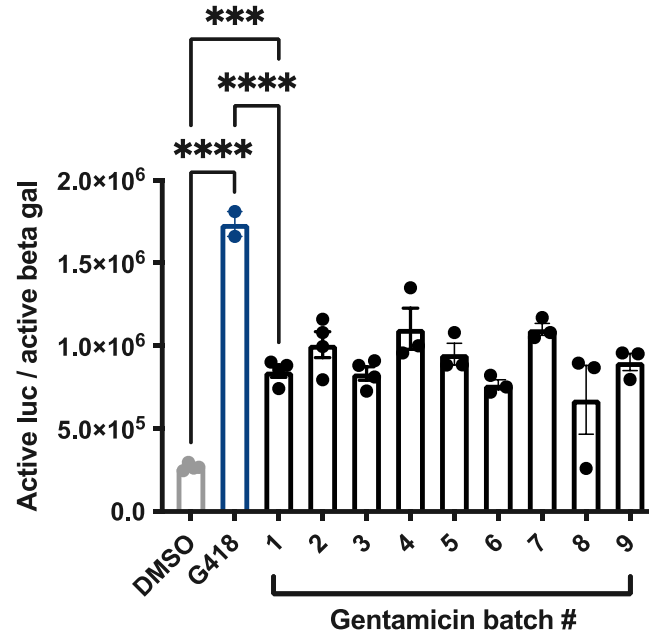


**Figure 5.6 Enzymatic screening for variability in gentamicin induced readthrough.**

**A)** Readthrough of the R241X PTC mutations in *Epm2a* was measured in HeLa cells with and without gentamicin (2.5 mM) or G418 (2.5 mM) treatment for 24 h. A different lot of gentamicin was used in each trial.

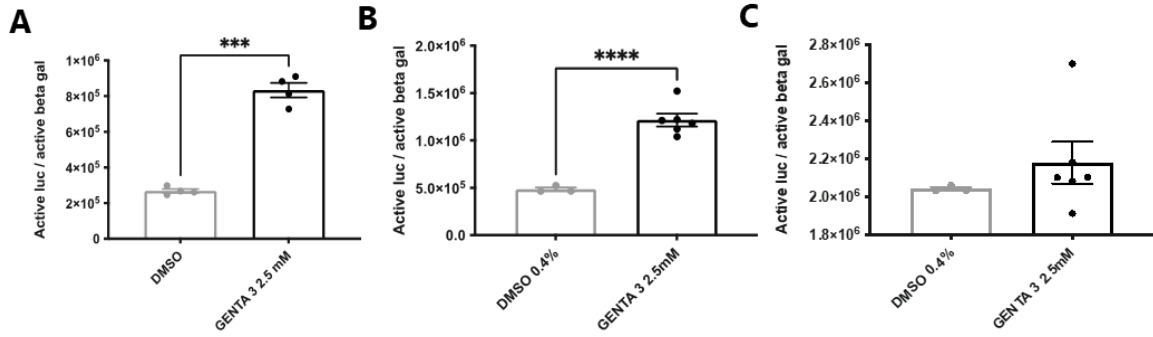


**Figure 5.7 Enzymatic screening of *Epm2a* R241X readthrough in NIH3T3 and HEK293 cells.**

Readthrough of the R241X PTC mutation in *Epm2a* was measured in **A**) HeLa (data is previously shown) **B**) NIH3T3, and **C**) HEK293 cells with and without gentamicin (lot 3) (2.5 mM) or escin (10  $\mu$ M) treatment for 24 h. \*\*\* =  $p = 0.0003$ , \*\*\*\* =  $p < 0.0001$

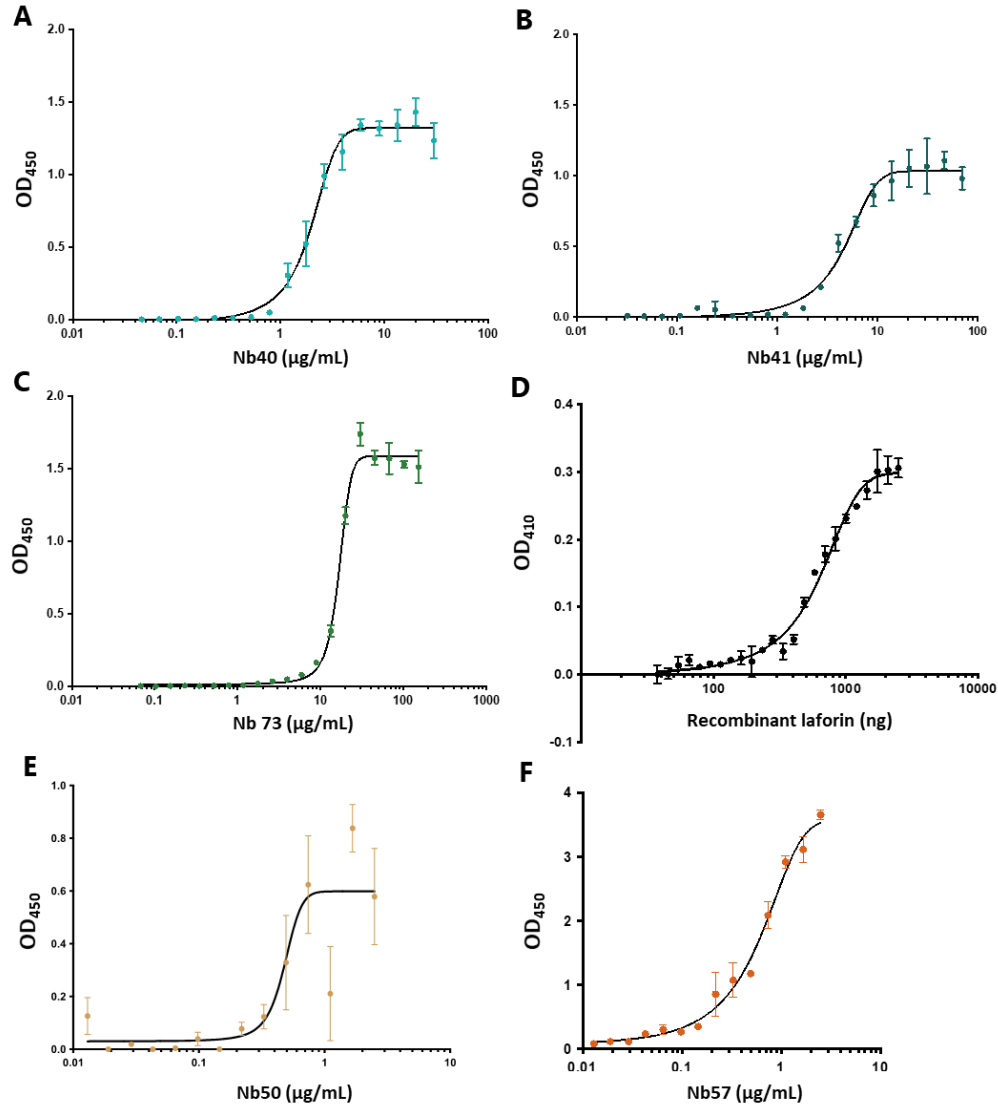


**Figure 5.8 Optimizing capture and detection nanobodies.**

**A-C)** Each putative capture nanobody was plated in a 96-well plate at increasing concentrations overnight. Saturation curves were determined by detecting each nanobody with an HRP-conjugated anti-camelid antibody. **A)** Nb40 **B)** Nb41 **C)** Nb73 **D)** To determine the working range of recombinant laforin, a standard curve using a pNPP assay was performed to detect laforin phosphatase activity. Nb41 was plated at 8  $\mu\text{g/mL}$  overnight. Increasing concentrations of recombinant laforin were incubated with pre-bound Nb41. **E-F)** To determine the saturation curves of putative detection nanobodies, Nb41 was plated at 8  $\mu\text{g/mL}$  overnight. 2000 ng per well of recombinant laforin was captured by Nb41. **E)** Increasing concentrations of Nb50-HRP detected recombinant laforin. **F)** Increasing concentrations of Nb57-HRP detected recombinant laforin.

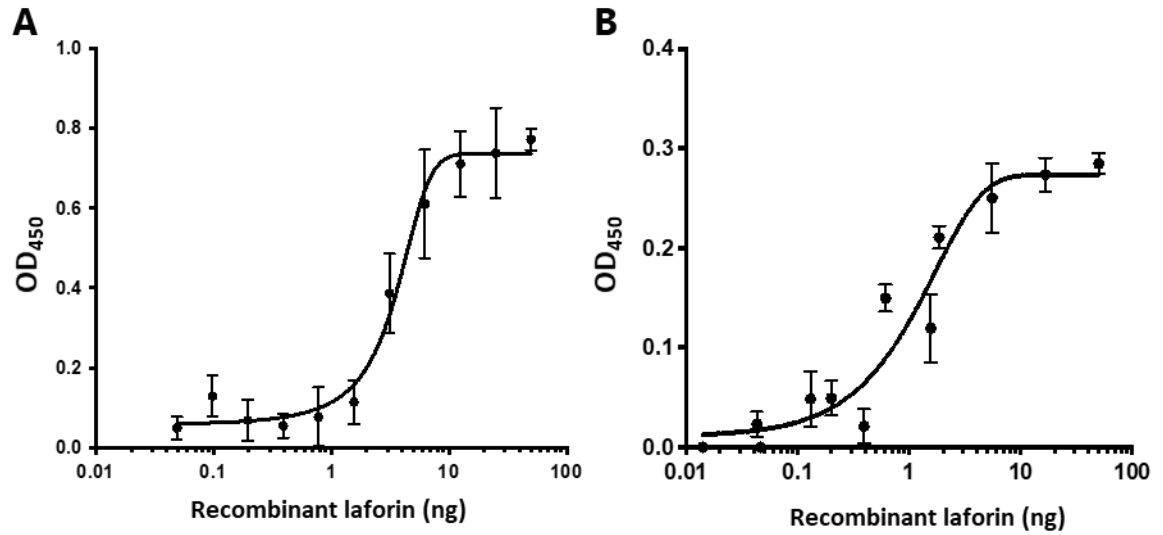


**Figure 5.9 Saturation curves of laforin detection antibodies, Nb57-HRP and polyclonal anti-laforin antibody #113.**

Nb41 was plated at 8  $\mu\text{g}/\text{mL}$  overnight. Increasing concentrations of recombinant laforin was captured by Nb41. **A)** Nb57-HRP at 0.18  $\mu\text{g}/\text{mL}$  was used to detect laforin. **B)** Polyclonal anti-laforin antibody #113 at 1  $\mu\text{g}/\text{mL}$  was used to detect laforin.

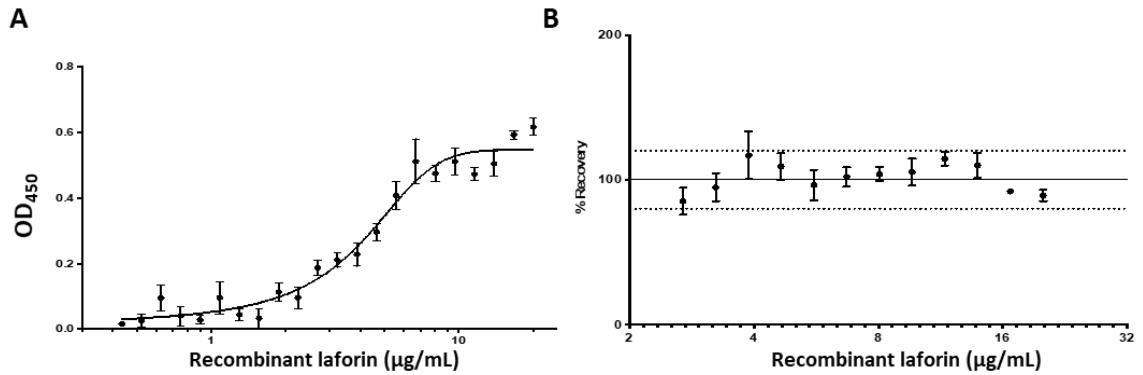


**Figure 5.10 Working range of recombinant laforin at optimized antibody concentrations.**

**A)** An absorbance versus concentration curve was generated for multiple concentrations to determine the working range of the laforin ELISA. The minimum detection is 2 μg/mL and signal saturation is reached above 10 μg/mL. The curve is fit with an FPL best fit curve and  $R^2 = 0.9153$ . The experiment uses  $n = 3$  replicates. **B)** Using the FPL model, percent recovery was determined by comparing concentration loaded vs the concentration as determined by the curve.



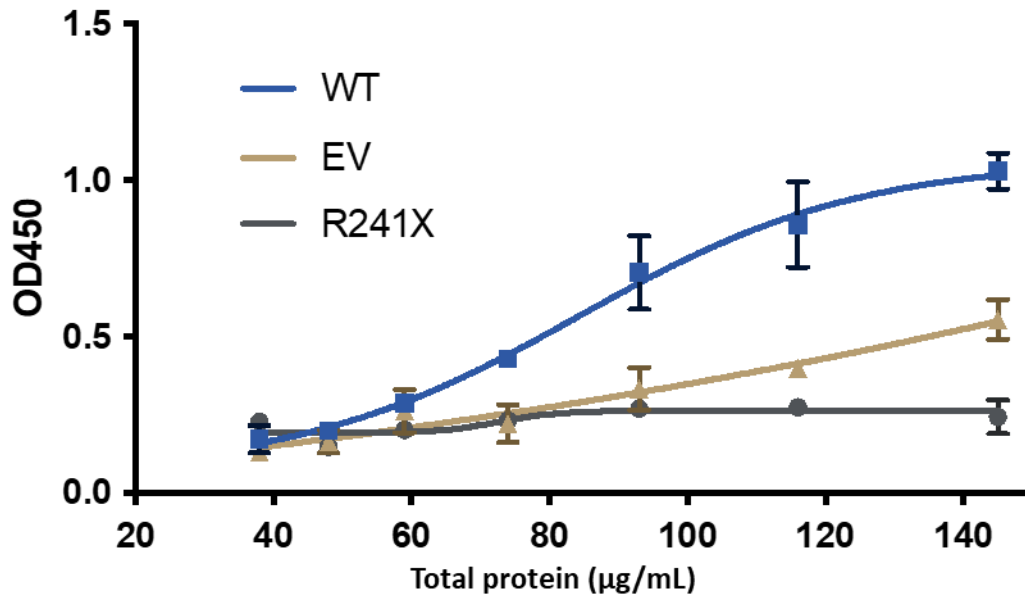


**Figure 5.11 Laforin nanobody ELISA detection from whole cell lysates.**

WT laforin, empty vector (EV), or R241X was overexpressed in HEK293 cells. Whole cell lysates were prepared using PLC-lysis buffer and flash frozen. 8 µg/mL Nb41 was plated in a 96-well plate overnight, increasing concentrations of whole cell lysate were incubated with Nb41, wells were washed, and laforin was detected using 0.18 µg/mL Nb57-HRP.

## CHAPTER 6. Concluding remarks

### 6.1.1 Summary and future directions

The pathophysiology of Lafora disease (LD) is centered around the overaccumulation of aberrantly structured glycogen called polyglucosan bodies (PGBs)<sup>81,324</sup>. Aberrant metabolism is a cause and consequence of LD PGBs resulting in early onset, rapid progression, and exacerbated symptomology common to many neurodegenerative diseases (**Chapter 1**)<sup>322,323</sup>. LD is one of 17 glycogen storage diseases (GSDs) that are defined by aberrant accumulation of glycogen/PGBs, where the contribution of PGBs to neuropathology is the most well studied in LD models<sup>17</sup>. From the atomic to pathological levels, the fundamentals of LD are understood. Several *in vitro* biochemical and structural techniques, *in situ* cell culture models, and *in vivo* mouse models have been generated to determine: 1. Mutations in laforin or malin result in LD PGBs that are hyperphosphorylated and aberrantly branched compared to normal glycogen<sup>78,222</sup>. 2. Laforin binds and dephosphorylates glycogen<sup>115</sup>. 3. The accumulation of LD PGBs causes disruptions to neuronal energetics resulting in defects in memory and cognition, and neurodegeneration<sup>25,26,28,81</sup>.

As the field tests putative therapeutics for LD in pre-clinical settings, our cellular, structural, biochemical, and physiological understanding of LD is being put to the ultimate test of translatability. In this work, we have scrutinized assumptions of the laforin knockout (LKO) model. We have confirmed and expanded on time dependent physiological aspects and challenged assumptions about the relationship of PGB accumulation to inflammation, a widely used marker of LD recovery (**Chapter 2**). Now that we have clarified benchmarks of pre-clinical therapeutic testing for LD, these references may act as guides for future studies. Additionally, the finding that microglia (not astrocytes) are activated throughout the lifespan of the LKO mouse indicate that they are possible therapeutic targets for neuroinflammation and should be examined further. The absence of astrocyte activation during the most acute time frame of LD PGB accumulation is curious, and future studies should explore whether astrocytic PGB accumulation is driving deleterious metabolic defects that influence their expected neuroinflammatory behavior. Furthermore, the coordination of activity between astrocytes and microglia may be disrupted and investigation of this matter in the LKO mouse model may reveal clues about the pathological cascade effect that is initiated by LD PGBs.

In the LKO mouse we utilized cutting edge metabolomics techniques to begin to understand the consequences of aberrant glycogen metabolism to cellular respiration (**Chapter 3**). This study opened an avenue for discovering metabolic therapeutic targets in LD and proposed a direct link between PGB accumulation and downstream metabolic defects in LD and normal aging. Although our insights into citric acid cycle metabolite load in LKO mice compared to WT have revealed clear respiratory consequences of PGB

accumulation, their biological impact should be thoroughly investigated (**Chapter 3**). This area of investigation will also lead to filling in the ripple effect events that link PGBs to downstream brain dysmetabolism. Moreover, our methods for characterizing LD pathophysiology should be used as a model for similar investigations of other neurodegenerative diseases that are also affected by aberrant glycogen/PGB accumulation. Of the 17 GSDs, only a handful have been discovered to have glycogen/PGB accumulation that is neurotoxic. Most GSDs are clinically classified as myopathies or cardiopathies. However, in several GSDs, secondary CNS symptomology has been documented but understudied, for example, patients with GSD0 are often afflicted by seizures. Furthermore, the contribution of peripheral and/or motor neuron glycogen/PGB accumulation to GSDs should be re-examined as its contribution to defects in muscular and cardiac failure may be significant.

One major gap in our understanding of biochemical aspects of LD is the mechanism of laforin's phosphatase activity on glycogen, and moreover, the biological relevance of glycogen phosphate. To tackle these important questions about glycogen metabolism, we have made significant advancements in generating tools. The generation of six anti-laforin nanobodies and their defined epitopes opens the doors for discovering the role of laforin interactions and mechanisms (**Chapter 4**).

Although LD is a very rare disease, this body of work has shown that studying LD offers a unique window into understanding issues that are universal among mammals including glycogen metabolism, neurodegenerative disease, and aging. Our last study again aimed to use the in-depth genetic and biochemical understanding of LD to generate a translatable drug screening system for all other genetic diseases (**Chapter 5**). Though more work is required to realize the potential of these assays, these explorations have set up the tools and framework for pre-clinical testing of laforin rescue. The laforin nanobody enzyme linked immunosorbent assay (ELISA) can be immediately useful for current efforts to development an AAV therapy for LD.

Although this work and the hypotheses generated herein are directly applicable to LD, future findings may impact other neurodegenerative diseases and epilepsies. LD shares key cellular processes with many diseases and developments in our understanding of their translation to treatments will provide similar valuable insight for others. Additionally, these findings may assist in resolving some of the questions and controversies surrounding the significance of glycogen to brain energy metabolism.

### **6.1.2 Final conclusions**

This work has contributed to the advancements of biomarkers, tools, and therapeutics for LD. These studies have also laid a model for the investigation of aberrant glycogen and aberrant glycogen metabolism in other neurodegenerative diseases, paving the way for novel therapeutic target discovery.

## BIBLIOGRAPHY

1. Muddapu VR, Dharshini SAP, Chakravarthy VS, Gromiha MM. Neurodegenerative Diseases – Is Metabolic Deficiency the Root Cause? *Front Neurosci.* 2020;14(March):1-19.
2. Ortman JM, Velkoff V a., Hogan H. An aging nation: The older population in the United States. *Econ Stat Adm US Dep Commer.* 2014;1964:1-28.
3. Hou Y, Dan X, Babbar M, et al. Ageing as a risk factor for neurodegenerative disease. *Nat Rev Neurol.* 2019;15(10):565-581.
4. Vespa J, Medina L, Armstrong D. Demographic turning points for the United States: Population projections for 2020 to 2060. Current Population Reports, P25–1144. Washington, DC: US Census Bureau. *US Census Bur.* Published online 2020:1-13.
5. Lilienfeld DE, Perl DP. Projected Neurodegenerative Disease Mortality in the united States 1990-2040. *Neuroepidemiology.* 2003;12(4):1-12.
6. Forman MS, Trojanowski JQ, Lee VM-Y. Neurodegenerative diseases: a decade of discoveries paves the way for therapeutic breakthroughs. *Nat Med.* 2004;10(10):1055-1063.
7. Trushina E, Cunnane SC, Prigione A, et al. Brain energy rescue: an emerging therapeutic concept for neurodegenerative disorders of aging. *Nat Rev Drug Discov.* 2020;19:609-633.
8. Boland B, Yu WH, Corti O, et al. Promoting the clearance of neurotoxic proteins in neurodegenerative disorders of ageing. *Nat Rev Drug Discov.* 2018;17(9):660-688.
9. Aldana BI. Microglia-Specific Metabolic Changes in Neurodegeneration. *J Mol Biol.* 2019;431(9):1830-1842.
10. Zilberter Y, Zilberter M. The vicious circle of hypometabolism in neurodegenerative diseases: Ways and mechanisms of metabolic correction. *J Neurosci Res.* 2017;95(11):2217-2235.
11. Fu H, Hardy J, Duff KE. Selective vulnerability in neurodegenerative diseases. *Nat Neurosci.* 2018;21(10):1350-1358.
12. Brown AM, Rich LR, Ransom BR. Metabolism of Glycogen in Brain White Matter. *Adv Neurobiol.* 2019;23:187-207.
13. Brewer MK, Gentry MS. Brain glycogen structure and its associated proteins: past present and future. *Adv Neurobiol.* 2019;23:17-81.
14. Dienel GA, Carlson GM. Major Advances in Brain Glycogen Research: Understanding of the Roles of Glycogen Have Evolved from Emergency Fuel

- Reserve to Dynamic, Regulated Participant in Diverse Brain Functions. *Adv Neurobiol.* 2019;23:1-16.
15. Oe Y, Akther S, Hirase H. Regional Distribution of Glycogen in the Mouse Brain Visualized by Immunohistochemistry. *Adv Neurobiol.* 2019;23:147-168.
  16. Sun RC, Young LEA, Bruntz RC, et al. Brain glycogen serves as a critical glucosamine cache required for protein glycosylation. *Cell Metab.* 2021;33:1-14.
  17. Ellingwood SS, Cheng A. Biochemical and clinical aspects of glycogen storage diseases. *J Endocrinol.* 2018;238(3):R131-R141.
  18. Wu L, Butler NJM, Swanson RA. Technical and Comparative Aspects of Brain Glycogen Metabolism. *Adv Neurobiol.* 2019;23:169-185.
  19. Cavanagh JB. Corpora-amylacea and the family of polyglucosan diseases. *Brain Res Rev.* 1999;29:265-295.
  20. Brewer MK, Putaux JL, Rondon A, Uittenbogaard A, Sullivan MA, Gentry MS. Polyglucosan body structure in Lafora disease. *Carbohydr Polym.* 2020;240:116260.
  21. Augamp E, Duran J, Guinovart JJ, Pelegramp C, Vilaplana J. Exploring the elusive composition of corpora amylacea of human brain. *Sci Rep.* Published online September 4, 2018:1-13.
  22. Riba M, Vilaplana J, Augé E, et al. Corpora amylacea act as containers that remove waste products from the brain. *Proc Natl Acad Sci U S A.* 2019;116(51):1-11.
  23. de Castro F. Cajal and the Spanish Neurological School: Neuroscience Would Have Been a Different Story Without Them. *fncel-13-00187.tex.* Published online May 2019:1-14.
  24. Lafora GR, Glueck B. Beitrag zur Histopathologie der myoklonischen Epilepsie. *Zeitschrift für die gesamte Neurol und Psychiatr.* 1911;6(1):1-14.
  25. Turnbull J, DePaoli-Roach AA, Zhao X, et al. PTG depletion removes Lafora bodies and rescues the fatal epilepsy of Lafora disease. Frankel WN, ed. *PLoS Genet.* 2011;7(4):e1002037.
  26. Turnbull J, Epp JR, Goldsmith D, et al. PTG protein depletion rescues malin-deficient Lafora disease in mouse. *Ann Neurol.* 2014;75(3):442-446.
  27. Duran J, Gruart AA, Garcia-Rocha M, et al. Glycogen accumulation underlies neurodegeneration and autophagy impairment in Lafora disease. *Hum Mol Genet.* 2014;23(12):3147-3156.
  28. Pederson BA, Turnbull J, Epp JR, et al. Inhibiting glycogen synthesis prevents Lafora disease in a mouse model. *Ann Neurol.* 2013;74(2):297-300.
  29. Navarro PP, Genoud C, Castaño-Díez D, et al. Cerebral Corpora amylacea are

- dense membranous labyrinths containing structurally preserved cell organelles. *Sci Rep.* 2018;8(1):526.
30. Rai A, Ganesh S. *Polyglucosan Bodies in Aged Brain and Neurodegeneration: Cause or Consequence?*; 2019.
  31. Auge E, Cabezón I, Pelegri C, Vilaplana J. New perspectives on corpora amylacea in the human brain. *Sci Rep.* 2017;7(1):41807.
  32. Dodge JC, Treleaven CM, Fidler JA, et al. Metabolic signatures of amyotrophic lateral sclerosis reveal insights into disease pathogenesis. *Proc Natl Acad Sci.* 2013;110(26):10812-10817.
  33. Taksir T V, Griffiths D, Johnson J, Ryan S, Shihabuddin LS, Thurberg BL. Optimized Preservation of CNS Morphology for the Identification of Glycogen in the Pompe Mouse Model. *J Histochem Cytochem.* 2007;55(10):991-998.
  34. Loiseau H, Marchal C, Vital A, Vital C, Rougier A, Loiseau P. Occurrence of polyglucosan bodies in temporal lobe epilepsy. *J Neurol Neurosurg Psychiatry.* 1992;55(11):1092-1093.
  35. Mann DMA, Sumpter PQ, Davies CA, Yates PO. Glycogen accumulations in the cerebral cortex in Alzheimer's disease. *Acta Neuropathol.* 1987;73:181-184.
  36. Irimia JM, Tagliabracci VS, Meyer CM, Segvich DM, Depaoli-Roach AA, Roach PJ. Muscle glycogen remodeling and glycogen phosphate metabolism following exhaustive exercise of wild type and laforin knockout mice. *J Biol Chem.* 2015;290(37):22686-22698.
  37. Heinicke K, Dimitrov IE, Romain N, et al. Reproducibility and absolute quantification of muscle glycogen in patients with glycogen storage disease by <sup>13</sup>C NMR spectroscopy at 7 tesla. *PLoS One.* 2014;9(10):1-6.
  38. McManus JFA. Histological and Histochemical Uses of Periodic Acid. *Stain Technol.* 1948;23(3):99-108.
  39. Oe Y, Baba O, Ashida H, Nakamura KC, Hirase H. Glycogen distribution in the microwave-fixed mouse brain reveals heterogeneous astrocytic patterns. *Glia.* 2016;64(9):1532-1545.
  40. Young LEA, Brizzee CO, Macedo JKA, et al. Accurate and sensitive quantitation of glucose and glucose phosphates derived from storage carbohydrates by mass spectrometry. *Carbohydr Polym.* 2020;230:115651.
  41. Chen X, Pan W. The Treatment Strategies for Neurodegenerative Diseases by Integrative Medicine. *Integr Med Int.* 2015;1(4):223-225.
  42. Yacoubian TA. Neurodegenerative Disorders: Why Do We Need New Therapies? In: *Drug Discovery Approaches for the Treatment of Neurodegenerative Disorders.* Elsevier Inc.; 2016:1-16.

43. Stobart JL, Anderson CM. Multifunctional role of astrocytes as gatekeepers of neuronal energy supply. *Front Cell Neurosci.* 2013;(MAR).
44. Gibbs ME, Lloyd HGE., Santa T, Hertz L. Glycogen Is a Preferred Glutamate Precursor During Learning in 1-Day-Old Chick: Biochemical and Behavioral Evidence Marie. *J Neurosci Res.* 2007;85:3326-3333.
45. Gibbs ME, Anderson DG, Hertz L. Inhibition of glycogenolysis in astrocytes interrupts memory consolidation in young chickens. *Glia.* 2006;54(3):214-222.
46. Gentry MS, Guinovart JJ, Minassian BA, Roach PJ, Serratosa JM. Lafora disease offers a unique window into neuronal glycogen metabolism. *J Biol Chem.* 2018;293(19):7117-7125.
47. Kobylarek D, Iwanowski P, Lewandowska Z, et al. Advances in the Potential Biomarkers of Epilepsy. *Front Neurol.* 2019;10:426-475.
48. Toniolo S, Sen A, Husain M. Modulation of Brain Hyperexcitability: Potential New Therapeutic Approaches in Alzheimer's Disease. *Int J Mol Sci.* 2020;21(23):9318.
49. Worby CA, Gentry MS, Dixon JE. Malin decreases glycogen accumulation by promoting the degradation of protein targeting to glycogen (PTG). *J Biol Chem.* 2008;283(7):4069-4076.
50. García-Gimeno M, Knecht E, Sanz P. Lafora Disease: A Ubiquitination-Related Pathology. *Cells.* 2018;7(8):87.
51. Valles-Ortega J, Duran J, Garcia-Rocha M, et al. Neurodegeneration and functional impairments associated with glycogen synthase accumulation in a mouse model of Lafora disease. *EMBO Mol Med.* 2011;3(11):667-681.
52. Suzuki A, Stern SA, Bozdagi O, et al. Astrocyte-Neuron Lactate Transport Is Required for Long-Term Memory Formation. *Cell.* 2011;144(5):810-823.
53. Calì C, Tauffenberger A, Magistretti P. The Strategic Location of Glycogen and Lactate: From Body Energy Reserve to Brain Plasticity. *Front Cell Neurosci.* 2019;13:587.e7.
54. Hertz L, O'Dowd BS, Ng KT, Gibbs ME. Reciprocal changes in forebrain contents of glycogen and of glutamate/glutamine during early memory consolidation in the day-old chick. *Brain Res.* 2003;994(2):226-233.
55. Duran J, Saez I, Gruart A, Guinovart JJ, Delgado-García JM. Impairment in long-term memory formation and learning-dependent synaptic plasticity in mice lacking glycogen synthase in the brain. *J Cereb Blood Flow Metab.* 2013;33(4):550-556.
56. Delgado-Escueta A V. Advances in Lafora Progressive Myoclonus Epilepsy. *Curr Neurol Neurosci Rep.* 2007;7:428-433.

57. Sheehan B. Assessment scales in dementia. *Ther Adv Neurol Disord*. 2012;5(6):349-358.
58. Phelps CH. Barbiturate-induced glycogen accumulation in brain. An electron microscopic study. *Brain Res*. 1972;39(1):225-234.
59. Koizumi J. Glycogen in the Central Nervous System. *Prog Histochem Cytochem*. 1974;6(4):3-5.
60. Cataldo AM, Broadwell RD. *Cytochemical Identification of Cerebral Glycogen and Glucose-6-Phosphatase Activity under Normal and Experimental Conditions. II. Choroid Plexus and Ependymal Epithelia, Endothelia and Pericytes*. Vol 15.; 1986.
61. Mahmoud S, Gharagozloo M, Simard C, Gris D. Astrocytes Maintain Glutamate Homeostasis in the CNS by Controlling the Balance between Glutamate Uptake and Release. *Cells*. 2019;8(2):184.
62. Xu J, Song D, Xue Z, Gu L, Hertz L, Peng L. Requirement of Glycogenolysis for Uptake of Increased Extracellular K<sup>+</sup> in Astrocytes: Potential Implications for K<sup>+</sup> Homeostasis and Glycogen Usage in Brain. *Neurochem Res*. 2012;38(3):472-485.
63. Choi HB, Gordon GRJ, Zhou N, et al. Metabolic Communication between Astrocytes and Neurons via Bicarbonate-Responsive Soluble Adenylyl Cyclase. *Neuron*. 2012;75(6):1094-1104.
64. Hodgkin AL, Huxley AF. Movement of radioactive potassium and membrane current in a giant axon. *J Physiol*. 1953;121:403-414.
65. Henn FA, Haljamäe H, Hamberger A. Glial cell function: Active control of extracellular K<sup>+</sup> concentration. *Brain Res*. 1972;43(2):437-443.
66. Hajek I, Subbarao KVS, Leif Hertz. Acute and chronic effects of potassium and noradrenaline on Na<sup>+</sup>, K<sup>+</sup>-ATPase activity in cultured mouse neurons and astrocytes. *Neurochem Int*. 1996;28(3):335-342.
67. Honegger P, Pardo B. Separate neuronal and glial Na<sup>+</sup>,K<sup>+</sup>-ATPase isoforms regulate glucose utilization in response to membrane depolarization and elevated extracellular potassium. *J Cereb Blood Flow Metab*. 1999;19(9):1051-1059.
68. DiNuzzo M, Mangia S, Maraviglia B, Giove F. Does abnormal glycogen structure contribute to increased susceptibility to seizures in epilepsy? *Metab Brain Dis*. 2015;30(1):307-316.
69. Magistretti PJ, Allaman I. Lactate in the brain: from metabolic end-product to signalling molecule. *Nat Rev Neurosci*. 2018;19(4):235-249.
70. Pellerin L, Magistretti PJ. *Glutamate Uptake into Astrocytes Stimulates Aerobic Glycolysis: A Mechanism Coupling Neuronal Activity to Glucose Utilization (Glutamate Transporter/Na<sup>+</sup>/K<sup>+</sup>-ATPase/2-Deoxyglucose/Positron-Emission Tomography/Magnetic Resonance Imaging)*. Vol 91.; 1994.



71. JD R, S E, Rabinowitz JD, Enerbäck S. Lactate: the ugly duckling of energy metabolism. *Nat Metab.* 2020;2(7):566-571.
72. Brooks GA. Cell-cell and intracellular lactate shuttles. *J Physiol.* 2009;587(23):5591-5600.
73. Gizak A, Rakus D. Cell-to-cell lactate shuttle operates in heart and is important in age-related heart failure. *Aging (Albany NY)*. Published online February 2020:1-19.
74. Pellerin L, Pellegrini G, Bittar PG, et al. Evidence supporting the existence of an activity-dependent astrocyte-neuron lactate shuttle. *Dev Neurosci.* 1998;20(4-5):291-299.
75. M Z, Saab AS, Wyss MT, et al. Arousal-induced cortical activity triggers lactate release from astrocytes. *Nat Metab.* 2020;2(2):179-191.
76. Bastian C, Quinn J, Doherty C, et al. Role of Brain Glycogen During Ischemia, Aging and Cell-to-Cell Interactions. *Adv Neurobiol.* 2019;23:347-361.
77. DiNuzzo M, Walls AB, Öz G, et al. State Dependent Changes in Brain Glycogen. *Adv Neurobiol.* 2019;23:269-309.
78. Duran J, Gruart A, López-Ramos JC, Delgado-García JM, Guinovart JJ. Glycogen in Astrocytes and Neurons: Physiological and Pathological Aspects. *Adv Neurobiol.* 2019;23:311-329.
79. López-Ramos JC, Duran J, Gruart A, Guinovart JJ, Delgado-Garcia JM. Role of brain glycogen in the response to hypoxia and in susceptibility to epilepsy. *Front Cell Neurosci.* 2015;9(7):612-646.
80. Turnbull J, Tiberia E, Striano P, et al. Lafora disease. *Epileptic Discord.* 2016;18(Suppl. 2):S38-S62.
81. Minassian BA, Lee JR, Herbrick JA, et al. Mutations in a gene encoding a novel protein tyrosine phosphatase cause progressive myoclonus epilepsy. *Nat Genet.* 1998;20(2):171-174.
82. Serratosa JM, Gómez-Garre P, Gallardo ME, et al. A novel protein tyrosine phosphatase gene is mutated in progressive myoclonus epilepsy of the Lafora type (EPM2). *Hum Mol Genet.* 1999;8(2):345-352.
83. Chan EM, Young EJ, Ianzano L, et al. Mutations in NHLRC1 cause progressive myoclonus epilepsy. *Nat Genet.* 2003;35(2):125-127.
84. Gentry MS, Worby CA, Dixon JE. Insights into Lafora disease: Malin is an E3 ubiquitin ligase that ubiquitinates and promotes the degradation of laforin. *PNAS.* 2005;102(24):8501-8506.
85. Lohi H, Ianzano L, Zhao XC, et al. Novel glycogen synthase kinase 3 and

- ubiquitination pathways in progressive myoclonus epilepsy. *Hum Mol Genet.* 2005;14(18):2727-2736.
86. Worby CA, Gentry MS, Dixon JE. Laforin, a dual specificity phosphatase that dephosphorylates complex carbohydrates. *J Biol Chem.* 2006;281(41):30412-30418.
  87. Tagliabracci VS, Turnbull J, Wang W, et al. Laforin is a glycogen phosphatase, deficiency of which leads to elevated phosphorylation of glycogen in vivo. *PNAS.* 2007;104(49):19262-19266.
  88. Turnbull J, Wang P, Girard JM, et al. Glycogen hyperphosphorylation underlies Lafora body formation. *Ann Neurol.* 2010;68(6):925-933.
  89. Nitschke F, Wang P, Schmieder P, et al. Hyperphosphorylation of glucosyl C6 carbons and altered structure of glycogen in the neurodegenerative epilepsy lafora disease. *Cell Metab.* 2013;17(5):756-767.
  90. Duran J, Guinovart JJ, Tevy MF, et al. Deleterious effects of neuronal accumulation of glycogen in flies and mice. *EMBO Mol Med.* 2012;4(8):719-729.
  91. Aguado C, Sarkar S, Korolchuk VI, et al. Laforin, the most common protein mutated in Lafora disease, regulates autophagy. *Hum Mol Genet.* 2010;19(14):2867-2876.
  92. Criado O, Aguado C, Gayarre J, et al. Lafora bodies and neurological defects in malin-deficient mice correlate with impaired autophagy. *Hum Mol Genet.* 2011;21(7):1521-1533.
  93. Puri R, Ganesh S. Laforin in autophagy: A possible link between carbohydrate and protein in Lafora disease? *Autophagy.* 2010;6(8):1229-1231.
  94. Vernia S, Rubio T, Heredia M, Rodríguez de Córdoba S, Sanz P. Increased endoplasmic reticulum stress and decreased proteasomal function in Lafora disease models lacking the phosphatase laforin. *PLoS One.* 2009;4(6).
  95. Sinha P, Verma B, Ganesh S. Trehalose Ameliorates Seizure Susceptibility in Lafora Disease Mouse Models by Suppressing Neuroinflammation and Endoplasmic Reticulum Stress. *Mol Neurobiol.* Published online 2020.
  96. Auge E, Pelegri C, Manich G, et al. Astrocytes and neurons produce distinct types of polyglucosan bodies in Lafora disease. *Glia.* 2018;66(10):2094-2107.
  97. Rubio-Villena C, Viana R, Bonet J, et al. Astrocytes: new players in progressive myoclonus epilepsy of Lafora type. *Hum Mol Genet.* 2018;27(7):1290-1300.
  98. Duran J, Hervera A, Markussen KH, et al. Astrocytic glycogen accumulation drives the pathophysiology of neurodegeneration in Lafora disease. *Brain.* 2021;(2021).
  99. Sinadinos C, Valles-Ortega J, Boulan L, et al. Neuronal glycogen synthesis

- contributes to physiological aging. *Aging Cell*. 2014;13(5):935-945.
100. Auge E, Bechmann I, Llor N, Vilaplana J, Krueger M, Pelegri C. Corpora amylacea in human hippocampal brain tissue are intracellular bodies that exhibit a homogeneous distribution of neo-epitopes. *Sci Rep*. 2019;9(1):2063.
  101. Tagliabracci VS, Girard JM, Segvich DM, et al. Abnormal Metabolism of Glycogen Phosphate as a Cause for Lafora Disease. *J Biol Chem*. 2008;283(49):33816-33825.
  102. Janeway R, Ravens JR, Pearce LA, Odor DL, Suzuki K. Progressive myoclonus epilepsy with Lafora inclusion bodies. I. Clinical, genetic, histopathologic, and biochemical aspects. *Arch Neurol*. 1967;16(6):565-582.
  103. Sakai M, Austin J, Witmer F, Trueb L. Studies in myoclonus epilepsy (Lafora body form). II. Polyglucosans in the systemic deposits of myoclonus epilepsy and in corpora amylacea. *Neurology*. 1970;20(2):160-176.
  104. Yokoi S, Austin J, Witmer F. Isolation and characterization of Lafora bodies in two cases of myoclonus epilepsy. *J Neuropathol Exp Neurol*. 1967;26(1):125-127.
  105. Roach PJ, DePaoli-Roach AA, Hurley TD, Tagliabracci VS. Glycogen and its metabolism: some new developments and old themes. *Biochem J*. 2012;441(3):763-787.
  106. Sullivan MA, Nitschke S, Skwara EP, et al. Skeletal Muscle Glycogen Chain Length Correlates with Insolubility in Mouse Models of Polyglucosan-Associated Neurodegenerative Diseases. *CellReports*. 2019;27(5):1334-1344.e6.
  107. Nitschke F, Sullivan MA, Wang P, et al. Abnormal glycogen chain length pattern, not hyperphosphorylation, is critical in Lafora disease. *EMBO Mol Med*. 2017;9(7):906-917.
  108. Cenci U, Nitschke F, Steup M, Minassian BA, Colleoni C, Ball SG. Transition from glycogen to starch metabolism in Archaeplastida. *Trends plant Sci*. 2014;19(1):18-28.
  109. Smirnova J, Fernie AR, Steup M. Starch Degradation. In: Nakamura Y, ed. *Starch: Metabolism and Structure*. Springer Japan; 2015:239-290.
  110. Silver DM, Kötting O, Moorhead GBG. Phosphoglucan phosphatase function sheds light on starch degradation. *Trends plant Sci*. 2014;19(7):471-478.
  111. Cheng A, Zhang M, Gentry MS, Worby CA, Dixon JE, Saltiel AR. A role for AGL ubiquitination in the glycogen storage disorders of Lafora and Cori's disease. *Genes Dev*. 2007;21(19):2399-2409.
  112. Solaz-Fuster MC, Gimeno-Alcañiz JV, Ros S, et al. Regulation of glycogen synthesis by the laforin - Malin complex is modulated by the AMP-activated protein kinase pathway. *Hum Mol Genet*. 2008;17(5):667-678.

113. Vilchez D, Ros S, Cifuentes D, et al. Mechanism suppressing glycogen synthesis in neurons and its demise in progressive myoclonus epilepsy. *Nat Neurosci*. 2007;10(11):1407-1413.
114. Sun RC, Dukhande V V, Zhou Z, et al. Nuclear Glycogenolysis Modulates Histone Acetylation in Human Non-Small Cell Lung Cancers. *Cell Metab*. Published online August 29, 2019:1-22.
115. Tonks NK. Protein tyrosine phosphatases: From genes, to function, to disease. *Nat Rev Mol Cell Biol*. 2006;7(11):833-846.
116. Romá-Mateo C, Solaz-Fuster MDC, Gimeno-Alcañiz JV, et al. Laforin, a dual-specificity phosphatase involved in Lafora disease, is phosphorylated at Ser 25 by AMP-activated protein kinase. *Biochem J*. 2011;439(2):265-275.
117. Gentry MS, Romá-Mateo C, Sanz P. Laforin, a protein with many faces: glucan phosphatase, adapter protein, et alii. *FEBS J*. 2012;280(2):525-537.
118. Brewer MK, Uittenbogaard A, Austin GL, et al. Targeting Pathogenic Lafora Bodies in Lafora Disease Using an Antibody-Enzyme Fusion. *Cell Metab*. 2019;30:1-17.
119. Sparks SE, Krasnewich DM. Congenital Disorders of N-Linked Glycosylation and Multiple Pathway Overview. *GeneReviews*<sup>®</sup>. Published online 1993:1-23.
120. Muccioli L, Farolfi A, Pondrelli F, et al. FDG-PET assessment and metabolic patterns in Lafora disease. 2019;47(6):1576-1584.
121. Markussen KH, Macedo JKA, Machío M, et al. The 6th International Lafora Epilepsy Workshop: Advances in the search for a cure. *Epilepsy Behav*. 2021;119:107975.
122. Korlimarla A, Lim J-A, Kishnani PS, Sun B. An emerging phenotype of central nervous system involvement in Pompe disease: from bench to bedside and beyond. *Ann Transl Med*. 2019;7(13):289.
123. Nilsson MI, Kroos MA, Reuser AJ, et al. Novel GAA sequence variant c.1211 A > G reduces enzyme activity but not protein expression in infantile and adult onset Pompe disease. *Gene*. 2014;537:41-45.
124. Pena LDM, Proia AD, Kishnani PS. Postmortem Findings and Clinical Correlates in Individuals with Infantile-Onset Pompe Disease. In: *JIMD Reports, Volume 23*. Vol 23. Springer Berlin Heidelberg; 2015:45-54.
125. Chien Y-H, Lee N-C, Peng S-F, Hwu W-L. Brain Development in Infantile-Onset Pompe Disease Treated by Enzyme Replacement Therapy. Published online 2006.
126. Teng YT, Su WJ, Hou JW, Huang SF. Infantile-onset glycogen storage disease type II (Pompe disease): Report of a case with genetic diagnosis and pathological findings. *Chang Gung Med J*. 2004;27(5):379-384.

127. Spiridigliozzi GA, Keeling LA, Stefanescu M, Li C, Austin S, Kishnani PS. Cognitive and academic outcomes in long-term survivors of infantile-onset Pompe disease: A longitudinal follow-up. *Mol Genet Metab.* 2017;121(2):127-137.
128. Boucek D, Jirikowic J, Taylor M. Natural history of Danon disease. *Genet Med.* 2011;13(6):563-568.
129. Kashio N, Usuki F, Akamine T, et al. Cardiomyopathy, mental retardation, and autophagic vacuolar myopathy. Abnormal MRI findings in the head. *J Neurol Sci.* 1991;105(1):1-5.
130. Hobson-Webb LD, Proia AD, Thurberg BL, Banugaria S, Prater SN, Kishnani PS. Autopsy findings in late-onset Pompe disease: A case report and systematic review of the literature. *Mol Genet Metab.* 2012;106(4):462-469.
131. Lim JA, Li L, Raben N. Pompe disease: From pathophysiology to therapy and back again. *Front Aging Neurosci.* 2014;6(JUL):1-14.
132. Sidman RL, Shihabuddin LS. Temporal Neuropathologic and Behavioral Phenotype of 6neo/6neo Pompe Disease Mice. *J Neuropathol Exp Neurol.* Published online July 2008:1-16.
133. Lim JA, Yi H, Gao F, Raben N, Kishnani PS, Sun B. Intravenous Injection of an AAV-PHP.B Vector Encoding Human Acid  $\alpha$ -Glucosidase Rescues Both Muscle and CNS Defects in Murine Pompe Disease. *Mol Ther - Methods Clin Dev.* 2019;12(March):233-245.
134. Thurberg BL, Maloney CL, Vaccaro C, et al. Characterization of pre- and post-treatment pathology after enzyme replacement therapy for Pompe disease. *Lab Invest.* 2006;86(12):1208-1220.
135. Do H V., Khanna R, Gotschall R. Challenges in treating Pompe disease: an industry perspective. *Ann Transl Med.* 2019;7(13):291-291.
136. Guo J, Kelton CML, Guo JJ. Recent developments, utilization, and spending trends for pompe disease therapies. *Am Heal Drug Benefits.* 2012;5(3):182-189.
137. Kishnani P, Lachmann R, Mozaffar T, et al. Safety and efficacy of VAL-1221, a novel fusion protein targeting cytoplasmic glycogen, in patients with late-onset Pompe disease. *Mol Genet Metab.* 2019;126(2):S85-S86.
138. Rohn TT. Corpora Amylacea in Neurodegenerative Diseases: Cause or Effect? *Int J Neurol Neurother.* 2015;2(2):1-4.
139. Takeda T, Hosokawa M, Higuchi K, Hosono M, Akiguchi I, Katoh H. A novel murine model of aging, Senescence-Accelerated Mouse (SAM). *Arch Gerontol Geriatr.* 1994;19(2):185-192.
140. Hosokawa M, Kasai R, Higuchi K, et al. Grading score system: A method for evaluatoin of the degress of senescence in senescence accelerated mouse (SAM).

- Mech Ageing Dev.* 1984;26:91-102.
141. Ramsey HJ. Ultrastructure of Corpora Amylacea. *J Neuropathol Exp Neurol.* 1965;24:25-29.
  142. Cenacchi G, Papa V, Costa R, et al. Update on polyglucosan storage diseases. 2019;475:1-16.
  143. Lin A-L, Laird AR, Fox PT, Gao J-H. Multimodal MRI Neuroimaging Biomarkers for Cognitive Normal Adults, Amnesic Mild Cognitive Impairment, and Alzheimer's Disease. *Neurol Res Int.* 2012;2012(9):1-17.
  144. Jiang J, Sun Y, Zhou H, et al. Study of the Influence of Age in 18F-FDG PET Images Using a Data-Driven Approach and Its Evaluation in Alzheimer's Disease. *Contrast Media Mol Imaging.* 2018;2018(2):1-16.
  145. Ivanisevic J. Metabolic drift in the aging brain. *Aging (Albany NY).* 2016;8(5):1-14.
  146. Zhang F, Kerbl-Knapp J, Akhmetshina A, et al. Tissue-Specific Landscape of Metabolic Dysregulation during Ageing. 2021;11:235.
  147. Azzu V, Valencak TG. Energy Metabolism and Ageing in the Mouse: A Mini-Review. *Gerontology.* 2017;63(4):327-336.
  148. Gertz HJ, Cervos-Navarro J, Frydl V, Schultz F. Glycogen Accumulation of the Aging Human Brain. *Mech Ageing Dev.* 1985;31:25-35.
  149. Márquez M, Pérez L, Serafin A, Teijeira S, Navarro C, Pumarola M. Characterisation of Lafora-like bodies and other polyglucosan bodies in two aged dogs with neurological disease. *Vet J.* 2010;183(2):222-225.
  150. Kimura T, Takamatsu J, Miyata T, Miyakawa T, Horiuchi S. Localization of identified advanced glycation end-product structures, N $\epsilon$ -(carboxymethyl)lysine and pentosidine, in age-related inclusions in human brains. *Pathol Int.* 1998;48(8):575-579.
  151. Iwaki T, Hamada Y, Tateishi J. Advanced glycosylation end-products and heat shock proteins accumulate in the basophilic degeneration of the myocardium and the corpora amylacea of the glia. *Pathol Int.* 1996;46(10):757-763.
  152. Cisse S, Perry G, Lacoste-Royal G, Cabana T, Gauvreau D. Acta Neuropathologm Immunochemical identification of ubiquitin and heat-shock proteins in corpora amylacea from normal aged and Alzheimer's disease brains\*. *Acta Neuropathol.* 1993;85:233-240.
  153. Abdel Ghaffar NF, Asiri RN, AL-Eitan LN, et al. Improving public stigma, sociocultural beliefs, and social identity for people with epilepsy in the Aseer region of Saudi Arabia. *Epilepsy Behav Reports.* 2021;16:100442.
  154. Zack M, Kobu R. National and state estimates of the numbers of adults and

- children with active epilepsy. *Morb Mortal Wkly Rep.* 2017;66(31):821-825.
155. Annegers JF, Rocca WA. Causes of epilepsy: Contributions of the rochester epidemiology project. *Mayo Clin Proc.* 1996;71(6):570-575.
  156. Pyrzowski J, Le Douget JE, Fouad A, Siemiński M, Jędrzejczak J, Le Van Quyen M. Zero-crossing patterns reveal subtle epileptiform discharges in the scalp EEG. *Sci Rep.* 2021;11(1):1-11.
  157. Chen Z, Brodie MJ, Liew D, Kwan P. Treatment Outcomes in Patients With Newly Diagnosed Epilepsy Treated With Established and New Antiepileptic Drugs. *JAMA Neurol.* 2018;75(3):278-279.
  158. Gleichgerrcht E, Keller SS, Drane DL, et al. Temporal Lobe Epilepsy Surgical Outcomes Can Be Inferred Based on Structural Connectome Hubs: A Machine Learning Study. *Ann Neurol.* 2020;88(5):970-983.
  159. Jaisani Z, Miletich RS, Ramanathan M, Weinstock AL. Clinical FDG-PET Findings in Patients with Temporal Lobe Epilepsy: Concordance with EEG and MRI. *J Neuroimaging.* 2019;30(1):119-125.
  160. Sequeira KM, Tabesh A, Sainju RK, et al. Perfusion Network Shift during Seizures in Medial Temporal Lobe Epilepsy. *PLoS One.* 2013;8(1).
  161. Spencer SS, Spencer DD. Entorhinal-Hippocampal Interactions in Medial Temporal Lobe Epilepsy. *Epilepsia.* 1994;35(4):721-727.
  162. Spencer DD, Gerrard JL, Zaveri HP. The roles of surgery and technology in understanding focal epilepsy and its comorbidities. *Lancet Neurol.* 2018;17(4):373-382.
  163. Abubakr A, Wambacq I, Donahue JE, Zappulla R. The presence of polyglucosan bodies in temporal lobe epilepsy: its role and significance. *J Clin Neurosci.* 2005;12(8):911-914.
  164. Streichenberger N, Ryvlin P, Guénot M, Sindou M, Kopp N, Mauguière F. Polyglucosan bodies and temporal lobe epilepsy: an incidental finding or more? . *Clin Neurophathology.* 2001;20(4):172-175.
  165. MacKenzie JM. Polyglucosan bodies are not an unusual finding in temporal lobe epilepsy. 1993;56(5):577.
  166. Chung MH, Horoupian DS. Corpora Amylacea: A Marker for Mesial Temporal Sclerosis. 1996;55(4):403-408.
  167. Akman CI, Ichise M, Olsavsky A, Tikofsky RS, Heertum RLV, Gilliam F. Epilepsy duration impacts on brain glucose metabolism in temporal lobe epilepsy: Results of voxel-based mapping. *Epilepsy Behav.* 2010;17(3):373-380.
  168. Eid T, Tu N, Lee TSW, Lai JCK. Regulation of astrocyte glutamine synthetase in

- epilepsy. *Neurochem Int.* 2013;63(7):670-681.
169. Petroff OAC, Errante LD, Rothman DL, Kim JH, Spencer DD. Glutamate-glutamine cycling in the epileptic human hippocampus. *Epilepsia.* 2002;43(7):703-710.
  170. Choi JY, Kim SJ, Hong SB, et al. Extratemporal hypometabolism on FDG PET in temporal lobe epilepsy as a predictor of seizure outcome after temporal lobectomy. *Eur J Nucl Med Mol Imaging.* 2003;30(4):581-587.
  171. Wender R, Brown AM, Fern R, Swanson RA, Farrell K, Ransom BR. Astrocytic glycogen influences axon function and survival during glucose deprivation in central white matter. *J Neurosci.* 2000;20(18):6804-6810.
  172. Schousboe A, Sickmann HM, Walls AB, Bak LK, Waagepetersen HS. Functional Importance of the Astrocytic Glycogen-Shunt and Glycolysis for Maintenance of an Intact Intra/Extracellular Glutamate Gradient. *Neurotox Res.* 2010;18(1):94-99.
  173. Kivi A, Lehmann TN, Kovács R, et al. Effects of barium on stimulus-induced rises of  $[K^+]_o$  in human epileptic non-sclerotic and sclerotic hippocampal area CA1. *Eur J Neurosci.* 2000;12(6):2039-2048.
  174. Papageorgiou IE, Gabriel S, Fetani AF, Kann O, Heinemann U. Redistribution of astrocytic glutamine synthetase in the hippocampus of chronic epileptic rats. *Glia.* 2011;59(11):1706-1718.
  175. Binder DK. Astrocytes: Stars of the Sacred Disease. *Epilepsy Curr.* 2018;18(3):172-179.
  176. Brito MD, da Silva GFG, Tilieri EM, Araujo BG, Calió ML, Rosenstock TR. Metabolic Alteration and Amyotrophic Lateral Sclerosis Outcome: A Systematic Review. *Front Neurol.* 2019;10:315-346.
  177. Paramp B, Lehmann M, Beaudin M, et al. Misfolded SOD1 pathology in sporadic Amyotrophic Lateral Sclerosis. *Sci Rep.* Published online September 2018:1-13.
  178. Vandoorne T, De Bock K, Van Den Bosch L. Energy metabolism in ALS: an underappreciated opportunity? *Acta Neuropathol.* 2018;135(4):489-509.
  179. Pradat P-F, Rogers M-L, Longone P, et al. Biomarkers of Metabolism in Amyotrophic Lateral Sclerosis. *Biomarkers Metab Amyotroph Lateral Sclerosis Front Neurol.* 2019;10:191. [www.frontiersin.org](http://www.frontiersin.org)
  180. De Vocht J, Blommaert J, Devrome M, et al. Use of multimodal imaging and clinical biomarkers in presymptomatic carriers of C9orf72 repeat expansion. *JAMA Neurol.* 2020;77(8):1008-1017.
  181. Chew S, Atassi N. Positron Emission Tomography Molecular Imaging Biomarkers for Amyotrophic Lateral Sclerosis. *Front Neurol.* 2019;10:1113-1171.
  182. Miyazaki K, Masamoto K, Morimoto N, et al. Early and progressive impairment of



- spinal blood flow-glucose metabolism coupling in motor neuron degeneration of ALS model mice. *J Cereb Blood Flow Metab.* 2012;32:456-467.
183. Christidi F, Petri S, Pharaoh G, et al. Metabolic and Stress Response Changes Precede Disease Onset in the Spinal Cord of Mutant SOD1 ALS Mice. Published online 2019.
  184. Wills AM, Hubbard J, Macklin EA, et al. Hypercaloric enteral nutrition in patients with amyotrophic lateral sclerosis: A randomised, double-blind, placebo-controlled phase 2 trial. *Lancet.* 2014;383(9934):2065-2072.
  185. Manzo E, Lorenzini I, Barrameda D, et al. Glycolysis upregulation is neuroprotective as a compensatory mechanism in ALS. *Elife.* 2019;8.
  186. Kirby J, Ning K, Ferraiuolo L, et al. Phosphatase and tensin homologue/protein kinase B pathway linked to motor neuron survival in human superoxide dismutase 1-related amyotrophic lateral sclerosis. *Brain.* 2011;134(2):506-517.
  187. Dodge JC, Treleaven CM, Pacheco J, et al. Glycosphingolipids are modulators of disease pathogenesis in amyotrophic lateral sclerosis. *Proc Natl Acad Sci.* 2015;112(26):8100-8105.
  188. Vandoorne T, Veys K, Guo W, et al. Differentiation but not ALS mutations in FUS rewires motor neuron metabolism. *Nat Commun.* Published online September 2019:1-12.
  189. Rajan KB, Weuve J, Barnes LL, McAninch EA, Wilson RS, Evans DA. Population estimate of people with clinical Alzheimer's disease and mild cognitive impairment in the United States (2020-2060). *Alzheimers Dement.*
  190. Ward A, Crean S, Mercaldi CJ, et al. Prevalence of Apolipoprotein E4 genotype and homozygotes (APOE e4/4) among patients diagnosed with alzheimer's disease: A systematic review and meta-analysis. *Neuroepidemiology.* 2012;38(1):1-17.
  191. Adeniji AO, Adams PW, Mody V V. Amyloid  $\beta$  Hypothesis in the Development of Therapeutic Agents for Alzheimer's Disease. In: *Drug Discovery Approaches for the Treatment of Neurodegenerative Disorders.* Elsevier; 2017:109-143.
  192. Ganguly G, Chakrabarti S, Chatterjee U, Saso L. Proteinopathy, oxidative stress and mitochondrial dysfunction: Cross talk in alzheimer's disease and parkinson's disease. *Drug Des Devel Ther.* 2017;11:797-810.
  193. Braak H, Alafuzoff I, Arzberger T, Kretschmar H, Tredici K. Staging of Alzheimer disease-associated neurofibrillary pathology using paraffin sections and immunocytochemistry. *Acta Neuropathol.* 2006;112(4):389-404.
  194. Braak H, Braak E. *Neuropathological Stageing of Alzheimer-Related Changes.* Vol 82.; 1991.

195. Valasani KR, Carlson E, Vangavaragu JR, Yan SS. Mitochondria as a Therapeutic Target for the Treatment of Alzheimer's Disease. In: *Drug Discovery Approaches for the Treatment of Neurodegenerative Disorders*. Elsevier Inc.; 2016:195-209.
196. Brandon JA, Farmer BC, Williams HC, Johnson LA. APOE and alzheimer's disease: Neuroimaging of metabolic and cerebrovascular dysfunction. *Front Aging Neurosci*. 2018;10(JUN):1-8.
197. Chen Z, Zhong C. Decoding Alzheimer's disease from perturbed cerebral glucose metabolism: Implications for diagnostic and therapeutic strategies. *Prog Neurobiol*. 2013;108:21-43.
198. Costantini LC, Barr LJ, Vogel JL, Henderson ST. Hypometabolism as a therapeutic target in Alzheimer's disease. *BMC Neurosci*. 2008;9(SUPPL. 2):1-9.
199. Cunnane S, Nugent S, Roy M, et al. Brain fuel metabolism, aging, and Alzheimer's disease. *Nutrition*. 2011;27(1):3-20.
200. Zulfiqar S, Garg P, Nieweg K. Contribution of astrocytes to metabolic dysfunction in the Alzheimer's disease brain. *Biol Chem*. 2019;400(9):1113-1127.
201. Frost GR, Li Y-M. The role of astrocytes in amyloid production and Alzheimer's disease.
202. Halim ND, Mcfate T, Mohyeldin A, et al. Phosphorylation status of pyruvate dehydrogenase distinguishes metabolic phenotypes of cultured rat brain astrocytes and neurons. *Glia*. 2010;58(10):1168-1176.
203. Yao J, Rettberg JR, Klosinski LP, Cadenas E, Brinton RD. Shift in brain metabolism in late onset Alzheimer's disease: Implications for biomarkers and therapeutic interventions. *Mol Aspects Med*. 2011;32(4-6):247-257.
204. Ceravolo R, Borghetti D, Kiferle L, et al. CSF phosphorylated TAU protein levels correlate with cerebral glucose metabolism assessed with PET in Alzheimer's disease. *Brain Res Bull*. 2008;76(1-2):80-84.
205. Heckmann BL, Teubner BJW, Tummers B, et al. LC3-Associated Endocytosis Facilitates  $\beta$ -Amyloid Clearance and Mitigates Neurodegeneration in Murine Alzheimer's Disease. *Cell*. 2019;178(3):536-551.e14.
206. Tondo G, Iaccarino L, Caminiti SP, et al. The combined effects of microglia activation and brain glucose hypometabolism in early-onset Alzheimer's disease. *Alzheimer's Res Ther*. 2020;12(1):1-10.
207. Bass B, Upson S, Roy K, Montgomery EL, Jalonen TO, Murray IVJ. Glycogen and amyloid-beta: Key players in the shift from neuronal hyperactivity to hypoactivity observed in Alzheimer's disease? *Neural Regen Res*. 2015;10(7):1023-1025.
208. Koivisto H, Leinonen H, Puurula M, et al. Chronic Pyruvate Supplementation Increases Exploratory Activity and Brain Energy Reserves in Young and Middle-

- Aged Mice. *Front Aging Neurosci.* 2016;8(Pt 2):614-621.
209. Andres DA, Young LEA, Veeranki S, et al. Improved workflow for mass spectrometry-based metabolomics analysis of the heart. *J Biol Chem.* 2020;295(9):2676-2686.
  210. Bélanger M, Allaman I, Magistretti PJ. Brain Energy Metabolism: Focus on Astrocyte-Neuron Metabolic Cooperation. *Cell Metab.* 2011;14(6):724-738.
  211. Lord L-D, Expert P, Huckins JF, Turkheimer FE. Cerebral energy metabolism and the brain's functional network architecture: an integrative review. *J Cereb Blood Flow Metab.* 2013;33:1347-1354.
  212. Vaishnavi SN, Vlassenko AG, Rundle MM, Snyder AZ, Mintun MA, Raichle ME. Regional aerobic glycolysis in the human brain.
  213. Hirase H, Akther S, Wang X, Oe Y. Glycogen distribution in mouse hippocampus. *J Neurosci Res.* 2019;97(8):923-932.
  214. Zhou Z, Austin GL, Shaffer R, Armstrong DD, Gentry MS. Antibody-Mediated Enzyme Therapeutics and Applications in Glycogen Storage Diseases. *Trends Mol Med.* 2019;12:1094-1109.
  215. Sanchez-Elexpuru G, Serratosa JM, Sanchez MP. Sodium selenate treatment improves symptoms and seizure susceptibility in a malin-deficient mouse model of Lafora disease. *Epilepsia.* 2017;58(3):467-475.
  216. DePaoli-Roach AA, Tagliabracci VS, Segvich DM, Meyer CM, Irimia JM, Roach PJ. Genetic depletion of the malin E3 ubiquitin ligase in mice leads to lafora bodies and the accumulation of insoluble laforin. *J Biol Chem.* 2010;285(33):25372-25381.
  217. Ganesh S, Delgado-Escueta A V., Sakamoto T, et al. Targeted disruption of the Epm2a gene causes formation of Lafora inclusion bodies, neurodegeneration, ataxia, myoclonus epilepsy and impaired behavioral response in mice. *Hum Mol Genet.* 2002;11(11):1251-1262.
  218. Garcia-Cabrero AM, Marinas A, Guerrero R, de Cordoba SR, Serratosa JM, Sanchez MP. Laforin and malin deletions in mice produce similar neurologic impairments. *J Neuropathol Exp Neurol.* 2012;71(5):413-421.
  219. Garcia-Cabrero AM, Sanchez-Elexpuru G, Serratosa JM, Sanchez MP. Enhanced sensitivity of laforin- and malin-deficient mice to the convulsant agent pentylenetetrazole. *Front Neurosci.* 2014;8:291.
  220. Tiberia E, Turnbull J, Wang T, et al. Increased Laforin and Laforin Binding to Glycogen Underlie Lafora Body Formation in Malin-deficient Lafora Disease. *J Biol Chem.* 2012;287(30):25650-25659.
  221. Lopez-Gonzalez I, Viana R, Sanz P, Ferrer I. Inflammation in Lafora Disease:

- Evolution with Disease Progression in Laforin and Malin Knock-out Mouse Models. *Mol Neurobiol.* 2017;54(5):3119-3130.
222. Chan EM, Ackerley CA, Lohi H, et al. Laforin preferentially binds the neurotoxic starch-like polyglucosans, which form in its absence in progressive myoclonus epilepsy. *Hum Mol Genet.* 2004;13(11):1117-1129.
  223. Ahonen S, Nitschke S, Grossman TR, et al. Gys1 antisense therapy rescues neuropathological bases of murine Lafora disease. *Brain.* Published online 2021:1-21.
  224. Hotchkiss RD. A microchemical reaction resulting in the staining of polysaccharide structures in fixed tissue preparations. *Arch Biochem.* 1948;16(1):131-141.
  225. Yokota T, Ishihara T, Yoshida H, Takahashi M, Uchino F, Hamanaka S. Monoclonal Antibody Against Polyglucosan Isolated from the Myocardium of a Patient with Lafora Disease. *J Neurophathology Exp Neurol.* 1988;47(5):572-277.
  226. Yokota T, Ishihara T, Kawano H, et al. Immunological homogeneity of lafora body, corpora amylacea, basophilic degeneration in heart, and intracytoplasmic inclusions of liver and heart in type IV glycogenosis. *Acta Pathol.* 1987;37(6):941-946.
  227. Reusche E, Aksu F, Goebel HH, Shin YS, Yokota T, Reichmann H. A mild juvenile variant of type IV glycogenosis. *Brain Dev.* 1992;14(1):36-43.
  228. Goebel HH, Shin YS, Gullotta F, et al. Adulte Polyglucosan Body Myopathy. *J Neuropathol Exp Neuropathol Exp.* 1992;51(1):24-35.
  229. Yamanami S, Ishihara T, Takahashi M, Uchino F. Comparative Study of Intra neuronal Polyglucosan Bodies in Brains from Patients with Lafora Disease and Aged Dogs. *Japanese Soc Pathol.* 1992;42(11):787-792.
  230. Tamura S, Takahashi M, Kawamura S, Ishihara T. Basophilic degeneration of the myocardium: histological immunohistochemical and immunoelectronmicroscopic studies. *Histopathology.* 1995;26:501-508.
  231. Ortolano S, Vieitez I, Agis-Balboa RC, Spuch C. Loss of GABAergic cortical neurons underlies the neuropathology of Lafora disease. *Mol Brain.* 2014;7(1):1-17.
  232. O'Shea AM, Wilson GJ, Ling SC, Minassian BA, Turnbull J, Cutz E. Lafora-like ground-glass inclusions in hepatocytes of pediatric patients: A report of two cases. *Pediatr Dev Pathol.* 2007;10(5):351-357.
  233. Hashimoto K, Hoshii Y, Takahashi M, et al. Use of a monoclonal antibody against Lafora bodies for the immunocytochemical study of ground-glass inclusions in hepatocytes due to cyanamide. *Histopathology.* 2001;39(1):60-65.
  234. Mitsuno S, Takahashi M, Gondo T, et al. Immunohistochemical, conventional and immunoelectron microscopical characteristics of Periodic Acid-Schiff-positive

- granules in the mouse brain. *Acta Neuropathol.* 1999;98(1):31-38.
235. Baba O. [Production of monoclonal antibody that recognizes glycogen and its application for immunohistochemistry]. *口腔病学会雑誌 [[コウコウビョウガツカイザッシ]]*. 1993;60(2):264-287.
236. Ganesh S, Tsurutani N, Suzuki T, et al. The carbohydrate-binding domain of Lafora disease protein targets Lafora polyglucosan bodies. *Biochem Biophys Res Commun.* 2004;313(4):1101-1109.
237. Yasuda M, Furuyashiki T, Nakamura T, Kakutani R, Takata H, Ashida H. Immunomodulatory activity of enzymatically synthesized glycogen and its digested metabolite in a co-culture system consisting of differentiated Caco-2 cells and RAW264.7 macrophages. *Food Funct.* 2013;4(9):1387-1393.
238. Van De Weerd R, Berbís MA, Sparrius M, et al. A Murine Monoclonal Antibody to Glycogen: Characterization of Epitope-Fine Specificity by Saturation Transfer Difference (STD) NMR Spectroscopy and Its Use in Mycobacterial Capsular  $\alpha$ -Glucan Research. *ChemBioChem.* 2015;16(6):977-989.
239. Koliwer-Brandl H, Syson K, van de Weerd R, et al. Metabolic Network for the Biosynthesis of Intra- and Extracellular  $\alpha$ -Glucans Required for Virulence of *Mycobacterium tuberculosis*. *PLoS Pathog.* 2016;12(8):1-26.
240. Nakamura-Tsuruta S, Yasuda M, Nakamura T, et al. Comparative analysis of carbohydrate-binding specificities of two anti-glycogen monoclonal antibodies using ELISA and surface plasmon resonance. *Carbohydr Res.* 2012;350:49-54.
241. Oe Y, Wang X, Patriarchi T, et al. Distinct temporal integration of noradrenaline signaling by astrocytic second messengers during vigilance. *Nat Commun.* 2020;11(1):3-8.
242. Oe Y, Wang X, Patriarchi T, et al. Author Correction: Distinct temporal integration of noradrenaline signaling by astrocytic second messengers during vigilance (Nature Communications, (2020), 11, 1, (471), 10.1038/s41467-020-14378-x). *Nat Commun.* 2020;11(1):41467.
243. Sani M, Houben ENG, Geurtsen J, et al. Direct visualization by Cryo-EM of the mycobacterial capsular layer: A labile structure containing ESX-1-secreted proteins. *PLoS Pathog.* 2010;6(3).
244. Skurat A V., Segvich DM, Depaoli-Roach AA, Roach PJ. Novel method for detection of glycogen in cells. *Glycobiology.* 2017;27(5):416-424.
245. Van De Weerd R, Boot M, Maaskant J, et al. Inorganic phosphate limitation modulates capsular polysaccharide composition in mycobacteria. *J Biol Chem.* 2016;291(22):11787-11799.
246. Vainchtein ID, Molofsky A V. Astrocytes and Microglia: In Sickness and in Health.

*Trends Neurosci.* 2020;43(3):144-154.

247. Nitschke S, Chown EE, Xiaochu Z, et al. An inducible glycogen synthase-1 knockout halts but does not reverse lafora disease progression in mice. *J Biol Chem.* 2021;296:1-12.
248. Wang Y, Ma K, Wang P, et al. Laforin Prevents Stress-Induced Polyglucosan Body Formation and Lafora Disease Progression in Neurons. *Mol Neurobiol.* 2013;48(1):49-61.
249. Berthier A, Paya M, Garcia-Cabrero AM, et al. Pharmacological Interventions to Ameliorate Neuropathological Symptoms in a Mouse Model of Lafora Disease. *Mol Neurobiol.* 2016;53(2):1296-1309.
250. Sanz P, Serratosa JM. Neuroinflammation and progressive myoclonus epilepsies: From basic science to therapeutic opportunities. *Expert Rev Mol Med.* 2020;22.
251. Lahuerta M, Gonzalez D, Aguado C, et al. Reactive Glia-Derived Neuroinflammation: a Novel Hallmark in Lafora Progressive Myoclonus Epilepsy That Progresses with Age. *Mol Neurobiol.* 2020;57(3):1607-1621.
252. Sinha P, Verma B, Ganesh S. Dexamethasone-induced activation of heat shock response ameliorates seizure susceptibility and neuroinflammation in mouse models of Lafora disease. *Exp Neurol.* Published online 2021:113656.
253. Hedberg-Oldfors C, Oldfors A. Polyglucosan storage myopathies. *Mol Aspects Med.* 2015;46(C):85-100.
254. Machado-Salas J, Avila-Costa MR, Guevara P, et al. Ontogeny of Lafora bodies and neurocytoskeleton changes in Laforin-deficient mice. *Exp Neurol.* 2012;236(1):131-140.
255. Ai-Ling Lin DLR. What have novel imaging techniques revealed about metabolism in the aging brain? *Future Neurol.* 2014;9(3):341-354.
256. Siegel GJ, Agranoff BW. *Basic Neurochemistry : Molecular, Cellular and Medical Aspects.* 6th ed. (Siegel GJ, Agranoff BW, eds.). Lippincott-Raven; 1999.
257. Melendez-Hevia E, Waddell TG, Shelton ED. Optimization of molecular design in the evolution of metabolism: The glycogen molecule. *Biochem J.* 1993;295(2):477-483.
258. Contreras CJ, Segvich DM, Mahalingan K, et al. Incorporation of phosphate into glycogen by glycogen synthase. *Arch Biochem Biophys.* 2016;597:21-29.
259. Chandramouli C, Varma U, Stevens EM, et al. Myocardial glycogen dynamics: New perspectives on disease mechanisms. *Clin Exp Pharmacol Physiol.* 2015;42(4):415-425.
260. Lowery OH, Passonneau J V., Hasselberger FX, Schulz DW. Effect of ischemia on

- known substrates and cofactors of the glycolytic pathway in the brain. *J Biol Chem*. 1964;239(1):18-30.
261. Hutchins DA, Rogers KJ. Physiological and drug-induced changes in the glycogen content of mouse brain. *Br J Pharmacol*. 1970;39(1):9-25.
  262. López-Otín C, Blasco MA, Partridge L, Serrano M, Kroemer G. The hallmarks of aging. *Cell*. 2013;153(6):1194.
  263. Tiberia E, Turnbull J, Wang T, et al. Increased Laforin and Laforin Binding to Glycogen Underlie Lafora Body Formation in Malin-deficient Lafora Disease. *J Biol Chem*. 2012;287(30):25650.
  264. Srivastava S. Emerging Insights into the Metabolic Alterations in Aging Using Metabolomics. *Metabolites*. 2019;9(12):301-316.
  265. Uchitomi R, Hatazawa Y, Senoo N, et al. Metabolomic Analysis of Skeletal Muscle in Aged Mice. *Sci Rep*. Published online July 2019:1-11.
  266. Houtkooper RH, Argmann C, Houten SM, et al. The metabolic footprint of aging in mice. *Sci Rep*. 2011;1(1):9-11.
  267. Parihar R, Rai A, Ganesh S. Lafora disease: from genotype to phenotype. *J Genet*. 2018;97(3):611-624.
  268. Hunsberger HC, Greenwood BP, Tolstikov V, Narain NR, Kiebish MA, Denny CA. Divergence in the metabolome between natural aging and Alzheimer's disease. *Sci Rep*. 2020;10(1):1-15.
  269. Kizuka Y, Kitazume S, Taniguchi N. N-glycan and Alzheimer's disease. *Biochim Biophys Acta - Gen Subj*. 2017;1861(10):2447-2454.
  270. Endo T. Glycans and glycan-binding proteins in brain: galectin-1-induced expression of neurotrophic factors in astrocytes. *Curr Drug Targets*. 2005;6(4):427-436.
  271. Tang B, Frasinuk MS, Chikwana VM, et al. Discovery and Development of Small-Molecule Inhibitors of Glycogen Synthase. *J Med Chem*. 2020;63(7):3538-3551.
  272. Tagliabracci VS, Roach PJ. Insights into the mechanism of polysaccharide dephosphorylation by a glucan phosphatase. *PNAS*. 2010;107(35):15312-15313.
  273. Sakai M, Austin J, Witmer F, Trueb L. Studies of Corpora Amylacea I. Isolation and Preliminary characterization by Chemical and Histochemical Techniques. *Arch Neurol*. 1969;21:1-20.
  274. Gentry MS, Brewer MK, Vander Kooi CW. Structural biology of glucan phosphatases from humans to plants. *Curr Opin Struct Biol*. 2016;40:62-69.
  275. Meekins DA, Vander Kooi CW, Gentry MS. Structural mechanisms of plant glucan phosphatases in starch metabolism. *FEBS J*. 2016;283:2427-2447.

276. Raththagala M, Brewer MK, Parker MW, et al. Structural Mechanism of Laforin Function in Glycogen Dephosphorylation and Lafora Disease. *Mol Cell*. 2015;57(2):261-272.
277. Romá-Mateo C, Sanz P, Gentry MS. Deciphering the role of malin in the lafora progressive myoclonus epilepsy. *IUBMB Life*. 2012;64(10):801-808.
278. Gayarre J, Duran-Trio L, Criado-Garcia O, et al. The phosphatase activity of laforin is dispensable to rescue Epm2a mice from Lafora disease. *Brain*. 2014;137(3):806-818.
279. Beghein E, Gettemans J. Nanobody technology: A versatile toolkit for microscopic imaging, protein-protein interaction analysis, and protein function exploration. *Front Immunol*. 2017;8:1-14.
280. Muyldermans S. Nanobodies: natural single-domain antibodies. *Annu Rev Biochem*. 2013;82(1):775-797.
281. Hamers-Casterman C, Atarhouch T, Muyldermans S, et al. Naturally occurring antibodies devoid of light chains. *Nature*. 1993;363(June):446-448.
282. Könning D, Zielonka S, Grzeschik J, et al. Camelid and shark single domain antibodies: structural features and therapeutic potential. *Curr Opin Struct Biol*. 2017;45:10-16.
283. Sánchez-Martín P, Raththagala M, Bridges TM, et al. Dimerization of the Glucan Phosphatase Laforin Requires the Participation of Cysteine 329. Bogoy M, ed. *PLoS One*. 2013;8(7):e69523-11.
284. Larkin MA, Blackshields G, Brown NP, et al. Clustal W and Clustal X version 2.0. *Bioinformatics*. 2007;23(21):2947-2948.
285. Letunic I, Bork P. Interactive Tree of Life v2: Online annotation and display of phylogenetic trees made easy. *Nucleic Acids Res*. 2011;39(SUPPL. 2):475-478.
286. Chow KM, Whiteheart SW, Smiley JR, et al. Immunization of alpacas (*Lama pacos*) with protein antigens and production of antigen-specific single domain antibodies. *J Vis Exp*. 2019;2019(143):1-7.
287. Zhang Z, Liang WG, Bailey LJ, et al. Ensemble cryoEM elucidates the mechanism of insulin capture and degradation by human insulin degrading enzyme. *Elife*. 2018;7:1-28.
288. Stefely JA, Reidenbach AG, Ulbrich A, et al. Mitochondrial ADCK3 employs an atypical protein kinase-like fold to enable coenzyme Q Biosynthesis. *Mol Cell*. 2015;57(1):83-94.
289. Zhang Z, Smith DL. Determination of amide hydrogen exchange by mass spectrometry: A new tool for protein structure elucidation. *Protein Sci*. 1993;2(4):522-531.



290. Sherwood AR, Paasch BC, Worby CA, Gentry MS. A malachite green-based assay to assess glucan phosphatase activity. *Anal Biochem.* 2013;435(1):54-56.
291. Sharma S, Vander Kooi CD, Gentry MS, Vander Kooi CW. Oligomerization and carbohydrate binding of glucan phosphatases. *Anal Biochem.* 2018;563(October):51-55.
292. Gentry MS, Downen RH, Worby CA, Mattoo S, Ecker JR, Dixon JE. The phosphatase laforin crosses evolutionary boundaries and links carbohydrate metabolism to neuronal disease. *J Cell Biol.* 2007;178(3):477-488.
293. Ianzano L, Young EJ, Zhao XC, et al. Loss of function of the cytoplasmic isoform of the protein laforin (EPM2A) causes Lafora progressive myoclonus epilepsy. *Hum Mutat.* 2004;23(2):170-176.
294. Meekins DA, Raththagala M, Auger KD, et al. Mechanistic insights into glucan phosphatase activity against polyglucan substrates. *J Biol Chem.* 2015;290(38):23361-23370.
295. Blennow A, Bay-Smidt AM, Olsen CE, Møller BL. The distribution of covalently bound phosphate in the starch granule in relation to starch crystallinity. *Int J Biol Macromol.* 2000;27(3):211-218.
296. Ianzano L, Young EJ, Zhao XC, et al. Loss of Function of the Cytoplasmic Isoform of the Protein Laforin (EPM2A) Causes Lafora Progressive Myoclonus Epilepsy. *Hum Mutat.* 2004;23(2):170-176.
297. Tagliabracci VS, Heiss C, Karthik C, et al. Phosphate Incorporation during Glycogen Synthesis and Lafora Disease. *Cell Metab.* 2011;13(3):274-282.
298. DePaoli-Roach AA, Contreras CJ, Segvich DM, et al. Glycogen phosphomonoester distribution in mouse models of the progressive myoclonic epilepsy, Lafora disease. *J Biol Chem.* 2015;290(2):841-850.
299. Cheloha RW, Harmand TJ, Wijne C, Schwartz TU, Ploegh HL. Exploring cellular biochemistry with nanobodies. *J Biol Chem.* 2020;295(45):15307-15327.
300. Schumacher D, Helma J, Schneider AFL, Leonhardt H, Hackenberger CPR. Nanobodies: Chemical Functionalization Strategies and Intracellular Applications. *Angew Chemie - Int Ed.* 2018;57(9):2314-2333.
301. Moreno D, Towler MC, Hardie DG, Knecht E, Sanz P. The laforin-malin complex, involved in Lafora disease, promotes the incorporation of K63-linked ubiquitin chains into AMP-activated protein kinase  $\beta$  subunits. *Mol Biol Cell.* 2010;21(15):2578-2588.
302. Rubio-Villena C, Garcia-Gimeno MA, Sanz P. Glycogenic activity of R6, a protein phosphatase 1 regulatory subunit, is modulated by the laforin-malin complex. *Int J Biochem Cell Biol.* 2013;45(7):1479-1488.

303. Ganesh S, Lal Agarwala K, Ueda K, et al. Laforin, defective in the progressive myoclonus epilepsy of Lafora type, is a dual-specificity phosphatase associated with polyribosomes. *Hum Mol Genet.* 2000;9(15):2251-2261.
304. Minassian BA, Ianzano L, Meloche M, et al. Mutation spectrum and predicted function of laforin in Lafora's progressive myoclonus epilepsy. *Neurology.* 2000;55(3):341-346.
305. Panza P, Maier J, Schmees C, Rothbauer U, Sollner C. Live imaging of endogenous protein dynamics in zebrafish using chromobodies. *Development.* 2015;142(10):1879-1884.
306. Traenkle B, Rothbauer U. Under the Microscope: Single-Domain Antibodies for Live-Cell Imaging and Super-Resolution Microscopy. *Front Immunol.* 2017;8:86.
307. Bertier L, Boucherie C, Zwaenepoel O, et al. Inhibitory cortactin nanobodies delineate the role of NTA- and SH3-domain-specific functions during invadopodium formation and Cancer cell invasion. *FASEB J.* 2017;31(6):2460-2476.
308. Dawkins HJS, Draghia-Akli R, Lasko P, et al. Progress in Rare Diseases Research 2010–2016: An IRDiRC Perspective. *Clin Transl Sci.* 2018;11(1):11-20.
309. Keeling K, Bedwell DM. Therapeutics Based on Stop Codon Readthrough . *Annu Rev Genomics Hum Genet.* 2014;15:371-394.
310. Bidou L, Allamand V, Rousset J-P, Namy O. Sense from nonsense: therapies for premature stop codon diseases. *Trends Mol Med.* 2012;18(11):679-688.
311. Mutyam V, Du M, Xue X, et al. Discovery of Clinically Approved Agents That Promote Suppression of Cystic Fibrosis Transmembrane Conductance Regulator Nonsense Mutations. *Am J Respir Crit Care Med.* 2016;194(9):1092-1103.
312. Linde L, Kerem B. Introducing sense into nonsense in treatments of human genetic diseases. *Trends Genet.* 2008;24(11):552-563.
313. Palmer E, Wilhelm JM. Mistranslation in a eucaryotic organism. *Cell.* 1978;13(2):329-334.
314. Kapoor G, Saigal S, Elongavan A. Action and resistance mechanisms of antibiotics: A guide for clinicians. *J Anaesthesiol Clin Pharmacol.* 2017;33(3):300-305.
315. Burke JF, Mogg AE. Suppression of a nonsense mutation in mammalian cells in vivo by the aminoglycoside antibiotics G-418 and paromomycin. *Nucleic Acids Res.* 1985;13(17):6265-6272.
316. Ng MY, Li H, Ghelfi MD, Goldman YE, Cooperman BS. Ataluren and aminoglycosides stimulate read-through of nonsense codons by orthogonal mechanisms. *PNAS.* 2021;118(2).

317. Dabrowski M, Bukowy-Bieryllo Z, Zietkiewicz E. Advances in therapeutic use of a drug-stimulated translational readthrough of premature termination codons. *Mol Med*. 2018;24(1):1-15.
318. Landfeldt E, Sejersen T, Tulinius M. A mini-review and implementation model for using ataluren to treat nonsense mutation Duchenne muscular dystrophy. *Acta Paediatr*. 2018;108(2):224-230.
319. Kozauer N, Bastings E, Dunn B. *FDA Briefing Document.*; 2017.
320. Campbell C, Barohn RJ, Bertini E, et al. Meta-analyses of ataluren randomized controlled trials in nonsense mutation Duchenne muscular dystrophy. Published online 2020.
321. Wangen JR, Green R. Stop codon context influences genome-wide stimulation of termination codon readthrough by aminoglycosides. *Elife*. 2020;9:1-29.
322. Keeling KM, Wang D, Conard SE, Bedwell DM. Suppression of premature termination codons as a therapeutic approach. *Crit Rev Biochem Mol Biol*. 2012;47(5):444-463.
323. Floquet C, Hatin I, Rousset J-P, Bidou L. Statistical Analysis of Readthrough Levels for Nonsense Mutations in Mammalian Cells Reveals a Major Determinant of Response to Gentamicin. Flanigan KM, ed. *PLoS Genet*. 2012;8(3):e1002608-12.
324. Singh S, Ganesh S. Lafora progressive myoclonus epilepsy: A meta-analysis of reported mutations in the first decade following the discovery of the EPM2A and NHLRC1 genes. *Hum Mutat*. 2009;30(5):715-723.
325. Varea O, Duran J, Aguilera M, Prats N, Guinovart JJ. Suppression of glycogen synthesis as a treatment for Lafora disease: Establishing the window of opportunity. *Neurobiol Dis*. 2020;147:105173.
326. Gumusgoz E, Guisso DR, Kasiri S, et al. Targeting Gys1 with AAV-SaCas9 Decreases Pathogenic Polyglucosan Bodies and Neuroinflammation in Adult Polyglucosan Body and Lafora Disease Mouse Models. *Neurotherapeutics*. Published online 2021.
327. Maidorn M, Olichon A, Rizzoli SO, Opazo F. Nanobodies reveal an extra-synaptic population of SNAP-25 and Syntaxin 1A in hippocampal neurons. *MAbs*. 2019;11(2):305-321.
328. Dong JX, Lee Y, Kirmiz M, et al. A toolbox of nanobodies developed and validated for use as intrabodies and nanoscale immunolabels in mammalian brain neurons. *Elife*. 2019;8:1-25.
329. Simmons ZR, Sharma S, Wayne J, Li S, Vander Kooi CW, Gentry MS. Generation and characterization of a laforin nanobody inhibitor. *Clin Biochem*. 2021;(April):5:S0009-9120(21)00099-0.

330. Nguyen VT, Morange M, Bensaude O. Firefly luciferase luminescence assays using scintillation counters for quantitation in transfected mammalian cells. *Anal Biochem.* 1988;171(2):404-408.
331. Neumann J, Morency C, Russian K. A novel rapid assay for chloramphenicol acetyltransferase gene expression. *Biotechniques.* 1987;5:444-448.
332. Miller JH. *Experiments in Molecular Genetics.* Cold Spring Harbor Laboratory, Cold Spring Harbor, N.Y.; 1972.
333. Kervestin S, Jacobson A. NMD: a multifaceted response to premature translational termination. *Nat Rev Mol Cell Biol.* 2012;13(11):700-712.
334. mez-Garre PG, Sanz Y, de Córdoba SR \iguez, et al. Mutational spectrum of the EPM2A gene in progressive myoclonus epilepsy of Lafora: high degree of allelic heterogeneity and prevalence of deletions. *Eur J Hum Genet.* 2000;8(12):946-954.
335. Poyrazolu HG, Karaca E, Per H, et al. Three Patients With Lafora Disease: Different Clinical Presentations and a Novel Mutation. *J Child Neurol.* 2015;30(6):777-781.
336. Lesca G, Boutry-Kryza N, De Toffol B, et al. Novel mutations in EPM2A and NHLRC1 widen the spectrum of Lafora disease. *Epilepsia.* 2010;51(9):1691-1698.
337. Jara-Prado A, Ochoa A, Alonso MEME, et al. Late onset Lafora disease and novel EPM2A mutations: Breaking paradigms. *Epilepsy Res.* 2014;108(9):1501-1510.
338. Ferlazzo E, Canafoglia L, Michelucci R, et al. Mild Lafora disease: Clinical, neurophysiologic, and genetic findings. *Epilepsia.* 2014;55(12):e129--e133.
339. Chatzistefanidis D, Giaka K, Georgiou I, Kyritsis AP, Markoula S. A novel nonsense mutation of the EPM2A gene in Northwest Greece causing myoclonic epilepsy. *Seizure Eur J Epilepsy.* 2013;22(4):315-317.
340. Popescu A, Sidorova E, Zhang G, Eubanks J. Aminoglycoside-Mediated Partial Suppression of MECP2 Nonsense Mutations Responsible for Rett Syndrome in Vitro. *J Neurosci Res.* 2010;(88):2316-2324.
341. Baradaran-Heravi A, Niesser J, Balgi AD, et al. Gentamicin B1 is a minor gentamicin component with major nonsense mutation suppression activity. *Proc Natl Acad Sci.* 2017;114(13):3479-3484.
342. Friesen WJ, Johnson B, Sierra J, et al. The minor gentamicin complex component, X2, is a potent premature stop codon readthrough molecule with therapeutic potential. Stoecklin G, ed. *PLoS One.* 2018;13(10):e0206158.
343. Sherwood AR, Johnson MB, Delgado-Escueta A V., Gentry MS. A bioassay for Lafora disease and laforin glucan phosphatase activity. *Clin Biochem.* 2013;46(18):1-8.

344. Austin GL, Simmons ZR, Klier JE, et al. Central Nervous System Delivery and Biodistribution Analysis of an Antibody-Enzyme Fusion for the Treatment of Lafora Disease. *Mol Pharm*. Published online July 2019.

## VITA

### Zoe Raine Simmons

#### Degree

- BS Biology (concentrations: neuroscience, pre-med), Stony Brook University

#### Professional positions held

- Neurotechnology Manager, Brain Wellness Center. September 2012 – Fall 2015.
- Student Research, Department of Neurobiology & Behavior, Stony Brook University. Fall 2011, Spring 2012.
- Research Assistant, Department of Cellular & Molecular Neuroscience, Langone Medical Center, New York University Summer 2010 & 2011.

#### Scholastic and professional honors

- National Institute of Health (NIH) Clinical and Translational Science Fellowship (TL1)

#### Professional publications

- **Simmons, Z.R.**, and Sharma, S., Wayne, J., Li, S., Vander Kooi C.W., Gentry, M.S. Generation and characterization of a laforin nanobody inhibitor (2021). *Clinical Biochemistry*.
- **Simmons, Z.R.**, Macedo, M., Markussen, K., Kim, J.R., Bolten, K.E., Schmitt, S.M., Sun, R., and Gentry, M.S. Pathological biomarkers of a glycogen storage disorder on the aging brain (in preparation).
- **Simmons, Z.R.**, and Gentry, M.S. The glycogen dysmetabolism hypothesis of neurodegenerative diseases: convergent clues from neuropathology and biochemistry (in preparation).
- Brewer, M.K., Machio-Castello, M., Viana, R., Wayne, J., Kuchtová, A., **Simmons, Z.R.**, Sternbach, S., Li, S., Garcia-Gimeno and M.A., Serratos, J., Sanz, P., Vander Kooi, C.W., Gentry, M.S. An empirical pipeline for personalized diagnosis of Lafora disease mutations (2021). *BioRxiv*.
- Brewer, M.K., Uittenbogaard, A., Austin, G.L., Segvich, D.M., DePaoli-Roach, A., Roach, P.J., McCarthy, J.J., **Simmons, Z.R.**, Brandon, J.A., Zhou, Z., Zeller, J., Young, L.E.A., Sun, R.C., Pauly, J.R., Aziz, N.M., Hodges, B.L., McKnight, T.R., Armstrong, D.D., and Gentry, M.S. Targeting pathogenic Lafora Bodies in Lafora Disease Using an Antibody-Enzyme Fusion (2019). *Cell Metabolism*.
- Austin, G. L., **Simmons, Z. R.**, Klier, J. E., Rondon, A., Hodges, B. L., Shaffer, R., Aziz, N.M., McKnight, T.R., Pauly, J.R., Armstrong, D.D., Vander Kooi, C.W., and Gentry, M.S. Central Nervous System Delivery and Biodistribution Analysis of an Antibody-Enzyme Fusion for the Treatment of Lafora Disease (2019). *Molecular Pharmaceutics*.